The Dissertation Committee for Saeid Enayatpour
certifies that this is the approved version of the following dissertation:

Numerical Modeling of Thermal Fracture Development in Unconventional Reservoirs

Committee:

Tadeusz W. Patzek, Supervisor

Jon Olson

John Tassoulas

Kamy Sepehrnoori

Mukul M. Sharma

Numerical Modeling of Thermal Fracture Development in Unconventional Reservoirs

by

Saeid Enayatpour, B.S.C.E.; M.S.C.E.; M.S.

DISSERTATION

Presented to the Faculty of the Graduate School of

The University of Texas at Austin

in Partial Fulfillment

of the Requirements

for the Degree of

DOCTOR OF PHILOSOPHY

THE UNIVERSITY OF TEXAS AT AUSTIN

May 2015

To Him,

who knows everything!

To my wife and daughters,

Maryam, Parisa, and Parinaz.

To my mother and father,

whose unconditional love, support and sacrifice have lit my life.

Acknowledgments

I would like to express sincere gratitude to my supervisor Dr. Tad Patzek, for facilitating the best graduate school experience that I could have hoped for. His guidance, enthusiasm, and generosity have made the last five years an exciting journey of challenges and discovery, which was as satisfying as the end. I am deeply indebted for that. I would also like to thank my other committee members, Drs. Olson, Sepehrnoori, Sharma, and Tassoulas, for their comments, compliments, criticisms, and corrections.

I have also benefitted from many hours of discussions that have spurred an idea or warm encouragement delivered unwittingly. For much of that, I would like to thank my friends and colleagues: Javad Behseresht, Mohamad Hosein Kalaei, Behzad Eftekhari, HamidReza Lashgari, Chih-Hung Chen, Rasoul Khaledialidusti, and Frank Male. Special thanks to Ali Najafi from ANSYS for collaborating on this project and Mahdi Kefayati for providing help with document preparation in LaTeX.

Weekly meetings and discussions with Dr. Marder and Dr. Patzek were insightful research experience and I would like to appreciate the team comments and discussions which were of great help to me. Many thanks go to the UT PGE staff, Roger Terzian, Geln Baum, Lydia Pruneda, and Sandy Taylor for always being so helpful, patient and friendly. Acknowledgements

are also due to the Texas Advanced Computing Center for providing high-performance computing resource for this research.

I would like to thank my family for their unconditional love and support: my parents, my wife and my daughters who have made innumerable sacrifices for me.

Finally, I would like to thank financial support from the Department of Petroleum and Geosystems Engineering at The University of Texas at Austin.

Numerical Modeling of Thermal Fracture Development in Unconventional Reservoirs

Publication No. _____

Saeid Enayatpour, Ph.D.
The University of Texas at Austin, 2015

Supervisor: Tadeusz W. Patzek

Rapid depletion of hydrocarbons in conventional reservoirs and the availability of abundant oil and gas resources in unconventional forms demand new technology to economically produce these energy resources. From exploration to consumption of hydrocarbons, a great number of complex physical, chemical, mechanical, electrical, and thermal phenomena occurs in reservoir from reservoir rock to surface facilities. In addition to good rock samples and cores which could represent the reservoir rock for laboratory experiments, numerical tools should always be used to provide predictive capability of reservoir rock and fluid behavior. A great number of numerical methods have been developed and used over the past decades for rock mechanics problems. In this research the main focus is on thermal fracturing, heat transfer in rock, flow in porous media and stress-deformation analysis. We use three numerical methods for thermal fracturing of reservoir rock and investigate their capabilities in providing a solution for fracture propagation in rock. We finally propose the

best numerical method among the ones we used in this work. We finally show two applications of thermal rock fracturing for improvement of hydrocarbon recovery in tight formations.

Table of Contents

List of Tables

List of Figures

Chapter 1

Introduction

1.1 Overview of the Dissertation

This dissertation presents two inter-related studies. Chapter 2 presents a mathematical model of micro-fracture initiation and propagation in low permeability rocks. We solve the nonlinear rock damage PDE to gain insights into patterns of damage propagation in reservoir rock. We then obtain material-dependent parameters of rock which dictate damage propagation mode. These include damage diffusion parameter and the microstructural length of rock damage.

The damage diffusion parameter is by far the most important parameter needed for rock damage analysis. Experimental observations in conjunction with inverse analysis is required to obtain it. Damage diffusion leads to permeability enhancement. The most effective means to induce damage is to elevate the pore pressure (similar to hydraulic fracturing). For the elevated pore pressure to diffuse into the rock, open pathways are required. Chapter 3 covers just enough details from the theory of rock fracture mechanics to clarify the ideas presented in this dissertation. The main objective of Chapter 3 is to introduce to the reader the terminology of fracture mechanics in general,

and the concepts of stress intensity factor and energy release rate so as to set the scene for the reader to appreciate the concept and formulation of thermal fracturing in shale plays. In Chapter 4 we present a thermo-elastic technic whereby the rock around the wellbore will be subjected to thermal loading shocks. This creates the initial pathways to facilitate pore pressure diffusion in low permeability rock (now, higher permeability rock in the zones where the thermal shocks are imposed). Numerical simulations are then used to describe the thermo-elastic behavior of reservoir rock in terms of coupled stress, temperature and pore pressure fields. We will present the effectiveness of thermal shocking technic through finite element analysis of the reservoir rock around the wellbore. In Chapter 5, we use the discrete element method (DEM) to obtain the thermal fractures network that evolves as the rock is cooled. The permeability can then be calculated using a pore network model which is not the subject of this work. Here we present Discrete Element Method (DEM) analysis for thermal fracturing and show the effect of key DEM parameters, including rock stiffness and time-step, on the solution. In Chapter 6, we propose a physics-based continuum approach combined with fracture mechanics to simulate the thermal fracturing process. Cohesive zone elements are used to treat de-bonding between continuum elements. By combining both fracture cohesive and continuum elements, we show that the physics of transport in a continuum framework as well as crack propagation can be effectively captured in an implicit integration scheme in a finite element model. This approach allows us to investigate the uncertainty associated with shale properties (elas-

tic modulus, heat conductivity, etc) and formation fracture properties. The present quantitative approach is used to perform global statistical sensitivity analysis to investigate the robustness of the thermal fracturing process with respect to the input parameters such as the freezing temperature level and the exposure time. In Chapter 7, we compare the numerical tools used in this dissertation for the problem of rock fracture (Table 7.1). We show that there does not exist a single tool which can carry out all the simulation needs, including: selection of computation time and material behavior; accounting for mesh adjustments due to fracturing and the coupled nature of problem, etc. As a result, it is not quite possible to introduce a flawless software package or method for fracturing analysis in a coupled physics framework. In Chapter 8, based on our numerical modeling of thermal fracturing propagation potential in the near wellbore zone in Section 4.7 and analytical modeling of thermal fracturing in the vicinity of hydraulic fractures in Section 4.4, we compute hydrocarbon recovery improvement due to thermal fracturing in two application scenarios. In Chapter 9, we present the conclusion of this study and propose future directions for this research.

Chapter 2

Volumetric Rock Stimulation

2.1 Introduction

Solid mechanics and strength of materials are two of the oldest engineering mechanics problems. The fundamental works of Galileo [88] and Griffith [99] were the early steps in predicting the fracture strength of materials using an energy balance approach. In "Two New Sciences" (1638), Galileo asked the question how long an object under load can last before it fails due to damage. This question was much deeper and very different than those asked by Robert Hooke in 1660, when he discovered the laws of elasticity. In petroleum engineering, the problem of rock fracturing is one of the problems which has been looked into for years. However, rock fracture is more important now due to demand for production from the low permeability mudstone reservoirs. Continuum damage mechanics (CDM) is a branch of solid mechanics which deals with the formation and coalescence of micro-fractures at various scales, called in general, micro-defects. Micro-defects are created by mechanical or environmental loads. These loads result in deterioration of the microstructure of materials, leading to the loss of material stiffness. Damage mechanic looks into the formation of damage. As the damage propagates, the material body becomes fragmented. To study fragmented materials, fracture mechanics is

used to deal with discrete micro-cracks in a continuum material. Another approach to study such materials is damage mechanics which brings in the effect of flaws in a volume of rock in the form of scalar parameter called damage parameter. This later approach is what we are presenting in this chapter.

Here we study the mathematical model of initiation and propagation of micro-fractures in low permeability rocks. We solve a nonlinear PDE that describes rock "damage" to gain an insight on patterns of damage propagation in reservoir rock. We then obtain the material-dependent parameters of rock such as damage diffusion parameter and the microstructural length of rock damage which dictate the mode of propagation of damage. This is by far the most important parameter to obtain for rock damage analysis; therefore, experimental observations in conjunction with inverse analysis will be used to obtain it. The most effective means of fracture creation in rock is to elevate the pore pressure as it has been used for hydraulic fracturing; however, to induce damage in the volume of rock for permeability enhancement, the elevated pore pressure has to diffuse into rock for which it requires to have open pathways. To create conductive pathways in rock, we are coming up with thermo-elastic technic whereby the rock around the wellbore will be subjected to thermal loading shocks. This creates the initial pathways to facilitate the pore pressure diffusion in low permeability rock (now, higher permeability rock in the zones where the thermal shocks are imposed). Numerical simulations are then used to study the thermo-elastic behavior of reservoir rock. For this, the coupled stress, temperature and pore pressure fields have to be

solved. We will present the effectiveness of thermal shocking technic through the finite element analysis of reservoir rock around the wellbore. Finally the damaged or stimulated rock properties by combination of pore pressure elevation and temperature reduction are incorporated into a permeability model of k=k(damage). This will then be plugged into the flow rate to obtain the transient flow rate of hydrocarbon in porous media taking into account the enhancing effect of progressive damage.

The concept of damage as a basis for fracture mechanics was first introduced by Kachanov[126, 127]. He introduced the concept of endurance strength, i.e., the stress leading to failure at a given temperature, after a finite time. That failure was called the "life time" or "rupture time". The first attempt in determining the failure time was made by Hoff[112]. He studied the stretching of a cylindrical rod subject to constant load. According to the concept he introduced, the time to failure is infinite for infinite elongation of rod when cross sectional area approaches zero. Hoff's definition does not correspond to experimental results. Staniukovich[222] extended the work of Hoff and obtained by experiment the cumulative strain to the instant of failure. Kachanov studied damage or bond breakage mechanism. He showed that the coalescence of cracks could lead to material rupture. He also classified failure to brittle and ductile failures. The former occurs along the grain boundaries and is called "fracture" and the latter occurs as a result of plasticity of grains and is called "damage". He characterized the state of partial damage by a scalar quantity ψ called continuity, $(0 \leq \psi \leq 1)$. Some articles use the damage

parameter ω instead of continuity parameter. Damage parameter is related to continuity using $\omega = 1 - \psi$. Kachanov also showed that the lifetime for ductile failure is greater than that of brittle failure. This is in good agreement with Hoff's scheme, i.e., the cross sectional area of the rod vanishes before the continuity ψ is exhausted.

Application of load to a certain level on a solid material could create damage. The presence of microstructure affects the damage accumulation process and leads to a nonlinear parabolic partial differential equation with a source term [21]. This equation is of diffusion type with a strongly stress-dependent diffusion coefficient. Due to the non-healing nature of damage, the rate of damage accumulation cannot be negative, adding another level of nonlinearity to the equation. This section studies the numerical solution of the damage equation. Depending on the value of a dimensionless constant parameter, essentially two regimes of damage accumulation are observed for a given initial damage distribution. In the first type, damage accumulation remains local about the initially damaged zone. The lifetime or the time to rupture is determined by how fast damage increases locally. In this case a big portion of specimen cannot contribute to total load carrying capacity. The second type of process is nonlocal damage accumulation in which damage becomes homogenous in specimen or part of the specimen and then advances uniformly over the specimen. The numerical calculations presented here demonstrate the existence of these two regimes of damage propagation. They demonstrate in particular that in the second regime, the ultimate value of damage parameter

is not of much significance as the major portion of the lifetime is taken for damage to propagate uniformly over the specimen below the blow-up limit.

2.1.1 Damage evolution in rock

Damage at a point can be physically interpreted as the properly averaged fraction of broken bonds among microstructural elements of the body. Since every broken bond would preclude the material from load carrying or load transfer we could express isotropic damage in terms of stresses in the case of a prismatic rod as

$$\omega = \frac{S - S_r}{S} \tag{2.1}$$

S_r in equation (2.1) is the portion of the total cross subsection, S, that remains intact and can carry load. The damage parameter at continuum scale is a quantity that describes the ability of a solid body to transport the momentum. Therefore in isotropic damage mechanics, the damage parameter ω is introduced as a scalar, or equivalently a continuity factor ψ=$1 - \omega$, so that in original pristine material ω=0, ψ=1. Fracture then corresponds to ω=1, ψ=0. In practice, ω can never attain 1.0 and failure occurs earlier, at ω <1, by stress localization [193].

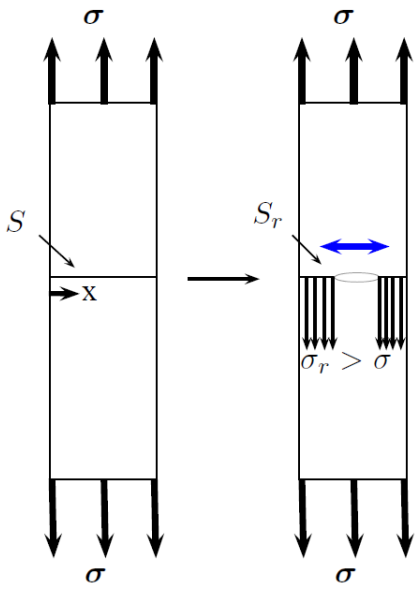

Figure 2.1: Macroscopic interpretation of isotropic damage

The stress that can be carried across a partially damaged cross section of the material is σ, which is related to the bulk stress σ_0 and damage parameter ω by the equation;

$$\sigma = \frac{\sigma_0}{(1-\omega)} \tag{2.2}$$

Notice that the stress is applied along the bar and the damage propagates along the x axis.

The isotropic, homogenous damage theory, originally developed by Kachanov [126, 127] is based on simple ordinary differential equation of the

form;

$$\dot{\omega} = \tau^{-1} q(\omega, \sigma, T) \tag{2.3}$$

which governs the evolution of damage. Here τ is the characteristic time of damage evolution and q is the dimensionless damage accumulation term which is a non-negative function specified for a given material, Equation (2.6).

Arrhenius' equation is a simple empirical relationship [56] to express the temperature dependence of reaction rates. It can be used to model the temperature variation of many thermally-induced reactions such as diffusion coefficient. The equation was proposed by Svante Arrhenius in 1889, based on the work of Dutch chemist J. H. van't Hoff(1884). Arrhenius provided a physical justification and interpretation for the formula [143]. This relationship can be expressed as Equations (2.4) or (2.5) to give the dependence of the rate constant q of a chemical reaction on the absolute temperature T (in kelvin), where A is the pre-exponential factor, E_a is the activation energy, k, the multiplier of temperature T, is the Boltzmann constant, and R is the Universal gas constant.

$$q = Ae^{\frac{-E_a}{(RT)}} \tag{2.4}$$

or alternatively,

$$q = Ae^{\frac{-E_a}{(kT)}} \tag{2.5}$$

E_a is the energy per mole in Equation (2.4), which is common in chemistry and is the energy per molecule in Equation (2.5), which is common in physics.

The units of the pre-exponential factor A are identical to those of the rate constant and will vary depending on the order of the reaction. If the reaction is first order it has the units s^{-1}, and for that reason it is often called the frequency factor or attempt frequency of the reaction. Most simply, k is the number of collisions that result in a reaction per second, A is the total number of collisions (leading to a reaction or not) per second and $e^{-E_a/(RT)}$ is the probability that any given collision will result in a reaction. It can be seen that either increasing the temperature or decreasing the activation energy (for example through the use of catalysts) will result in an increase in rate of reaction.

Given the small temperature range kinetic studies occur in, it is reasonable to approximate the activation energy as being independent of the temperature. Similarly, under a wide range of practical conditions, the weak temperature dependence of the pre-exponential factor is negligible compared to the temperature dependence of the $\exp(-E_a/RT)$ factor; except in the case of "barrierless" diffusion-limited reactions, in which case the pre-exponential factor is dominant and is directly observable.

An Arrhenius-type kinetic law with stress-dependent activation energy is used to calculate damage accumulation [21]:

$$q(\omega, \sigma, T) = (1-\omega)^p \exp\left(-\frac{(U-\gamma\sigma)}{kT}\right) \tag{2.6}$$

Understanding the parameters in Equation (2.6) is essential to analyze dam-

age; therefore, this section is devoted to explaining the physics behind these parameters.

k in (2.6) is the universal Boltzmann constant; U, the zero-stress activation energy, is another constant specific for a given bond-breaking chemical reaction; p, the constant kinetic 'reaction order' ; T is the temperature; τ is the characteristic time for damage accumulation. U can be interpreted as the magnitude of the energy barrier determining the probability of breakage of the bonds responsible for strength. The kinetic law expressed in (2.6) assumes that the breaking of bonds is thermally activated. In presence of tensile stress σ, the net activation energy required to initiate the bonds breakage is $U - \gamma\sigma$, (effective barrier). γ is another kinetic constant, a dimensionless parameter which is a function of material properties. It should be noted that this effective barrier decreases with increasing tensile stress. The pore pressure in a reservoir rock must increase in order to increase tensile stress in the rock matrix, and initiate and propagate fracture.

In a stressed body, thermal fluctuations break chemical bonds and the possibility of this process depends strongly on the magnitude of tensile stress. The tensile stress excites the bonds to be ruptured and reduces the activation energy. The magnitude of decrease of the effective energy barrier is determined by γ. It can be shown that the tensile strength of solids or the critical tensile load at rupture–σ_{critical}, is inversely proportional to the parameter γ [265].

$$\sigma_{\text{critical}} = A/\gamma \ \ (A\text{=constant})$$

Arrhenius-type kinetic law is based on the physical interpretation of damage as the fraction of the broken bonds averaged so that the macroscopic damage equation can be obtained from the evolution of damage within the micro-scale representative elementary volume of rock.

It should also be noted that in Equation (2.6), the quantities in the exponent, U/kT and $\gamma\sigma/kT$ are of the order of ten or even several tens. This is to say that the rate of damage accumulation has a stronger dependence on the stress and temperature than on the current state of damage which is governed by pre-exponential factor. The pre-exponential factor indicates that the rate of damage accumulation is proportional to some power of the number of unbroken bonds or the portion of the cross section which has load carrying capacity. For our analysis, we assume p=1 everywhere (i.e., the rate of increase of damage parameter is proportional to the relative number of unbroken bonds).

Equations for material rupture were first proposed by Zhurkov [265]. He performed a number of experiments on 50 materials including metals, alloys, non-metallic crystals and polymers to study the life-time of solids under temperature and stress. He then proposed the equation (2.7) for the life-time of solids under tensile stress:

$$\tau = \tau_0 \exp\left(\frac{(U - \gamma\sigma)}{kT}\right) \tag{2.7}$$

He introduced an equation for bond rupture rate as:

$$\dot{\omega} = \frac{c}{\tau_0} \exp\left(-\frac{(U - \gamma\sigma)}{kT}\right) \tag{2.8}$$

which is similar to equation (2.3) with the kinetic law (2.6), except for the factor of $(1-\omega)^p$ which captures the portion of unbroken bonds of the kinetic law. In proposing these equations Zhurkov used results of the experiments he performed. He also assumed that the life-time of a stressed material is completely determined by the rate of accumulation of the ruptured bonds. Therefore, he concluded that the product of the life-time and the bond rupture rate for a material should be constant and verified it by experiment, i.e.,

$$\tau\dot{\omega} = c \text{ (constant)}$$

Zhurkov carried out experiments on several materials including polycrystalline aluminum, silver chloride and plexiglass. As shown in Figure 2.2, Zhurkov observed that the time and temperature dependence of the strength of solids with different types of interatomic bonding, is identical. The relationship shown in this figure and expressed in Equation (2.7) has been found correct as a general rule and valid for describing the strength properties of all solids that Zhurkov investigated. The parameter τ_0 is constant for all solids and it is the lifetime for material at fracture tensile load. As tensile stress is increased on a solid, the solid eventually ruptures at a critical fracture stress. If however this load is applied instantaneously, it takes the time τ_0 for the material to fracture. In other words, τ_0 is the blow-up time for material at no damage diffusion. Later on we make this parameter dimensionless for numerical analysis and

call it θ_0. The value of τ_0 for the solids shown in Figure 2.2 is 10^{-13} sec. Experimental data for other solids show the same order of magnitude for this parameter. Figure 2.2 supports Equation (2.7)

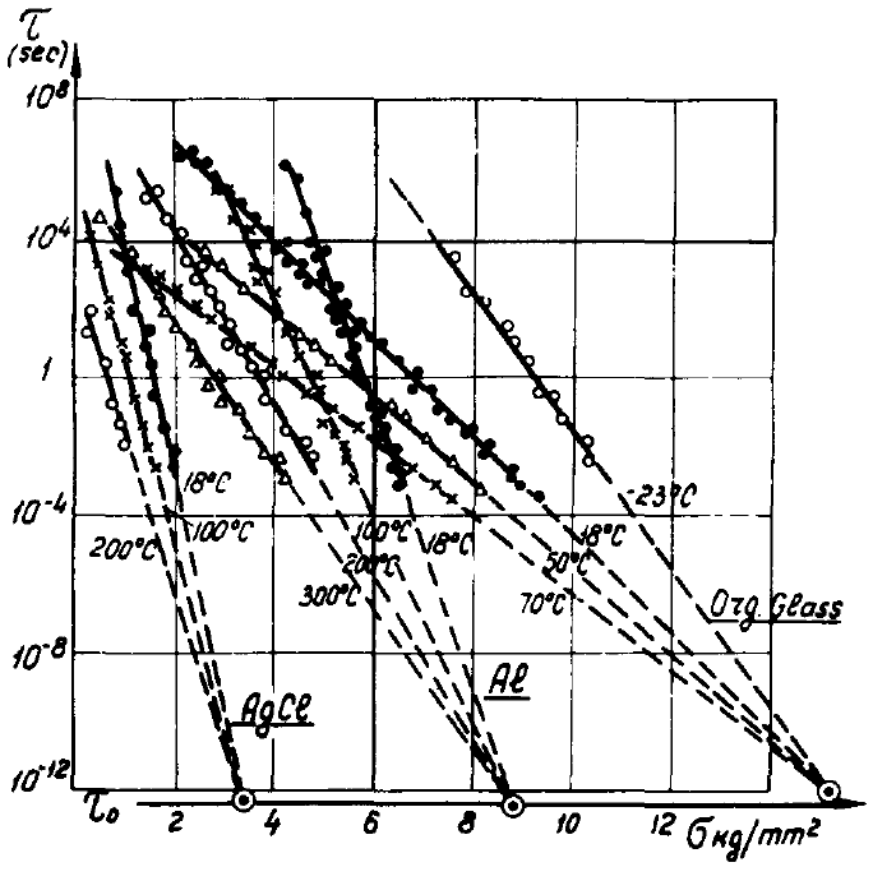

Figure 2.2: Time and temperature dependence of the lifetime of solids under tensile stress (From [265]).

The kinetic concept of strength of materials splits the fracture process into three stages:

1. Tensile stress makes it easier for the chemical bonds to be ruptured;

2. Thermal fluctuations break the excited bonds;

3. Accumulation of broken bonds results in stress concentration and a loss of stability in the body, leading to breakdown.

An important question that needs to be answered is how real materials break. Material fracturing studies show that real materials such as metal, ceramics and rocks are made up of grains and inter-granular bonds among the grains. There are always two forms of rupture; grain rupture and grain interface rupture. Figure 2.3 shows single grains attached to one another by a weak cementation bond to form a cluster of grains. These clusters of elements could then be attached to one another by a stronger bond. Figure 2.4 shows the particles of sand and sedimentary rock formed by the bond between sand particles.

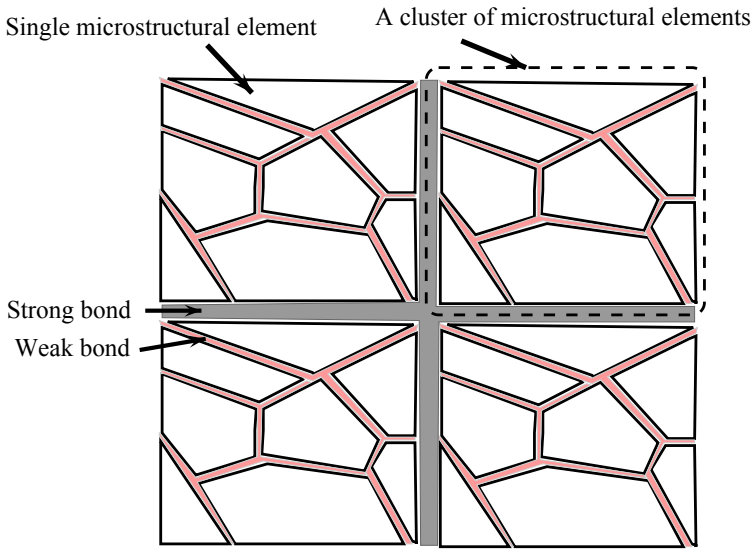

Figure 2.3: The cluster of grains formed through the attachment of single grains by a weak cementation bond. The clusters of elements are attached to one another by a stronger bond.

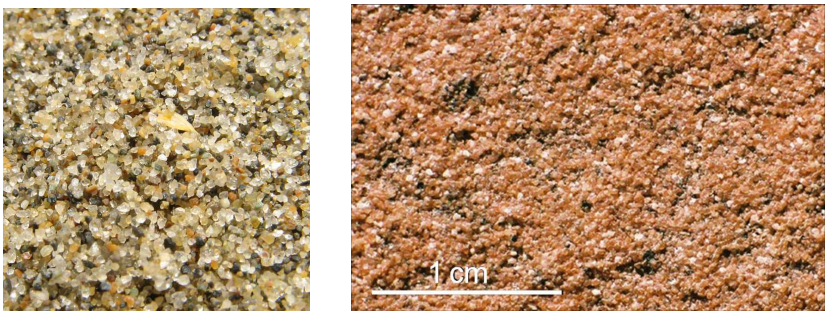

(a) Beach sand particles (b) Sandstone

Figure 2.4: (a) The unbonded particles of sand and (b) A sedimentary rock formed by bonding these sand particles.

Damage is the process of breaking bonds between the microstructural

elements and/or inside these elements. Elements are either grains or clusters of grains as defined above. The particles have various sizes and their properties vary. Therefore the damage process is micro-inhomogeneous due to these variations in size and property. When a rock specimen is subjected to tensile stress as in the case of injection of fluid to rock pores, the initiation of cracks at grain boundaries increases the local stresses and, therefore, increases the local rate of damage accumulation. Conversely, when a crack reaches a stronger bond, local inhibition of crack propagation reduces the local damage accumulation rate. In other words, as an external load imposes crack formation in the rock matrix, an internal system of self-balanced micro-stresses appears. Various types of micro-stress systems are created by:

- Thermal oil recovery processes: During thermal processing, heat is injected and transported into reservoir rock. As a result, rock expands; however, due to all around confinement, thermal micro-stresses develop in the rock microstructure.

- Micro-inhomogeneity of rock: size and property variations of grain constituents contribute to micro-inhomogeneity of rock. Any loadings on rock whether thermal loading as described above or loading from injection of fluid when faced with a micro-inhomogeneous structure, develops new stresses which depend not only on the loading itself, but also on different strengths of rock constituents. In other words, elements of rock exhibit different compliance to the load they are exposed to, hence they

will be subjected to different loads. The more compliance they possess, the less load they will be subjected to. The term compliance has to do with geometry and material property of a structure. For instance, the compliance for a spring is k^{-1}, where k is the spring stiffness. For a rod of constant cross section A, length L and Young's modulus E, the compliance is $\frac{L}{AE}$.

If a micro-inhomogeneous rock is replaced with a microscopically homogenous rock subjected to tensile load, the local micro-stresses in the later specimen will differ from those of the real (inhomogeneous) specimen due to the self-balanced micro-stresses described earlier. This in turn contributes to the formation of a micro-stress field which is a function of the geometry and strength of bonds in the microstructure of rock. The mathematical equation of damage evolution in rock is derived and explained in detail in Appendix A. The effect of microstructure of rock is described in the "Measurement of characteristic length".

2.2 Description of the Problem

The recovery of hydrocarbons from reservoir rock could be improved by the rock permeability enhancement, here called "rock damage" or "matrix stimulation". In tight formations, such as oil shales or gas shales with very low permeabilities[69], rock stimulation is essential to improving recovery. However, the stimulation of rock results in degradation of matrix stiffness which

could result in subsidence of reservoir and well and casing failures. For example, the giant diatomaceous oil fields in California, Lost Hills and Belridge, contain some 10 billion barrels of oil in place [92]. The diatomite rock has a very fragile structure, high porosity, low permeability and low fracture toughness. The SEM microphotograph of the diatomite rock shows its complex and fragile microstructure, (Figure 2.5). Therefore production from diatomite can start only after changing the rock microstructure. Due to the complex and disordered pattern of damage, the current models of fluid-rock system cannot capture the rearrangement of the diatomite microstructure caused by fluid withdrawal and injection and have little predictive capability.

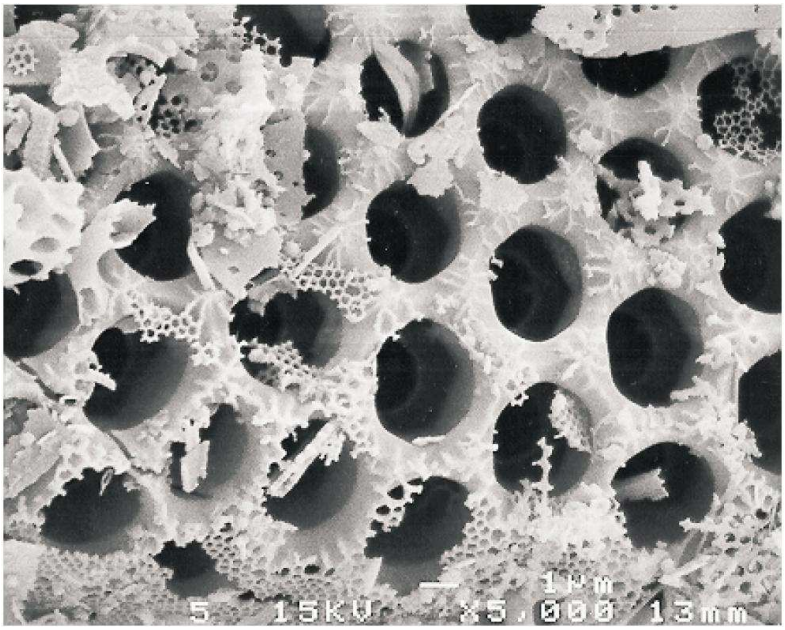

Figure 2.5: The fragile microstructure of the diatomite rock in SEM microphotograph. Courtesy of T.W. Patzek.[92]

The process of rock damage has been studied extensively in engineering applications. In petroleum engineering, however, these studies are limited to macro-scale fracture analysis. Fracture takes place only when rock has undergone a considerable amount of damage. To understand the complex evolution of rock damage, a micro-scale study is necessary.

During hydraulic fracturing operations, the rock microstructure undergoes damage. The ongoing damage is a function of stress, temperature and the current state of damage. As the rock damage which is a non-healing process goes on, the stiffness of rock degrades. If the degradation is enough for fracture to open then fracture initiates. Once initiated, if fracture is to propagate, the same process of damage takes place, but this time the damage zone is contained on the tip of the crack called the fracture process zone (FPZ).

The main factors that affect damage and fracture in rock are:

1)At the micro-structural level:

- Stress distribution near the fracture zone
- Current distribution of damage
- Temperature
- Microstructure of rock

2)At the macro-structural level:

- Reservoir rock's mechanical properties such as toughness and stiffness

- Stress changes and re-orientation due to a crack opening[182]
- The presence of layers that bound the pay zone[182]
- The presence of natural fractures and possible interaction between induced and natural fractures[62]
- Magnitude of anisotropy of the in-situ stresses
- Orientation of natural fractures relative to hydraulic fractures
- Rate of loading
- Leak-off effect
- Temperature (shale toughness and tensile strength degrade drastically with temperature)[69].

To maximize oil recovery in tight formations, proper stimulation of reservoir rock should be conducted. Depending on the rock type, this stimulation should take into account a combination of the above factors. For instance, what rate of injection should we use for a rock with certain microstructure? Does shale fracture similarly at different temperatures?

To answer questions like these, we need to know the physics of rock damage. Once we know the physics involved, and obtain the governing equations, numerical methods should be invoked to find solutions. Due to simultaneous action of the equation coefficients, the obtained governing equations are extremely nonlinear, hence the analytical solutions are not available and

numerical solutions are the only means of finding solutions. But how can damage diffuse in rock? What is damage propagation in rock a function of? What is the fundamental equation or law to start from?

To fully appreciate the process of damage or bond breakage in rock, we need to step back and look into this process from microstructure level and study the physical law which explains this phenomenon. This law has first been proposed by Kachanov [126] as follows:

$$\frac{\mathrm{d}\omega}{\mathrm{d}t} = B\sigma^n \tag{2.9}$$

In this equation, σ is the stress and the constants B and n are obtained from experiment. This empirical kinetic equation is non-local and does not include the bond breaking mechanism. Since the rupture of bonds is a dynamic process, we are using the kinetic equation proposed and studied by Barenblatt and Prostokishin [21].

$$\frac{\mathrm{d}\omega}{\mathrm{d}t} = \tau^{-1}\left(1-\omega\right)^p \exp\left(-\frac{(U-\gamma\sigma)}{kT}\right) \tag{2.10}$$

The parameters of Equation (2.10) are defined earlier in this section. For detailed definition of these parameter see [265]. The kinetic law (2.6) assumes a thermo-fluctuational mechanism for breaking bonds. Equation (2.10) shows that the activation energy decreases with increasing tensile stress. The pre-exponential factor $(1-\omega)^p$ indicates that the damage accumulation rate is assumed to be proportional to some power of the number of unbroken bonds, i.e., of the cross sectional area that remains undamaged (reaction of pth order).

To study the propagation of damage, the spatial averaging of rock micro-inhomogeneities is required. The derivation of spatial averaging is presented in detail in Appendix A. The result is shown in Equation(2.11), which contains the microstructural properties of the rock embedded in the microstructural length scale, Λ.

$$\underbrace{\frac{\mathrm{d}\omega}{\mathrm{d}t}}_{\text{Damage accumulation term}} = \underbrace{\Lambda^2 \frac{\partial^2}{\partial x^2}[(1-\omega)\exp(\frac{\mu_0}{1-\omega})]}_{\text{Damage diffusion term}} + \underbrace{(1-\omega)\exp(\frac{\mu_0}{1-\omega})}_{\text{Source term}} \tag{2.11}$$

Equation (2.11) is a nonlinear differential equation valid at any point of the rock. It requires initial and boundary conditions. The initial results of solving this PDE show two distinct regimes of damage which depend upon the microstructure of the rock.

The question that arises here is do we need to understand damage and effects of stress changes on the evolution of damage in hydrocarbon recovery process? The answer is obviously, yes. For example, in tight formations, hydraulic fracturing and providing the highest possible conductive pathway to facilitate flow of hydrocarbon to wellbore is the key to improving recovery. Yet, despite the extensive research and significant achievements on rock damage and fracturing over the past two decades, there are applications which are fairly new and unknown to researchers such as fracturing in horizontal wells. The following shortcomings are still observed in the studies performed and should be addressed:

-The effect of pore pressure changes (pressure pulsing) on progressive damage

and fracture.

-The effect of in-situ stress changes due to progressive damage.

-Nonlinear behavior of rock.

-The effect of temperature on rock in macrostructure level (Tensile strength and toughness reduction in shale due to temperature), and

-The effect of rock microstructure on damage evolution of rock.

2.2.1 Averaging of damage evolution function

Let's take a time-independent geometrical domain Ω_0 for the rev, centered at the origin O of the coordinate system. For any translation vector x, let's assume that the elementary volume $\Omega(x)$ being obtained from Ω_0 using vector x, is a rev for material at that macroscopic point x, in it's current configuration. Furthermore, let the weight function or correlation function $\rho(\xi)$ be a C^∞ function defined at the microscopic scale. It is equal to zero outside Ω_0 and satisfies:

$$\int \rho(\xi)\, \mathrm{dV}_\xi = 1 \tag{2.12}$$

or in 1D it can be written as;

$$\int_{-\infty}^{\infty} \rho(x-\xi)\, \mathrm{d}\xi = 1 \tag{2.13}$$

The average $\overline{\Phi}(x)$ at the macroscopic point x of a physical quantity represented in $\Omega(x)$ by the volume density $\Phi(\xi)$ in 3D or linear density in 1D, is defined by:

$$\overline{\Phi}(x) = \int_{-\infty}^{\infty} \Phi(\xi)\rho(x-\xi)\,\mathrm{d}\xi \tag{2.14}$$

For the sake of simplicity the weight function is assumed to be symmetric, so that

$$\int_{-\infty}^{\infty} (x-\xi)\rho(x-\xi)\,\mathrm{d}\xi = 0 \tag{2.15}$$

"The weight function $\rho(x-\xi)$ determines the relative number of elements of cross sectional area, where the damage accumulation rate corresponds to the average stress in a neighboring cross-section having a certain coordinate ξ: This always can be done in principle"[21].

The microstructural length scale is then defined in [21] by the relation:

$$\lambda^2 = \int_{-\infty}^{\infty} \left[\frac{(x-\xi)^2}{2}\right] \rho(x-\xi)\,\mathrm{d}\xi \tag{2.16}$$

The reason λ^2 is defined in the form (2.16) is to simplify mathematical derivations in Appendix A, $\big($Equation (A.10)-III$\big)$. Moreover, λ^2 possesses a physical meaning which will be discussed here. We will see that it is related to the geometry of the rock matrix. This length scale is the size of the aggregates of coherent microstructural elements. It can also be interpreted as the maximum length at which, elements of rock still interact or transfer stresses. It is obvious that the stress at any point in a body is correlated to stresses at the neighboring points, but only up to a certain distance away from that point. Once that length is exceeded, we could say that the value of the weight function will be negligible outside the zone of this length. The length scale has to do only with the geometry of the rock matrix and loading does not play a role in obtaining

the weight function. In order to see the effect of the form of function $\rho(\xi)$ on λ^2, let's use the probability density function of the normal distribution as a function of the standard deviation σ and integrate (2.16):

$$\lambda^2 = \int_{-\infty}^{\infty} \left[\frac{(x-\xi)^2}{2}\right] \frac{1}{\sigma\sqrt{2\pi}} \exp\left[-\frac{(\xi-x)^2}{2\sigma^2}\right] \, \mathrm{d}\xi \tag{2.17}$$

Notice that x denotes both the average of normal distribution and the location of the REV in the global coordinate system. The two extreme values of the microstructural length scale are 10^{-2} and 10^{-5} and the values of standard deviation leading to these extreme values are consecutively, 0.141 and 4.48×10^{-3}.

2.2.2 Measurement of characteristic length of nonlocal continuum

The modeling of nonlocal damage mechanics has been the subject of extensive studies over the last years. A wide review of such problems can be found in [130, 139]. Among the large number of models, two main approaches may be highlighted: The continuum damage modeling and the micromechanical damage modeling. In continuum damage models the thermodynamic state of the rock and its changes are described by a damage variable ω [65, 130, 216]; therefore, the effect of evolving damage in a material on the response of the material is incorporated using these continuum damage models [93]. The most significant capability of these models is the simplicity of writing the constitutive relations and in their implementation into numerical codes. The micromechanical models however, are directly based on the descriptions of the various physical mechanisms involved. The sliding-crack

model is most often used as the basis for the formulation of micromechanical models [114, 128, 129, 135, 179].

The micromechanical models can be used to investigate the behavior of rock samples rather than of rock masses. One of the parameters required for micromechanical studies is the representative elementary volume (rev). From practical standpoint, rev is by far one of the most important parameters to be assigned when studying micromechanics of materials, for instance solving a fracture problem in rock. The importance of the rev is mainly because the rupture of polycrystalline materials including rock involves a number of physical mechanisms, such as nucleation and diffusive growth of grain boundary cavities and grain boundary sliding, which take place at different length scales in the material. Giessen [93] studied the effect of random variations in the microstructure of the material on its lifetime using a micromechanical model.

He put emphasis on the geometrical variation in the microstructure rather than variations in the material properties, i.e., he studied the effects of random variations in size and shape of grains in an aggregate.

2.2.3 Stress variation and correlation length in Porous Media

In the derivation of the damage equation outlined in Appendix A, equation (A.3) highlights the role of the weight function. As discussed earlier, the weight function, is a function of the rock matrix geometry, i.e., pore size and pore size distribution. Here an effort is made to obtain a relation between this function and the pore size of rock. The finite element modeling is utilized to

see the stress variations along a section which is simulating a cross section of rock under tension. The pore spaces in rock are modeled as voids in a two-dimensional rectangle under tensile load. Without the voids, the tensile stress in the direction of the applied load remains uniform, however when voids are present, the stress becomes non-uniform and its variation is a function of the void inclusions in the matrix. A few efforts have been made to find the weight function analytically for single inclusion of a crack in a homogenous solid, nevertheless for complex geometry of multiple voids, an analytical solution is not available. Numerical and experimental solutions are apparently the suitable means to look into the weight function. Equation (2.18) is a simple way to clarify the steps taken below in the finite element analysis. This is to say that to find the average of a non-uniform stress distribution on a cross sectional area S, one could multiply the uniform stress on elements of cross section multiplied by the weight function and integrate over the cross section.

$$\bar{\sigma} = \frac{\int_s \sigma(x) dS}{S} = \int_{-\infty}^{\infty} \sigma(x-\xi)\rho(x-\xi)d\xi \tag{2.18}$$

A number of finite element simulations have been carried out to obtain stresses in rock at microscale level. The objective is the distribution of stress along a cross section in a rock specimen under uniaxial tension. It is assumed that the pattern of stress variation in a rock specimen can be represented by a high resolution finite element simulation model. Figure 2.6 shows a model of heterogeneous rock using a high-resolution finite element. The mesh and the voids used in the finite element model reflect the sizes of pores and grains in

the rock specimen. Figure 2.6(top) shows the linear elastic model of rock and Figure 2.6(bottom) shows the vector plot of stress components in the direction of the applied load. It should be noted that, we are only interested in the magnitude of stress S_{22} along the applied load. The average pore diameter is 1 mm. This is an arbitrary radius for pore spaces to study the impact of stress concentration in a solid material with circular void inclusions as a function of void radius.

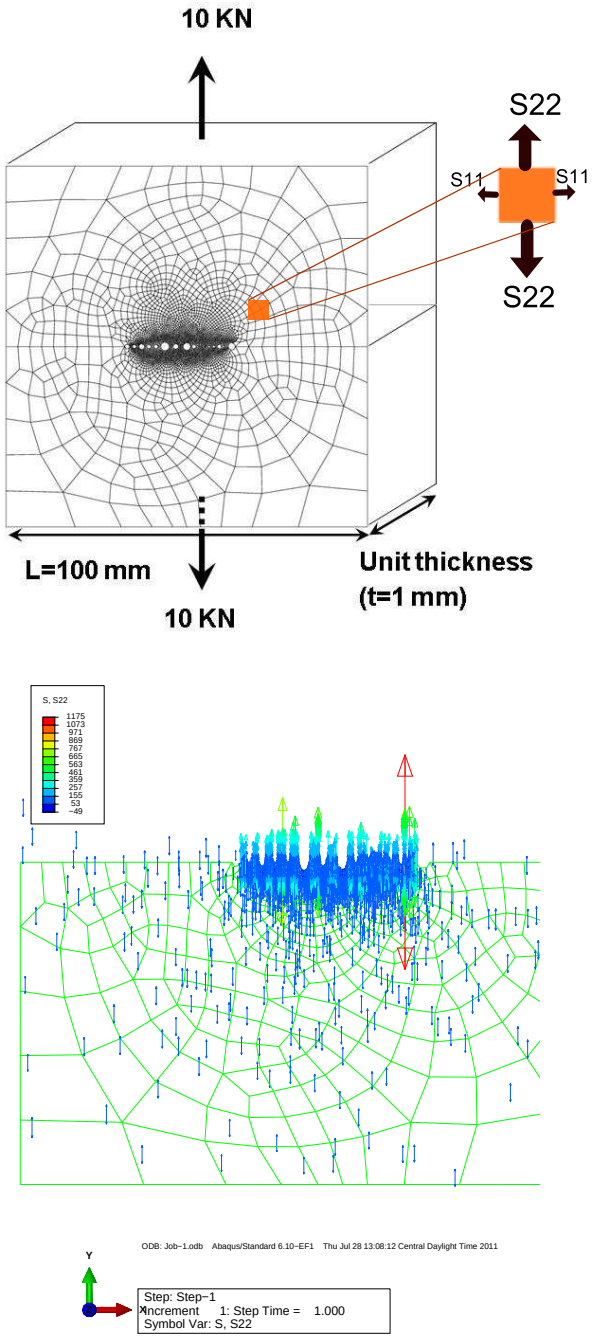

Figure 2.6: Linear elastic model of rock using high resolution finite element.

Under the tensile load of 10 KN on the cross section of size 100 mm^2, the stress distribution as shown in Figure 2.7 is obtained. The directions of principal stresses in the rock model are shown in Figure 2.6. The distribution of tensile stress in the direction of load, S_{22}, is shown only on the segment of the cross section where pore spaces or voids are included (x=37 to x=75 mm) and for the remaining segments of the cross section, tensile stress is 100 N/mm^2. Due to the presence of voids, stress concentration and reduction of cross sectional area, stresses range from 100 to 1000 N/mm^2. This drastic increase in the value of stress is observed when damage progresses leading to a reduction of the load carrying area. The reduction of cross sectional area, expedites the progress of damage and is taken into account in the damage diffusion equation that we solve.

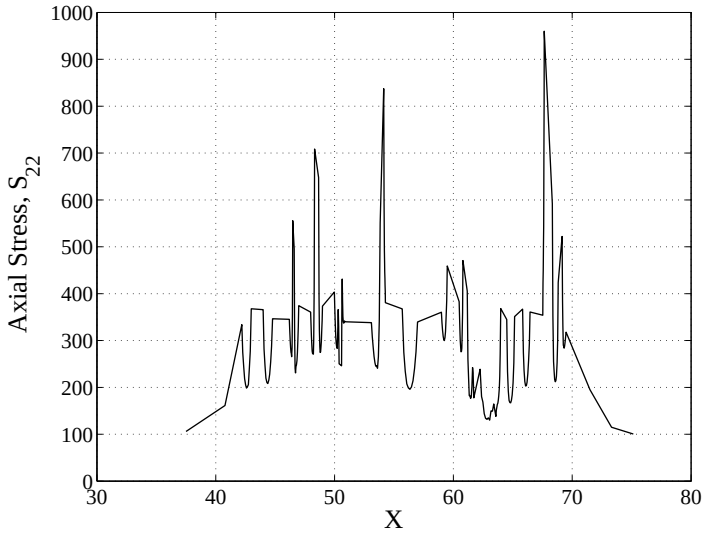

(a)

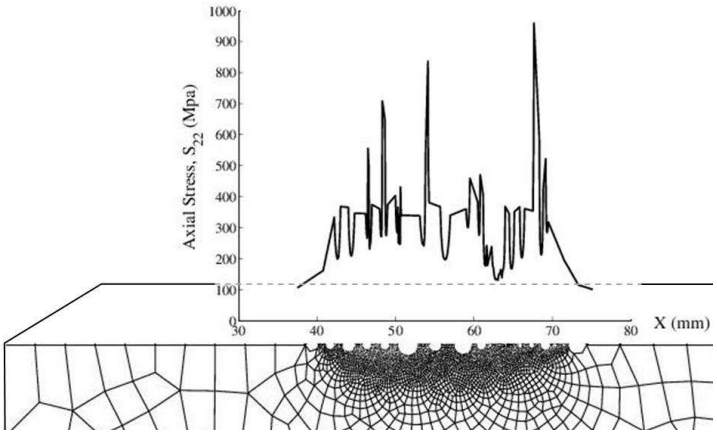

(b)

Figure 2.7: The variation of tensile stress along the section of rock where pores are included.

Once the stress variations is obtained we make use of variograms to find the correlation length for stress. Correlation length is the length at which

stresses interact, in other words stresses are correlated. The variogram analysis is used to characterize the spatial continuity of the data from a heterogeneous reservoir. The variogram is a function obtained by plotting the semivariance of the differences between the properties (here, stresses) at two locations separated by a distance h, versus h. The variogram is defined as;

$$V_s(h) = \frac{\text{Var}\left[\Phi(x) - \Phi(x+h)\right]}{2} \tag{2.19}$$

where

V_s = semi-variance

h = lag distance

$\Phi(x)$ = value of property at location x

$\Phi(x+h)$ = value of property at location $x+h$

When equation (2.19) is plotted, it can be observed that, with increasing correlation length, the range of influence of one value on its neighbors increases up to the correlation length. At lag distances greater than the correlation length, the data are no longer correlated; therefore, we pick the maximum lag distance at which the data are correlated to obtain the weight function, as discussed earlier.

The variogram is a means to quantify the correlation structure of the variable of interest. The variogram of the sample data is known as the experimental

variogram. After computing the experimental variogram, a smooth theoretical variogram model is usually fitted to the experimental variogram and the model is then used for estimation.

The variogram of stress as shown by dots in Figure 2.8 is obtained from the above stress results. Before proceeding to calculating the correlation length, the data need to be fit to one of the available variogram models. A spherical variogram model is fitted to experimental variogram (Figure 2.8) and the correlation length of about 3.15 mm is calculated from plot. Since the pore sizes (the diameter of the circles included in FE model) are in the order of 1 mm, it is concluded that the correlation length for stress variogram is about 3 times the void size or pore size of rock.

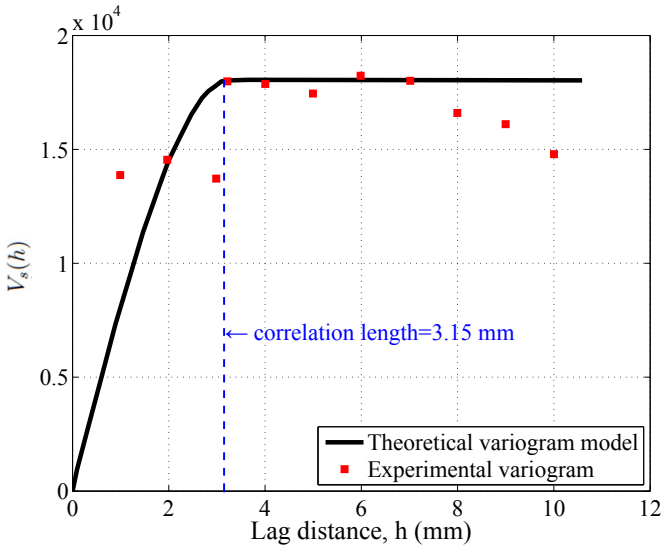

Figure 2.8: The variogram for uniaxial stress and correlation length.

Figure 2.9(a) shows surface plot of tensile stress in a general plane strain model of rock under tension with a single circular void which serves as pore space among the rock grains. It can be seen that the majority of rock undergoes the tensile stress of 100 N/mm^2 as expected and around the void stress increases to three times the average stress which is equal to 300 N/mm^2. These results are used to create the variogram for stress as shown in Figure 2.10.

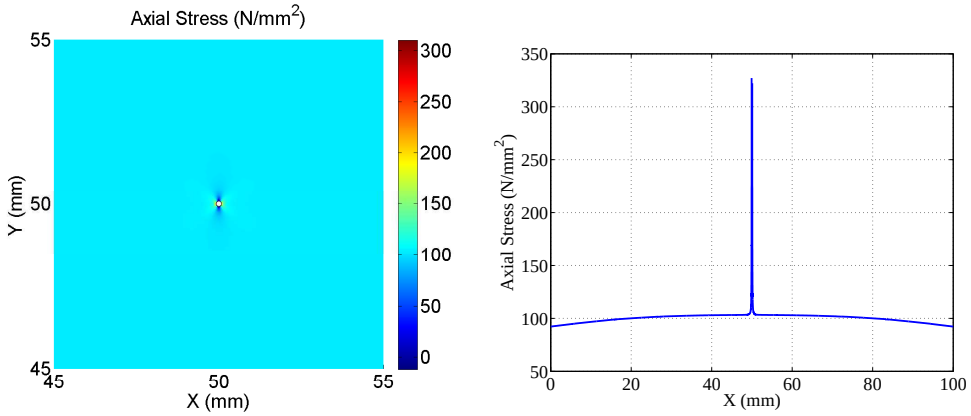

(a) Surface plot of tensile stress in rock

(b) The variation of tensile stress along y=50 mm where the void(s) are included.

Figure 2.9: Variogram analysis of tensile stress in rock.

The theoretical variogram in Figure 2.10 shows a perfect fit to experimental variogram for the case of r=0.1 mm. The correlation length of 0.58 mm is 3 times the diameter of the void.

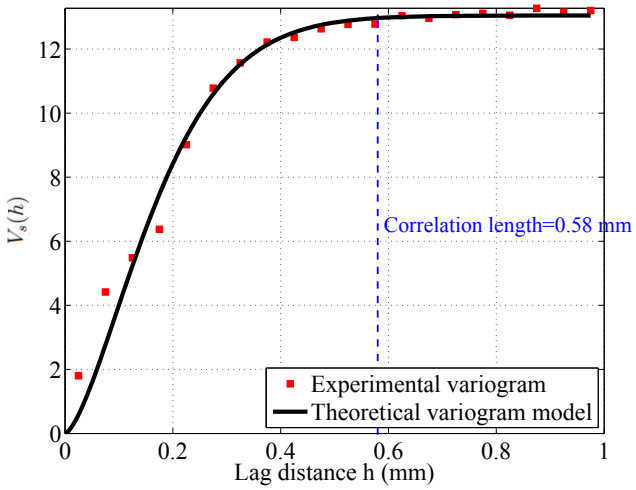

Figure 2.10: The variogram of tensile stress for a single void of radius r=0.1 mm in rock.

In the third simulation, a uniform pore size distribution with pore diameters of = 0.6 mm is used. Figure 2.11 shows the mesh used to simulate stresses in a rock sample with uniform pore size distribution.

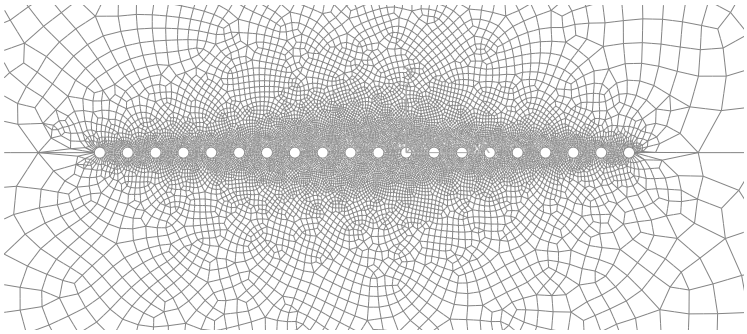

Figure 2.11: The mesh used to model rock with similar pore sizes.

Figure 2.12 shows the stress distribution obtained from FE model for this rock. The stress distribution is periodic as expected.

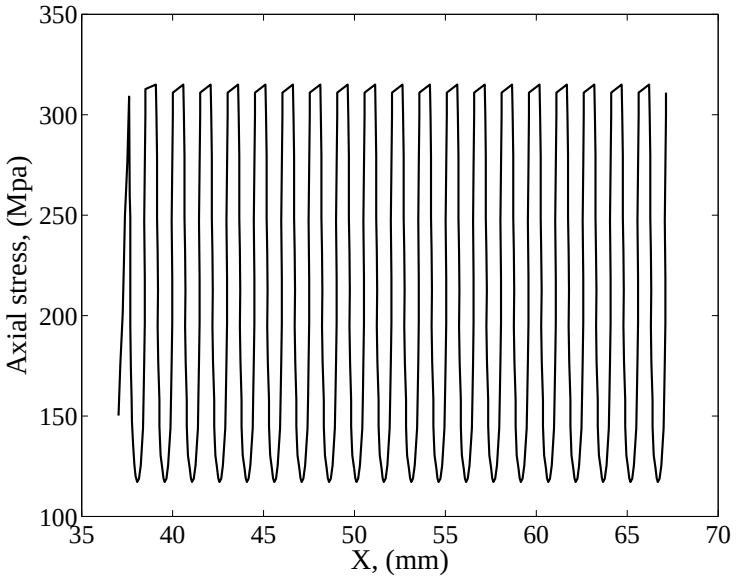

Figure 2.12: Stress distribution obtained from FE model for a rock sample with uniform pore size distribution.

Similarly to the previous case, the variogram along with the best fit is obtained for this simulation in Figure 2.13. The correlation length is about 1.96 mm which is 3.3 times the pore diameter of 0.6 mm.

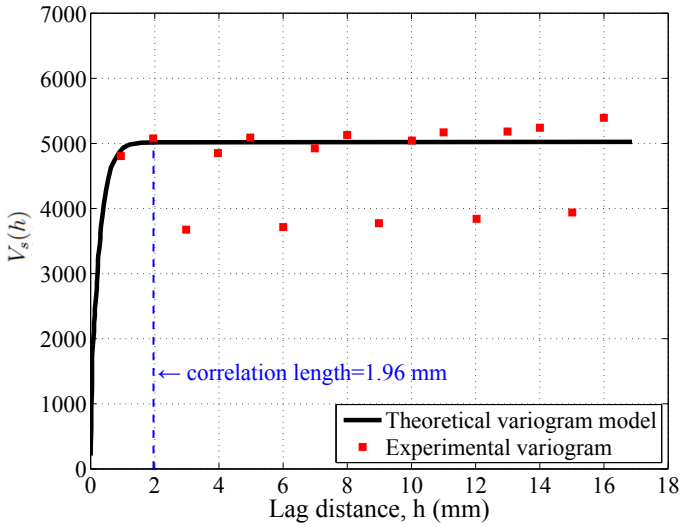

Figure 2.13: The variogram for uniaxial stress for the case of uniform pore size distribution

These three scenarios show that the correlation length is about 3 times the pore diameter. We know that the weight function is an even function. Let's assume that this function behaves similarly to a normal distribution function for which three standard deviations account for 99.7% of the sample population. Equating $0.5 \times 3\sigma$ with the correlation lengths obtained above we get

$0.5 \times 3\sigma = 3.15$ mm, therefore

$\sigma = 2.1$ mm; hence, the weight function is now obtained as a probability density function for a normal distribution with the standard deviation of $\sigma = 2.1$ mm.

From the above results and equation(2.17) we can obtain the microstructural

length scale parameter λ^2;

$$\lambda^2 = \int_{-\infty}^{\infty} \left[\frac{(x-\xi)^2}{2}\right] \frac{1}{\sigma\sqrt{2\pi}} \exp\left[-\frac{(\xi-x)^2}{2\sigma^2}\right] \, \mathrm{d}\xi$$

for $\sigma = 2.1$ we get;

$$\lambda^2 = \int_{-\infty}^{\infty} \left[\frac{(x-\xi)^2}{2}\right] \frac{1}{2.1\sqrt{2\pi}} \exp\left[-\frac{(\xi-x)^2}{2 \times 2.1^2}\right] \, \mathrm{d}\xi = 2.205$$

The proposed approach to determine the weight function ρ from stress measurement experiments or finite element simulations knowing the structure of rock matrix and obtain the damage diffusion parameter λ^2 could be verified against an inverse analysis of damage. In inverse analysis, for a given rock, the distribution of damage is observed in time and space and from these results, the damage diffusion parameter is calculated. So far, we have obtained the pore size distribution and stress variation from finite element analysis and calculated the correlation length from which we could get a σ for a Gaussian distribution. The value of σ could then be plugged into equation (2.17) to obtain λ^2.

2.3 Finite Element Solution of Rock Damage

2.3.1 Problem Statement

The increasing energy demand calls for advances in technology which translates into more accurate and complex simulations of physical problems. We are trying to understand volumetric rock stimulation, which is essential

to understanding the geomechanics of oil and gas reservoirs. The fragile microstructure of some rocks, makes it difficult to predict the propagation of fracture in them; therefore, a mathematical model is required to predict the fracture mechanisms in such materials. The governing equation of rock damage is a nonlinear parabolic partial differential equation (PDE). The physics of the problem imposes a number of complexities that should be handled numerically. In this paper, we present the results we obtained using COMSOL 3.5a and we show how a complicated problem can be solved using the finite element method incorporated in COMSOL. The input file for this simulation is given in Appendix B. The results could be used in similar geomechanical and structural damage problems such as failure and rupture of Steel, Aluminum, Concrete, etc. Moreover, the pattern of rock damage in oil and gas reservoirs is of great significance in obtaining the permeability and recovery enhancement of hydrocarbon in petroleum engineering.

The damage parameter and governing equation are now defined; therefore we can outline the problem we wish to solve. Given the initial distribution of damage in a domain Ω. we are interested in knowing how damage is propagated in rock. The damage parameter or state variable changes with time and space. Figure 2.14 shows the domain and boundary conditions of the problem. Vector n is the outward normal vector to the domain boundary at any point $\mathbf{X}$. Here, $\mathbf{X}$ is a vector quantity. The damage parameter is a scalar as defined in Figure 2.1 and it is equal to zero on the boundary.

The flux of damage is also zero across the boundary. What we are

interested to know is the distribution of damage over the domain as time increases. It should be noted that when material undergoes damage and failure, it ruptures. The rupture or what is mathematically known as blow-up time is of great interest in our application. When blow-up occurs, due to numerical problem damage parameter jumps to values greater than one and the solution to PDE ceases to exist. Studying the convergence of solution becomes significant in this problem; therefore we present here the convergence plot as well.

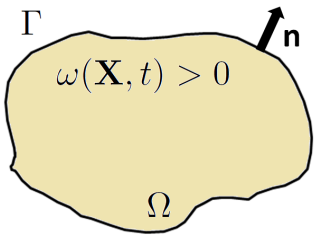

$$\begin{cases} \omega : \Omega \to R \\ \omega = 0, \ D\dfrac{\partial \omega}{\partial n} = 0 \quad \text{on} \quad \Gamma \end{cases}$$

Figure 2.14: The time-dependent domain Ω of damaged rock.

To solve Equation (2.11) in 1D, the equation has to be in the form of a general parabolic PDE in COMSOL, shown in Equation (2.20):

$$\frac{\mathrm{d}\omega(\mathbf{X}, t)}{\mathrm{d}t} = [\nabla \cdot [\kappa \nabla (f(\omega)) + f(\omega)]]_+ \tag{2.20}$$

in which $f(\omega)$ is an exponential function in the following form

$$f(\omega) = (1-\omega)\exp\left(\frac{\mu_0}{1-\omega}\right) \tag{2.21}$$

κ is the damage diffusion parameter. The positive sign in the right hand side of the equation indicates that the rate of damage has to remain non-negative ($\geq$) during simulation time. This constraint is imposed by the physics of damage as a non-healing process. We access the solution vector and manipulate the vector such that the rate of damage is always positive. We will explain the steps we took to modify the solution to make sure we get a positive damage rate. μ_0 is a dimensionless constant which is related to the stress level applied to rock. In all analysis performed here, we use the constant value of 10 for μ_0.

Notice that, the partial differential equation (2.20) presented here, is nonlinear parabolic PDE and does not have an analytical solution; therefore, it has to be solved numerically. Here we present the method of solution and demonstrate the technics which we came up with to solve this PDE using COMSOL3.5a and present the results we obtained. The derivation of this equation is given in [21] and a more detailed derivation is given in Appendix A.

We utilize the coefficient form of PDE in COMSOL. The coefficient form is used to model a physics problem using a system of one or more time-dependent partial differential equations and is in the form of Equation (2.22).

$$e_a\frac{\mathrm{d}^2u}{\mathrm{d}t^2} + d_a\frac{\mathrm{d}u}{\mathrm{d}t} + \nabla\cdot(-c\nabla u - \alpha u + \gamma) + \beta\nabla u + \alpha u = f \tag{2.22}$$

Assigning coefficients of Equation (2.22) forms the Equation (2.20) To assign the coefficients in Equation (2.22), we use zero for d_a, α,γ, β, and Equations (2.23) and (2.24) for f and c coefficients.

$$f = (1-u)\exp\left(\frac{\mu_0}{1-u}\right) \tag{2.23}$$

$$c = \kappa\left(\frac{\mu_0+u+1}{1-u}\right)\exp\left(\frac{\mu_0}{1-u}\right) \tag{2.24}$$

Once the coefficient form is created, the transient problem of rock damage can be solved. The following sections give the details of this analysis. To have a better control on problem variables and post processing features, we use Livelink for MATLAB and the script which demonstrates this method is presented in Appendix B.

2.3.2 Numerical Schemes for Solution of Rock Damage

So far we have developed the partial differential equation of damage and looked into the methods of finding damage diffusion parameter. In this section we show how this nonlinear parabolic PDE can be solved and explain some of the numerical pitfalls of solving this PDE. Here we look at this problem in 1D, Equation (2.25).

$$\frac{\mathrm{d}\omega}{\mathrm{d}t} = (1-\omega)\exp\left(\frac{\mu_0}{1-\omega}\right) + \Lambda^2\frac{\partial^2}{\partial x^2}\left[(1-\omega)\exp\left(\frac{\mu_0}{1-\omega}\right)\right] \tag{2.25}$$

This second order parabolic PDE is an initial and boundary condition problem, therefore it requires one initial condition and two boundary conditions to obtain the distribution of damage within the length of bar over time. We

use the finite difference method. We have tried several numerical schemes, including explicit, implicit, and Crank-Nicholson, to study the convergence and stability of solution. In implicit scheme, the Newton-Raphson method is invoked for solving the set of nonlinear equations. The stability and convergence of these methods are looked into and finally the best method of solution is used for higher dimensions. The solution is verified by available analytical solutions of simpler parabolic PDEs.

The left hand side of equation (2.25) contains the rate of damage accumulation and is in the form of a first order differential equation which can be discretized using one of the single or multi-step methods explained here. The right hand side includes a source term and a second derivative in space for which one of the forward, backward or centered discretization methods is used.

To obtain a solution for Equation (2.25), we have used two methods which we explain in coming sections. These are finite element method and finite difference method. For these methods an analysis of stability and convergence is performed and results are presented in coming sections.

2.3.3 Assessment of Blow-up Time

As the solution time goes on, the onset of rupture is reached. This time is when the solution ceases to exist and is called the life time of material also known as blow-up time in mathematics. This is a known phenomenon

in parabolic problems and occurs when the rate of input into the system is larger than that of output. Here we first obtain the blow-up time for the case of $\kappa = 0$, numerically, and call it the blow-up time for no damage diffusion case denoted by tbu_0. This is used as a reference time in all our analysis and it shows how long it takes for a rock sample under tensile load to fracture, if damage is accumulated in one point. This is similar to the case of brittle material undergoing rupture. In other words, when the tensile load is applied to a brittle rock, damage is accumulated at one point and may not diffuse through rock because of brittle nature of material. Obviously, if the same load is applied to a ductile material, the life time or the time required to rupture is larger.

2.3.3.1 Blow-up Time

Table 2.1 lists the values of the dimensionless blow-up time in terms of the damage parameter ω at blow-up. It can be observed that, beyond the damage parameter of about 60% the blow-up occurs very fast and can not be captured using numerical simulations. This is in agreement with experiment in which the catastrophic failure happens extremely fast when part of the cross section is still carrying the load.

Figure 2.26 shows the onset of blow-up for $\kappa = 0$. It can be seen that damage increases around the mid-point of the 1D bar under tension.

Damage parameter ω at blow-up	Dimensionless blow-up time
0.40	3.775701×10^{-8}
0.50	4.093855×10^{-8}
0.60	4.103637×10^{-8}
0.65	4.103689×10^{-8}
0.70	4.103691×10^{-8}
0.80	4.103691×10^{-8}
0.90	4.103691×10^{-8}
0.98	4.103691×10^{-8}

Table 2.1: Kachanov's blow-up time

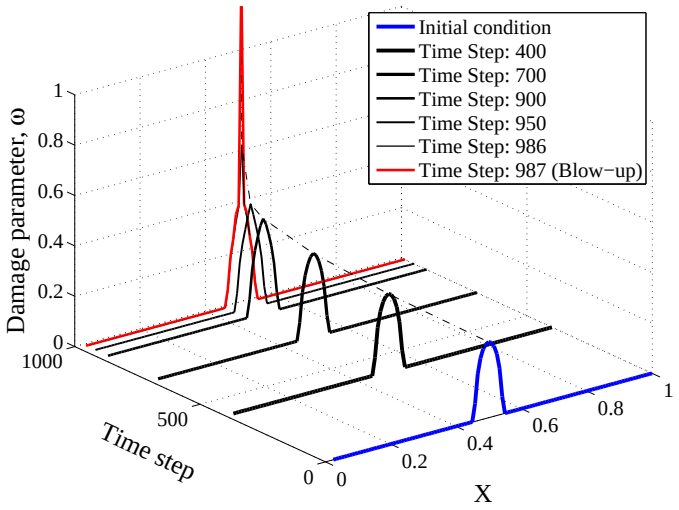

Figure 2.15: Solution at the onset of blow-up to obtain the tbu_0

The dimensionless solution time for time steps 986 and 987 are 8.36×10^{-11} and 8.37×10^{-11} respectively. These two times are related to the physics of this problem. It can be seen that a minute change in time is required for

the solution to blow-up. In other words, to get the exact time of rupture for a material or to obtain the exact values of damage distribution right before the rupture, extremely small time steps are required. In engineering applications, however; the level of accuracy that we have considered here is not required.

2.3.4 Non-healing Effect of Rock Damage

Figure 2.16 shows the distribution of damage with time for $\kappa = 0.06$. A quadratic function is used to create the initial distribution of damage, plotted in blue in Figure 2.16.

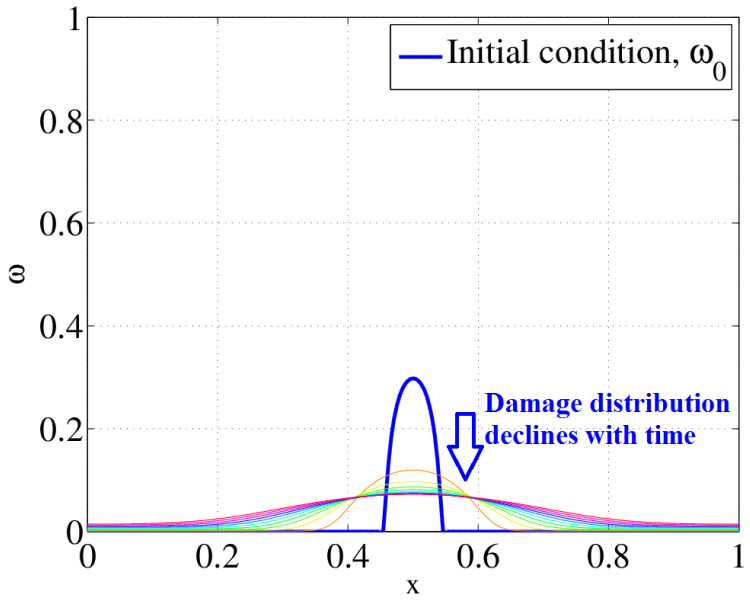

Figure 2.16: Solution without taking into accounts the non-healing effect of damage

Since damage at any points in the domain of problem remains either constant or increases due to the non-healing nature of damage process, the solution has to be either constant or ever increasing. Therefore, to honor the physics of the problem, the solution vector has to be manipulated such that the rate of damage remains non-negative. This is achieved by accessing the structure of solution and making modifications through scripting in MATLAB. Once the converged solution is obtained, nodal values and degrees of freedom are saved in "nodes" and "dofs" variables (Lines 1-2). These can be accessed using the following commands (Lines 1-9) listed in Figure 2.17, which is also part of the input file in Appendix B.

Line (1), retrieves the nodal information from the finite element solution. Line (2), retrieves the degree of freedom of nodes. Line (3), provides the coordinates of the degrees of freedom obtained in line (2). Line (4), saves the solution vector in variable **X** for modifications.

```
1  nodes = xmeshinfo(fem,'out','nodes');
2  dofs=nodes.dofs;
3  coords=nodes.coords;
4  X=fem.sol.u;

5  for i=1:length(dofs)
6      if (X(i,2))<(X(i,1))
7          X(i,2)=X(i,1);
8      end
9  end
```

Figure 2.17: Accessing the solution and post processing to impose non-healing effect of damage

To eliminate the declining values of damage in Figure 2.16, the lines (5-9) in Figure 2.17 are used in MATLAB to impose the condition of $\frac{\partial \omega}{\partial t} \geq 0$ to the solution of the PDE.

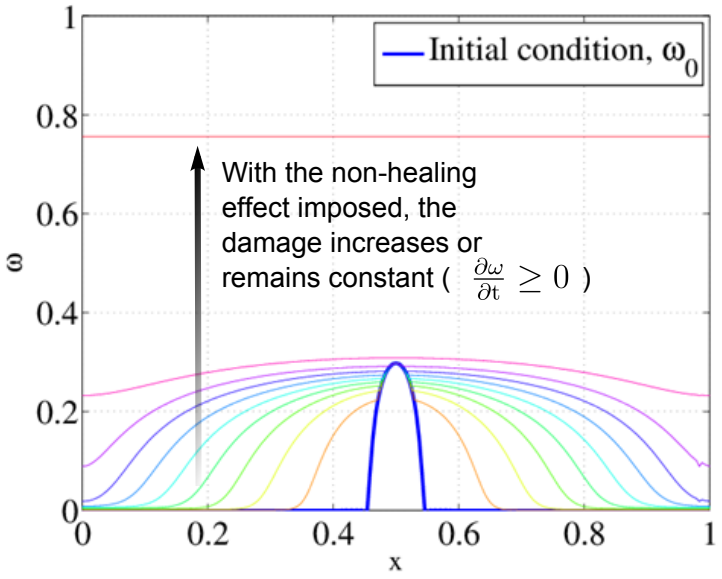

Figure 2.18: Solution corrected for non-healing effect of damage

2.4 Finite Difference Solution of Rock Damage

To verify the finite element solution of the PDE of damage, we are solving this equation using the finite difference method.

$$\frac{\partial \omega}{\partial t} = (1-\omega)^p \exp(\frac{\mu_0}{1-\omega}) + \Lambda^2 \frac{\partial^2}{\partial x^2}[(1-\omega)^p \exp(\frac{\mu_0}{1-\omega})] \tag{2.26}$$

in which the only variable is ω changing with time and space, i.e, $\omega = \omega(x,t)$. For this current case that is being solved the value of 1 is used for p,

$(p = 1)$.

In order to solve this equation numerically, let's call the first part of the right-hand side of the equation, $Q = Q(\omega)$. Therefore the equation (2.26) can be written as:

$$\frac{\partial \omega}{\partial t} = Q(\omega) + \Lambda^2 \frac{\partial^2}{\partial x^2}[Q(\omega)] \tag{2.27}$$

then the second derivative in (2.27) is

$$\frac{\partial^2}{\partial x^2}[Q(\omega)] = \frac{\partial}{\partial x}\left[\frac{\partial Q}{\partial \omega}.\frac{\partial \omega}{\partial x}\right] \tag{2.28}$$

$\frac{\partial Q}{\partial \omega}$ in (2.28) can be obtained by taking the derivative of Q (The first part in the RHS of (2.26)) with respect to ω as follows:

$$\frac{\partial Q}{\partial \omega} = \mu\left((1-\omega)^{p-2}\right).\exp\left(\frac{\mu_0}{1-\omega}\right) - p(1-\omega)^{p-1}\exp\left(\frac{\mu_0}{1-\omega}\right) \tag{2.29}$$

The function D calculates the right-hand side of (2.29). So let's now rewrite the right-hand side of (2.28) as:

$$\frac{\partial^2}{\partial x^2}[Q(\omega)] = \frac{\partial}{\partial x}\left[D(\omega).\frac{\partial \omega}{\partial x}\right] \tag{2.30}$$

plugging (2.30) into the right-hand side of (2.27), we could write (2.27) as:

$$\frac{\partial \omega}{\partial t} = Q(\omega) + \Lambda^2 \frac{\partial}{\partial x}\left[D(\omega).\frac{\partial \omega}{\partial x}\right] \tag{2.31}$$

Also, the function Q calculates the $Q(\omega)$ in (2.31).

Let's now approximate the damage parameter from equation (2.31). The second derivative on the right-hand side can be calculated as follows:

$$\begin{aligned}\frac{\partial}{\partial x}\left[D(\omega)\frac{\partial \omega}{\partial x}\right] &= \frac{D(\omega)\frac{\partial \omega}{\partial x}\mid_{(i+\frac{1}{2})} - D(\omega)\frac{\partial \omega}{\partial x}\mid_{(i-\frac{1}{2})}}{\Delta x} \\ &= \frac{D(\omega)\mid_{(i+\frac{1}{2})}\cdot\left(\frac{\omega_{i+1}-\omega_i}{\Delta x}\right)}{\Delta x} - \frac{D(\omega)\mid_{(i-\frac{1}{2})}\cdot\left(\frac{\omega_i-\omega_{i-1}}{\Delta x}\right)}{\Delta x} \\ &= \frac{\left[\frac{D(\omega_{i+1})+D(\omega_i)}{2}\right]\cdot\left(\frac{\omega_{i+1}-\omega_i}{\Delta x}\right)}{\Delta x} - \frac{\left[\frac{D(\omega_i)+D(\omega_{i-1})}{2}\right]\cdot\left(\frac{\omega_i-\omega_{i-1}}{\Delta x}\right)}{\Delta x}\end{aligned}$$

Now that both sides of the Equation (2.26) is discretized we can code this and solve for the damage parameter $\omega(\mathrm{x},\mathrm{t})$. The rest of this calculation and dealing with nonlinearity is presented in Appendix C

2.4.1 Sensitivity of solution to mesh refinement

To determine how many space discretization points are required, the convergence of solution with mesh refinement is studied. For the 1D problem of damage, the space divisions are increased from 10 to 400 and the variation of the damage parameter at mid-point and quarter-point of the bar are plotted versus the number of elements in Figure 2.19(a and b). It can be seen that the solution is not stable for coarse mesh (small J), however as the mesh gets finer, the solution converges to ω=0.313. It should also be noted that the convergence occurs beyond J=100. This result will be used later in solving the PDE of damage by the finite difference method.

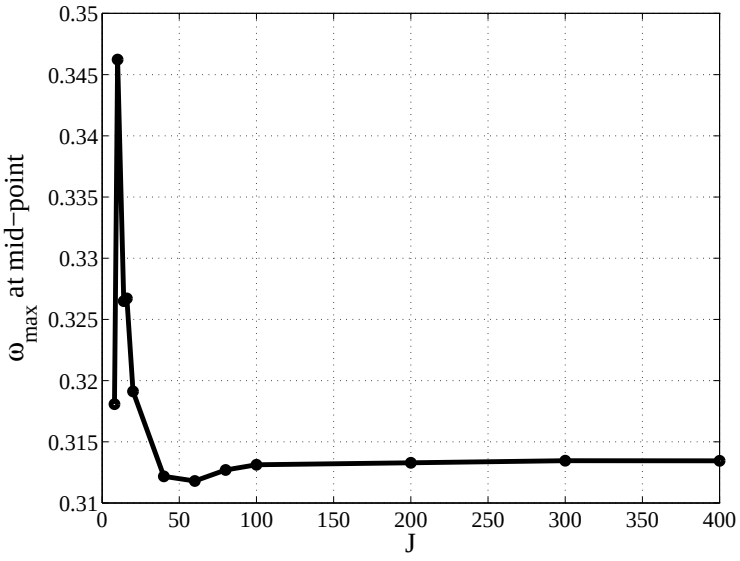

(a) Convergence of solution at mid-point

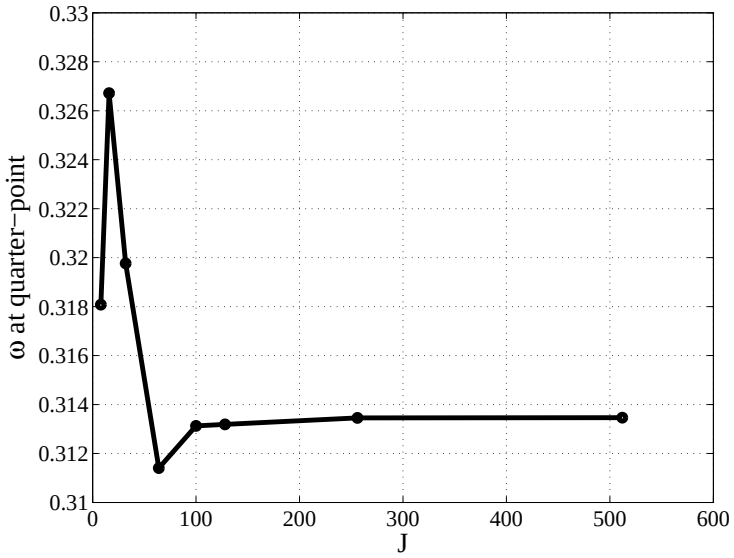

(b) Convergence of solution at quarter-point

Figure 2.19: The analysis of solution convergence for 100 time steps and various mesh sizes.

2.4.2 Sensitivity of Solution to Time Step Size

To get a stable solution of the nonlinear equation of damage, time steps should be very small. The question is how small is small enough to meet this requirement. The convergence analysis of several cases for space discretizations of J=20, 50, 100 and 200, and time steps from 10 to 30,000 is plotted in Figure 2.20. The plot shows convergence beyond 10,000 time steps. This result has been anticipated and it is now confirmed by the plot. Therefore, to get accurate results from a numerical analysis, the number of mesh points, in general, should be no less than 100 and the total time should be divided to 10,000 or more time steps.

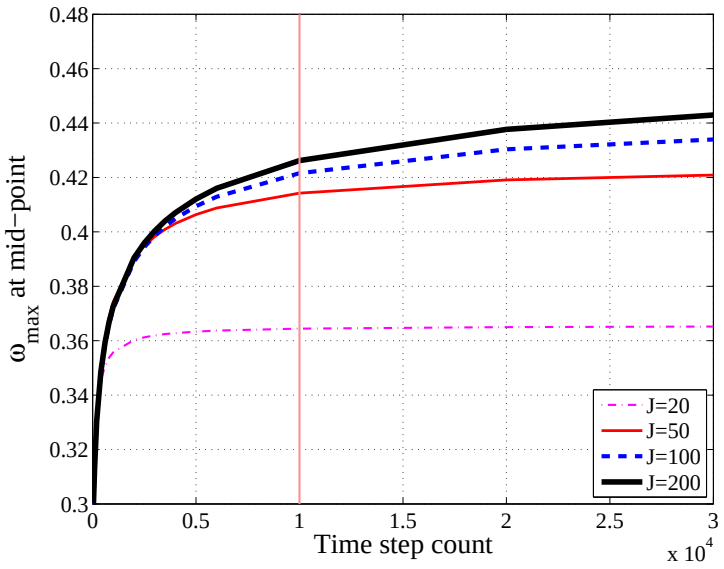

Figure 2.20: The analysis of solution convergence for various time step and mesh sizes.

2.4.2.1 Round-Off Error in Implicit and Explicit Schemes

We solve the nonlinear partial differential equation of damage evolution problem in which, the time steps to obtain a stable solution have to be very small. To study the possible numerical errors that arise from machine round-off or the scheme used, we use a simple form of a linear parabolic PDE in one dimension. This is the PDE (2.32) in which the boundary conditions are zero at both ends of the domain and initial condition is a sin function. The initial condition used here is similar to that of the rock damage problem, Equation (2.25). To investigate the appropriate numerical scheme to solve the Equation (2.25), we use the analytical solution of this simpler PDE [230], in which we don't have to deal with nonlinearity and the non-healing nature of damage. We also show the impact of the applied scheme and time discretization on the relative magnitude of error.

$$\frac{\partial \omega}{\partial t} = \frac{\partial^2 \omega}{\partial x^2} \tag{2.32}$$

where

$$\omega = \omega(x, t) \tag{2.33}$$

the initial condition follows a sin function

$$\omega_0 = \omega(x, 0) = sin(\pi x) \tag{2.34}$$

and the boundary conditions are:

$$\omega(0, t) = 0 \tag{2.35}$$

$$\omega(1, t) = 0 \tag{2.36}$$

This problem is solved numerically and the numerical results are compared with analytical solution to verify the accuracy of our candidate scheme in the finite difference method used in Section 2.4. Solution at T=1(s) is used to verify the numerical approximations. It is expected that with smaller time steps Δt, the relative error between the numerical and exact solutions get smaller. Numerical results confirm this for the implicit scheme; however, the explicit scheme shows a reduction of error as expected only up to a certain point and then the error increases. The error from explicit scheme gets smaller as Δt gets smaller. Due to truncation error associated with the scheme used, the error associated with the explicit scheme never becomes zero. The relative error used here is defined as;

$$\text{Relative error}(\%) = \frac{||\omega - \tilde{\omega}||}{||\omega||} \times 100 \tag{2.37}$$

in which ω is the analytical solution of the PDE and $\tilde{\omega}$ is the approximate solution, both of which are vectors of solutions at mesh points for a fixed final time T=1 sec. We use the l_2-norm, which is simply the length of vector to calculate the relative error. Based on this definition, the relative error is the ratio of length of absolute error vector to the length of the vector of exact or analytical solution, and expressed in percent.

Figure 2.21 shows the variation of the relative error with the number of time steps. It can be observed that unlike explicit method, implicit method

has a monotonic decrease in error as Δt decreases. It is expected that less error is incurred as time steps get smaller; however, looking into the trend of error in Figure 2.21, we observe that for very small time steps, machine error or round-off error becomes quite large and when combined with truncation error, the relative error increases unfavorably. Truncation error accumulates in numerical algorithms that take a finite number of steps in computation. It is present even with infinite-precision arithmetic, because it is caused by truncation of the infinite Taylor series to form an algorithm. The source of the truncation and round-off errors should be studied before starting to solve the nonlinear PDE of damage using the finite difference method. Use of arbitrarily small steps in numerical computation is prevented by round-off error, which are the consequence of using finite precision floating point numbers in computers.

It is concluded that, with finite-precision arithmetic, the error associated with explicit scheme in parabolic PDEs is a combination of truncation error and round-off error[42]. This holds true if one of the two (Δx or Δt) remains fixed and the other varies as in Equation (2.38). These equations show that with finite precision on computers, taking smaller Δx or Δt will not necessarily lead to smaller error.

if only Δt varies:

$$||\text{Error}|| \leq C_1 \Delta t + C_2 \frac{1}{\Delta t}, \tag{2.38a}$$

and if only Δx varies:

$$||\text{Error}|| \leq D_1 \Delta x + D_2 \frac{1}{\Delta x}, \tag{2.38b}$$

C_1, C_2, D_1, and D_2 are constants and depend on the machine precision and the numerical scheme used. The trend of error can be seen in Figure 2.21 in which Δx and J are fixed ($\Delta x = L/20$ and J=20) and Δt decreases. The parameter J, is the number of space discretizations and L is the length of the 1D domain on which the state variable ω was calculated.

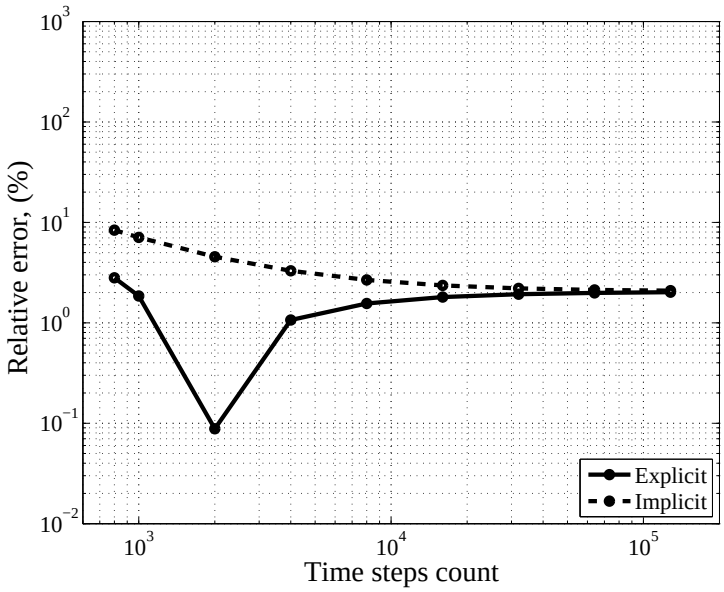

Figure 2.21: The variation of relative error with the number of time steps for implicit and explicit schemes for J=20

In the next step, to see the effect of space discretization in explicit scheme, Δx was made two and five times smaller than the above analysis to 40 and 100 discretizations and relative errors were calculated. It can be

seen in Figure 2.22 that the relative error of explicit method behaves non-monotonically regardless of step size (Δx) reduction. This also indicates that the time steps can not be reduced arbitrarily as error starts to build up below a smaller Δt. Being aware of this problem is extremely important when solving a nonlinear problem such as the one we solved here, Equation (2.25), in which we have to take the time step sizes extremely small to get over the stability and convergence problems associated with nonlinear nature of damage problem.

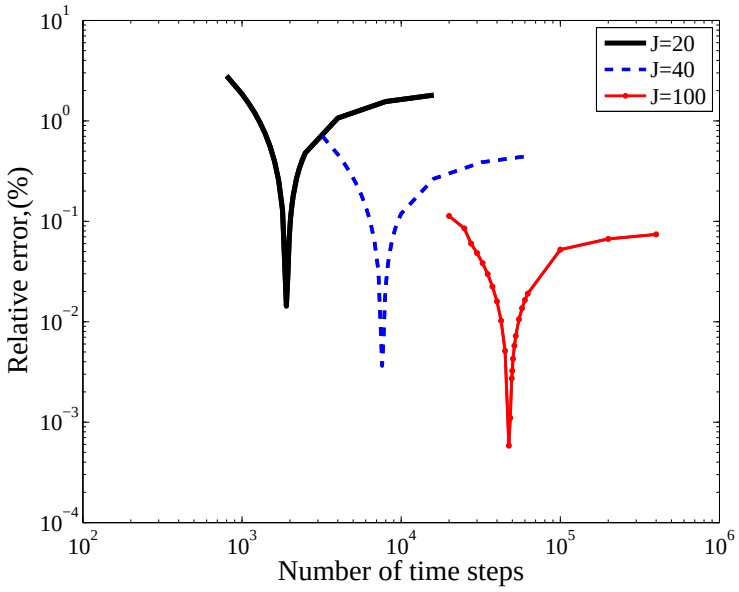

Figure 2.22: The variation of relative error with the number of time steps for various space discretizations using explicit scheme.

2.4.3 Parameters Affecting the Diffusion of Damage

We have looked into time and space discretization effects on the solution of damage problem. Now we will be looking in detail into the effect

of damage diffusion parameter on the transient solution. Earlier we saw that damage diffusion parameter is related to the weight function and from the interpretation of the weight function, we concluded that the diffusion parameter is related to the rock matrix structure. The numerical solutions are in good agreement with the physics behind the diffusion parameter. We have also seen that the diffusion parameter of $\Lambda^2 = 10^{-5}$, resulted in the standard deviation of 4.48×10^{-3} which translates to a small correlation length. Such a small diffusion parameter corresponds to damage not going far away from the initial damaged section and accumulating locally around this zone. This trend is similar to brittle rupture of materials. More about the brittle and ductile rupture of materials and their relationship to the characteristic length Λ^2, can be found in [15]. Figure 2.23 shows the distribution of damage for a case where damage increases locally and diffusion to the boundaries is extremely small. θ is the dimensionless time defined in Appendix A. θ_0 is the dimensionless blow-up time for $\Lambda^2 = 0$ as defined by Kachanov and calculated in Table 2.1. The initial condition is assigned as shown and the transient solution is plotted for three times of θ=$0.21\theta_0$, $0.95\theta_0$ and $1\theta_0$.

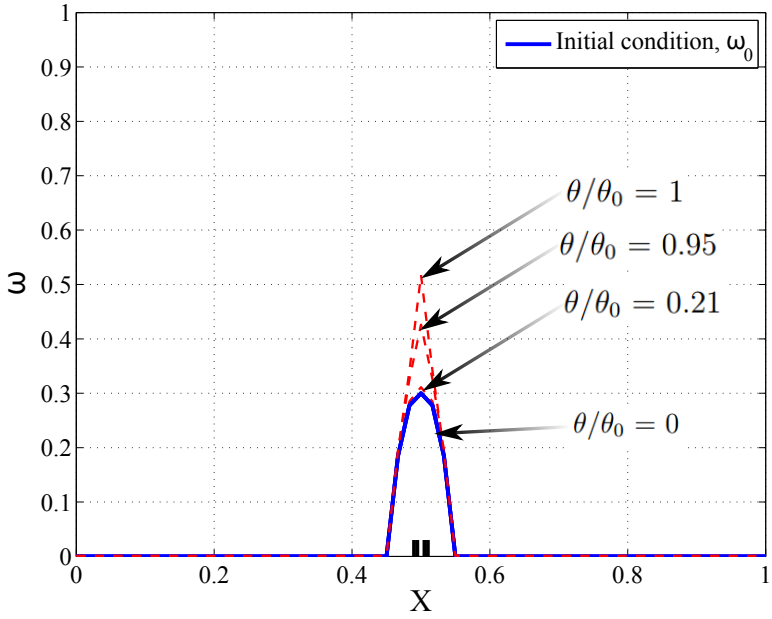

Figure 2.23: Distribution of damage from initial condition to the vicinity of blow-up for $\Lambda^2 = 10^{-5}$ ($\theta/\theta_0 = 0.21$, 0.95 and 1)

The blow-up time for $\Lambda^2 > 0$ should be greater than that of $\Lambda^2 = 0$, because the case of no damage diffusion does not have time to dissipate energy applied to material through diffusion of damage and breaking the bonds. Therefore if we look at the case of $\Lambda^2 = 10^{-2}$, the solution should go on for multiple times the θ_0 for the blow-up to take place. Figure 2.24 exhibits the onset of blow-up at $12.5\theta_0$ beyond which, the solution ceases to exist.

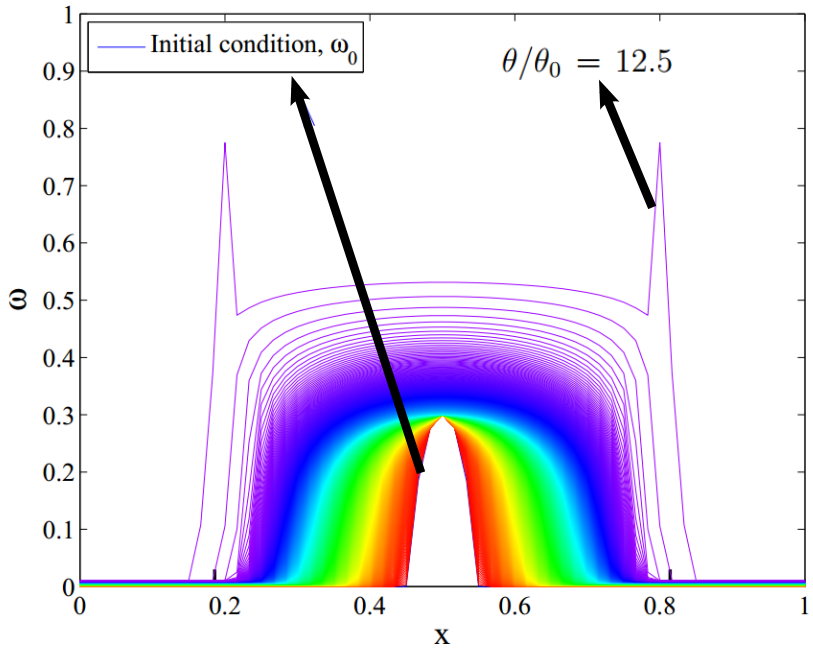

Figure 2.24: Distribution of damage from initial condition to the vicinity of blow-up for $\Lambda^2 = 10^{-2}$ ($\theta/\theta_0 = 12.5$)

Once we know the onset of blow-up for a given damage diffusion parameter, we are able to limit the analysis to the time of blow-up. Figure 2.25 shows the results for three times, the latest of which is $12\theta_0$, right before the blow-up time.

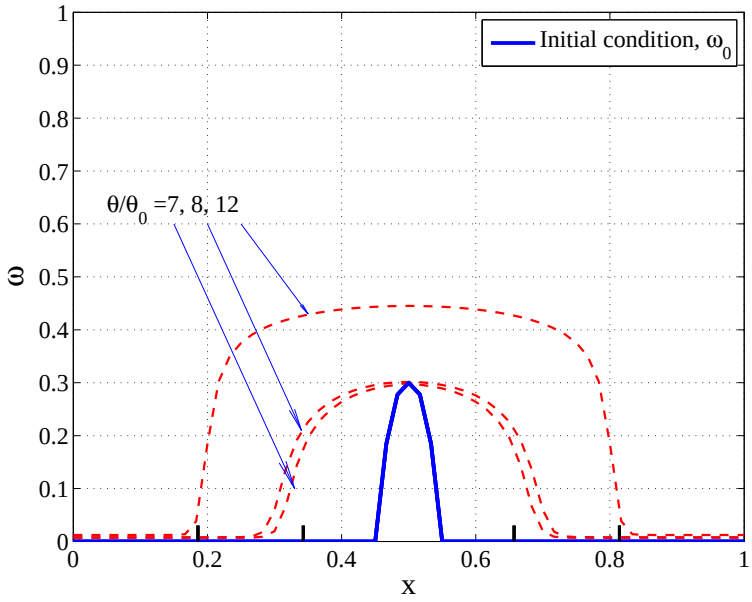

Figure 2.25: Distribution of damage from initial condition to the vicinity of blow-up for $\Lambda^2 = 10^{-2}$ ($\theta/\theta_0 = 7$, 8 and 12)

It can be seen in Figure 2.25 that the damage diffuses laterally, however the maximum ceases at about ω =0.45, if we increase the damage diffusion parameter from 10^{-2} to 6×10^{-2} as in Figure 2.26, we observe that first of all the blow-up time increases to $20\theta_0$, secondly, the maximum damage at mid-point goes beyond ω =0.45; however, in theory, the damage parameter can only approach the value of ω =1. Attaining the values of damage parameter close to 1 in reality corresponds to the time of material rupture. Numerically, damage parameter could approach ω =1 only if extremely small time steps are used. For all practical purposes, we do not have to use such small time

steps to capture the onset of theoretical blow-up, i.e., ω =1, because the final stage of rupture takes place in a negligibly short time. Blow-up is a well-known phenomenon in dealing with partial differential equations. It is similar to explosion, rupture, and shocks in which the solution ceases to exist. There are a great number of articles on the theory of non-existence of solution and mathematical justification for blow-up phenomenon for nonlinear partial differential equations, including [17, 18]. We know that rock under tensile load eventually could rupture at certain level of load, therefore the damage diffusion parameter for rock should be less than the value assigned for the case, Figure 2.26.

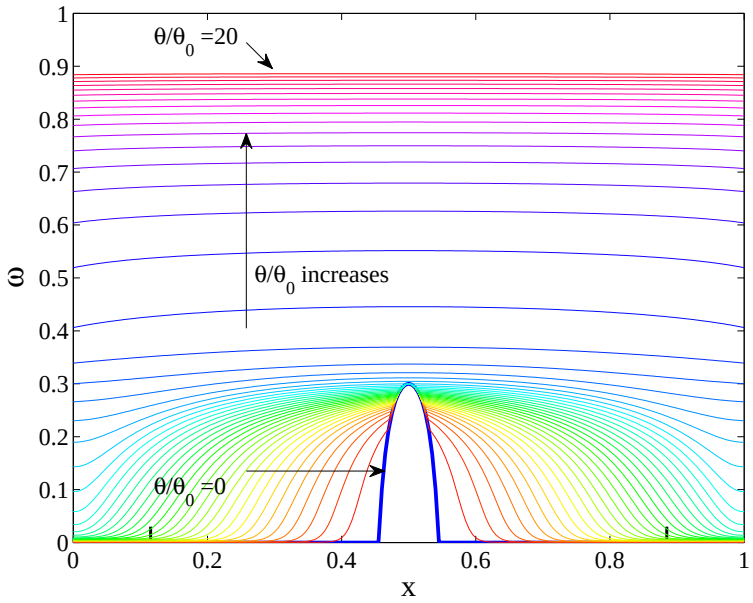

Figure 2.26: Distribution of damage from initial condition to the vicinity of blow-up for $\Lambda^2 = 6 \times 10^{-2}$ $(\theta/\theta_0 = 20)$

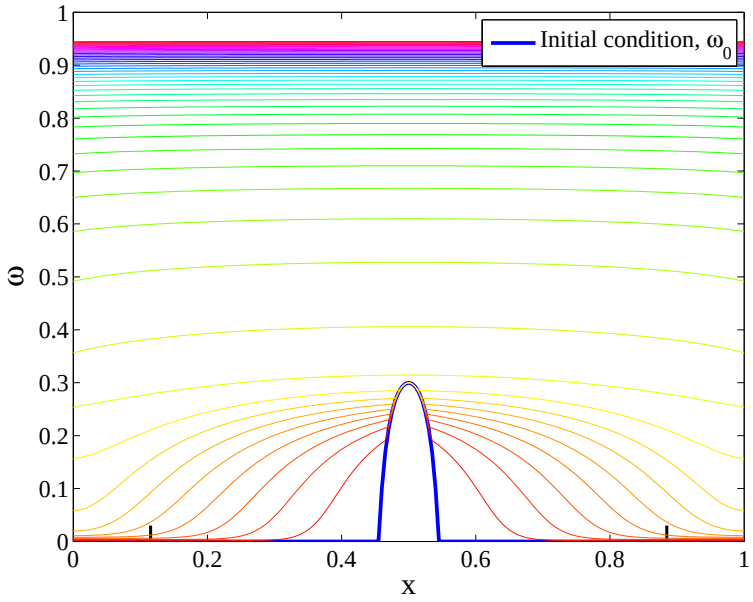

Figure 2.27: Distribution of damage from initial condition to the vicinity of blow-up for $\Lambda^2 = 6 \times 10^{-2}$ ($\theta/\theta_0 = 100$)

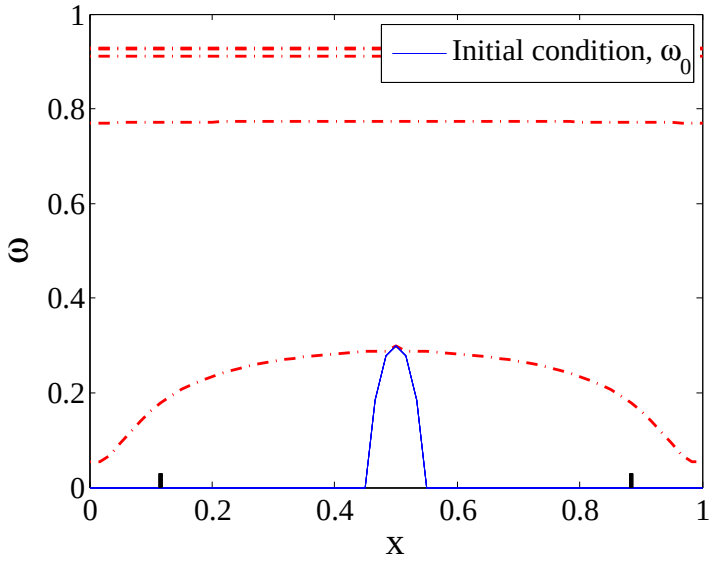

Figure 2.28: Distribution of damage from initial condition to the vicinity of blow-up for $\Lambda^2 = 6 \times 10^{-2}$ ($\theta/\theta_0 = 10$, 20, 100, 1000, 10000) and $\mu = 10$

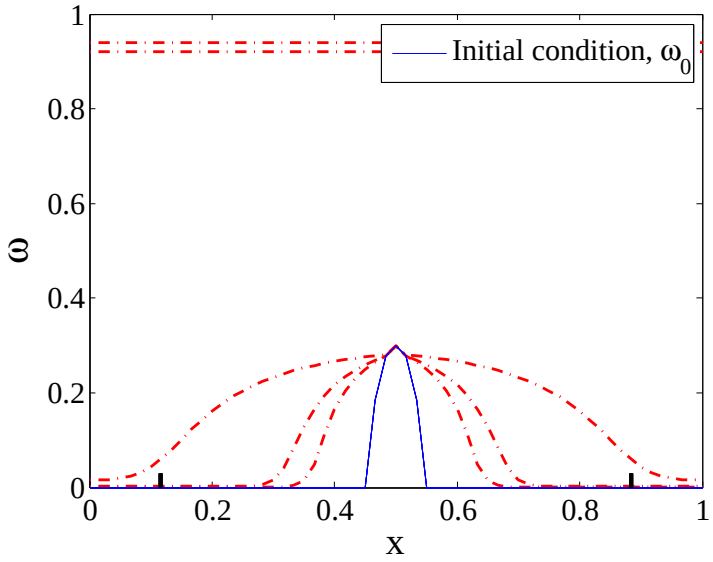

Figure 2.29: Distribution of damage from initial condition to the vicinity of blow-up for $\Lambda^2 = 6 \times 10^{-2}$ ($\theta/\theta_0 = 10$, 20, 100, 1000, 10000) and $\mu = 8$

2.5 Inverse problem

The solution of the forward problem requires the damage diffusion parameter Λ^2 and the forward model which is the nonlinear equation of damage diffusion. The results of forward solutions have been presented earlier. In order to perform an inverse analysis to obtain the actual value of the diffusion parameter, we first look into the stability of the forward algorithm. A high diffusion case, where Λ^2 is greater than 10^{-3} is selected so we can see large diffusion away from the initial damaged zone, toward the boundaries. Then a 1D forward analysis with certain damage diffusion parameter (e.g. $\Lambda^2 = 10^{-2}$) is performed and the distribution of damage at several dimensionless times

(below the blow-up time) is then obtained and plotted in Figure 2.30(a) in which the initial damage distribution is assumed to have the form shown at t=0. If the algorithm is stable, then we could perform inverse analysis using laboratory measurements of damage and retrieve the damage parameter for the reservoir rock type of interest. We expect that if we perturb the damage distribution $\omega(\mathbf{x}, t)$ of Figure 2.30(a) as we would get from the measured or observed damage in a 1D bar under tension, the perturbed or noisy data, $\omega^{\text{obs}}(\mathbf{x}, t)$ like the one shown in the Figure 2.30(b), will result in a damage diffusion parameter close to what we started with, here ($\Lambda^2 = 10^{-2}$).

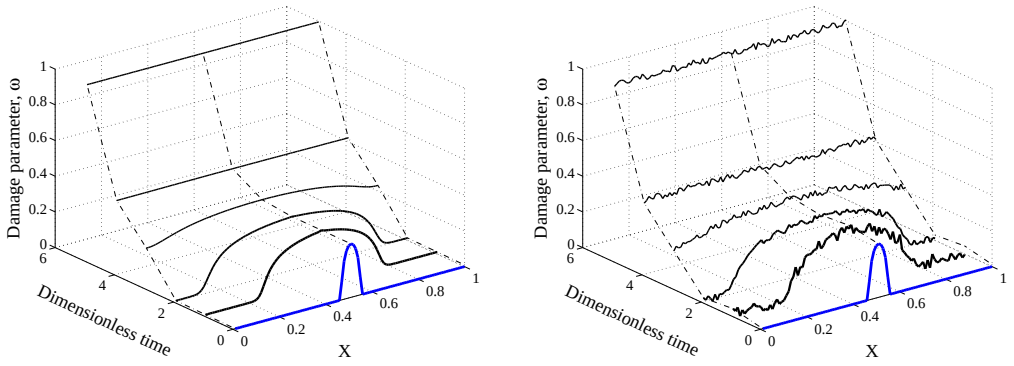

(a) Forward solution (b) Perturbed solution

Figure 2.30: 1D transient damage distribution for $\Lambda^2 = 10^{-2}$ (a)without and (b)with perturbation

The relation (2.39) is used to generate the perturbed data in Figure 2.30(b). The uniform probability distribution function (Rand) generates random numbers between 0 and 1, so (1-2×Rand) generates random numbers

between -1 and 1. To scale the damage parameter the coefficient α is used in this relation. It will be ranging from 10^{-3} to 10^{-1}.

$$\omega^{\text{perturbed}} = \omega + \alpha(1 - 2 \times \text{Rand}) \tag{2.39}$$

For $\alpha > 0.1$, the forward solution is not stable. In other words, the inverse analysis can not retrieve the damage diffusion parameter from the data.

Denote the forward model of damage as F, the input parameter (the damage diffusion, Λ^2) as m, and the calculated damage distribution using this forward model as d. Then the the forward model set up in simplest form can be shown as

$$F(m) = d \tag{2.40}$$

Equation (2.40) indicates that when the forward PDE model operates on the material property m, it calculates the damage distribution. It can be concluded from this statement that, to go in reverse, one has to follow the equation (2.41)

$$m = F^{-1}(d^{\text{obs}}) \tag{2.41}$$

The noisy data can be written as $d^{\text{obs}} = d + d^{\text{noise}}$ (similar to (2.39)), in which d^{noise} is the perturbation we will impose for sensitivity analysis or

the noise we get from measurement in the laboratory. We will perform inverse analysis later and show that as expected the matrix resulting from the inverse operator is ill-posed, in other words the matrix is close to singular with large condition number, which makes the results of damage diffusion parameter (m) invalid. To fix this problem we use the regularization methods which will be discussed later.

In the next step we choose damage parameters m or $\Lambda^2 = 10^{-3},\ 5\times10^{-3},\ 10^{-2},\ 2\times10^{-2},\ 4\times10^{-2}$ and 6×10^{-2} and run the forward model for each of these input parameters to obtain the distribution of damage at a few times. The objective here is to see which of the damage diffusion parameters from the list leads to a damage distribution as close as possible to the noisy measurement. It can then be concluded that we could perform inverse analysis by going from noisy measurement to obtain the candidate damage parameter Λ^2. Notice that the times at which damage is calculated are below the blow-up time at which solution ceases to exist. Let's call this discrete calculated damage vector, $\omega^{\text{calc}}(\mathbf{x}, t)$. These calculated solutions correspond to a certain damage diffusion parameter. If we measure how far off these calculated results are from the noisy data and use proper error norm for this distance, then the minimum error yields the right parameter m, which we expect to be very close to m=0.01 for a stable forward model.

The relative error used here is defined as follows;

$$\text{Relative error} = \frac{\left|\left|\omega^{\text{calc}} - \omega^{\text{perturbed}}\right|\right|}{||\omega^{\text{calc}}||} \tag{2.42}$$

Where ω's are both vectors. The vector norm here is the l_2-norm. For example, the numerator can be written as

$$\left|\left|\omega^{\text{calc}} - \omega^{\text{perturbed}}\right|\right| = \left(\sum_{j=1}^{J}\sum_{n=1}^{N}\left(\omega_{(j,n)}^{\text{calc}} - \omega_{(j,n)}^{\text{perturbed}}\right)^2\right)^{(1/2)} \tag{2.43}$$

Figure 2.31 shows the variation of error with the damage diffusion parameter Λ^2 for various α as defined in Equation (2.39). It can be seen that for $\alpha \leq 0.1$, the error is minimum at $\Lambda^2 = 10^{-2}$. This confirms the stability of forward solution in small perturbation imposed to the solution.

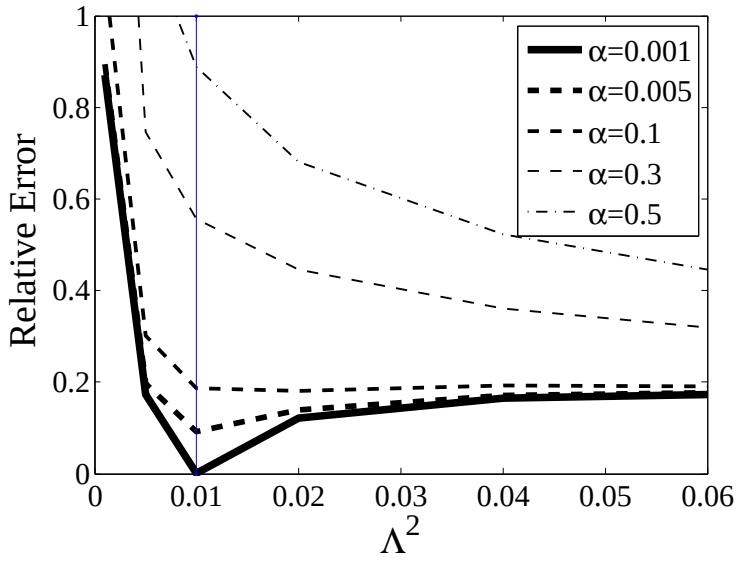

Figure 2.31: The plot of relative error versus damage diffusion parameter

2.6 Conclusions

1. We have shown that the weight function for stress in rock can be obtained using a Gaussian distribution. The finite element analysis results indicate that within rock matrix, stress at any point is correlated only to the stress at neighboring points which are up to three pore diameters away from that point. Since we are looking into the effect of fracture size, the dimension used for correlation has to be the opening or the void size. Therefore, the damage diffusion coefficient depends on the rock matrix connectivity. Loading, however does not play a role in the form of the weight function. The two scenarios of rock pore size distribution indicate that the correlation length is about three times the pore diameter.

2. A variogram analysis performed in conjunction with a finite element calculation or a laboratory stress measurement could be used to obtain the weight function for stress in reservoir rock. Once this function is obtained, the damage diffusion parameter, a material property, can be calculated and the governing PDE of damage can be solved.

3. The sensitivity analysis we performed shows that the forward problem is stable, hence enabling us to utilize inverse problem method to obtain the damage diffusion parameter.

Chapter 3

Fracture Mechanics Review

3.1 Introduction

This chapter briefly covers the theory of rock fracture mechanics and goes into the detail just to the extent to clarify the ideas presented in this dissertation. Some ideas such as dynamic fracture propagation and instability of fracture are not covered here, as they are off the main subject of this research work. The main objective of this section is to introduce the reader to the terminology of fracture mechanics in general, and the concepts of stress intensity factor and energy release rate so as to set the scene for the reader to appreciate the concept and formulation of thermal fracturing in shale plays as a novel method to improve recovery of hydrocarbons.

Rock failure studies should start from microstructure level where thermodynamics and energy of bonds govern the physics of rupture and fracture creation. We have looked into the phenomenon of rock damage and bond breakage, in the first chapters of this dissertation. Some terminology including the range of discontinuities will then be explained. The works of Inglis [118], Irwin [119] and Griffith [99] were the fundamental efforts in development of fracture mechanics and explained in this chapter.

3.2 History of fracture mechanics

The first efforts to understand the source of fracture in materials are attributed to the experiments of Leonardo da Vinci to find the tensile strength of metal wires. The results of his experiments revealed that the strength of wires are inversely proportional to the length of wires. In other words, as the length of the wire increases, it becomes more prone to having material defects, hence it's strength decreases. The results he presented were qualitative and the first quantitative relation between failure stress and size of crack was proposed by the works of Griffith in 1920[99]. Inglis[118] in 1913 obtained the stress around an elliptic crack and Griffith used those results to come up with a criterion for unstable propagation of fractures. To achieve this result, he used the first law of thermodynamics to write an energy balance equation. In this equation, a crack becomes unstable when the variation of strain energy due to crack growth exceeds the surface energy of the material. Griffith's theory clearly exhibits the relation between strength and fracture size in a glass specimen which in internally notched by a crack. Future efforts to extend Griffith's idea to metals were not successful, because his model assumes that the energy required for fracturing is composed of surface energy only. This is true only for brittle materials, so Griffith's idea can only predict the fracture behavior in brittle materials.

The second world war and the failures of Liberty ships, made the fracture mechanics go from a scientific research to an engineering branch of science. Unlike all other ships of that era whose bodies had riveted joints and con-

nections, the bodies of Liberty ships where entirely welded. Figure 3.1 shows the early Liberty ships which suffered hull and deck cracks and were lost to such structural defects. During world war II, there were nearly 1,500 instances of significant brittle fractures. Nineteen ships broke in half without warning, including the SS John P. Gaines, which sank on 24 November 1943 with the loss of 10 lives.

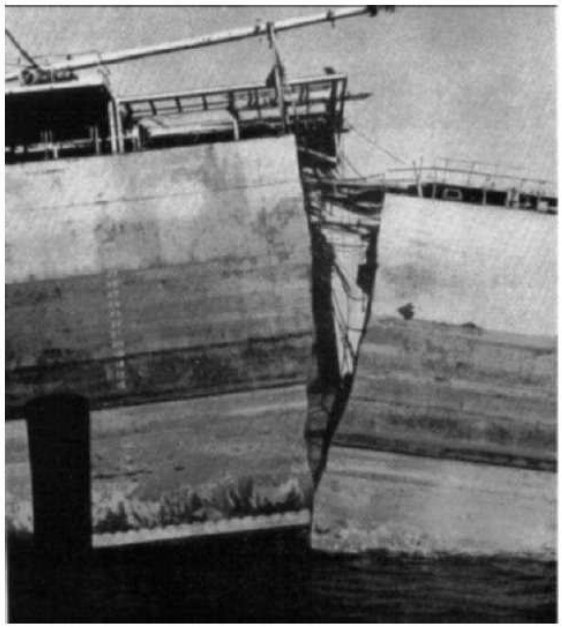

Figure 3.1: Early Liberty ships which suffered hull and deck cracks.

Later, research revealed that the steel used in these ships possessed a low fracture strength. The failure event made a group of researchers, supervised by Dr. George Rankine Irwin, study the problem of fracture in detail. The main contribution of Irwin was to use the previous works of Inglis, Griffith

and others and add the plastic energy release to extend Griffith's idea from brittle materials to metals in 1948.

In 1957, Irwin [119] presented the idea of energy release rate. Based on the works of Westergaard[247], Irwin proposed the stress intensity factor (SIF) constant whereby the stress and displacement fields around the crack tip can be related to the energy release rate.

By 1960, the fundamentals of linear elastic fracture mechanics (LEFM) were completed and studies of fracture mechanics were directed toward plasticity at the crack tip. When plastic deformations at the crack tip become large, the assumptions of LEFM are not valid any more and the results from such analysis may not be used. In a short time, many researchers including Irwin [119], tried to rectify the effects of plasticity at the crack tip. Wells introduced the displacement of the two crack surfaces as a replacement for plastic failure criterion when plasticity effect is not negligible. His works led to the development of the method of crack tip opening displacement (CTOD)[246]. In 1968, Rice[208] defined another parameter for description of the nonlinear material behavior at the crack tip. He invented the J-integral, based on the works of Eshelby in development of path independent integrals. He showed that this integral is equal to the energy release rate. In the same year, Hutchinson put forward the so-called HRR (Hutchinson-Rice-Rosengren) theory of elastic-plastic stress fields in power hardening materials, which paved the road to the modern Non-Linear or Elasto-Plastic Fracture Mechanics (NLFM, Hutchinson, 1968, and Rice and Rosengren, 1968). In the HRR theory, they related the J-integral to

the stress distribution in the crack tip of nonlinear materials.

In order to make use of fracture mechanics in engineering design applications, the mathematical relations among toughness, stress, and crack size should be fully determined. This happened for LEFM, but the J-integral method advanced only until 1976. The subsequent research results of Shih and Hutchinson were not published and construction of a theoretical foundation for this approach did not take place.

3.3 The nature of fracture

Creation of fracture is the loss of connection of a solid material's constituents and is the main topic of fracture mechanics. Cracks in solid bodies could be pre-existing such as voids, notches, and pore spaces or they could be randomly created and distributed in material during the formation process. Failure is the final stage of fracture propagation, in which complete separation of the two parts of a body takes place in a short time. In general, crack propagation in different from failure. Fractures are classified as brittle and ductile. In brittle failure, the plastic deformation before failure is small; as a result, the solid material absorbs little energy before failure. In ductile failure; however, a large plastic deformation at the crack tip could be created and significant energy could be dissipated before fracture initiates. Material behavior is shown in Figure 4.4, in which the brittle material shows small strain and large stress at failure, the ductile material shows large strain and small stress at the failure point. The area under the stress-strain plot in Figure 4.4 is the

energy absorbed per unit volume. Toughness is the property of material to absorb energy and it's proportional to the area under the stress-strain plot.

3.4 Terminology of fracture mechanics

The science of fracture mechanics is shared by many engineering disciplines, as a result, the literature uses various terms for openings in the rock mass. To avoid confusion, the terms used in this dissertation are defined below.

Various openings including, voids or pore spaces, cracks, joints, veins, dikes, fractures, and faults, may exist in the rock body. Notice that the two words, separation and discontinuity are used to indicate opening and the word rupture is used to indicate the failure mechanism which leads to the creation of discontinuity. To provide a clear classification of these terms, let's look into the external sources that create such ruptures in rock. The rock behavior is a function of pressure, temperature, rate of loading, and lithology of the rock. Another classification for rock behavior is brittle versus ductile behavior. In geology, the process of failure for a brittle rock, is called faulting, fracturing, or elastic failure. Failure of a ductile rock, is called folding, rock flow, or plastic failure. There are two types of fracture types in terms of loading mechanism; there are: tensile and shear failures. Tensile failure is the type of failure in which the relative displacement is perpendicular to fracture faces, in other words, the failure takes place in an opening mode. In shear failure, the relative displacement is parallel to the fracture faces. Shear failure, creates faults and fractures, but tensile failure, creates, micro-cracks, fractures, joints, veins, and

dikes. Since we are mainly dealing with openings in rock, the veins and dikes which are either partially or fully filled with other minerals, are excluded in the following description of the rock discontinuities.

A *crack* is a three dimensional opening or a void-like inclusion in rock, in which one dimension is extremely smaller than the other two dimensions. The smallest dimension is called, thickness, aperture, or width of crack. Across the width, traction is reduced. The other two dimensions are length and height of crack. The aspect ration of a crack is the ratio of width to length and is typically in the order of 10^{-5} to 10^{-3} [217]. A crack in a solid body creates stress concentration at the crack tip, which may lead to breaking or shearing of atomic bonds. The openings in the rock exist across several scales, for example, cracks may be observed in micro-, meso-, and macro- scales. Micro-scale cracks are planar discontinuities whose maximum dimension is about a few grain diameters which could be in the range of one thousandth to one thousand microns. A meso-crack is a one to few millimeter discontinuity, which spans more than one grain and is formed thorough a complicated rupture event. Meso-cracks may be formed through connection of several micro-cracks. The macro-cracks span millimeters to decimeters. In reservoir geomechanics, fracture is any opening in the range of meso- and macro-cracks. The strength of material is largely infuenced by the existence of cracks at various scales. Figure 3.2 shows various sizes of cracks. The continuum scale is the size larger than $100\mu m$ for which the fracture properties, elasticity and yield can be defined and formation of yield regions occurs at meso-scale [41]. The rock damage

evolution studies in this research focuses on molecular and meso- scales, and thermal fracturing is studied at continuum scale (Figure 3.2). The aim of this research is to facilitate the hydraulic fracturing process in tight formations using thermal shocks and extend the thermal and hydraulic fractures to in-situ fractures and joints. Studying faults is beyond the scope of our work. Joints are parallel sets of discontinuity in rock which are formed during cooling or tectonic movements. Joints are characterized by displacements normal to crack surfaces and no displacement parallel to crack surfaces. Faults are formed by shear deformation; therefore, they are characterized by displacement parallel to fracture surfaces [197].

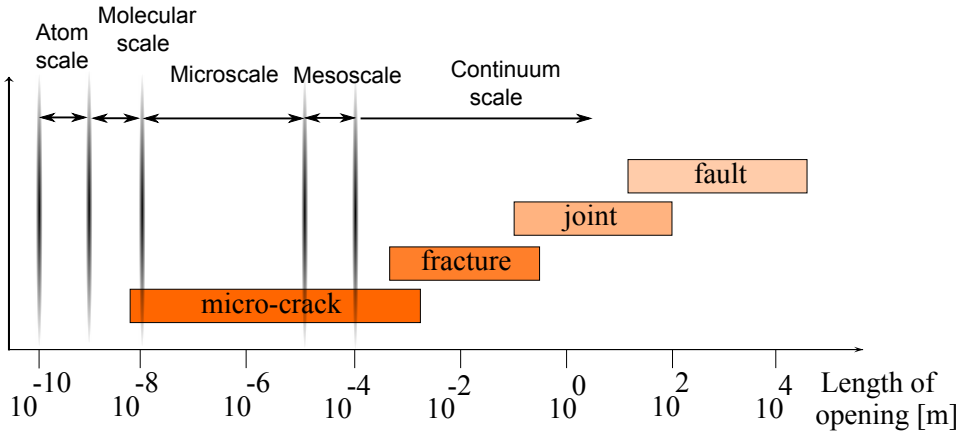

Figure 3.2: Various sizes of cracks [41, 77]

3.4.1 Fracture System

Figure 3.3 shows the nomenclature of a fracture system. A fracture system is composed of the main fracture, which is an opening formed by two traction free surfaces, and a process zone containing micro- and meso-cracks. The meso- or macro-cracks could emanate from the main fracture. These are called branching cracks. Prior to the process of main fracture growth, extensive micro- and meso-cracks form ahead of the fracture tip.

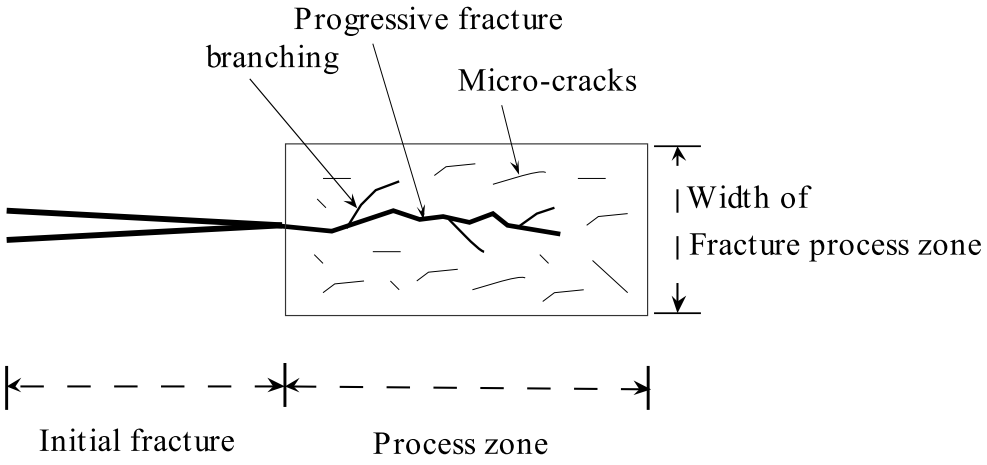

Figure 3.3: Nomenclature and schematic of fracture process zone (not drawn to scale) (modified after Liu et al. 2000 [155])

The small zone at the crack tip in which the bonds break due to sliding and separation as the fracture growth initiates, is called the Fracture Process Zone (FPZ). The size of the FPZ is mainly a function of the rock grain size and loading nature e.g. [111, 142, 253, 258, 260]. The size of the FPZ is about five

to ten times the average grain size [111, 253]; However, greater values up to 40 grain diameters have been reported [248]. Broberg [38] defines the fracture process zone as the area ahead of fracture tip where micro-cracks extend to coalesce and form an inelastic deformation zone. In ductile materials, a major portion of energy used to extend the fracture is imparted to the FPZ.

3.5 Modes of Fracture

Depending on the applied load, there are three modes of fracture as shown in Figure 3.4. In our application in hydraulic fracturing, most of the times, the first two modes take place.

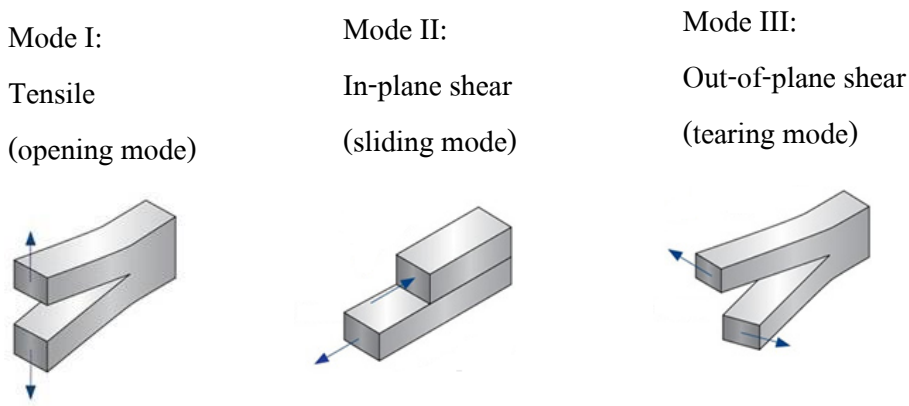

Figure 3.4: Three modes of fracture.

3.6 Rock Failure in Micro Scale

Cracks exist in solid materials at all scales. The existence of cracks plays a significant role in the strength of the solid. Experiments performed by Inglis[118], showed how defects and flaws control the strength of a material. He applied tensile loading on a bar made of glass in which a flaw of length L was made until failure and measured the failure load. He then changed the length of the flaw and repeated the experiment. He showed that as the flaw length increases, the failure load decreases, i.e., the strength of material decreases. This is a significant finding which suggests that the strength obtained from laboratory experiments for a certain sample size can not be used for a sample of a different size and the effect of cracks, voids, and flaws should be taken into account. Here we utilise atomistic scale analysis to show the maximum possible strength of a solid material with no voids or flaws. The results provide an insight in understanding the effect of bond energy and deformation at which a material could fail. These results would then be used in defining the Cohesive Zone Law (CZL), which is presented in Section 3.8.

Let's consider a lattice model for a solid material as shown in Figure 3.5 with mass points for atoms and springs for bond forces. Applying a force F will separate the atoms further to point $X > X_0$ until the theoretical value F_C is reached and the bonds start to break. The atomic potential function Ψ and the force function, which is the derivative of the potential function with respect to displacement X ($F = \frac{\partial \Psi}{\partial X}$), are shown in Figure 3.5. The atomic force function F can be approximated as a half of a sine function, Equation (3.1) in which

F_c is the maximum load or the load at which the bonds start to break. F_c is also known as the cohesive force; X_0 is the equilibrium spacing; $X - X_0$ is the distance between atoms when deformed from equilibrium state; λ is the length of a full sine function.

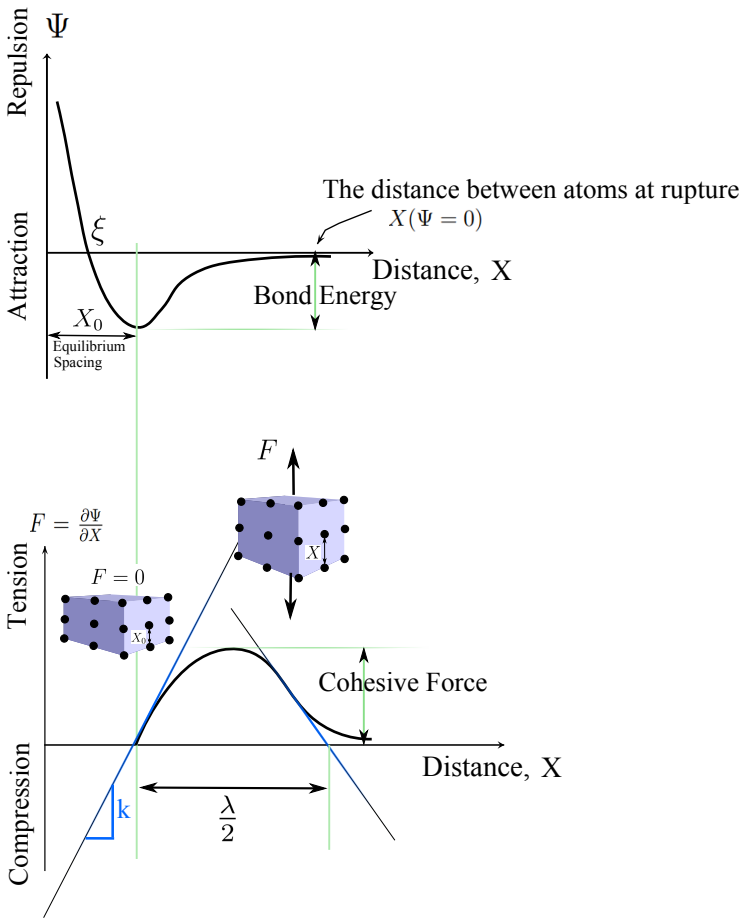

Figure 3.5: Atomic forces and fracture in atomic scale

$$F = F_c \sin\left(\frac{2\pi(X - X_0)}{\lambda}\right) \tag{3.1}$$

for small displacement x, we have $\sin x \approx x$, therefore;

$$F = F_c \left(\frac{2\pi(X - X_0)}{\lambda}\right) \tag{3.2}$$

comparing Equation (3.2) with Hooke's law, the stiffness of the material can be found as expressed in Equation (3.3);

$$K = \frac{2\pi}{\lambda} F_c \tag{3.3}$$

if the number of bonds is known, Equation (3.3) can be used to obtain the stiffness of a single bond; however, let's shift from force to stress to investigate the strength of material as a function of the Young's modulus and study the impact of scale of sample on the strength of the sample.

Stress in one dimension is defined as;

$$\sigma = E\left(\frac{X - X_0}{X_0}\right) \tag{3.4}$$

in which E is the Young's modulus. Equation (3.4) is useful in finding the cohesive strength or the maximum stress that can be applied to a material in atomistic scale at the onset of bond breakage. As shown in Figure 3.5, maximum load occurs when $X - X_0 = \lambda/4$; therefore, the cohesive strength can be obtained from Equation (3.4) as;

$$\sigma_c = \frac{E\lambda}{4X_0} \tag{3.5}$$

Bond energy is an important parameter which is used in atomistic analysis of fracture. It is worth mentioning that, given the force displacement plot shown in Figure 3.5, the bond energy E_b can be calculated using Equation (3.6)

$$E_b = \int_{X_0}^{\infty} F \, dX = \Psi(X)|_{X_0}^{\infty} = -\Psi(X_0) \tag{3.6}$$

this is the area of the force-displacement or the traction-separation plot. This will be explained in more detail later when we study the cohesive zone law. For now, let's write the Equation (3.2) in terms of stress instead of force;

$$\sigma = \sigma_c \left(\frac{2\pi(X - X_0)}{\lambda} \right) \tag{3.7}$$

let's replace the left-hand side of Equation (3.7) with Equation (3.4) to get;

$$E \left(\frac{X - X_0}{X_0} \right) = \sigma_c \left(\frac{2\pi(X - X_0)}{\lambda} \right) \tag{3.8}$$

and the cohesive strength can be calculated as;

$$\sigma_c = \frac{E\lambda}{2\pi X_0} \tag{3.9}$$

for a reasonable value for deformation at failure $X_0 = \lambda/2$, the theoretical cohesive strength will be;

$$\sigma_c = \frac{E}{\pi} \tag{3.10}$$

experiments suggest that the true fracture strength is typically 3-4 times below the theoretical value of Equation (3.10).

3.6.1 Fracture Surface Energy

Now that we have defined the theoretical value of the cohesive strength, we can use atomic force function and define another important parameter, called surface energy in fracture mechanics. The surface energy is the energy required to create a fracture surface and can be calculated using integration of the work done to break the bonds. The energy required to break the bonds is equal to the area under the stress deformation plot using Equation (3.11). It should be noted that the surface energy creates one surface; since the energy that creates fracture, creates two surfaces, we have;

$$2\gamma = \int_0^{\lambda/2} \sigma_c \sin\left(\frac{2\pi X}{\lambda}\right) dX = \sigma_c \frac{\lambda}{\pi} \tag{3.11}$$

we can then find σ_c as

$$\sigma_c = \frac{2\pi\gamma}{\lambda} \tag{3.12}$$

λ from Equation (3.9) is then plugged into Equation (3.12) which results the value for the cohesive strength given in Equation (3.13).

$$\sigma_c = \sqrt{\frac{E\gamma}{X_0}} \tag{3.13}$$

for most of the solids, the surface energy is $\gamma \approx 0.01\ EX_0$ [57, 229]. This results in the following value for the cohesive strength;

$$\sigma_c = \frac{E}{10} \tag{3.14}$$

using this theoretical value, for shale and most metals with $E = 50$ GPa, the cohesive strength is $\sigma_c = 5$ GPa (7×10^6 psi), whereas the experimental

cohesive strength for metals is 10-100 times, and for shale 10,000 times less than this theoretical value. The reason behind these discrepancies as pointed out already by Leonardo da Vinci, Griffith, and others, is 1)the existence of flaws in solids which leads to stress concentrations, and 2) the planes of weakness such as grain boundaries in rock. The second of the two justifies the four orders of magnitude difference between the practical and theoretical values of the cohesive strength for shale.

3.7 Rock Failure at Different Scales

Rock failure is a complicated phenomenon because it encompasses a wide range of temporal and spatial scales. At different observation scales, materials could behave differently as the load transfer mechanism and strength are both scale dependent. At macro-scale, the effect of microstructural crack development is not seen in the strength formulation used in rock mechanics. For example, Mohr-Coulomb criteria compares the shear stress and shear strength at the most critical surface inside material and determines whether or not the body fails under shear stress. The final failure state of a material goes through a series of failures at smaller scales in which micro-cracks due to localized shear of atomic lattice also known as dislocation, leads to inter-granular failures and the coalescence of these smaller cracks results in macro-scale shear displacement. The brittle and ductile properties of a material which depend on toughness are the result of failure and deformation mechanism at atomic scale. In ductile materials, deformation is mediated by creation of dislocation

networks and in brittle materials, fracture propagates by spreading of cracks, which is mediated by continuous breaking of atomic bonds [41]. Figure 3.6 shows an idealization of rock failure at different scales. Molecular bond rupture is in fact, the starting stage of material failure irrespective of observation level. In spite of similar failure law at all levels of failure investigation, the numerical studies at smaller scales are extremely time-consuming as a result of many components involved in analysis. Unless high performance computing (HPC) and multiprocessor computational resources are used, obtaining the results at smaller scales is impossible. It should be noted that, despite this computational hurdle, small-scale analysis provides invaluable insight toward material behavior under investigation. A fully detailed analysis of failure includes molecular forces and interactions into creation of fractures. For reservoir scale simulations, molecular scale simulation is impossible. This is why micro-scale simulations are so popular. Besides, the molecular properties could be lumped into material properties of a micro-scale model and run a simulation much faster.

In this research, we start with molecular-scale rock failure to gain the insight to rock failure process and move into studies at micro- to macro-scale reservoir rock failure in oil and gas industry. Whenever a need arises, for instance, in thermal rock failure studies for research objectives, we resort to micro-scale numerical analysis such as particle method and discrete element method (DEM). These simulations are normally quite fast; however a high resolution model requires a lot of CPU hours for which we utilize super

computer facility at the University of Texas at Austin known as Texas Advanced Computing Center (TACC). The main direction of this research is to use a micro-scale model to investigate how micromechanical properties of rock, characterize the macroscopic response. The model established this way will be capable of predicting the macro-scale behavior of reservoir rock for other loading scenarios, including thermal loads and hopefully sheds light on rock failure mechanism and promote our understanding of rock failure process.

3.8 Cohesive Zone Law (CZL)

3.8.1 Introduction

The structure of rock can be idealized as an assembly of pieces stuck together along the boundaries using cohesion and friction. In rock mechanics, the pieces are called fragments and the cohesive zone along the boundaries is called the contact zone. Depending on the rock material properties and the applied load, when the material is subjected to external loads, the failure could occur within the boundaries of fragments, also known as contact zones. In Figure 3.6, the fragments are idealized as mass particles or mass blocks and the contact zone or the potential failure zone is idealized as springs. The rupture of the contacts follows a cohesive zone model which follows a traction-separation law, as shown in the right column of Figure 3.6.

The concept of the CZL was first put forward by Elliott [71] who introduced an interatomic attraction-repulsion force per unit area to investigate the amount of energy required to fracture a crystalline substance. Later,

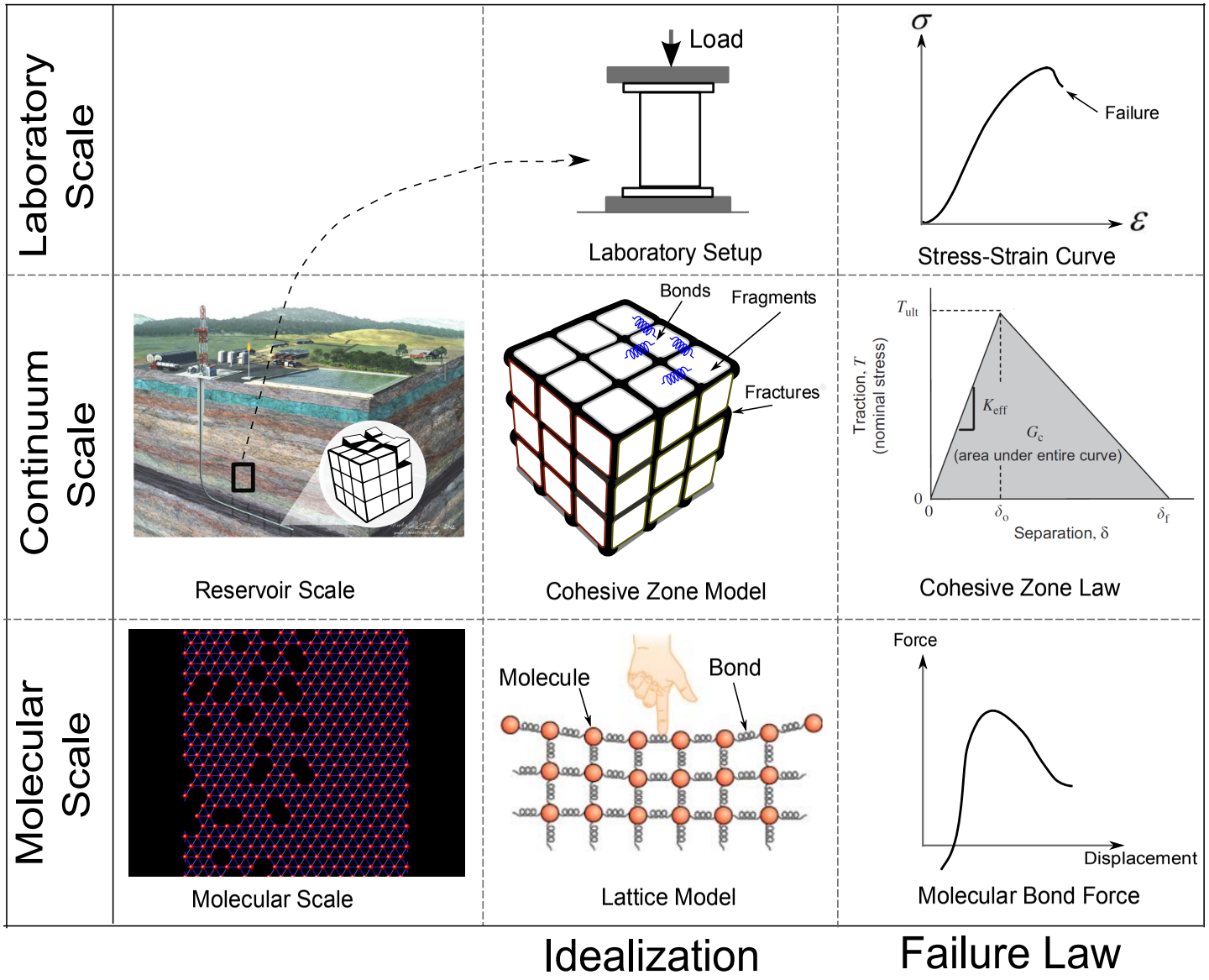

Figure 3.6: Idealization of rock failure at different scales

Barenblatt [19, 20] and Dugdale [68] looked into the concept of CZM from energy standpoint in brittle materials. Dugdale's work was more focused on the size of the plastic zone. Later, Smith [219] developed a general theory for cohesive behavior of rocks and provided a series of traction-separation plots based on the displacement along the fracture tip. An extended CZL called the fictitious crack model has been employed for quasi-brittle materials such as fiber-reinforced concrete and rocks in cases where the size of fracture process zone is not negligible [13, 35, 70, 110, 209]. Hillerborg *et al.* [110] introduced a softening regime using fracture energy and the tensile strength of rock. CZM has been widely used for several application in rock fracturing including thermal fracturing [202]. Studying failure of materials using cohesive depending the rock material properties and the applied load model (CZM) contains four distinct stages:

1. Pre-failure; this stage is mainly linear deformation of the fragments and contacts. At this stage, the contacts are not broken yet, in other words, there is no separation normal to or along the contact boundaries (no gap or sliding).

2. Failure; when the normal and shear strength of contacts are exceeded by the external load (also known as traction), one or a number of fragments undergo excessive displacements and local fractures are initiated. This stage is initiation of damage i.e., local rupture of contacts or bonds. Failure is the peak point in CZM plot in Figure 3.6.

3. Post-failure; this stage starts from the first bond rupture and may continue if the external load keeps increasing. This phase is the evolution of local failure or damage evolution stage of rock fracturing, during which the rock loses its strength and exhibits a softening behavior. Softening behavior is due to the reduction of Young's modulus of elasticity or the slope of stress-strain plot. In Chapter 2 we study the evolution of damage using solution of a nonlinear parabolic partial differential equation without looking into each single bond failure. The damage evolution is the declining section of the stress-deformation plot (also known as traction-separation model or CZM). The declining section of the CZM could be linear or nonlinear and will be explained in detail in Section 3.9.

4. Fracture; if the external load keeps increasing, the post-failure stage terminates by creation of a populated crack density zone and creation of distinct failure surfaces.

In Chapter 7 we will compare the capabilities and limitations of the numerical methods used for rock thermal fracturing. A few of these methods are studied in this dissertation. We will show in detail an application of CZM in conjunction with numerical simulation and its application in fracturing rock for the oil and gas industry. Problems such as uniaxial loading, three-point bending of a beam, and wellbore stability will be used in the context of best numerical method to validate and introduce the most efficient method of using CZM for rock fracturing purposes.

3.8.2 Damage and Failure

In this section, the terms "damage" and "failure" are explained as they are used in fracture and rock mechanics terminology. All material failures or rupture has to go through a stage of damage evolution. This phase could be either very fast or slow depending on material behavior. In Chapter 2, the evolution of damage was studied whereby an effort was made to investigate the impact of key rock parameters in the form of the declining segment of Cohesive Zone Model in Figure 3.6.

To understand the difference between damage and fracture on a solid body one has to see the solid body as a component such as the one shown in Figure 3.7 (left), which is made up of smaller constituents (i.e., small elements in Figure 3.7). As the load is applied to the solid body, the entire component undergoes stresses; as a result, each smaller constituent undergoes stress. If the stress reaches a maximum value of tangential or normal stress, the elements start to fail. The failure of an element is called damage for the solid body. The damage would then increase as the local element load continues to increase until a final stage is reached, when all the elements fail, a catastrophic failure occurs as shown in Figure 3.7 (Right).

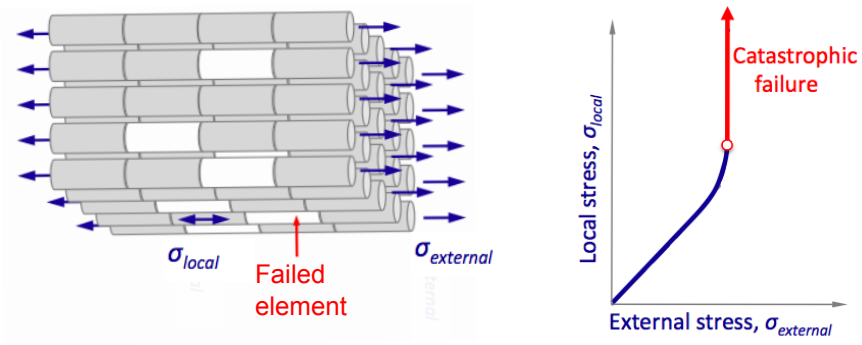

Figure 3.7: Progressive damage in elements and failure in the entire solid body, called fracture

As the solid material is subjected to external load, there is always a linear stress-strain segment for the material behavior. This could be a small segment compared to the entire segment before the stress reaches a maximum value shown in Figure 3.8. During the stages of material behavior prior to maximum load, the deformations are elastic; in other words, if the load is removed the strains in the body go back to initial state of strains no residual strain is accumulated. The peak of the plot is where the damage starts to initiate by developing voids in the body. Under the action of external load, the voids undergo additional level of stress and coalesce to extend the damage zone. This is depicted in the declining segments of the load-displacement plots in Figure 3.9. The entire declining segment is the damage evolution zone for the solid body or progressive failure regime for the local elements. Damage parameter was defined in Chapter 2. The value of damage parameter at the peak of the force-displacement plot is zero and at the final stage, where the

two parts of the body get fully separated, is equal to 1. The progress of damage in materials, reduces the stiffness of material from initial stiffness to a reduced stiffness shown in Figure 3.8. To attain a level of displacement, the external load imparts some energy G_I which is equal to the area under force-displacement plot. An energy equal to the entire area under the force-displacement plot is required to fail a material. This energy depends on the strength of material and is called the critical energy release rate. This is depicted by G_Ic and $G_{II}c$ for the two modes of failure which are two general cases of failure in Figure 3.9.

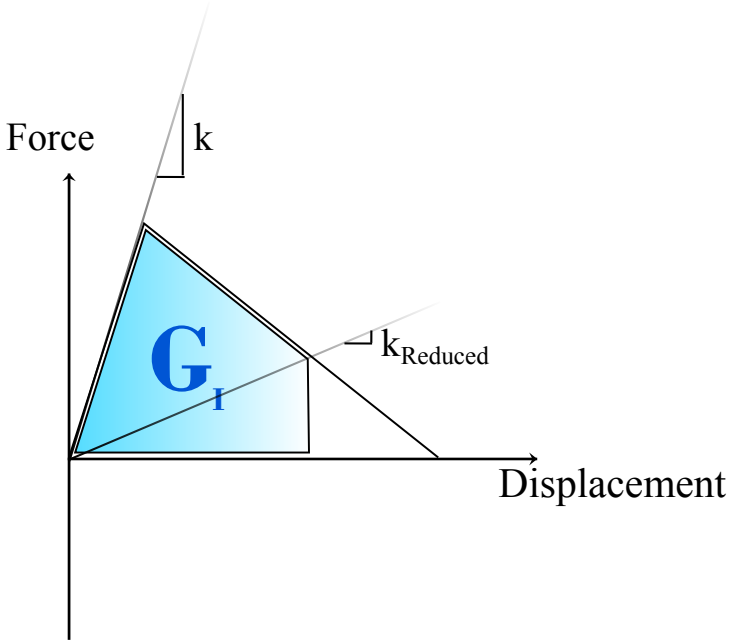

Figure 3.8: Initial stiffness, reduced stiffness, and energy used during deformation of solid material before fracture is created.

These two plots are required to give the damage and failure properties of a certain material. Most finite element codes, which utilize the cohesive zone method for fracturing purposes, use either one of the two forms of load-displacement or traction separation plots. It should be noted that both plots lead to the same results; however, it is a matter of what laboratory data are available to a user. One form of plot uses fracture energy and the value of the strength of material, i.e., the peak value of the plot. The other form of the plot uses the peak value and displacement at de-bonding, which is the maximum displacement in the traction-separation plot in Figure 3.9 for fracture simulation using CZM in the finite element code. We have used CZM and DEM in Chapter 6 and compared the results of these numerical methods in Chapter 7.

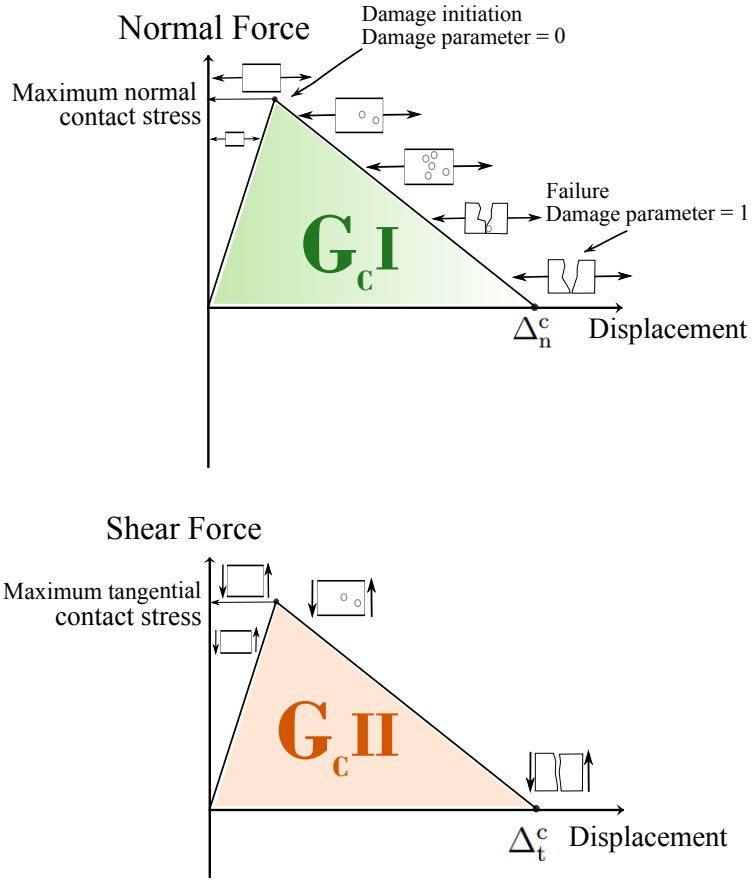

Figure 3.9: Two modes of the traction-separation plots for damage and failure of materials. Δ_n^c and Δ_t^c: Contact gaps at the completion of de-bonding

$\omega = 1$ $\omega = 0$

3.8.3 The Nature of Rock Fracturing Process, dynamic or quasi-static?

Rock failure which encompasses the stages of initial void creation (damage initiation), coalescence of voids, damage evolution, and fracture (ultimate failure) is a scale dependent problem. Depending on the scale of investigation, what is called fracture propagation at a certain scale can be regarded as evolution of damage at a larger scale. The classic fracture mechanics is based on the propagation of a single fracture in a homogeneous medium for which the accumulation of the energy from the external load is not considered to be happening over time. As a result, to study propagation of a single fracture in a solid body, time is simply used for tracking the occurrence of events, in other words, the fracture propagation under static load can be solved using quasi-static formulation. In other words, we can claim that in hydraulic fracturing process, the effects of inertia (inertial loads) are much lower than the loads due to injecting fluid pressure. So, the process is driven by the applied pressure and stops upon termination of pressure application. This is typical of a quasi-static process.

To study fracturing problem at a larger scale, say reservoir scale at which in-situ and hydraulic fractures tend to grow, intersect, and in other words promote the level of damage at reservoir scale, a time dependent equation is required. We started this dissertation with the idea of damage evolution in rock to investigate the impact of loading and rock properties in damage evolution of rock. The solution of hydraulic fracturing problem is not part of this

research work and all the time dependency of equations are due to damage evolution which is the fundamental step prior to onset of the fracture initiation.

With this introductory definition of damage and failure in the context of CZM, we can now go over two approaches for fracture analysis in fracture mechanics and then present the formulation of the CZM used in the finite element code and set the scene for thermal fracturing simulation using the fundamentals of material failure explained here.

3.8.4 Two approaches for Fracture Mechanics Problems

There are two main approaches to study fracture problems; stress-strain and energy approaches. There are briefly reviewed here and it is shown that for linear elastic materials, these two approaches yield exactly the same results.

Classic fracture mechanics or linear elastic fracture mechanics (LEFM) was developed based on the idea of stress i.e., whenever the applied stress gets to the point of maximum stress, the solid material fractures. The biggest problem with the classic fracture mechanics is the existence of stress singularity at the fracture tip. The magnitude of the stress singularity at a fracture tip is captured by stress intensity factor K. Figure 3.10 shows the schematic representation of the two modeling approach in fracture mechanics. In reality, there is an inelastic zone called fracture process zone (FPZ) at the fracture tip; however, LEFM assumes there is no FPZ and stress is theoretically approaching infinity at the tip. This problem can not be solved using classic

finite elements by refining the mesh at the crack tip and the singularity of stress is proportional to $1/\sqrt{\mathrm{r}}$, where r is the distance from the fracture tip. Even though the stress is not bounded at the fracture tip, the energy is always bounded. This brings the idea of cohesive zone model to overcome the stress singularity problem.

3.8.5 Stress-Strain Approach

One of the significant achievements of Irwin and his colleagues was to calculate the amount of energy available for fracture in terms of the asymptotic stress and displacement fields around a crack tip in a linear elastic solid [119]. Using Irwin's work and elasticity relations, it is shown in stress-strain approach that the stress around a crack tip can be calculated using a single parameter K. This parameter represents the singularity of stress at the tip of fracture. Irwin called this parameter the stress intensity factor. Using this parameter, the asymptotic expression for the stress field around a crack tip is as Equation (3.15),

$$\sigma_{ij} \approx \left(\frac{\mathrm{K}}{\sqrt{2\pi r}} \right) f_{ij}(r, \theta) \tag{3.15}$$

where σ_{ij} are the stresses, r is the distance from the crack tip, θ is the angle with respect to the plane of the crack, and f_{ij} are dimensionless functions that depend on the crack geometry and loading conditions. Since f_{ij} is dimensionless, the stress intensity factor can be expressed in units of MPa-$\sqrt{\mathrm{m}}$.

The stress intensity factor K can be defined for all three modes of fracture using indices as K_I, $,\mathrm{K}_{II}$, K_{III}. Since the stress at the crack tip

is defined by the stress intensity factor, the criterion for fracture is that the stress intensity factor attain its critical value K_c. This critical value is called toughness and has the units of stress times square root of length. Toughness for rock is obtained from compaction tension (CT) test. In general the criteria for fracture initiation are a combination of the Stress Intensity Factors (SIF)s. In many cases, due to the domination of one mode over the others, the SIF for that mode is used in the fracture initiation criterion. In two dimensional analysis, the value of SIF is normally more critical in plane strain than in plane stress; therefore, the SIF value from plane strain experiment, K_c, is normally used in fracture mechanics studies. Based on stress-strain approach, the criterion for fracture is $K = K_c$.

3.8.6 Energy Approach

The energy approach was first introduced by Griffith in 1921 [99]. In this approach crack initiates when the energy used to create fracture G, overcomes the strength of material. The strength of material against fracture creation R, could be surface energy, energy dissipation due to plastic deformations or any other forms of energy dissipation as a result of fracture propagation. The surface energy is defined in detail in Section 3.6.1. Griffith defined the energy release rate G. It can be shown that in the load-control or displacement-control loadings, the parameter G is equal to the rate of strain energy release, Equation (3.16).

$$G = \left| \frac{dU}{da} \right| \tag{3.16}$$

in other words, G is the rate of release of energy per unit thickness per unit increase in fracture length a; therefore the unit of G is energy per unit area or force per unit length of fracture. Based on energy approach the criterion for fracture propagation is;

$$G \geq R \tag{3.17}$$

Figure 3.10 shows the state of stress at the fracture tip in reality, when assumption of no FPZ is made, and how CZM approach eliminates the singularity at the tip.

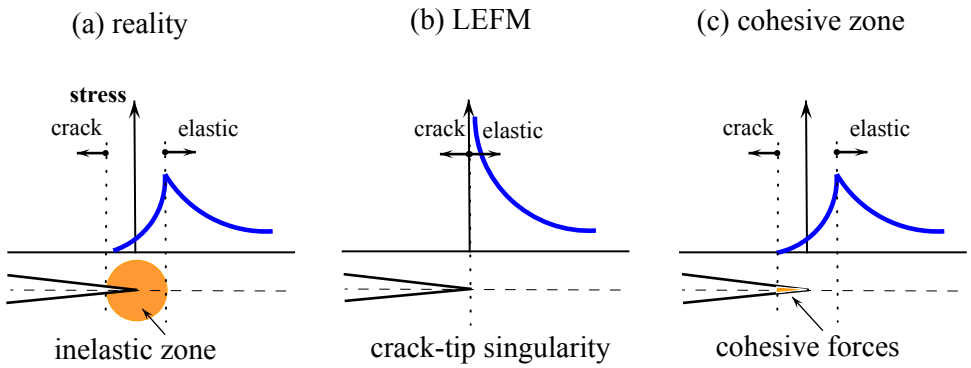

Figure 3.10: Schematic representation of the two modeling approaches for stress analysis at the crack tip (modified after [174]).

3.9 Formulation of the Cohesive Zone Model (CZM)

One of the fundamental aspects in cohesive zone modeling is the definition of the traction-separation relationship across fracture surface. The cohesive zone model was developed to both diminish the stress singularities

in the LEFM and approximate the nonlinearity of material separation during fracturing [3, 14, 38, 131, 231]. Here we explain the formulation in detail so we appreciate the parameters we put into the finite element code and have a better understanding of the fracture mechanics problems solved using CZM. Let's now focus our effort on defining the main parameters of the traction-separation plot and from there define the energy required for fracturing and extend the formulation to the case of mixed mode fractures and general case of a three dimensional CZM model. Figure 5.9 shows several possible forms of the traction-separation plot. Here the objective is to define the key parameters in defining a traction-separation plot so we focus on the most widely used plot in literature, among these (plot (e) in Figure 5.9). [188]

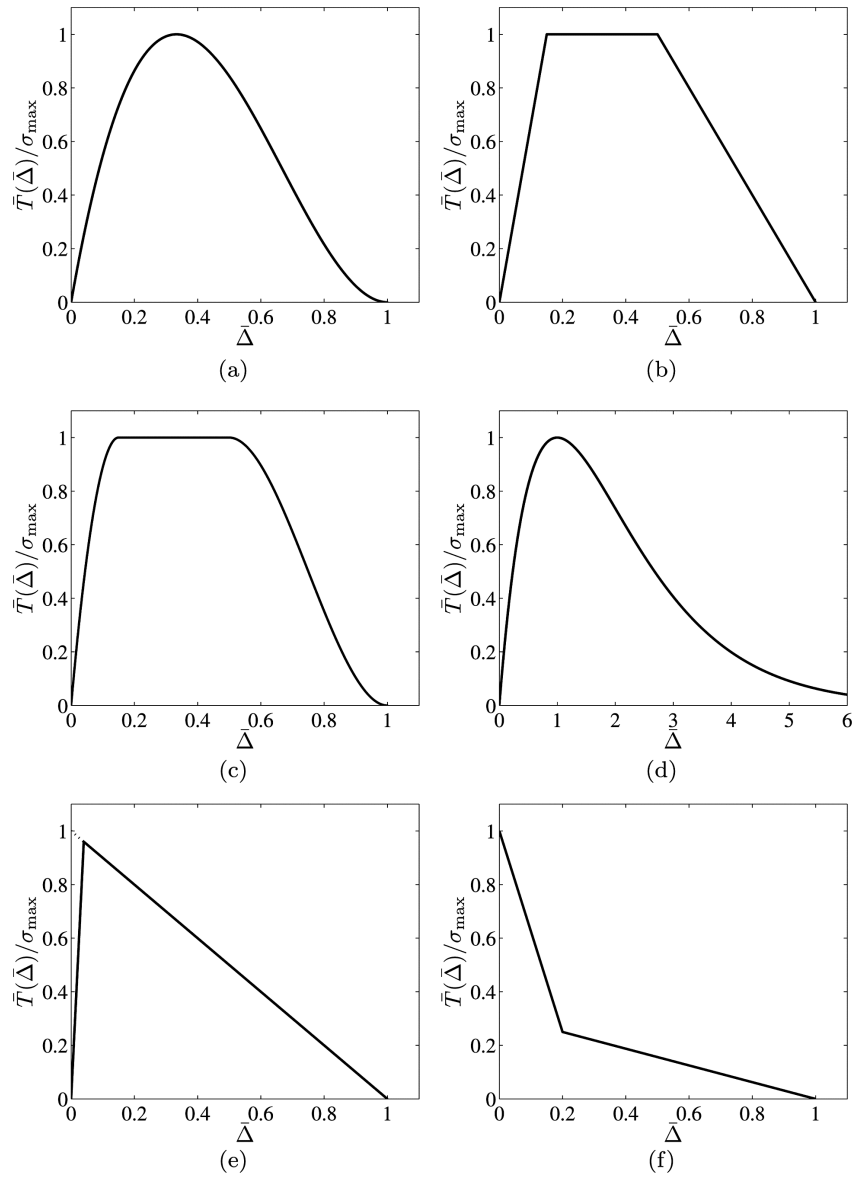

Figure 3.11: Effective traction-separation relationships: (a) cubic polynomial, (b) trapezoidal, (c) smoothed trapezoidal, (d) exponential, (e) linear softening, and (f) bilinear softening

Figure 3.12 shows the most common form of the CZM plot used in the literature and it shows the key parameters for traction-separation behavior of a mode-I fracture. Now let's define these parameters as follows;

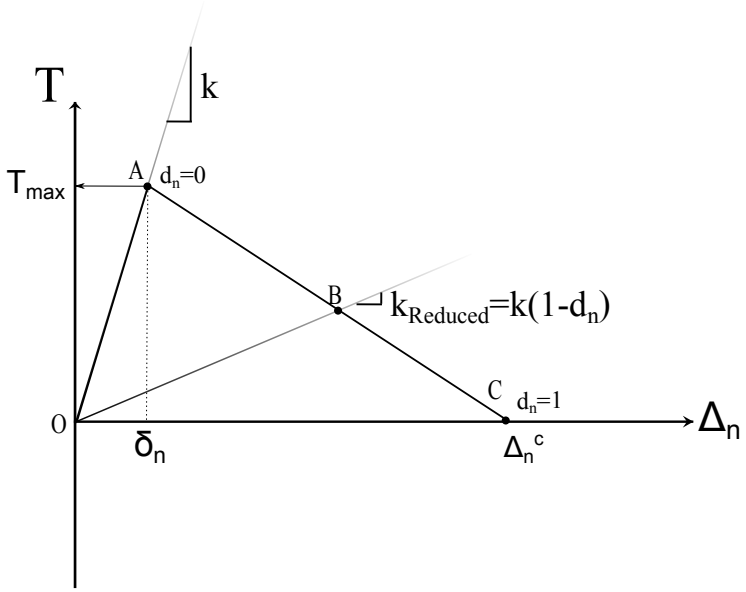

Figure 3.12: The most common form of the CZM plot with linear elastic and linear softening segments

The parameter d_n in Figure 3.12, is the same parameter as the damage parameter ω that we defined in Chapter 2. Table 3.1 lists the key parameters for the definition of a traction-separation plot.

Parameter	Definition
T	normal contact (tensile) force
Δ_n	contact gap or normal separation
Δ_n^c	contact gap at the completion of de-bonding
T_{max}	maximum normal contact (tensile) force
σ_{max}	maximum normal contact (tensile) stress
δ_n	contact gap at the maximum normal contact (tensile) stress
d_n	damage or de-bonding parameter, 0 at A and 1 at point C
k	normal contact stiffness
$k_{Reduced}$	reduced normal contact stiffness
$\bar{\Delta}$	dimensionless displacement, $\frac{\Delta_n}{\delta_n}$

Table 3.1: Key parameters for the definition of a traction-separation plot

The normal critical fracture energy for mode I de-bonding is the energy required to fracture a material and is equal to the area under strain-displacement curve as

$$G_cI = \frac{1}{2}\sigma_{max}\Delta_n^c \tag{3.18}$$

the equation of the AC segment of the plot is

$$T = k\Delta_n(1 - d_n) \tag{3.19}$$

where $0 < d_n < 1$ and for mode I de-bonding, d_n can be obtained as

$$d_n = \left(\frac{\Delta_n - \delta_n}{\Delta_n}\right)\left(\frac{\Delta_n^c}{\Delta_n^c - \delta_n}\right) \tag{3.20}$$

with dimensionless displacement $\bar{\Delta}$ defined as

$$\bar{\Delta} = \frac{\Delta_n}{\delta_n} \tag{3.21}$$

the de-bonding parameter is

$$\bar{\Delta} \leq 1 \Rightarrow \mathrm{d_n} = 0$$

and

$$\bar{\Delta} > 1 \Rightarrow 0 < \mathrm{d_n} \leq 1$$

similar equations are valid for mode II de-bonding, except that the subscript n is changed to t for tangential mode and the normal stress σ in changed to the shear stress τ for mode II fracture. Mode II de-bonding is referred to as the mode of separation of the interface surfaces where tangential slip dominates the separation normal to the interface. The equation for the tangential contact stress and tangential slip distance behavior is written as

$$\tau_{\mathrm{t}} = \mathrm{k_t}\Delta_{\mathrm{t}}(1 - \mathrm{d_t}) \tag{3.22}$$

where $\mathrm{d_t}$ is the de-bonding parameter for mode II or shear mode of fracture. The tangential critical fracture energy for mode II de-bonding is the energy required to fracture a material is shear mode II and is equal to the area under strain-displacement curve for pure shear mode II, as

$$\mathrm{G_c II} = \frac{1}{2}\tau_{\max}\Delta_{\mathrm{t}}^{\mathrm{c}} \tag{3.23}$$

where τ is the shear stress and $\Delta_{\mathrm{t}}^{\mathrm{c}}$ is tangential slip distance at the completion of de-bonding.

3.9.1 Mixed Mode Traction-Separation Plot

To obtain the above equations for the case of mixed mode fractures, the effective quantities for the force $\bar{\mathrm{T}}(\bar{\Delta})$ and the displacement $\bar{\Delta}$ are defined as

$$\bar{\mathrm{T}}(\bar{\Delta}) = \sqrt{(\sigma)^2 + (\tau)^2} \tag{3.24}$$

and

$$\bar{\Delta} = \sqrt{(\Delta_{\mathrm{n}}/\delta_{\mathrm{n}})^2 + (\Delta_{\mathrm{t}}/\delta_{\mathrm{t}})^2} \tag{3.25}$$

the parameters of Equation (3.25) were defined in Table 3.1 except that the subscript t is used for shear mode and subscript n is used for normal mode. Tvergaard [242] related the above effective quantities $(\bar{\mathrm{T}}, \bar{\Delta})$ to the normal and tangential tractions $(\mathrm{T_n}, \mathrm{T_t})$ as follows;

$$\mathrm{T_n} = \frac{\bar{\mathrm{T}}(\bar{\Delta})}{\bar{\Delta}} \frac{\Delta_{\mathrm{n}}}{\delta_{\mathrm{n}}} \tag{3.26}$$

and

$$\mathrm{T_t} = \frac{\bar{\mathrm{T}}(\bar{\Delta})}{\bar{\Delta}} \alpha_{\mathrm{e}} \frac{\Delta_{\mathrm{t}}}{\delta_{\mathrm{t}}} \tag{3.27}$$

where α_{e} is a dimensionless constant associated with mode mixity. For the mode I case ($\Delta_{\mathrm{t}} = 0$), the normal cohesive traction ($\mathrm{T_n}$) is the same as $\bar{\mathrm{T}}(\bar{\Delta})$, but for the mode II case ($\Delta_{\mathrm{n}} = 0$), the tangential cohesive traction ($\mathrm{T_t}$) is equal to $\alpha_{\mathrm{e}}\bar{\mathrm{T}}(\bar{\Delta})$, see Equation (3.27). Therefore, the dimensionless constant (α_{e}) is a scaling factor between tangential and normal cohesive tractions.

3.9.2 CZM Formulation in 3D

The two dimensional traction-separation model (i.e., the effective displacement model) has been extended to three dimensions to study the general 3D cohesive zone models [85, 185]. The effective displacement in this case is defined as

$$\bar{\Delta} = \sqrt{(\Delta_1/\delta_1)^2 + (\Delta_2/\delta_2)^2 + (\Delta_3/\delta_3)^2} \tag{3.28}$$

where Δ_1, Δ_2, and Δ_3 are separations and δ_1, δ_2, and δ_3 are characteristic lengths along the local coordinates. Figure 3.13 shows the cohesive fracture gap (Δ_1) and sliding (Δ_2,Δ_3) along the local coordinate system with axes normal and tangential to the fracture surface.

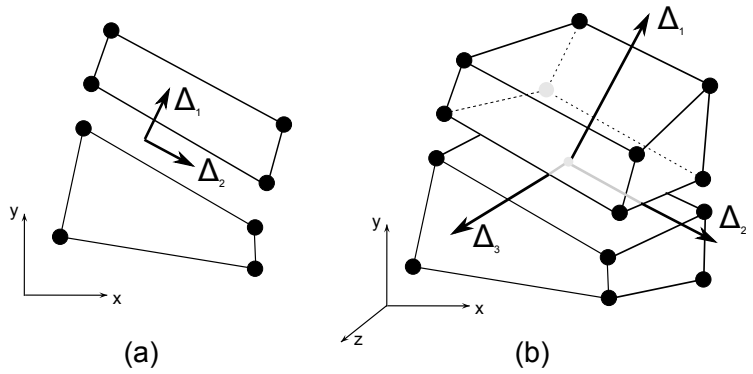

Figure 3.13: Cohesive fracture gap (Δ_1) and sliding (Δ_2,Δ_3) along the local coordinate system (a)two-dimensions and (b)three-dimensions

Chapter 4

Finite Element Simulation of Thermal Fracturing

4.1 Introduction

Injection of cold fluids into reservoir rock induces thermal crfacks. This has been observed in the injection of cold CO_2 into reservoir rock for sequestration purposes and from extensive studies of thermal loading on rock properties [120, 134, 137]. Successful production of oil and gas from shales with nano-Darcy range permeability calls for an understanding of the complex behavior of reservoir rock. To study thermal cracks, we utilize the finite elements analysis (FEA) of the coupled physics (thermal, flow and stress deformation) behind these behaviors.

We also need to know about basics of fracture mechanics to investigate the rock behavior beyond the failure point. A background review of fracture mechanics was presented in Chapter 3. Fracture mechanics started with the works of Inglis [118] and Griffith [99]. They showed the effect of size of a component in the strength of that component. Inglis studied the stresses around a crack and found out that the stress at the crack tip of an elliptical crack is a function of the curvature of the crack tip and the size of the crack.

In Chapter 4, we introduce a method for manipulation of rock strength using injection of cold fluid that makes the rock more susceptible to a ramified pattern of fracture. To understand the physics behind this method we utilize three numerical methods. These methods are: single or coupled Finite Element Method (Chapter 4), Discrete Element Method (Chapter 5), and Fragment model which uses cohesive elements within the framework of the classic finite element method (Chapter 6). Method three, is essentially a combination of the first two methods which utilizes the advantages of both methods to offer a more efficient numerical tool for rock fracturing purposes. In general, there are two distinct analysis classes for quantifying the well productivity enhancement: the Finite Elements and Discrete Elements methods, (FEM and DEM). Our focus in this chapter is the FEM.

Currently, the popular industry approach to production from tight formations is massive hydraulic fracturing that creates extensive surface area exposed to flow. Our numerical investigations in Chapter 4 indicate that hydraulic fracturing can be improved by taking advantage of the combined effect of the fracturing fluid temperature and reduced effective stress on flow properties to create a larger surface area and a more ramified pattern of conductive flow pathways.

Unlike pore pressure, heat diffuses easily in shales. Moreover, rocks in general are very weak in tension and, as a result, thermal reduction of the near wellbore region can lead to significant tensile stresses in the rock and drastic permeability enhancements. Simulation results for production from horizontal

gas wells stimulated by thermal shocks for three hours in a zone of two feet radius around the wellbore exhibit a 16% enhancement in recovery. Thermal stimulation of rock in the near wellbore zone could also facilitate the hydraulic fracturing process where the earth stresses are isotropic.

We look into the geomechanical challenges of producing tight formations and highlight a few rock properties which have the most significant role in the success of matrix stimulation of tight formations. During production of hydrocarbon, both components of a reservoir rock: fluid and rock matrix, undergo pressure and deformation through their compressibilities. Section 4.4 highlights the methods of improving the injectivity/productivity of wells placed in tight formations by inducing thermal shocks in reservoir rock. Efficiency of the thermal shock relies on the large stiffness and the complex structure of shale. The large stiffness and the complexity of shale matrix is not an obstacle to producing tight formations. In fact, the method of thermal shock that we propose here, heavily relies on the large stiffness of reservoir rock. We have shown that the stiffer the rock, the easier the thermal fracture initiation [74]. There are shale reservoirs with extremely stiff matrix around the world, for example in China [144], for which thermal shock and creation of thermal strains required for fracturing could work efficiently; hence, thermal shock is the potential candidate to stimulate matrix and enhance recovery in such tight and stiff shale formations. What makes the matrix stimulation process successful, is the grain disintegration process which in turn depends on the complex structure of shale. The numerical simulations in this chapter

are carried out using Finite Element method. Here we solve the coupled system of equations for flow, stress, and temperature diffusion in rock to study how fast and how far the reservoir heat diffuses. Once we obtain the zone of thermally frozen rock around the wellbore, we can determine the permeability enhancement in this zone which leads to improved recovery. Here we have not investigated the permeability enhancement aspect of the study; rather, we have assumed that when thermal cracks are created around the wellbore and connected to natural fractures, permeability could increase 10 to 10,000 times relative to initial permeability of formation. Studying this assumption is the subject of our future research.

4.2 Field observations of thermal fracturing

Before we start to simulate thermal fracturing in reservoir rock, let's have a look at a number of field observations of rock fracturing as a result of cold fluid injection into hot reservoir rock during water flooding, CO_2 storage and CO_2 EOR. Water has much more enthalpy than CO_2 and cold water will cause a lot more thermal fracturing than cold gas; however, our focus is on the impact of cold fluid injection on thermal fracturing. As a result, we provide field evidence of the effects of both water injection and CO_2 injection. It should be noted that the enhancement of permeability associated with injection of cold fluid are localized; however, by establishing new connectivity between induced thermal fractures and existing high-permeability fractures, thermal fractures lead to improved productivity. This has been shown in a number

of recent studies on the impact of cold water injection on thermal fracture creation [91, 183, 196].

The impact of cold fluid injection is twofold, in which cold water injection induces mechanical instability not only due to hydraulic effects, but also due to coupled thermal effects which leads to reduction of effective stresses [218]. The effects of cold water injection on injectivity and permeability enhancement have been observed at many geothermal fields. For some fields, such enhancements are quite significant, for example, increase in injectivity in Hellisheidi field, SW Iceland was measured to be six times larger when the water injection temperature was decreased from 120°C to 20°C [100]. Other researchers such as Grant *et al.* [97] utilized field data from thermal stimulation tests and came up with a relationship between injectivity enhancement and injection temperature. They also demonstrated that injectivity scales with duration of injection as t^n, where t is the injection time and n varies between 0.4 and 0.7.

Bonneville *et al.* [33] studied the thermal impact of injected CO_2 temperature on a geological reservoir. They 1)investigated the impact of temperature variations of injected CO_2 on the mechanical integrity of a reservoir, 2)studied heat transfer during CO_2 transport through the injection well as well as its interaction with the reservoir host rock, and 3)used a geothermal gradient of 1.22×10^{-2}°C/m in their simulations based on in-situ measurement of temperature from nearby wellbores. Their results indicate that for similar injection pressures, the cause for exceedance of the fracture criterion around and at the wells was thermal effects. Dikken and Niko [64] studied the fracturing

in water injection wells as a result of injection of cold fluid. They 1)showed that the cause of fracturing is the cooling of hot formations by injection of cold water, and 2)analyzed injection induced fracture growth and its impact on CO_2 plume migration by a semi-analytical quasi-steady state model.

The thermally induced stresses due to injection of CO_2 is the main mechanism for fracture growth. Dikken and Niko [64] showed that the thermoelastic stresses reduce the minimum horizontal stress and as a result, the critical pressure for the fracture propagation at the fracture tip will be much lower than the pressure required for hydraulic fracturing treatment. The injection rate, formation condition, and formation material properties play a significant role in the reduction of minimum horizontal stress [158]. Luo and Bryant [158] showed that material properties such as porosity and rock heat capacity affect the fracture propagation rate. Their simulation results show that fracture propagation rate is higher in formation with low volumetric rock heat capacity and high porosity. Perkins and Gonzalez [190, 191] also studied the injection well fracturing as a result of induced thermoelastic stresses. Fracturing due to cold fluid injection during CO_2 sequestration, and water-flooding has been studied by many researchers including: Hagoort *et al.* [103], Dikken and Niko [64], Luo and Bryant [159, 160], Taylor and Bryant [236], Fakcharoenphol *et al.* [83], Xiaolu *et al.* [150], and Settari and Warren [215].

Settari and Warren [215] studied the theoretical background of modelling waterflood induced fractures and fractures which distinguish thermally induced fractures from hydraulic fractures. They claim that waterflood in-

duced fracturing is different from conventional fracturing in two important aspects, time scale, and injection fluid viscosities of the fracturing operation. They showed that waterflood fracturing is leak-off dominated as opposed to conventional fracturing which is leak-off controlled. They concluded that the physics of waterflood fracturing is very complex and consequently requires more rigorous models. With this introduction , we start to study the modeling challenges and perform the numerical simulation of fracture initiation and propagation.

4.3 Coupled Field FEM

4.3.1 Pore Pressure Mechanism

Permeability and diffusivity of reservoir rocks determine their viability for economical development. There are three methods for determining the permeability of very low permeability rocks in the laboratory. These are, using gas for: (i)core or (ii)crushed sample analysis; and use of mercury(Hg) intrusion curves (from Hg porosimetry). Figure 4.1 shows the mechanism of fracture initiation and propagation, as a result of increasing pore pressure in a porous media. The total remote pressure is the sum of the effective stress σ and pore pressure or fluid pressure p_f. In Figure 4.1 (a), external and internal loads are in equilibrium and the pressure in the cavity is equal to p_f. 4.1 (b) shows the situation in which the pressure in the cavity goes beyond the pore pressure p_f and 4.1 (c) shows that the propagation of fracture occurs when fluid pressure starts to exceed the fracture pressure which is equal to $\sigma_x + p_f$

in which σ_x is the minimum effective principal stress. To induce the level of build up pressure, fluid has to be connected to an outside source of pressure or the pore pressure should be elevated using the compressibility of matrix, both of which seem to be less likely to happen, the tighter the formation gets. Therefore, to reduce the effective stress, we turn our attention to other means of stimulation such as reducing the rock temperature in an effort to let the rock shrink and develop tensile stresses (i.e., smaller compressive stress). The tensile stress will then increase the chance of rock to fail and develop conductive pathways of thermally induced fractures.

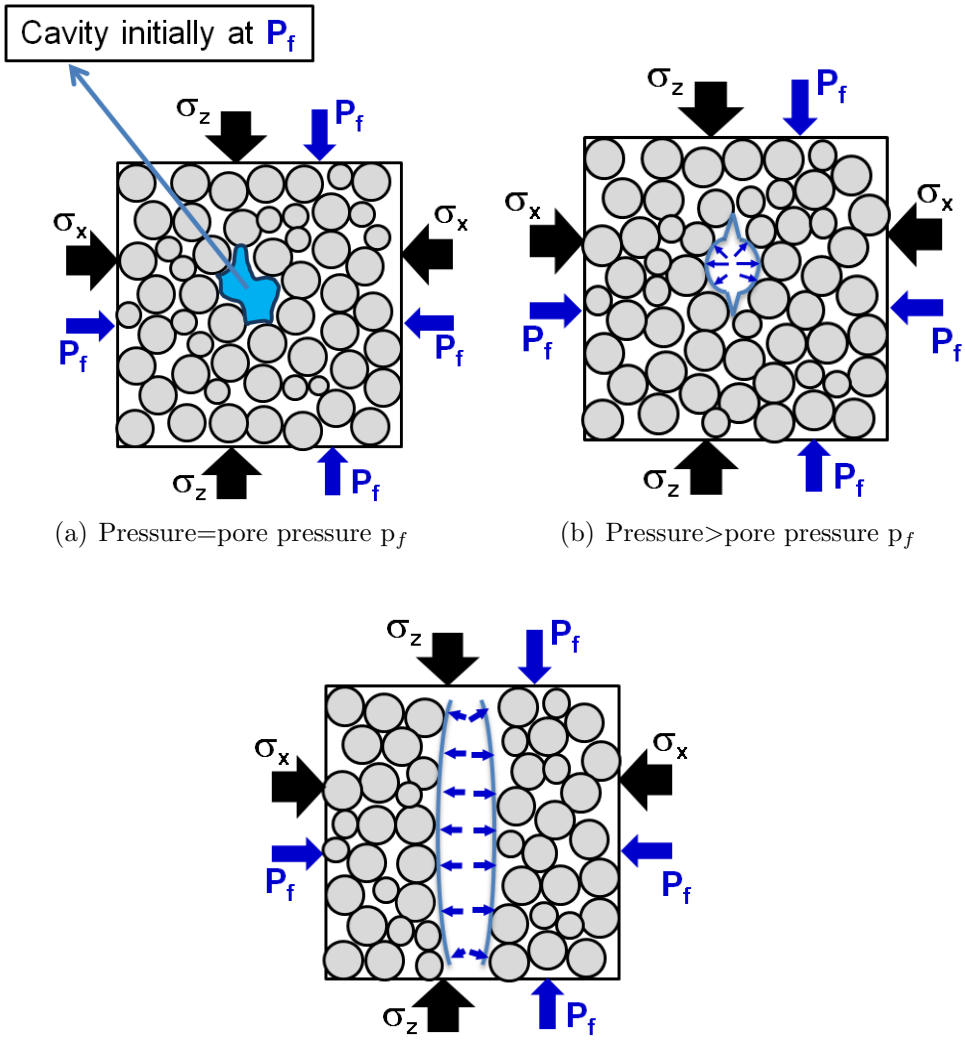

(a) Pressure=pore pressure p_f

(b) Pressure>pore pressure p_f

(c) Pressure=fracture pressure$\geq \sigma_x +$ p_f

Figure 4.1: Fracture opens against the least principal stress.

4.3.1.1 Pore Pressure Diffusion in Shale

The following section looks into the analysis of fluid pressure increase in a 200×200 feet reservoir. The objective of this analysis is to investigate the

rate of pressure diffusion in a tight shale play and study the impact of pore pressure built up on the effective stress reduction. The total in-situ stress is 1000 psi and the fluid pressure is initially taken as 433 psi; therefore, the initial effective stress is 1000-433=567 psi in compression. The pressure is increased from initial value of 433 psi to 2000 psi using the injection well and we expect the effective stress of 567 psi turns into tensile stress. Tensile stresses are indicated by a positive sign in the finite element package ABAQUS. The results show that, since the reservoir permeability is low, it takes a considerable time for pressure to diffuse into the rock.

Table 4.1 lists the key parameters for the problem of pore pressure diffusion and corresponding effective stress build-up in a shale reservoir. To have a feeling about how fast the fluid could flow in such a tight formation, we can calculate the hydraulic conductance. For the given fluid properties, the value of the reservoir matrix permeability, results in an equivalent hydraulic conductance of 0.7 mm/day. This is a very small rate of fluid transport in a reservoir rock and justifies the creation of fractures using matrix stimulation.

Property	Value
Young's modulus of stiffness, E	20 GPa (3×10^6 psi)
Poisson's ratio, ν	0.15
Permeability, k	2.5 md
fluid viscosity, μ	1 cp
fluid density, ρ	1000 kg/m^3

Table 4.1: Key parameters for the pore pressure diffusion and corresponding effective stress build-up problem

The objective here is to increase the pore fluid pressure so that the effective stress in rock matrix be decreased. Notice that the overburden stress in reservoir is constant at a fixed depth, hence increase of pore pressure results in reduction of the effective stress. As the effective stress reduces, it goes from initial compression state to tension and gets closer to damage and rupture under pore pressure increasing stress.

Figure 4.2 shows the contours of pore pressure and effective stress in reservoir for the times of 3 hours, 1 week, and two months after injection. The pore pressure distributions in the left column of Figure 4.2 show the slow rate of pressure diffusion in shale. Even after two months, the boundaries of reservoir have not observed the pressure change.

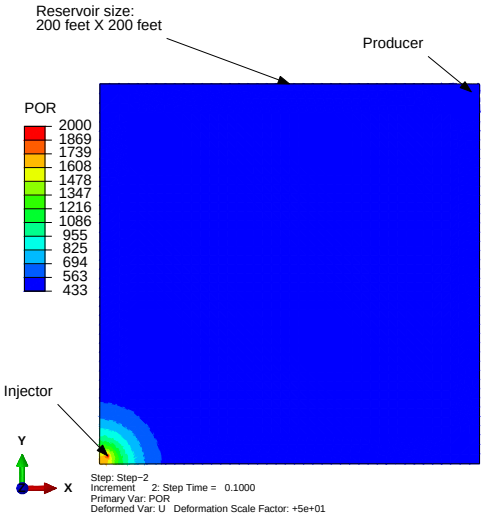

(a) Fluid pressure distribution, (3 hours)

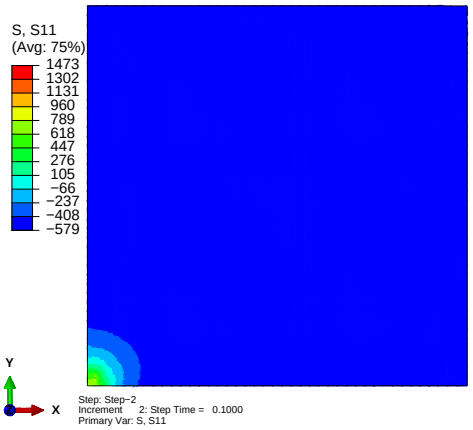

(b) Effective stress distribution, (3 hours)

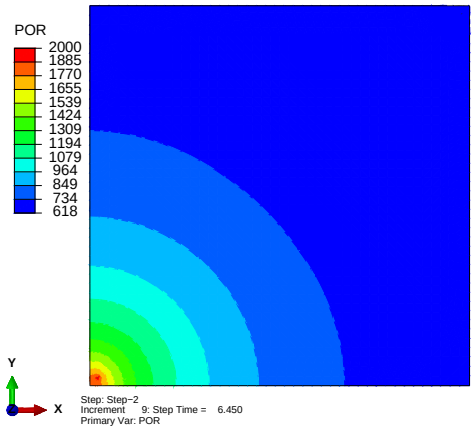

(c) Fluid pressure distribution, (1 week)

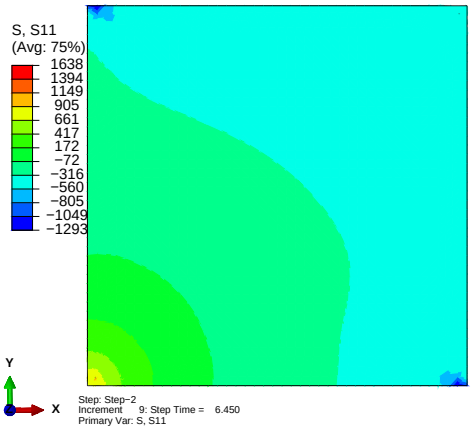

(d) Effective stress distribution, (1 week)

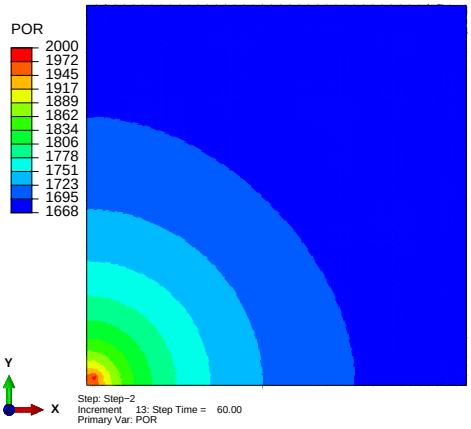

(e) Fluid pressure distribution, (2 months)

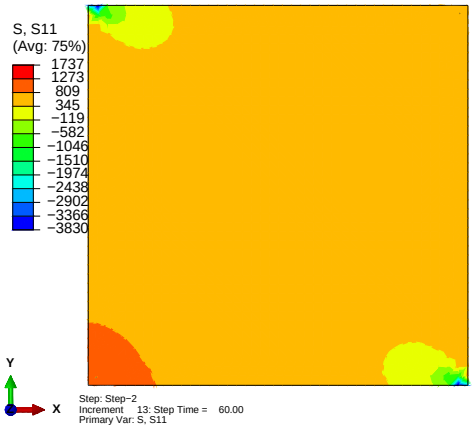

(f) Effective stress distribution, (2 months)

Figure 4.2: Fluid pressure and effective stress distribution with time in reservoir.

4.3.2 Thermal Fracturing of Reservoir Rock

The propagation of fracture is a dynamic process and should be simulated in software in a solution dependent fashion, i.e., the fracture locations should not be predetermined by user, rather they should be determined as stress state changes in the rock. Nevertheless for this preliminary analysis of thermo-mechanical process in shales, the exact locations of fractures are not of as much significance as the impact of fracture itself is. Therefore, we manually introduce fracture locations to investigate the possibility and extent of progress of the thermal freezing front. Our results determine that whenever the cold fluid gets into an in-situ fracture, the cold front would have the opportunity to start from the fracture faces and impose thermal shock to reservoir rock in those zones which could further promote thermal fracture propagation.

The results in Figure 4.3 (left column) show the temperature distribution for three hours of injection of cold fluid and the right column shows the average stress in the vicinity of the freezing zone. Figure 4.3 (d, left) clearly shows that running cold fluid into a fracture advances the cold zone deeper into reservoir and enhances the chance of thermal fracture creation.

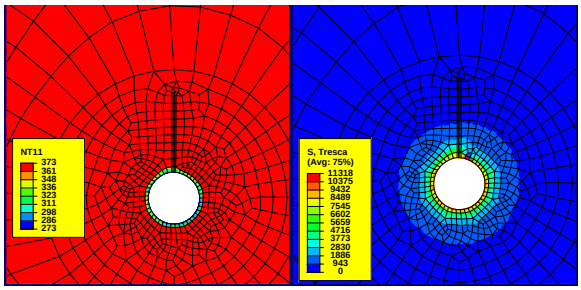

(a) Temperature and stress distribution around the wellbore at the start of freezing process

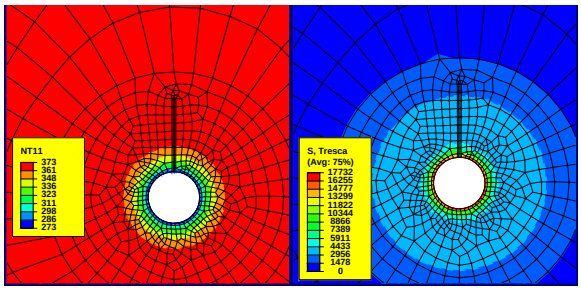

(b) Temperature and stress distribution around the wellbore right before fracture generation

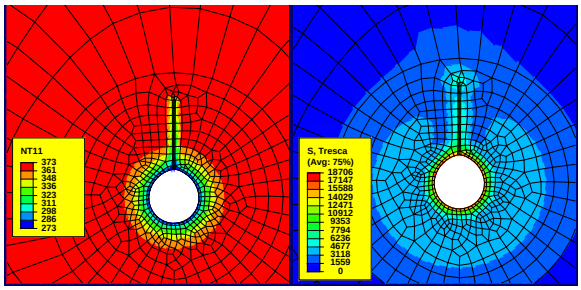

(c) Temperature and stress distribution around the wellbore right after fracture generation

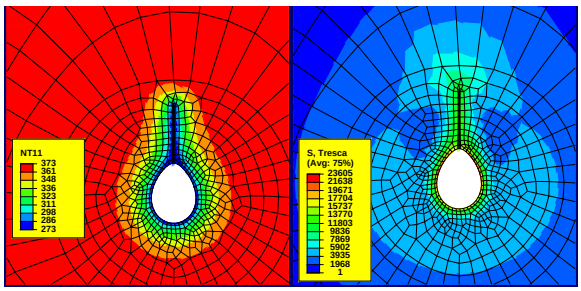

(d) Temperature and stress distribution around the wellbore 3 hours after fracture generation

Figure 4.3: Temperature and stress distribution around the wellbore in 3 hours

4.4 Thermal Stimulation Improves Hydraulic Fractures

Thermal shock occurs when a material's temperature is changed over a short period of time such that constituents of the material deform by different amounts. The deformation of material due to thermal load can be manifested through strain and stress. Once the stress at any point exceeds the strength of material, the body fails in one of the three modes of tension, compression or shear. In other words, a thermal load results in the creation and extension of cracks, crushing the grains, or sliding the grain interfaces. Here we look into the possibility of stimulating the rock matrix beyond hydraulic fracturing stimulation by cooling down the rock. The physics of temperature reduction in a solid dictates that when a solid is laterally fixed and undergoes temperature reduction, a thermal stress gradient is induced in the solid body. In rock, this thermal stress gradient leads to a differential contraction of the rock, which in turn creates openings, referred to as thermal cracks. We numerically solve the nonlinear gas diffusivity equation, using finite element method and show that thermal cracks in rock have the potential to improve the productivity of wells placed in tight formations by 20%.

4.4.1 Introduction

Injection of cold fracturing fluids into reservoir rock, induces thermal cracks. We know this from physics, from the injection of cold CO_2 into reservoir rock for sequestration purposes, and from extensive studies of thermal loading on rock properties. There are many references available, includ-

ing [120, 134, 137]. Here we are trying to quantify creation of thermal cracks during the cooling of a rock volume. For successful fracturing of rocks using temperature reduction, the following system[1] properties play a major role:

- Decrease of rock tensile strength by flaws in rock matrix
- Rapid application of thermal load, causing a steep temperature gradient
- Reduction of thermal conductivity of the rock, its fundamental material property. A progression of cracks reduces the thermal conductivity coefficient of the bulk rock.
- Confinement of rock. Boundary condition plays a major role as the more confined the rock is, the less compliance it exhibits to the load, leading to easier crack initiation.
- Increase of the coefficient of thermal expansion. This is also a fundamental material property and not much can be done to change this coefficient.
- Increase of the Young's modulus. This parameter exhibits the efficacy of thermal shock in shale. Some shales are extremely stiff such as the Qiongzhush Shale in China with the modulus of elasticity of 60 Gpa, which is an order of magnitude larger than the Marcellus shale with the

[1]The system consists of a cylindrical volume of rock around a horizontal wellbore and coolant. The system interface is a no-deformation cylindrical boundary some distance from the wellbore.

modulus of elasticity of 6 Gpa [144]. We will see later that large stiffness can enhance the efficiency of fracturing by cooling down the rock.

- Decrease of toughness. Fracture toughness, exhibits the level of resistance of a material to brittle rupture. The lower the fracture toughness, the closer-to-brittle the fracture could be and the less energy is required for rupturing the rock.

It can be concluded from the above properties of rock that the facility of thermal fracture is mainly proportional to the modulus of elasticity and coefficient of thermal expansion and inversely proportional to the thermal conductivity and tensile strength of rock. Here we are discussing equilibrium fracture and its imposed displacement. We basically impose thermal shrinkage on a solid (rock), which is laterally confined. We are not talking about how fast the fracture propagates, rather we are interested in seeing at what level of temperature reduction, the hot reservoir rock starts to develop thermal cracks.

At constant overburden pressure, increasing fluid pressure makes effective stress go from compression to tension or smaller values of compression. However, creation of tensile fracture due to fluid pressure build-up is not quite feasible in tight formations. This is the motivation of our research to find a feasible solution to reduce the effective stress to initiate fractures. The method proposed here is cooling down or freezing the reservoir rock. The physics behind the temperature diffusion in solids including rocks, leads to the promising results we present in this work. Notice that in this dissertation we use fluid

pressure and pore pressure interchangeably. The efficiency of thermal shock comes from the fact that temperature diffuses to the zones of rock where fluid pressure may not diffuse. Therefore, the temperature can be used as a means to attain the required level of the effective stress for fracture initiation.

4.4.2 Fracture initiation and propagation

Without loss of generality, many of the concepts of fracture mechanics can be applied to all cases in which an opening in rock extends in size, regardless of applied load. The main types of loads for fracture creation are the internal fracture fluid pressure and the external tensile stress. Here we go over only a few concepts to set the scene for understanding material described in this chapter.

The most important property of a rock relevant to fracturing is toughness. In order to understand what toughness means, one should understand two rock properties, its strength and ductility. Figure 4.4 explains these three properties. In a tensile experiment, a load T is applied to a component such as a rod of original length L and cross sectional area A and the rod deforms axially to increase the length by ΔL. Strain is defined as $\varepsilon = \Delta L/L$ and stress is defined as $\sigma = T/A$. Ductility is the ability of material to undergo large strains and strength is the ability of material to undergo large strains before failure. Toughness depends on these two properties and it can be calculated as the area under the stress-strain curve or energy dissipated by unit volume of material. Temperature, rate of loading, and existence of voids and cracks in-

fluence the toughness of a material. For example, a rock which remains intact under a static load could fracture under a dynamic load.

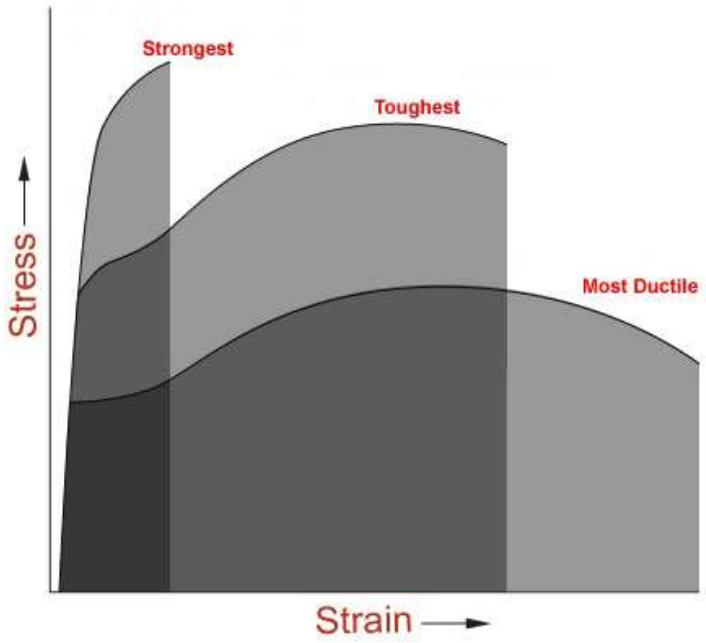

Figure 4.4: Definition of strength, ductility and toughness

Fracture mechanics started with the works of Inglis [118] and Griffith [99]. Inglis studied stresses around a crack and found out that the stress at the crack tip of an elliptical crack is a function of the curvature of the crack tip and the size of the crack. Griffith showed that when the size of flaws in a solid material increases, the level of stress before failure decreases. Their studies led to relation (4.1) for studying a material which has flaws or cracks.

$$K_I < K_{I_C} \tag{4.1}$$

in which, K_I is the stress intensity factor which is a function of the applied load and the geometry of crack and K_{I_C} is the fracture toughness which is a function of material properties. As K_I gets closer to K_{I_C}, unstable fracture occurs. The fracture toughness K_{I_C} is in the range of $1 - 5$ MPa$\sqrt{\text{m}}$ for sandstones and about 2 MPa$\sqrt{\text{m}}$ for siltstones and mudstones.

4.5 Theory and Method

Injection of cold fracturing fluid into reservoir rock, induces thermal fractures perpendicular to hydraulic fracture. Figure 4.5 shows the thermal cracks of depth d perpendicular to hydraulic fracture in a horizontal wellbore in a tight formation. Hydraulic fractures tend to grow normal to the minimum horizontal stress, σ_{hmin} shown here as σ_{h}. It should be noted that due to presence of fluid pressure in rock the stress required to fracture the rock should overcome the effective stress of rock; therefore, all the stresses in this section are effective stresses (minimum horizontal effective stress σ_{h} or maximum horizontal effective stress σ_{H}) not total stress (S_{hmin} or S_{Hmax}). As the cold fluid is injected into the fractures, the transient heat diffusion causes the heat to be transferred into the hydraulic fracture as it is colder. This heat transfer cools down the zone neighboring the fracture and the rock shrinks parallel to hydraulic fracture length. Since the reservoir rock is confined, thermal stresses are created in rock, leading to thermal cracks. Here we are looking at the physics behind this phenomenon and come up with a formulation of a model to obtain the depth d along x-axis, distance b, and width t of thermal cracks.

Figure 4.5 also shows that the thermal cracks have to open against the maximum in-situ horizontal stress σ_{H}. As we see from numerical simulations, these thermal cracks do not extend far from hydraulic fracture face, hence, we can assume these cracks as straight. This observation can justify that as the thermal cracks open, they do not interfere with heat transfer in x-direction.

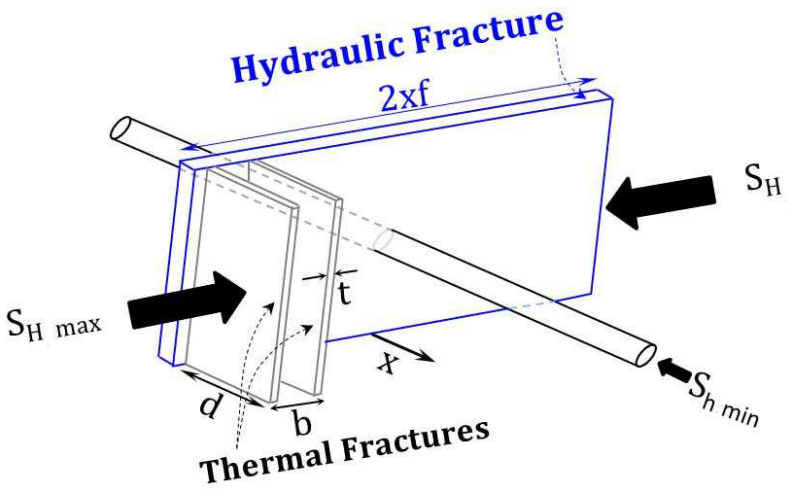

Figure 4.5: Thermal fractures created perpendicular to the hydraulic fracture

Similar studies [16, 102] on thermal fracturing in ceramic and glass, indicate that the average spacing of thermal cracks is expected to be roughly proportional to their lengths, i.e., $b \propto d$. Figure 4.6 shows the thermal shock crack pattern on a glass ceramic slab. It can be observed that the length of cracks is roughly proportional to the spacing of cracks, i.e., the smaller the cracks the shorter apart and the larger the cracks, the further apart they are. Due

to close material properties of shale and ceramic, we make use of this observation to obtain the two parameters b and t. The material properties reported for ceramic of the test [16] are: Fracture toughness, $K_{IC} = 1.89$ MPa$\sqrt{\text{m}}$; coefficient of thermal expansion, $\alpha = 1.15 \times 10^{-5}$ K^{-1}; and Young's modulus, $E = 60$ GPa. These properties characterize shales; therefore, we expect to see the same pattern of thermal cracks in shale.

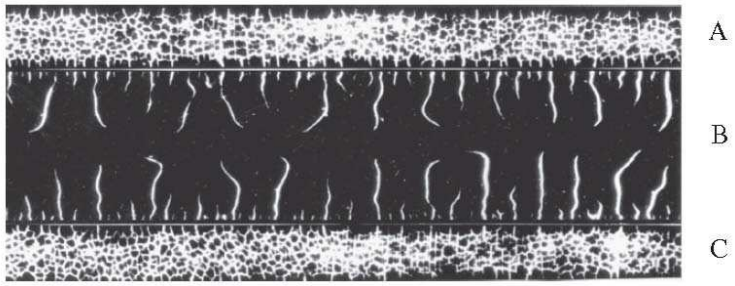

Figure 4.6: Thermal shock crack pattern on a glass ceramic slab[16]. Faces A and C were quenched at $\Delta T = 300$ K in water while faces B were kept thermally isolated.

To get an insight on the efficiency of the thermal crack creation during hydraulic fracturing, we solve the 1D heat conduction in a semi-infinite solid medium shown in Figure 4.7, numerically. The results are then compared to analytical heat diffusion solution, Figure 4.13. We assume that the diffusion of heat from the reservoir to the cold fracturing fluid is conducted along x axis and the fracture side (half-space), is an infinite medium.

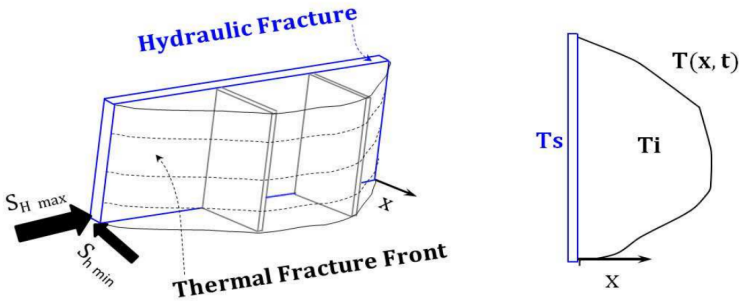

Figure 4.7: Thermal fracture front changes with time along x axis

The closed-form solution of the problem shown in Figure 4.7, is given in [117]

$$\frac{T(x,t) - T_s}{T_i - T_s} = \text{erf}\left(\frac{x}{2\sqrt{Dt}}\right) \tag{4.2}$$

The function "erf" in Equation (4.2), is the error function and is defined as:

$$\text{erf}(u) = \frac{2}{\sqrt{\pi}} \int_0^u \exp(-t^2) dt \tag{4.3}$$

Table 4.2 lists the properties used for both numerical and analytical solutions.

Parameter	Units
Young's Modulus, E	50 GPa
Thermal expansion coefficient, α	1×10^{-5} K^{-1}
Poisson's ratio, ν	0.22
Minimum horizontal stress, σ_{h}	2000 psi
Maximum horizontal stress, σ_{H}	3000 psi
Reservoir temperature, T_i	125°C
Fracturing fluid temperature, T_s	30°C
Thermal conductivity, k	2 $\frac{\mathrm{W}}{\mathrm{m°K}}$
Mass density of rock, ρ	2300 $\frac{\mathrm{kg}}{\mathrm{m}^3}$
Specific heat, C	1380 $\frac{\mathrm{J}}{\mathrm{kg°K}}$
Thermal diffusivity, D	[a]0.63×10^{-6} m^2/s
Simulation time	1 day

[a]Thermal diffusivity is calculated as $D = k/(\rho C)$

Table 4.2: The properties used for the solution of thermal crack development problem

The distribution of temperature along x, for several times from 0 to 1 day is shown in Figure 4.10. It can be seen that, initially, the temperature in reservoir is equal to the reservoir temperature T_i and as time goes on, the temperature in reservoir decreases and the rock cools down. The temperature at the hydraulic fracture wall is kept at constant value of T_s. In order for the thermal cracks to initiate, the reservoir rock has to undergo contraction due to cooling down the rock. Since thermal cracks should open against the maximum in-situ stress σ_{H}, we can write the condition for critical temperature change ΔT_c at which the cracks initiate.

Figure 4.8 shows a rock model of arbitrary length which is fixed at both ends and is subjected to initial stress of σ_{H}. It is then cooled down by ΔT_c at which the compressive in-situ stress is reduced enough so that the rock fails in tension. Here we would like to show how the critical temperature reduction is related to rock properties and in-situ stress.

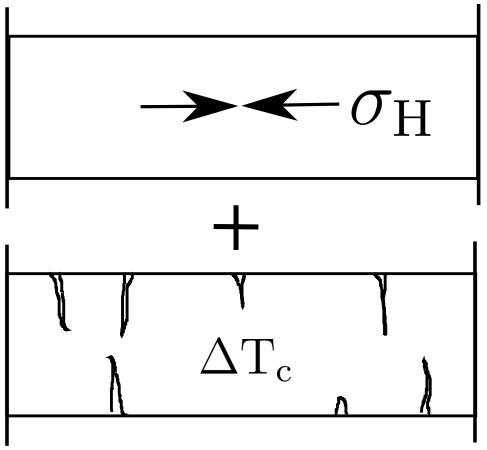

Figure 4.8: Schematic of Initial stress and cooling down on a rock model

Thermal strain is proportional to the coefficient of thermal expansion and the change of temperature, in other words,

$$\varepsilon_{thermal} = \alpha \Delta T \tag{4.4}$$

The deformation of shale is assumed to be linear elastic and the failure is known to be brittle. Also, the component of the normal stress of a solid body due to thermal changes, in a linear elastic material can be calculated as

$$\sigma_{thermal} = E\varepsilon_{thermal} = E\alpha\Delta T \tag{4.5}$$

The thermal stress at any point x in our 1D semi-infinite heat conduction problem is then

$$\sigma(x,t) = E\alpha[T_i - T(x,t)] \tag{4.6}$$

Equation (4.6) holds for plane stress condition and due to the effect of Poisson's ratio, for plane strain condition, it should be modified to

$$\sigma(x,t) = E(1+\nu)\alpha[T_i - T(x,t)] \tag{4.7}$$

When stress in Equation (4.6) exceeds the maximum in-situ stress σ_{H}, thermal cracks develop. Therefore, we can write the following condition for the initiation of thermal cracks:

$$E(1+\nu)\alpha[T_i - T(x,t)] \geqslant \sigma_{\mathrm{H}} \tag{4.8}$$

and the critical cooling down temperature for the initiation of thermal cracks, which is equal to $T_i - T(x,t)$, can be calculated as

$$\Delta T_c \geqslant \frac{\sigma_{\mathrm{H}}}{E(1+\nu)\alpha} \tag{4.9}$$

We can see from Equation (4.9) that the critical temperature reduction is proportional to the in-situ stress, i.e., the deeper the reservoir, the harder it is to thermally fracture the rock. Also, the critical temperature reduction is inversely proportional to the Young's modulus of rock. In other words, the stiffer the rock, the easier it is to fracture it by thermal shocks. These two

facts can be observed in Figure 4.9. We use a range of 5 to 100 GPa for Young's modulus of shales and calculate the critical temperature reduction for various in-situ stresses ranging from 50 to 3000 psi. Poisson's ratio is taken 0.25 and thermal expansion coefficient is taken $1 \times 10^{-5}\ \frac{1}{^\circ K}$. We can observe that for unconsolidated and less stiff shales with Young's modulus of about 5 GPa, a considerable reduction of temperature is required to reverse the effect of compressive stress and fail the rock in tension.

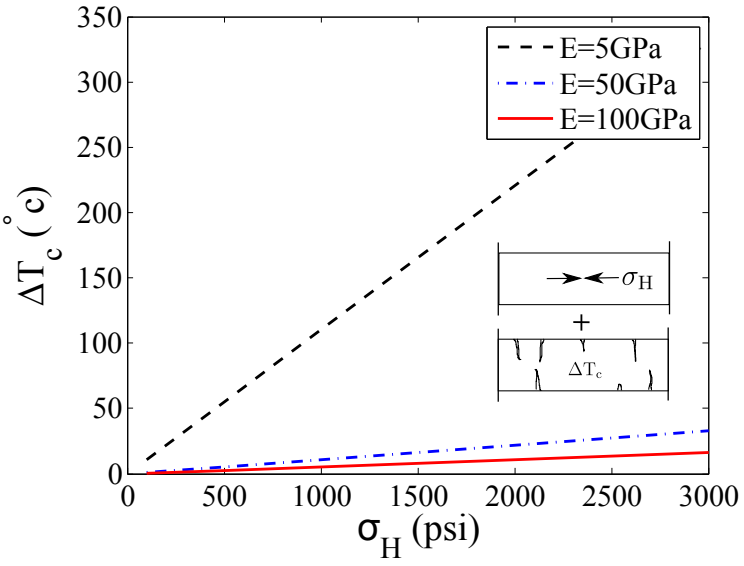

Figure 4.9: The impact of Young's modulus and in-Situ stress on critical temperature reduction required to initiate thermal fractures

The value of critical cooling down for the case of hydraulic fracturing problem we simulated is shown in Figure 4.10. This is another way to show the impact of cooling down on the extent of the freezing zone, away from hydraulic fracture

face.

Equation (4.6) exhibits an important relation in thermal fracturing of rocks in which the required cooling down for cracks to develop is shown to be a function of rock thermal and strength properties and reservoir condition. It also shows that, the shallower the reservoir is, the more efficient the process of thermal fracturing will be, as ΔT_c will be smaller. One of the great advantages of inducing thermal shock in rocks is that ΔT_c will be smaller as the modulus of elasticity of rock gets larger. For instance, thermal fracturing could be utilized to create thermal fractures for shales with very large modulus of elasticity, where the fracturing by fluid injection is hard. These openings could serve as seeds for easier and more frequent fracture initiation points as the fluid injection goes on.

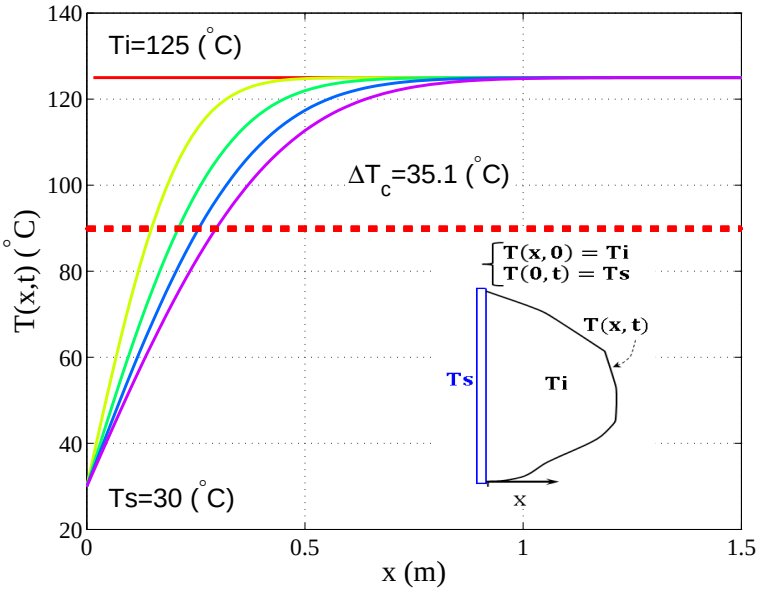

Figure 4.10: Distribution of temperature in 1D along the x-direction.

4.5.0.1 Thermal fracture growth

The length of a fracture plays a significant rule in calculation of the stress intensity factor K_I. Thus, we are interested in extension of thermal fractures with time. In order to do this, let's add and subtract T_i to the numerator of the Equation (4.2) and obtain $T_i - T(x,t)$ as

$$T_i - T(x,t) = \left[(T_i - T_s)\text{erfc}\left(\frac{x}{2\sqrt{Dt}}\right)\right] \tag{4.10}$$

The function "erfc" in Equation (4.10), is the complementary error function and is defined as:

$$\text{erfc}(u) = 1 - \text{erf}(u) = \frac{2}{\sqrt{\pi}} \int_u^{\infty} \exp(-t^2) dt \tag{4.11}$$

Now let's insert $[T_i - T(x,t)]$ from Equation (4.10) into Equation (4.8) and change the inequality sign to the equality sign for the onset of crack initiation. By doing this, we get

$$E(1+\nu)\alpha \left[(T_i - T_s)\text{erfc}\left(\frac{d}{2\sqrt{Dt}} \right) \right] = \sigma_{\text{H}} \tag{4.12}$$

Notice that x, the coordinate of crack tip is replaced with d, the thermal crack length. Solving Equation (4.12) for d and we get

$$d = (2\sqrt{Dt})\text{erfc}^{-1} \left[\frac{\sigma_{\text{H}}}{E(1+\nu)\alpha(T_i - T_s)} \right] \tag{4.13}$$

Figure 4.11 shows the extension of fracture length with time. It can be seen that the length of cracks are not very large even after 1 day of cooling down, nevertheless, the creation of such cracks, generate weakness notches for hydraulic fracturing.

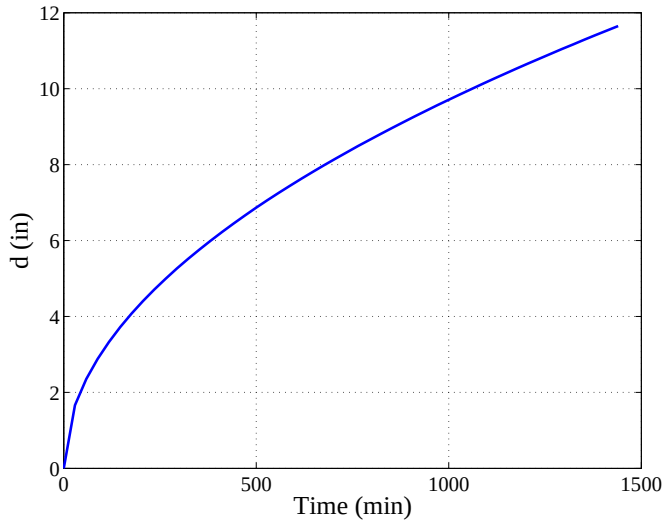

Figure 4.11: The extension of thermal crack length with time. See Figure 4.5 for the definition of depth d.

4.5.0.2 Results

As we continue to develop this model, we will be using a closed-form solution to come up with the geometry of thermal cracks. To make sure about the accuracy of the model, we compare the analytical model with the numerical solution.

The governing equations of heat transfer in rock are:

1. Equilibrium of forces:

$$\nabla \cdot \sigma = 0 \tag{4.14}$$

Because deformation along x does not affect heat diffusion in the x-

direction, the boundary conditions for the force equilibrium equation are fixed.

2. Heat transfer equation: In absence of convection and source term, the heat transfer equation is

$$\rho C_p \frac{\partial T}{\partial t} = \nabla \cdot (k \nabla T) \tag{4.15}$$

We have solved the coupled system of Equations (4.14) and (4.15) using a finite element method and Figure 4.12 shows the results of heat diffusion after 1 day. It can be seen that the rock cools down to the depth of 0.5m from the face of hydraulic fracture. However, to find the rock volume affected by thermal shock, we need to find the depth at which temperature decreases by the critical value ΔT_c. This is what we did in Figure 4.10, where we show that to attain ΔT_c, we should find the coordinate x at the intersection of the temperature profiles and the horizontal dashed line, which is the locus of points where the temperature has dropped to $T_i - \Delta T_c$. Figure 4.12 shows the numerical solution of Equations (4.14) and (4.15).

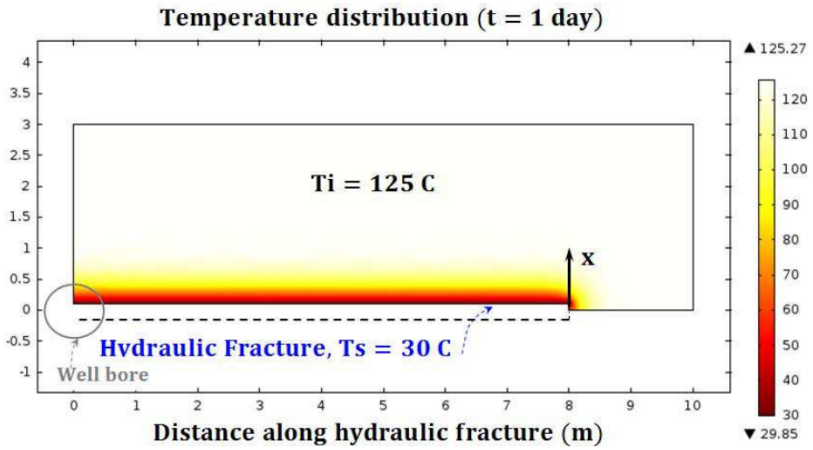

Figure 4.12: The numerical solution of temperature distribution in 1D.

Now, let's compare the numerical result with the closed-form solution. It can be seen that numerical simulation of this coupled heat transfer process in rock is in agreement with mathematical closed-form solution. Therefore, we continue to obtain the other parameters of thermal crack, b and t, using the closed-form solution and whenever need arises to confirm the accuracy of solution, we use numerical simulation. Figure 4.13 shows the comparison between closed-form and numerical solution.

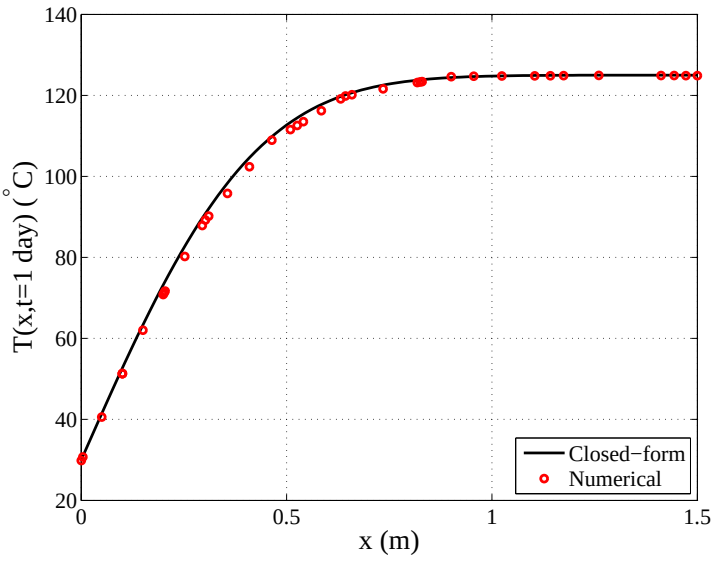

Figure 4.13: The comparison between closed-form and numerical solution of temperature distribution in 1D

4.6 Impact of Rock Properties on Thermal Fracturing

4.6.1 Introduction

With rapid depletion of conventional petroleum supplies and due to energy security concerns, the world is increasingly turning its attention to unconventional hydrocarbon reservers such as oil shales, gas shales, tight gas sands, coalbed methane, and gas hydrates. Despite the abundant unconventional resources, production is still hindered by many obstacles including lack of technology and knowledge of the physics of flow in tight porous media. Flowing the tightly-locked hydrocarbon to a well in such formations, unlike in

the conventional reservoirs, requires a large number of inter-connecting pathways for flow. The existing in-situ cracks in rock have to be connected in order for the hydrocarbon to flow into the wellbore. Here we go over the basic mechanisms of rock fracture in micro and macro levels, and then study the two parameters whose variations could reduce the effective stress and lead to rock fracturing. We then discuss the effect of inhomogeneity on the fracture load and show that the dominant load for thermal fracturing is the tensile stress. There are three governing equations of stress, heat transfer, and flow which should be solved in a coupled fashion, for which we are using the finite element software packages. Assuming that thermal cracks increase rock permeability in the near wellbore zone by 10-10,000 times, we show the impact of rock stimulation by thermal shock on cumulative production of gas from a sample case of a wellbore placed in a tight formation. The improved recovery for the sample case is 16%.

4.6.2 Rock Fracture

To improve the wellbore injectivity/productivity, we utilize the physical matrix stimulation as opposed to matrix acidizing; therefore, we have to deal with stresses between rock grains and study the parameters which impact intergranular effective stresses in rock. We then look into the mechanism and effect of rock fracturing due to freezing the reservoir rock in the near wellbore zone. To disintegrate rock constituents in an effort to increase permeability by opening pathways for flow, we should increase fluid pressure so as to reduce

the effective stress or the grain contact pressure. This is not quite feasible in tight formations; however, we could resort to a novel method of reducing the effective stress through inducing thermal strains by freezing the reservoir rock. In this method, the cold fracturing fluid or a freezing agent in the fluid, reduces the reservoir temperature in the near wellbore zone for certain period of time, for instance 30 minutes to 3 hours depending on rock properties. The contraction of the laterally-confined reservoir rock, results in thermal strains and tensile stresses. These tensile stresses, reduce the effective stress from the minimum horizontal stress to T_0: the rock tensile strength, as shown in Figure 4.16. Once the minimum horizontal stress in rock reaches the tensile strength of rock, the rock starts to rupture.

Let's start with a brief introduction to the mechanisms of rock fracturing in tight formations. The total overburden pressure on rock is taken by matrix and fluid in the pores of the rock. The former is called the effective stress of rock and the latter is called fluid pressure or pore pressure. The effective stress is the contact pressure between grains, in other words, it is the component which is holding the rock grains together. To initiate rupture in rock, the effective stress has to decline and go from compressive to tensile. Once the grains are under tensile stress, they begin to separate.

The fracture in rock is a function of loading and rock strength. The rock strength is a function of the compressive load; therefore, any reduction in the effective stress leads to lowering the rock strength and making the rock more prone to rupture. The rock grains are bonded by cements. As a result,

cracks in rock could initiate from each single grain (inter-granular rupture) or from the interface of each two grains (interface rupture). Depending on the strength of rock grains and bonds, either of the rupture zones could dominate rock fracture. In macro-scale studies, there are two modes for rupturing the rock: shear and tensile. These are shown in Figure 4.14.

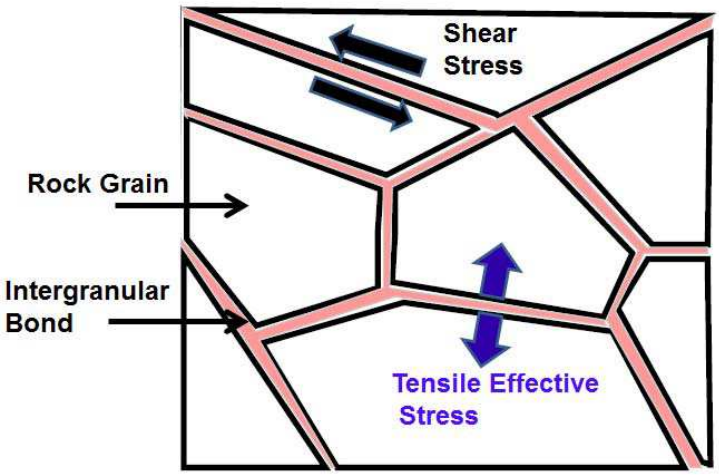

Figure 4.14: Modes of rupturing a rock

It should be noted that, in reality, due to inhomogeneity in rock properties, any loading would result in both modes of failure. Figure 4.15 exhibits a simple model of a homogenous rock (A), and an inhomogenous rock (B) which are both fixed at ends and then frozen. Due to thermal stresses, both samples tend to exhibit contraction, consequently, due to the presence of fixed boundaries which simulate the rock lateral confinement, thermal strains are developed. Notice that in (B), both shear and tensile stresses are developed;

however, the dominant mode is shear. At the moment, we base our studies on tensile failure mode for rock matrix stimulation and take only this component into consideration. Bear in mind that rock stimulation could potentially benefit even more from shear failure, which is not investigated in this Dissertation.

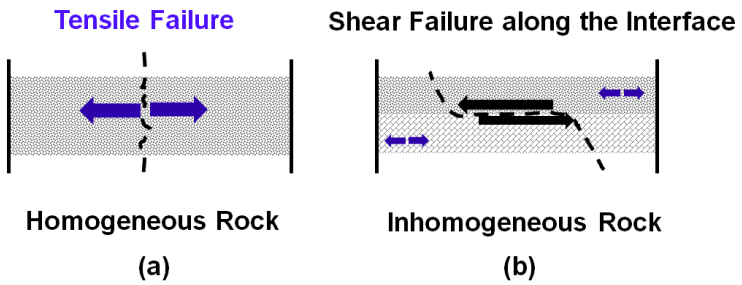

Figure 4.15: The effect of rock inhomogeneity on thermal fracturing.

At micro-scale, however, the tensile mode is the dominant mode; therefore, we focus on this type of failure. This failure mode occurs when the minimum horizontal stress exceeds the thermal strength of rock as shown in Figure 4.16. Figure 4.16 also shows the failure envelope for a tensile fracture in rock [213].

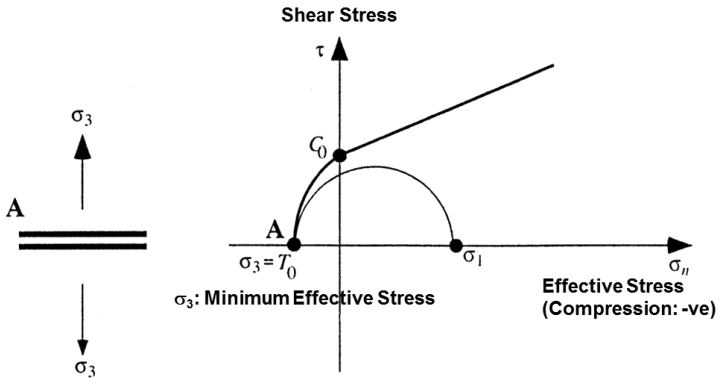

Figure 4.16: The failure envelope for a tensile fracture in rock.

4.6.2.1 Shale properties and structure

Shale is composed of clay, silt and water. The complex structure of clay, Figure 4.17 is due to the presence of plates of silica and aluminum. Our objective of illustrating the structure of shale is to emphasize the insufficiency of effective stress reduction as a result of pore pressure increase in tight formations. The excessive capillary pressure due to small pore throat size, makes the rate of pore pressure diffusion extremely small; therefore, fracturing by fluid pressure will not be successful. Although hydraulic fracturing in homogenous rock creates a bi-wing fracture, in reality rock is not homogenous; hence, the fractures open along weak planes forming a main bi-wing with multiple extensions along weak planes. In reservoir rocks with few weak planes, thermal shocks can create such weak planes through freezing the rock, leading to rock contraction in a confined medium. This opens up more voids which could then be pressurized by fracturing fluid resulting in propagation of fractures. The

pattern of fractures and the effect of such thermal fractures in increasing the permeability of rock is not the subject of this Dissertation; rather, how fast and how far the temperature could diffuse in rock, are the focus of this chapter. This preliminary numerical investigation has the potential to pave the road for field scale operations of thermal shock in oil and gas shales in near future. Figure 4.17 shows the geometry of a horizontal wellbore and the complex structure of shale.

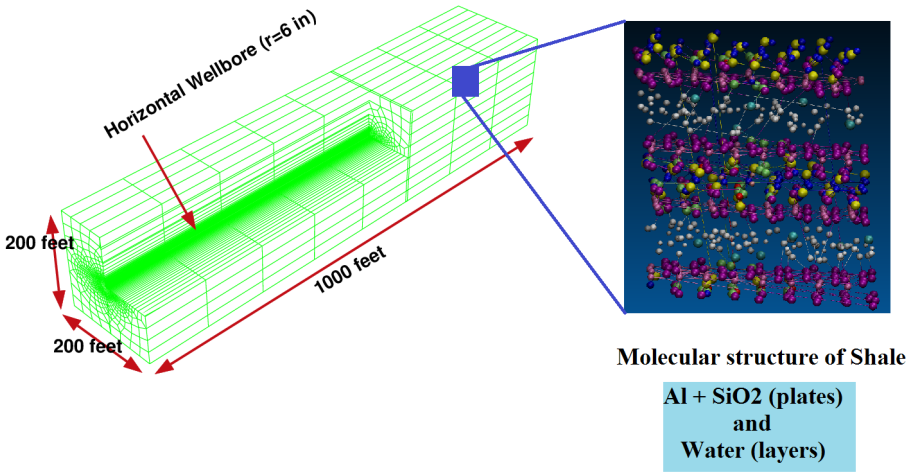

Figure 4.17: Geometry of a horizontal wellbore and the complex structure of shale

4.7 Extent of Thermal Fracturing Growth

4.7.1 Phase I: Effectiveness of freezing the rock

One way to induce volumetric rock stimulation in rock, is through pore pressure increase. Increasing pore pressure is an efficient way to break the

matrix bonds by introducing tensile stress in matrix and reducing the effective stress. This method works best in permeable rocks such as sandstone, however for impermeable rocks such as shale, the elevated fluid pressure can not be readily diffused into the rock pores, rather it is used to open a single fracture along the maximum horizontal stress. As a result, volumetric stimulation of an impermeable rock by pore pressure increase is not possible. To make this possible, initial openings are required and we believe that these openings or seeds for improved hydraulic fracture initiation, could be created by cooling down the rock and generating thermal fractures. It should be noted that, thermal stimulation is not a replacement for hydraulic fracturing; it is only a means of facilitating the initiation of hydraulic fracturing. The thermal process of freezing the body of rock where it is confined by surrounding rock, makes the rock undergo tension as it shrinks. This macro-scale process of rock shrinkage, leads to volumetric rock stimulation and permeability enhancement in rock. The extent of tensile stress away from wellbore is a function of the following parameters;

- The temperature reduction in wellbore
- Mechanical properties of rock: E and ν
- Thermal properties of rock and fluid such as specific heat C, thermal expansion α, and thermal conductivity K
- Permeability of rock k

- Presence of natural fractures and their types including joints, veins, and dikes

Natural fractures are normally filled with minerals. Joints are empty fractures with no mineralization. Veins, however, are open fractures with partial mineralization such as calcite or hematite and dikes are filled with igneous rocks or magma. Whether or not the fractures are filled with minerals, affects both fluid flow and heat transfer in fractured rock.

The rocks might be thought of as solids containing voids which hinder the heat transfer, but thermal conductivity of shales in our numerical simulations of the coupled heat transfer and effective stress reduction show the opposite.

Parameter	English units	SI
Reservoir properties		
Mass density of rock, ρ	0.08 $\frac{\text{lbm}}{\text{in}^3}$	2300 $\frac{\text{kg}}{\text{m}^3}$
Shale mechanical properties		
Modulus of elasticity, E	15×10^6 psi	100 GPa
Poisson's ratio, ν	0.3	0.3
Thermal expansion, β	9.7×10^{-6} $\frac{1}{^\circ\text{K}}$	9.7×10^{-6} $\frac{1}{^\circ\text{K}}$
Shale thermal properties		
Conductivity, k	0.45 $\frac{\text{lbf in}}{\text{s in }^\circ\text{K}}$	2 $\frac{\text{W}}{\text{m}^\circ\text{K}}$
Specific heat, C	5,500 $\frac{\text{lbf in}}{\text{lbm }^\circ\text{K}}$	1380 $\frac{\text{J}}{\text{kg}^\circ\text{K}}$
Fluid properties		
Hydraulic conductivity, K	39×10^{-14} $\frac{\text{in}}{\text{s}}$	1×10^{-14} $\frac{\text{m}}{\text{s}}$
[a]Void ratio, e	1	1
Specific weight, ρg	0.04 $\frac{\text{lbf}}{\text{in}^3}$	9,806 $\frac{\text{N}}{\text{m}^3}$

[a]Void ratio is related to porosity ϕ and defined as Equation (4.16)

Table 4.3: Input for numerical analysis

$$\phi = \frac{e}{1+e} \tag{4.16}$$

Notice that permeability used here is hydraulic conductance in velocity units. We have used the permeability so we could utilize the finite element code

ABAQUS for this simulation. This software uses hydraulic conductivity instead of permeability. The permeability from the above hydraulic conductivity can be obtained assuming viscosity $\mu = 1\,cp$ and density $\rho = 1000\,\frac{kg}{m^3}$ for water as k=1 nD.

Figure 4.18 shows the geometry of the model used to demonstrate the effectiveness of thermal fracturing in rocks. The parameters used for this simulation are shown in Table 4.3. In this model a core size rock sample is simulated under reservoir conditions of 1000 psi (7 MPa) pressure and 373.15°K temperature. The core is confined circumferentially around the outer diameter only on top and bottom to both allow for simulation and let the central hollow space which is acting as wellbore, deform radially. In the first step of simulation, the initial conditions are activated and in the second step, the constant temperature of 273.15°K is applied to the mid-section of the interior cylinder. This generates the heat flux from the core toward the low temperature zone of the central core. Since the rock is confined externally similar to rock confinement in reservoir, it will not be able to deform freely under this heat transfer process; hence, thermal stresses are developed in rock leading to tensile cracks.

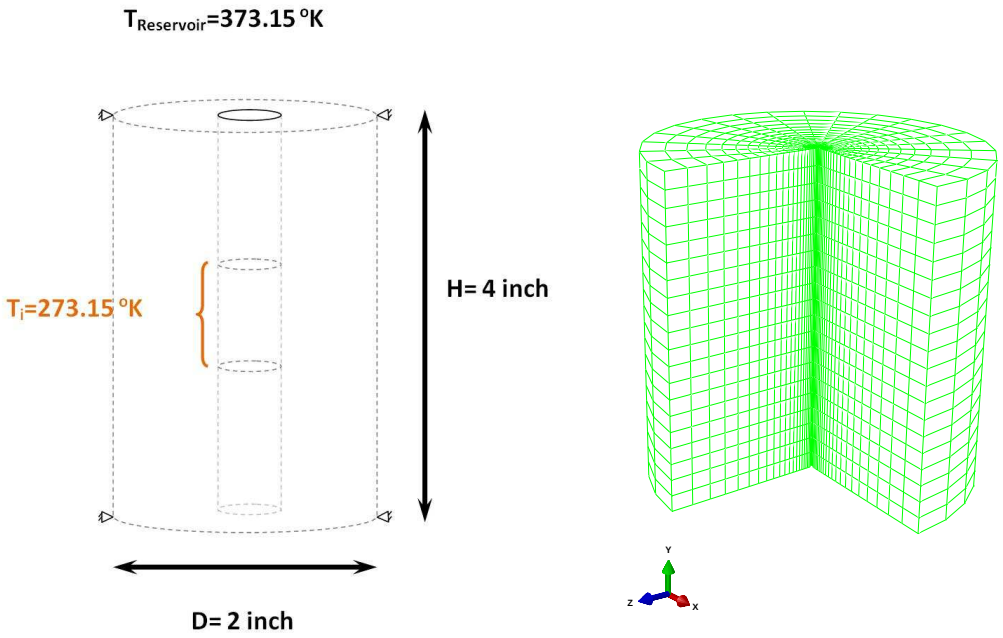

(a) The geometry of the model (b) The finite element mesh

Figure 4.18: Description of the model

The robustness of this technic can be seen in Figure 4.19(b) in which the stress distribution in rock after 2000 seconds is shown. In ABAQUS, the compressive stresses are negative and tensile stresses are positive. It can be seen that a large zone around the wellbore has fallen into tensile stress mode which is more susceptible to tensile cracks. One more thing that should be noted is that, in order for elements of rock to fall into tensile mode they don't have to be frozen all the way from 373.15 to 273.15°K. In fact there are tensile zones in which the temperature has dropped only 25°K from the initial hot reservoir condition.

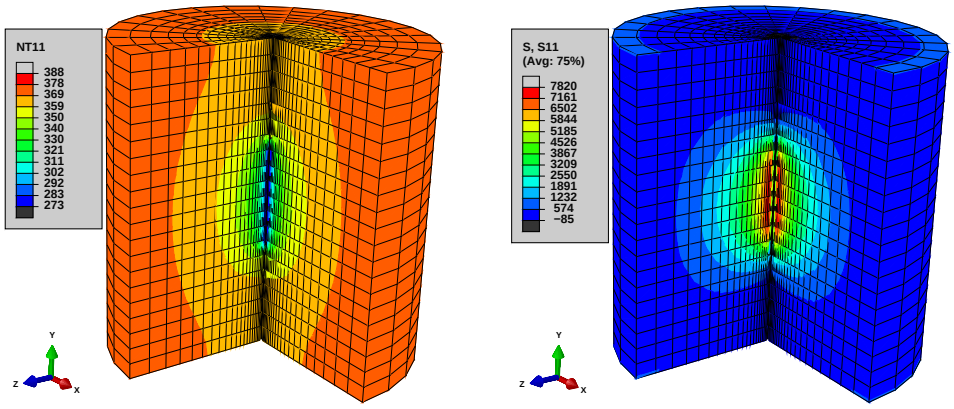

(a) Temperature distribution (b) Stress distribution

Figure 4.19: Temperature(a) in °K and stress distribution(b) in psi in the core after 2000 seconds.

Figure 4.20 shows the deformation (a) due to heat flux (b) in a core. The deformation plot shows the shrinkage of sample toward the freezing zone and exhibits the highest potential for tensile cracks and permeability enhancement around this zone. Next, we will look at the simulation results in reservoir scale to get an insight on temporal and space distribution of temperature and stresses in reservoir condition. For this analysis, the shale formation of very low permeability of 1 nano Darcy is modeled.

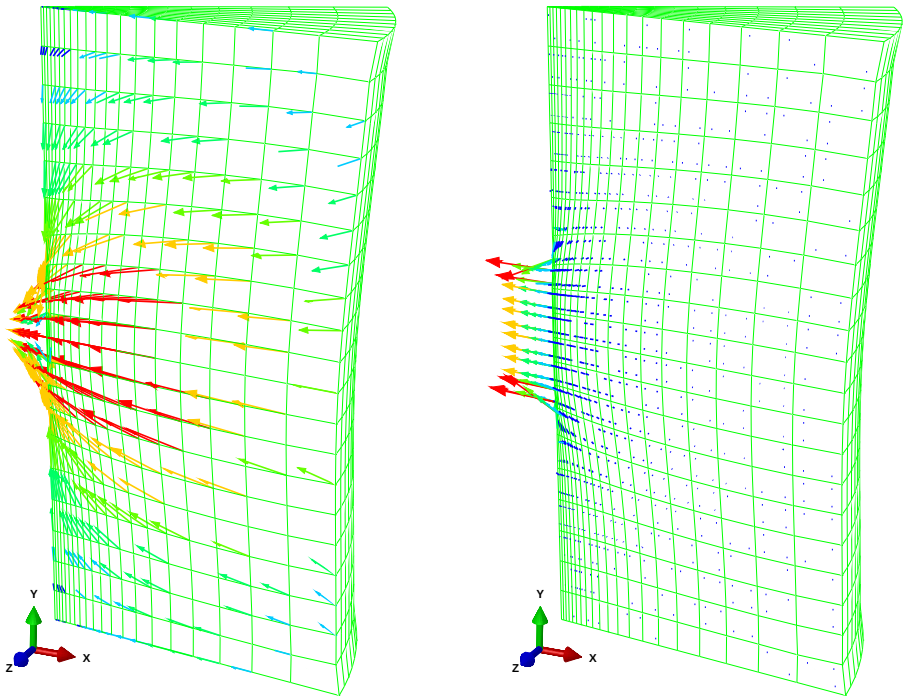

(a) Total deformation vector plot (b) Heat flux vector plot

Figure 4.20: The vector plots of (a)the total deformation and (b)heat flux.

In our numerical simulation we solve the coupled system of Equation (4.17) and (4.18) in the near wellbore zone.

- Stress-Deformation:

$$\nabla \cdot \sigma = 0 \tag{4.17}$$

- Temperature Diffusion:

$$\rho C_p \frac{\partial T}{\partial t} + \rho C_p u.\nabla T = \nabla \cdot (k \nabla T) + Q \tag{4.18}$$

4.7.2 Phase II: Obtaining the freezing zone

The problem of the creation of tensile stress in rock by freezing the rock is a coupled thermal-hydromechanical problem. The solution of heat transfer in shale using finite element analysis shows that if the reservoir temperature of 100 degrees centigrade could be dropped to and maintained at 0 degrees for 3 hours, the temperature reduction zone could go up to 1 foot from the wellbore walls as shown in Figure 4.22a for the lowest possible thermal conductivity. For higher thermal conductivities, this zone could go up to 10 feet (Figure 4.22b). As the formation rock is radially confined, the reduction of temperature causes tension in rock which could develop thermal fractures. The results are promising as the transfer of heat could be carried out in impermeable rocks without much involvement of pore pressure. Figure 4.21 describes a 3D finite element model used to study heat transfer to a horizontal well. The wellbore radius is 6 inches and the length of well is 1000 feet. In order to eliminate the effect of boundaries, the well is placed at the center of a 200 by 200 ft^2 square as shown in Figure 4.21b. The parameters in Table 4.3 are used for this analysis.

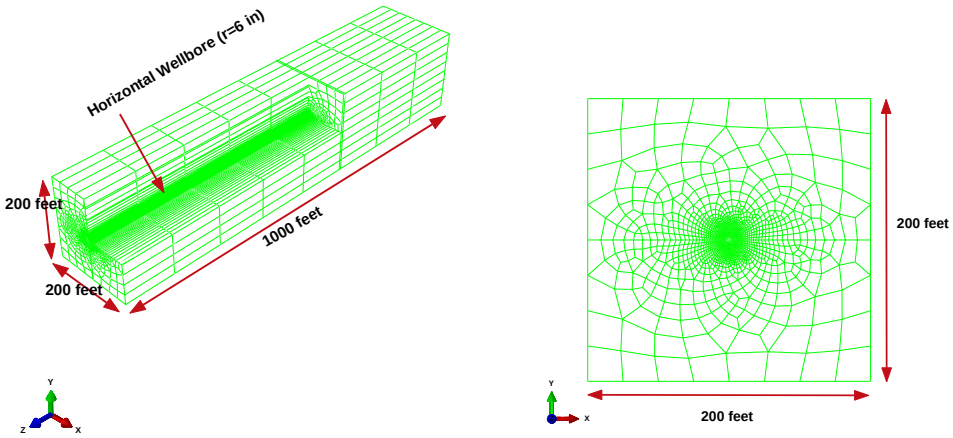

(a) Geometry, three dimensional mesh and horizontal wellbore model

(b) Two dimensional mesh for heat transfer analysis

Figure 4.21: Finite element model description for heat transfer analysis

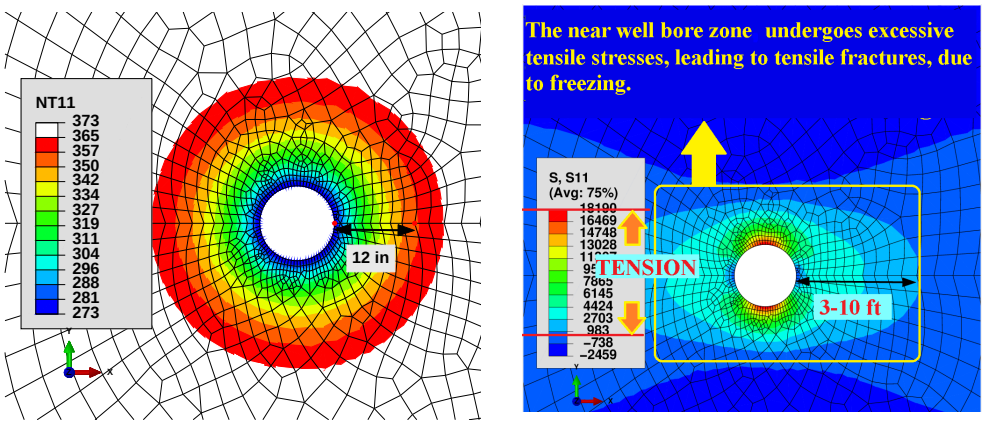

(a) Temperature distribution around the wellbore after 3 hours

(b) Stress distribution around the wellbore after 3 hours

Figure 4.22: Temperature and stress distribution around the wellbore after 3 hours

Similar analysis was performed for 24 hours of heat transfer and not much

change is seen beyond the 3-hour analysis. The results of temperature and stress distribution along the x-axis from the wellbore wall, for 3 and 24 hours of analysis are shown in Figure 4.24. It should be noted that to attain the stress level to initiate fracture, the maximum displacement required is 0.012 in (Figure 4.23) which is readily available.

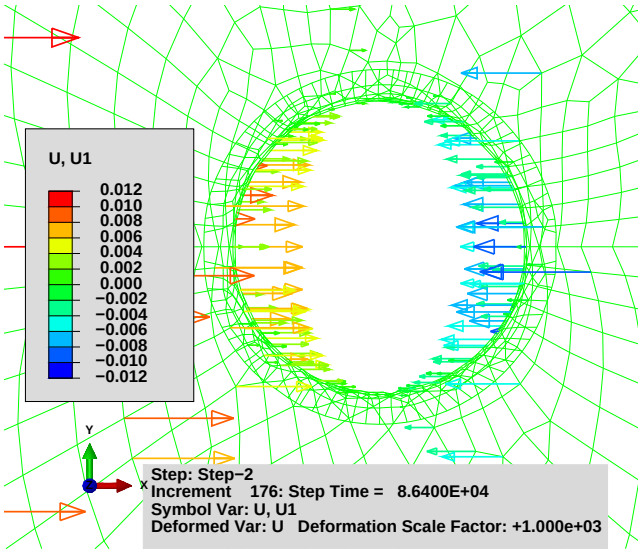

Figure 4.23: Displacement vectors of wellbore wall in X direction

The temporal and space extents of heat transfer are studied through previous simulations. This technic would not be efficient enough if the extent of stimulation of rock were limited to a short distance around the wellbore. The question that arises here is that if thermal cracks propagate to a certain distance away from the wellbore, could we inject the same chemicals that induced the temperature reduction and repeat the freezing process. If it is possible,

then we can create openings or more technically saying, the zones or pockets of susceptible and readily available to fracture propagation. This is a big achievement in the process of rock fracturing. Notice that, this technic has to be used prior to hydraulic fracturing to weaken the rock bonds and set up the pathways for fracturing fluid around the wellbore. Once the pathways are created, they can not be healed; therefore, even if the cracks get closed under the in-situ stresses, the later stages of fluid injection could open up these cracks and place proppants in the fractures.

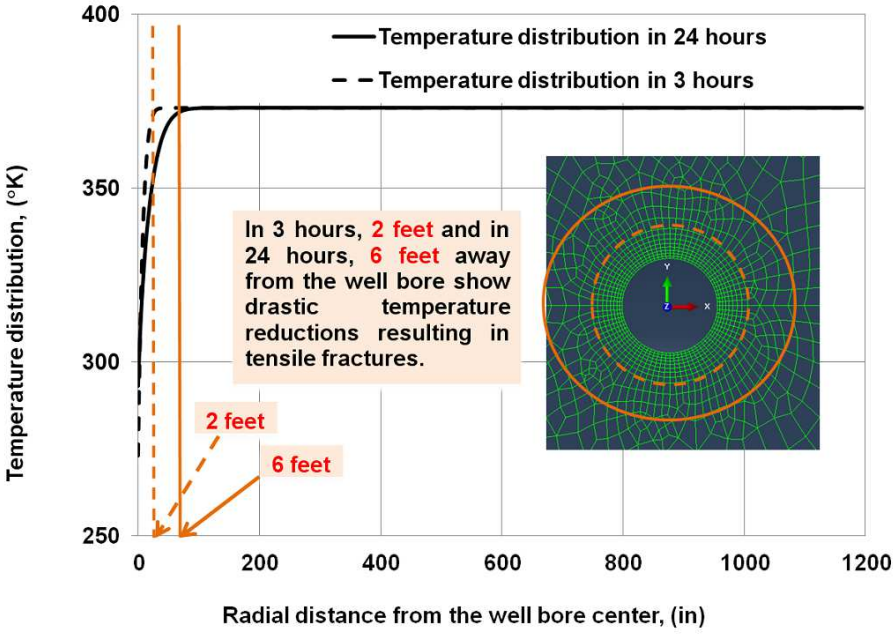

Figure 4.24: Variation of Temperature in X direction with radial distance from the center of the wellbore

4.8 Results

We studied the effect of thermal cracks induced by thermal shocks on the recovery of gas from a fractured horizontal well. We have studied the creation and extension of thermal cracks in our previous works [74, 76] which is also explained in detail in this Chapter.

Figure 4.25 shows the geometry of reservoir and finite elements discretization of the three domains used to simulate the gas flow. To add the flow component to the above coupled problems of stress-heat transfer, we first solved the stress-heat transfer problem and obtained the zone of thermal crack extensions around the wellbore. It should be noted that permeability changes are nonlinear in pressure, but we assume at this stage that permeability remains constant during analysis. Variation of permeability with fluid pressure is a possible future direction of this research. In other words, each flow analysis takes place in a domain of enhanced permeability. For flow problems in a wellbore with radial enhancement of permeability, Equation (4.19) should be solved.

$$\nabla^2 \mathrm{p} = \frac{\mu \mathrm{c_t} \phi}{\mathrm{k}} \frac{\partial \mathrm{p}}{\partial \mathrm{t}} \tag{4.19}$$

Equation (4.19) is the pore pressure diffusivity equation. The derivation of Equation (4.19) is shown in Appendix D

Figure 4.26 shows the improvement in total production as a result of thermal stimulation around the wellbore. It can be observed that the creation of hydraulic fracture increases the productivity profusely and volumetric rock stimulation around the wellbore within 4 feet radius improves the recovery by an additional 16%. Figure 4.27 shows the impact of the permeability of the stimulated zone in recovery improvement.

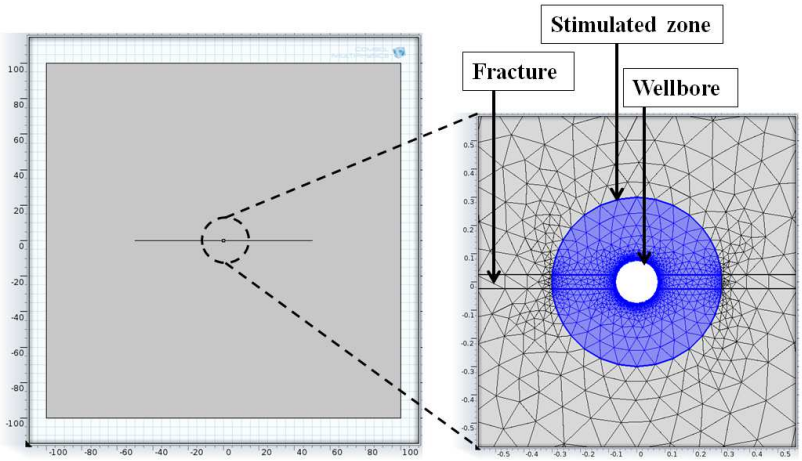

Figure 4.25: Geometry of reservoir and finite elements discretization of the three domains used to simulate the gas flow.

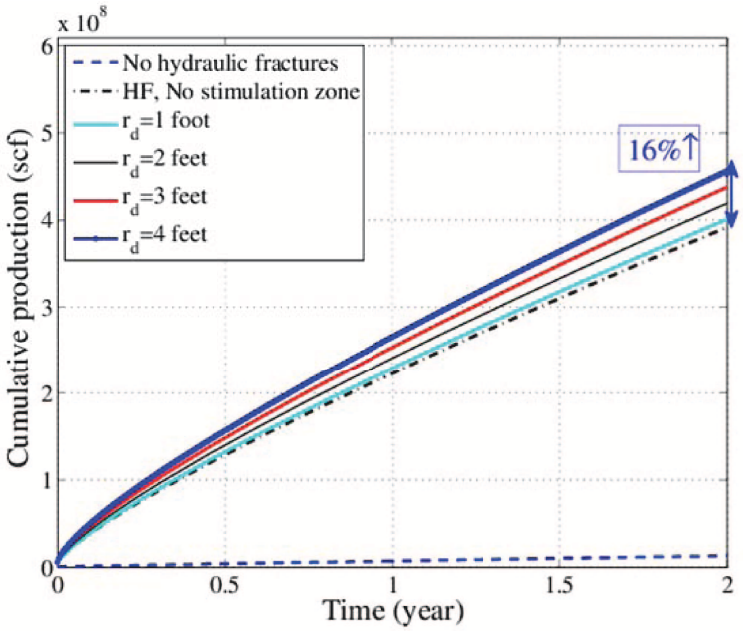

Figure 4.26: Improvement in total production as a result of thermal stimulation around the wellbore

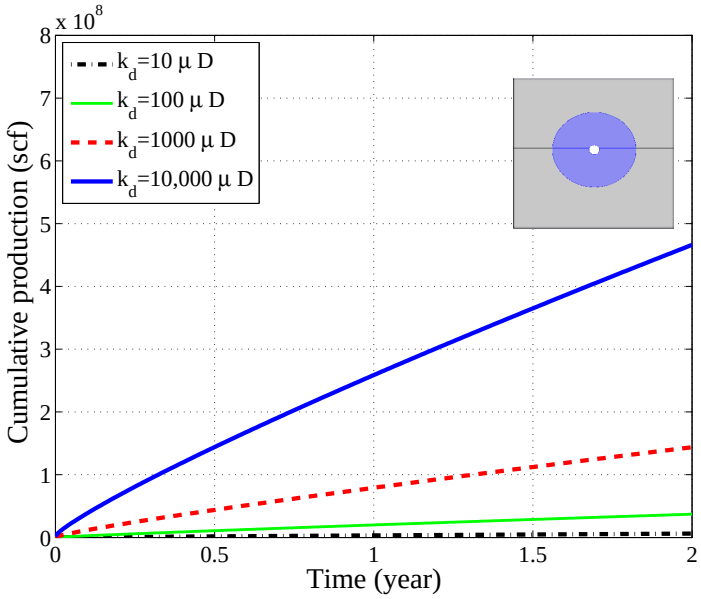

Figure 4.27: Improvement in total production as a result of thermal stimulation around the wellbore for various levels of permeability enhancement.

4.9 Conclusions

- The simulation results show an improvement of the calculated total production as a result of thermal stimulation around the wellbore. It can be observed from Figure 4.26 that the creation of hydraulic fracture increases the productivity profusely; moreover, the volumetric rock stimulation around the wellbore within 4 feet radius improves the recovery by an additional 16%.

- FEM is a robust method to predict the zone of temperature diffusion into

reservoir rock; however, to obtain the pattern of fracture propagation in rock, DEM is required and we investigate it in Chapter 5.

Chapter 5

Discrete Element Simulation of Thermal Fracturing

5.1 Introduction

Tight formations or the reservoir rocks with extremely low permeability, make vast hydrocarbon reservoirs in the United States and worldwide. In contrast to conventional reservoirs, production from tight formations is only economic when such formations are hydraulically fractured. Economic production from tight formations relies on the existence of a network of connected fractures in the rock to create a more volumetric pattern of fracture. To achieve this goal, we have proposed a novel method for fracturing rock by thermal means, in which the rock is cooled prior to hydraulic fracturing, leading to a reduction of effective stress and creation of thermal cracks. The question is how much is the effective rock permeability improved by cooling down the hot reservoir. We use the discrete element method (DEM) to obtain a network of thermal fractures as the rock is cooled. The permeability can then be calculated using a pore network model which is not the subject of this work. Here we present Discrete Element Method (DEM) analysis for thermal fracturing and show the effect of main parameters involved in the solutions obtained from DEM, including rock stiffness.

5.1.1 Production from Shale

The world has turned its attention to unconventional hydrocarbon reservoirs including gas shales, oil shales, and methane-rich coal seams. Production from such reservoirs is impossible unless the rock is fractured. To facilitate fracturing of shale, authors [74, 76] have proposed a novel thermal fracturing technique, whereby rock temperature in the near-wellbore zone is reduced. Reduction of temperature leads to the development of thermal fractures in the rock. The process of fracturing and finding the pattern of fractures in rock is difficult using finite elements (FE) programs, because except for the extended finite element method (XFEM), other FE-based codes deal with the continuous media. These codes are incapable of handling changes in the FE mesh, when a fracture propagates. We find that the Discrete Element Method (DEM) is a far more suitable tool to model fracture in rock. Shale is considered as a granular material in which the particles are either cemented or bonded by a cohesive force. The DEM package that we use in our simulations is capable of simulating shale as a granular material in which the individual grains are bound together. Here we present the suitability of the DEM software "LIGGGHTS" to calculate fracture propagation patterns in a shale-like granular material.

5.1.2 Granular Materials

A granular material is an assembly of many discrete solid elements or particles of different sizes and possibly different chemical compositions, densi-

ties, and shapes. More than 50% of all products sold are either in form of or involve granular materials [22]. These particles are randomly grouped together to form a bulk material in which particles interact with each other due to dissipative collisions [249]. The collisions and energy dissipation in mechanics of granular materials is defined by the force interactions between particles. The stiffness of particles and the bond forces between particles play a significant role in load transfer mechanism. Despite its significance, the mechanics of granular materials, it is not well understood at present [47]. One of the complexities arises from the fact that a granular system is composed of individual mass points and each mass point moves independently; therefore, obtaining the position of moving particles using continuum models is challenging. To overcome this problem, the discrete approach is utilized for particle scale granular flow modeling. This approach is called Discrete Element Method (DEM) [61]. The DEM is a powerful and reliable method to observe the resulting interaction of particles in a solid assembly composed of particles. The physics behind DEM simulation is Newton's second law, and modeling the system of particles and their surrounding environment. Particles start from an initial state of positions, velocities, and thermodynamic properties (temperature and pressure). When an external load is applied to the system, the particles next to the system boundary are subjected to this load and depending on the medium property, they impart the load to the neighboring particles resulting in a new position, velocity and thermodynamic properties. To obtain the new state of particles, DEM takes the continuous governing equations of motion for particle

displacements and rotations and converts it to a time-discretized form. The transport law used by DEM is a force-displacement relation which describes the particle interactions.

5.2 Discrete Element Method (DEM)

The computational method to study the behavior of molecules or particles to predict the granular material behavior is DEM. The behavior of complex systems of gas, liquid or solid, when regarded as discrete medium, can be studied over time using DEM.

5.2.1 The DEM Solver "LIGGGHTS"

We use DEM solver "LIGGGHTS" for our simulations [138]. LIGGGHTS is an Open Source software which uses Discrete Element Method for modeling granular material. LIGGGHTS stands for 'LAMMPS Improved for General Granular and Granular Heat Transfer Simulations' and is based on LAMMPS ('Large Atomic and Molecular Massively Parallel Simulator'), a successful open source Molecular Dynamics code by Sandia National Laboratories for massively parallel computing on distributed memory machines. LAMMPS is a classical molecular dynamics solver and provides potentials for soft materials (bio-molecules, polymers), solid-state materials (metals, semiconductors) and coarse-grained granular materials [195].

5.2.2 The Steps of a DEM Process

The main six steps to complete a DEM process are as follows:

- Initialization: Assign the initial configuration of particles, define geometric and material properties. The particles are defined by their position, radius, and shape. In most cases, sphere is used to represent each particle.

- Application of forces: Calculate the forces acting on each particle. The typical particle forces are gravity, pressure, friction caused by the contact with other particles and the boundaries of the model.

- Force calculations: Using the above forces, compute the acceleration and velocity of particles based on the momentum balance. When particles get in contact with each other or the boundaries of the model, they impart their energy to other particles in the forms of linear springs, dashpots, and joints in the normal and tangential directions.

- Integration: At each time step, calculate the new velocity and position of each particle. The time step size for DEM problems of rock behavior is small and in the order of 10^{-8} to 10^{-4}.

- Analysis: Compute the mechanical or thermal parameters at the end of each time step for all particles and repeat items 2 through 5 for the number of time steps to complete the solution time.

- Postprocessing: Study the parameters of interest and visualize the results.

In the past, experiments were carried out to characterize the behavior of granular materials. Even though experiment provides clear insight toward material behavior, in recent years, computational methods have replaced experiment on granular materials with numerical simulations. Due to the possibility of changing problem variables in a computer model, such simulations serve as an effective tool to help researchers appreciate the behavior of granular materials. DEM approach for granular materials was developed in 1979 by P. Cundall[61]. At about the same time, molecular dynamics(MD) was used for molecular systems. These two methods share the same physics; therefore, many authors mention them interchangeably when they refer to granular simulation. It should be noted that the major difference between the two methods is the contact law and inter-particle connections which are modified from the molecular scale to micro and particle size scale. This modification of energy transfer mechanism allows for simulation of larger particle sizes. Moreover, particle bonds in DEM are able to resist: tension/compression, shear, torsion, and bending up to a certain breakage limit. Once broken, the bond connection is lost permanently. Particle bonds and related models can be used to model soils, glued particles, particle breakage, crack formation in beams, etc.

5.3 Contact Force Models

As explained earlier, the main difference between DEM and MD is the definition of the potential function, whose derivative results in the force between particles. In contrast to MD, in DEM a contact law similar to Hooke's law is defined. Hooke's law is the first order approximation of the response of a mass-spring system to the load applied to mass. In the case of granular materials, due to the existence of both friction and normal contact forces (see Figure 5.1), the Hooke's model takes a more general form to account for both contact forces as follows:

$$F = \underbrace{(K_n \delta_{n_{ij}} - \gamma_n V_{n_{ij}})}_{\textbf{Normal force}} + \underbrace{(K_t \delta_{t_{ij}} - \gamma_t V_{t_{ij}})}_{\textbf{Tangential force}} \tag{5.1}$$

The parameters in Equation (5.1) are defined as follows;

K_n: Normal stiffness

K_t: Tangential stiffness

$\delta_{n_{ij}}$: Normal overlap distance of two particles

$\delta_{t_{ij}}$: Tangential overlap distance of two particles

$V_{n_{ij}}$: Normal relative velocity at the contact point

$V_{t_{ij}}$: Tangential relative velocity at the contact point

γ_n: Viscoelastic damping constant for normal contact

γ_t: Viscoelastic damping constant for tangential contact

Hooke's law is an accurate model for solid deformation as long as the deformations are small. For large deformation problems solved in DEM, the time steps should be small enough so that the deformations can be regarded as small and the application of Hooke's law is valid. We will discuss later how to choose the appropriate time step for the problem to get stable solution. For detailed review of contact models, the book by P̈oschel and Schwager [63] is recommended. Further detail on the contact law in DEM can be found in Campbell, 1990 [46]; Zhou et al., 1999 [263]; Matuttis et al., 2000 [165]; Bertrand et al., 2005 [28].

Figure 5.1 shows the spring-dashpot model used in DEM to define the contact law for particles of granular medium.

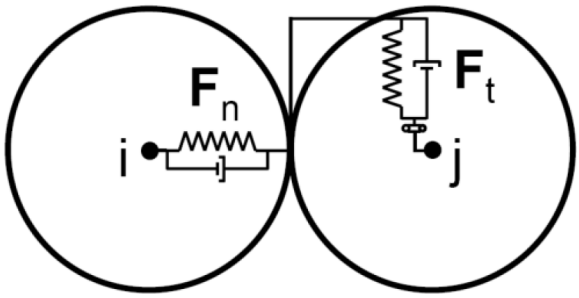

Figure 5.1: Spring-dashpot model used in DEM

5.4 Model Verification

To verify the behavior of the model, we take the simplest case of a uniaxial loading on a block of rock of size 10cm×10cm×5cm, apply a con-

stant load of 1000 psi and compare the vertical strain of the DEM model with the results of similar deformation obtained using solid mechanics. From solid mechanics, we know that, if a solid prismatic bar of length L, constant cross sectional area A and Young's modulus E is subjected to uniaxial load P along the length of the bar, it deforms by ΔL and the stress-strain relation in the bar $(\sigma - \varepsilon)$ can be obtained using the expression (5.2):

$$\sigma = E\,\varepsilon = \frac{E\,\Delta L}{L} \tag{5.2}$$

Figure 5.2 shows the reservoir (shale rock) model subjected to 1000 psi (7 Mpa) vertical stress which is used for verification purposes.

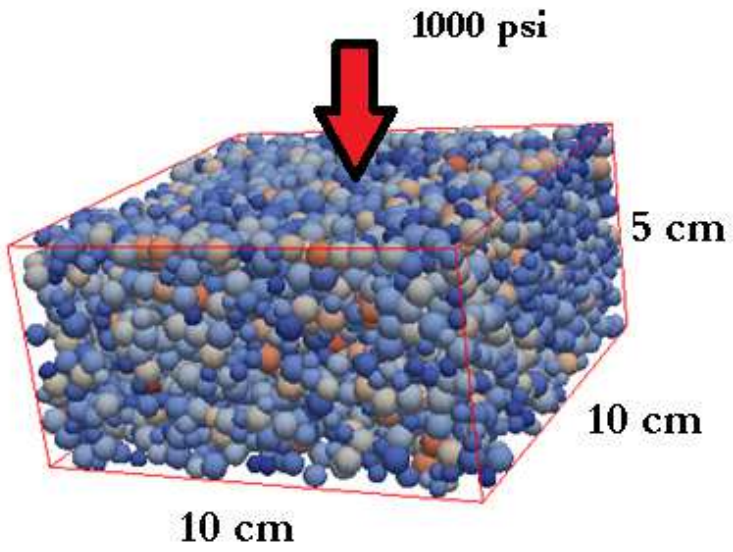

Figure 5.2: The model of uniaxial stress used for verification

The stiffness of rock for this model is E=10 Gpa; therefore, the deformation and axial strain can be obtained from Equation (5.2) as follows;

$$\varepsilon = \frac{\sigma}{E} = \frac{7 \times 10^6}{10 \times 10^9} = 0.0007 \text{ or } 0.07\%$$

We have simulated the axial loading problem in DEM for 1 second and the results of strain in the direction of loading (z) is presented in Figure 5.3. As shown in Figure 5.3, the strain obtained numerically is 0.135%. This DEM result is about twice the value that we get from solid mechanics. The larger value for DEM simulation can be attributed to the fact that, part of this strain is created during the stage of particles compression in which the pore volume fraction is reduced. This stage is not observed in the solid mechanics formulation (relation (5.2)) and that exhibits another good feature of the Discrete Element simulation.

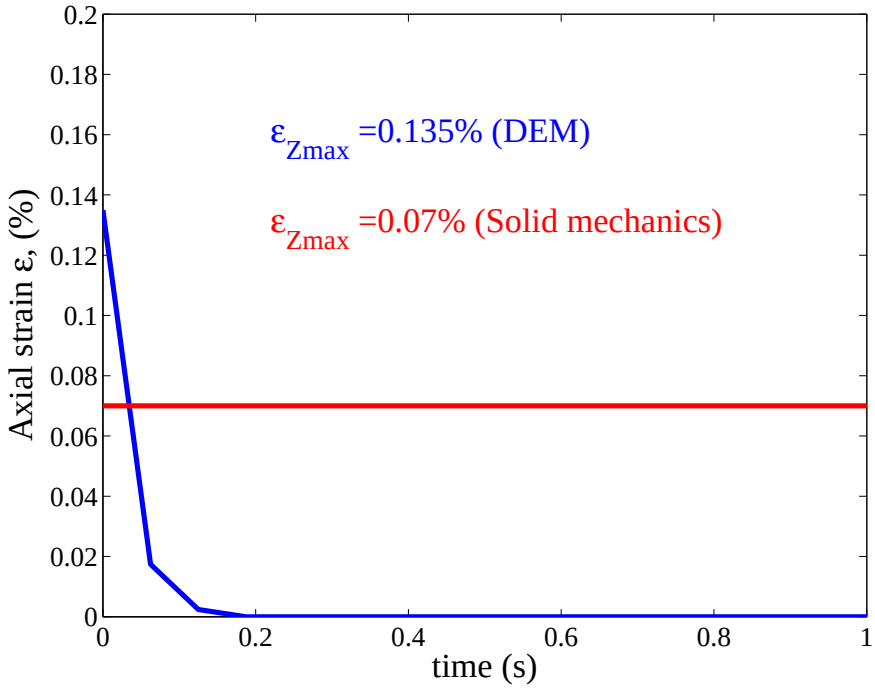

Figure 5.3: Comparison of the uniaxial strain (%), from DEM simulation and solid mechanics formulation for the block of rock shown in Figure 5.2

5.4.1 Particle Interactions

When two particles are at a distance from each other, whether in contact or not, they start applying attractive or repulsive forces to each other. When in contact, the particles apply normal and tangential forces. The latter, is known as Coulomb friction and causes shear stress. When the particles are not in contact, another component of shear stress may be developed due to van-der-Waals forces and it is known as cohesion. The combined effect of shear

sliding friction and cohesion creates the shear strength of granular material. The particles in DEM could be deformable or non-deformable. For deformable particles in contact, the elastic surface deformation of particles causes the repulsive force. Hertz theory is used to define this elastic deformation (Hertz, 1882)[108].

For non-deformable particles, Hamaker constant defines the van-der-Waals forces[104]. Our simulations are based on deformable particles using Hertz contact model. In our simulations, we use JKR model to bring in the effect of cohesion as a van-der-Waals force. We introduce JKR model briefly as we have utilized this model in our simulations. more detailed description of this model can be found in [200].

5.4.2 JKR Model

JKR model is a cohesion model developed by Johson et al[200]. Figure 5.4 shows a spherical particle of radius r which is in contact with a flat rigid plate and is subjected to external load P. Since the particle is deformable, it develops the contact length a. F is the adhesion force between particle and the plate.

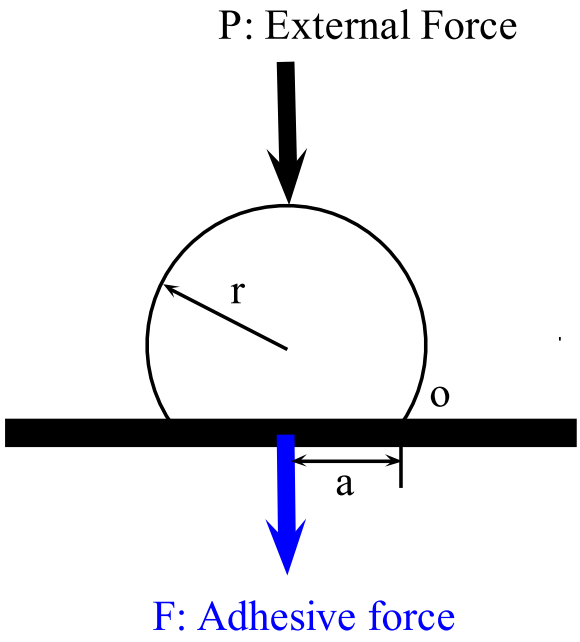

Figure 5.4: A deformable spherical particle under the external load P used for JKR model development

Hertzian elastic model which is the base model for JKR, assumes that the force developed between two particles is proportional to the area of overlap between two particles. Under this assumption, JKR model results in the expression (5.3):

$$a^3 = \frac{R^*}{E^*}\left[f_n + 3\gamma\pi R^* + \sqrt{6\gamma\pi R^* f_n + (3\gamma\pi R^*)^2}\right] \tag{5.3}$$

The parameters of Equation (5.3) are:

E^*: reduced elastic modulus

R^*: reduced radius of the particles in contact

γ: surface energy in J/m^2

f_n: normal force

5.5 The Impact of Time Step Size

Selection of time step size and estimate of simulation time is important in numerical simulations. In DEM, an important parameter is the size of particles. For a fixed size of model, as the size of particle (r) changes, both the number of particles and energy transfer rate change. We show below that energy transmission depends on the stiffness of a granular system. Also Rayleigh time T_R, which is the time required by the wave to propagate through a solid body, will be shown to be proportional to the particle size ($T_R \propto r$). For a 3D simulation using DEM, the number of particles is inversely proportional to volume of particles as shown in Figure 5.5. Also volume of particle is proportional to the cube of particle size (v$\propto r^3$). As a result, simulation time or numerical effort grows with 4th order with particle size (simulation time$\propto (1/r)^4$). This is to say that reducing the particle size to half, makes the simulation time 16 times longer.

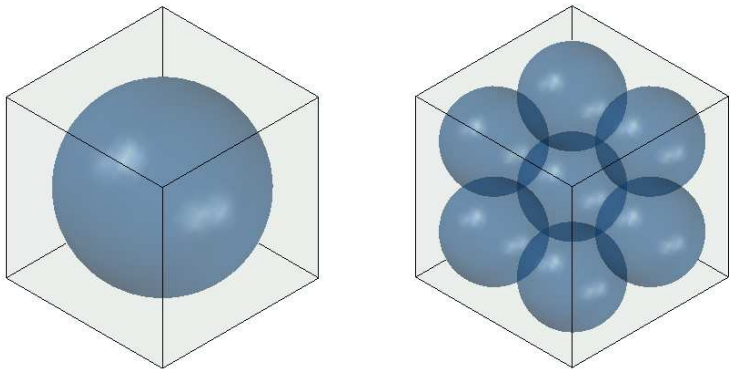

Figure 5.5: The impact of particle size in the total simulation time

5.5.1 Rayleigh-Waves

The energy transfer from particle to particle takes place over the time increments. This forces the time steps to be sufficiently small to be able to transport energy through wave propagation. Miller and Pursey (see Ref. [125, 151]) showed that 67% of the wave energy transport in granular materials is carried out by Rayleigh waves, 26% through shear wave or s-wave, and 7% through p-waves. Rayleigh waves are a type of surface wave that travel near the surface of solids. Rayleigh waves include both longitudinal and transverse motions that decrease exponentially in amplitude as distance from the surface increases [238]. We assume that all the energy is transmitted by Rayleigh waves. If the solid body has the density ρ, Poisson's ratio ν, and shear modulus G and is composed of particles of average radius R, The Rayleigh time

can be approximated as Expression (5.4):

$$T_R = \frac{\pi R \left(\frac{\rho}{G}\right)^{\frac{1}{2}}}{0.1631\nu + 0.8766} \tag{5.4}$$

We use the following values in our simulations to calculate T_R and limit the time step to $0.2T_R - 0.3T_R$ to get stable solutions.

$R = 0.001\ m$

$\rho = 2400\ \frac{kg}{m^3}$

$G = \frac{E}{2(1+\nu)} = \frac{50\times10^9}{2(1+0.25)} = 2 \times 10^{10}\ \frac{N}{m^2}$

then Rayleigh time will be:

$T_R = 1.2 \times 10^{-6}\ s$

we use 20%-30% of the T_R value for all simulations, unless the material properties changed, in which case we used the new values for time step sizes. For instance, for the above case, the time step that we use is $0.2T_R = 3 \times 10^{-7}s$.

Table 5.1 shows the appropriate values for the time step size for the problem to give stable solution.

E (Gpa)	time step size (s)
100[a]	1×10^{-7}
50	3×10^{-7}
5	8×10^{-7}
0.5	3×10^{-6}
0.05	8×10^{-6}

[a] Very stiff shale

Table 5.1: The appropriate time step size for stable solution for various Young's modulus E

Notice that these are only reference values to obtain an estimate for the time step size and other parameters could affect these values. For very stiff shale, the lower limit value of 1×10^{-7}s is applied in our simulations. Running simulations at this time scale is not possible on single node machines with limited processing units. We have used the Texas Advanced Computing Center (TACC) at The University of Texas at Austin for high performance computing. This enabled us to run lengthy simulations in a short time. With large step sizes, the simulation results are either not valid or leading to blow-up. In Figure 5.6, we have demonstrated a case of blow-up and instability, in which particles scatter due to a large time step size.

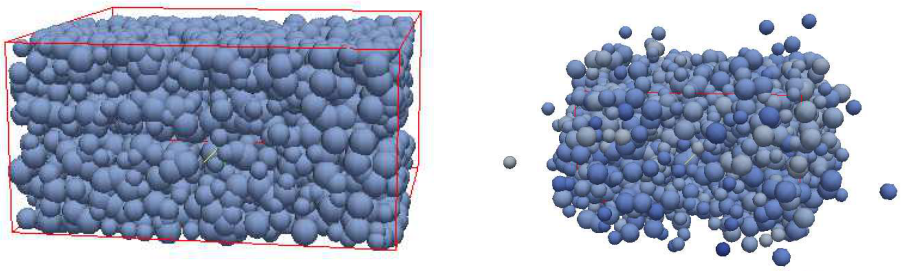

(a) Original state of particles before loading started

(b) Instability due to large time step size, leading to failure of solution

Figure 5.6: Impact of time step size in stability of DEM solution

5.6 Model and Results

Figures 5.7, 5.8, and 5.9 show the opening of natural fractures as a result of cooling the reservoir rock. Here we are cooling a block of rock of size 10cm×10cm×2cm in which we have placed two natural fractures of size 5cm×0.002cm. We place 110,000 mass particles of three different radii, then fix the boundaries against displacement and cool down the rock by 100°C. We run the simulation for two in-situ stresses of case 1)100 psi and case 2)1000 psi. As the rock is cooled down, the fractures open up normal to the fracture length and their width extend from 0.02mm to 2mm for case 1. The simulation for case 1, took 30 minutes on 32 processors. The cracks in case 2 open from 0.02mm to 0.1mm and it took 6 hours on 32 processors. This difference in simulation time is due to the requirement for equilibrium of particle movements. Under larger in-situ stresses, the equilibrium condition of particles demand smaller time steps. As we increase the in-situ stress to beyond 3000

psi, it becomes almost impossible to get a converged solution. In case 1, some openings also appear in the frozen rock, confirming that cooling down the rock leads to its contraction and creation of voids. Since the rock is laterally confined in reservoir, this contraction leads to the reduction of effective stress and lowering the tensile strength of rock, hence facilitating the rock stimulation process. Moreover, propagation of these thermal fractures enhance the permeability of rock and leads to improvement of hydrocarbon production from reservoir rocks.

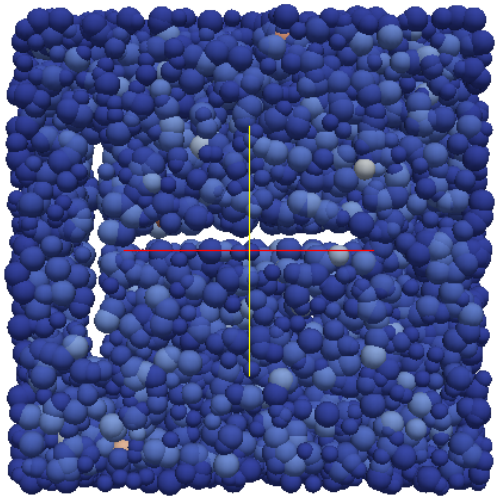

Figure 5.7: Initial natural fractures

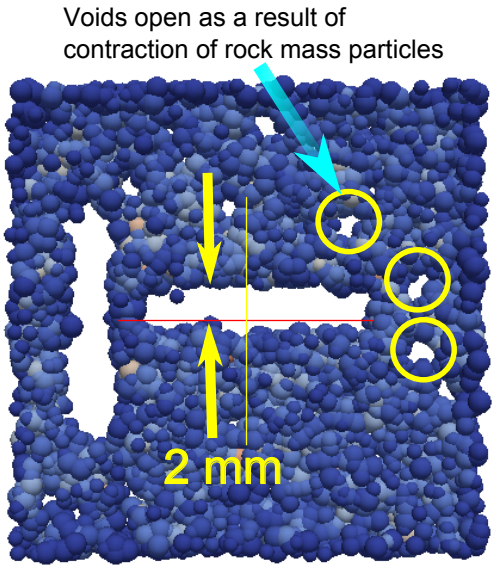

Figure 5.8: Opening of natural fractures as a result of freezing the reservoir rock, at in-situ stress of 100 psi

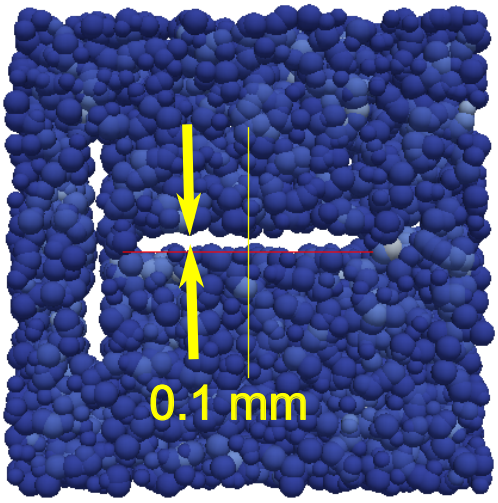

Figure 5.9: Opening of natural fractures as a result of freezing the reservoir rock, at in-situ stress of 1000 psi

5.7 Conclusions

- The time step required for DEM simulations depends on the stiffness of rock and the in-situ stresses. The values presented in Table 5.1 indicate that for an increase of the stiffness by two orders of magnitude, the time step size decreases by one order of magnitude.

- For a certain size of simulation, as the size of particles decrease, the computational efforts increase due to not only, a)the larger number of particles, but also b)the smaller time step size required for stability, as explained in Equation (5.4). As a result, simulation time or numerical

effort grows with 4th order with particle size (simulation time$\propto (1/r)^4$).

- Thermal fracturing enhances the permeability of rock through reduction of the effective stress and lowering the tensile strength of rock; however it is efficient at the small in-situ stresses. In other words, the shallower the reservoir, the more efficient is the process of thermal fracturing.

Chapter 6

Thermal Fracturing using Embedded Multiple-Site Cohesive Zone Elements

6.1 Introduction

In Chapters 4 and 5 we studied the effects of temperature reduction in the near wellbore zone. Several methods are studied to investigate the efficacy of thermal fracturing in rock. Due to the potential shortcomings of these methods, yet another method is proposed for thermal fracturing. In discrete element simulation (DE), a potential problem is the simulation time which was shown to be hours or days for a sample of 100,000 mass particles. Another potential problem with the DE simulation is that the heat transport which is essential to our simulation of thermal fracturing. Here we use another method in Finite Element method to simulate the thermal fracturing in reservoir rock using embedded multiple-site cohesive zone elements. Figure 6.1 shows the cube model for thermal fracturing simulation of a reservoir rock.

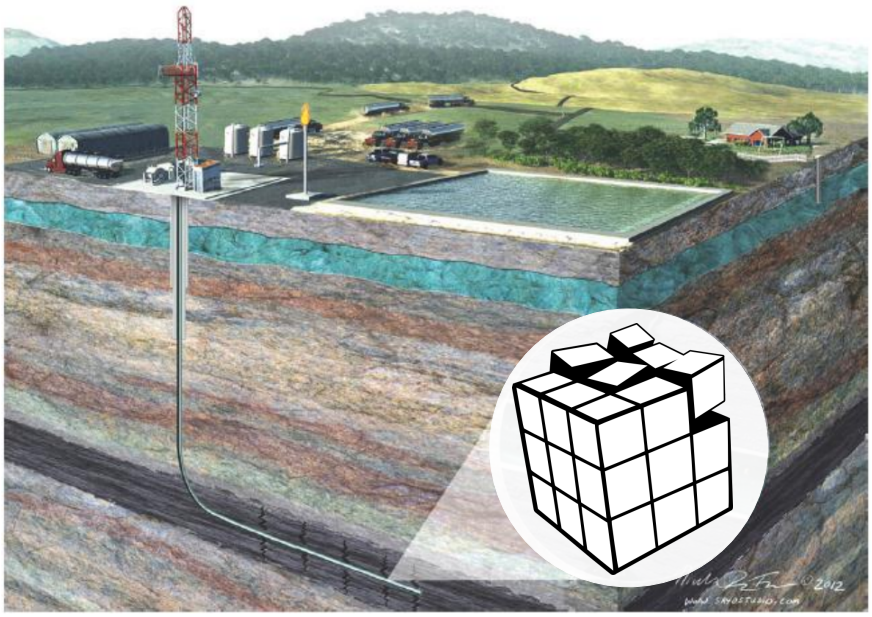

Figure 6.1: Thermal fracturing of shale due to freezing the reservoir rock.

We have already presented a novel method called freezfrac to create a more ramified pattern of fracture around the wellbore. This method introduces a thermal gradient around the wellbore by freezing the wellbore which imposes thermal stress and causes multiple-site fractures.

Complexity and high cost of field tests motivated us to explore different simulation approach to design a robust way to impose an effective pattern of thermal fracture in virtual environment. Discrete element method (DEM) was employed in our previous approach as it does not have the limitations involved with the continuum approaches. In this approach, fracture pattern

can be captured by incorporating a failure criterion between the particles. However, this approach, despite its advantages, suffers from lack of accuracy to represent the transport phenomenon and the energy balance.

In this study, we propose a physics-based continuum approach combined with fracture mechanics to simulate the thermal fracturing process. Cohesive zone elements based on fracture mechanics laws have been incorporated as a de-bonding criterion between continuum elements. By combining both fracture cohesive and continuum elements, we have shown that both physics of transport phenomenon in continuum framework as well as crack propagation can be effectively captured in implicit integration scheme in a finite element model. This approach allowed us to investigate the field uncertainties associated with the variation of the shale properties around the wellbore in terms of both physical properties such as elastic modulus and heat conductivity as well as the fracture properties of the formation due to the presence of different failure planes. The present quantitative approach is used to perform global statistical sensitivity studies to investigate the robustness of the thermal fracturing process with respect to the input parameters such as freezing temperature level and the exposure time.

6.2 Methodology

For simulation of thermal fracturing using continuum models we assume that a block of rock is made up of smaller cubic blocks, Figure 6.2(a). These blocks are in touch through contact elements which possess the fracture

properties of rock, Figure 6.2(b). Thermal stresses and deformations occur in the blocks and load transfer between blocks is carried out by contact elements. There are several criteria for fracture initiation and propagation. Here we focus on strain and energy criteria. In these two criteria, whenever the strain or energy in contact elements exceeds a critical value, the contacts will fail in shear or tension.

To obtain a critical value for deformation of blocks at contact points which leads to fracture initiation, we use an energy approach in which when the potential energy of contacts or springs reaches the fracture energy of rock, fracture initiates.

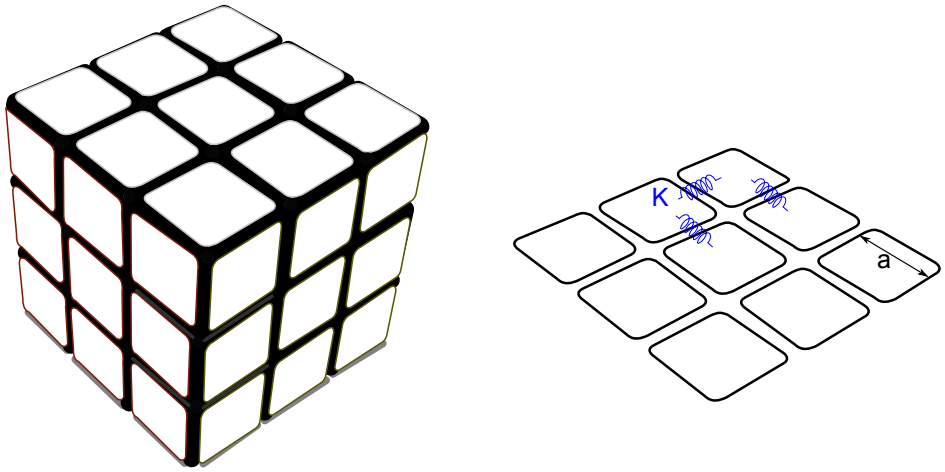

(a) The Rubik's cube model of rock (b) Geometry and contact elements

Figure 6.2: Rock model for thermal fracture propagation simulation

The critical value of crack opening for fracture initiation can be ob-

tained using Equations (6.1), (6.2), and (6.3) in which, K is the stiffness of springs, a is the size of cubes, Δ is the deformation of the space between the two blocks, G_c is the fracture energy release rate, E, is the Young's modulus of rock and A is the area of each block.

The stiffness of spring can be related to the Young's modulus using Equation (6.1).

$$K = \frac{F}{\Delta} = \frac{\sigma A}{\Delta} = \frac{E\varepsilon A}{\Delta} = \frac{E\frac{\Delta}{a}A}{\Delta} = \frac{EA}{a} \tag{6.1}$$

From fracture mechanics, we know that the energy release rate is the energy required to create a unit surface of fracture. Then, to obtain the deformation, the energy release rate is made equal to the potential energy of springs as they deform.

$$G_c = \frac{1}{2}K\Delta^2 \Rightarrow \Delta = \sqrt{\frac{2G_c}{K}} = \sqrt{\frac{2G_c a}{EA}} \tag{6.2}$$

finally, the critical value of deformation is obtained from Equation (6.1) and for the case of Shale, its value is obtained from Equation (6.3).

$$\Delta = \sqrt{\frac{2 \times 100(J/m^2) \times 1(m)}{50 \times 10^9 \times 1(m^2)}} = 63\mu m \tag{6.3}$$

More detailed discussion on the method and formulation of the cohesive zone model is presented in Section 3.9.

6.2.1 Fracture Propagation Criterion

Fracture propagation criterion that we use in our simulations is the fracture energy criterion. This requires two parameters to define the traction-

separation plot that we explained earlier using Figure 3.9. These two parameters are the maximum contact stress and the fracture energy for the two modes of failure.

We could also use the maximum contact stress and the contact gaps at the completion of de-bonding $\Delta_{\mathrm{n}}^{\mathrm{c}}$ as the two parameters required to define the damage and failure criteria; however, we use the fracture energy based criterion for the simulations that we performed in this chapter, as we have better information on the fracture energy for shale compared to contact gaps at the completion of de-bonding, $\Delta_{\mathrm{n}}^{\mathrm{c}}$.

6.3 Model Verification

The method of rock fracturing simulation which is based on rock fragments and contacts at the interface of fragments relies heavily upon formulation of sliding and separation of fragments. The fundamental material properties used for such simulations are obtained from a load-displacement plot, also known as traction-separation curve. To verify our CZM simulations for rock fracturing which will be presented in Section 6.4, we show three verification models to demonstrate the applicability of this CZM-based numerical tool that we used in this dissertation.

The idea of cohesive zone law has been used on many engineering application including ceramic failure, rock fracture, and rock blasting. When the general concept is used in conjunction with a numerical tool such as finite element, the solution is always sensitive to the features of the numerical

analysis such as discretization scheme, mesh size, time steps used, and how stability is enforced during simulation. As a result, in general, two different numerical methods which use CZM do not provide exact same solutions. Here we use the finite element code ANSYS 15.0 and compare the results with the finite element method used by Mergheim *et al.* [168]. They use discontinuous elements method in which they add additional degrees of freedom at the crack tip to make the solution independent from the mesh.

6.3.1 Verification Model 1- Tensile Mode Failure

In the first example, we use a 1mm×1mm square plate and apply a uniform tensile stress at one end. Geometry, loading and boundary condition of the problem are shown in Figure 6.3. The top edge is subjected to uniform displacement and can freely move upward. The lateral movement of the two top corner nodes are constrained by two rollers and the bottom edge is fully constrained against displacement in x and y directions. The material parameters in our simulation are taken from the reference paper, which are as follows; Young's modulus $E = 100\ N/mm^2$, Poisson's ratio $\nu = 0$, tensile strength $f_t = 1.0\ N/mm^2$, and fracture energy $G_f = 0.1\ N/mm$ which is equal to 100 J/m^2. In this example, if the fracture zone is defined along the entire length of the domain, the propagation of fracture takes place in an instant and the solution can not converge. To avoid this, a small seed of fracture is placed on the left side of the fracture shown in Figure 6.3 and from there, fracture can propagate through the domain. G_I or fracture energy for the first

mode of fracture in Figure 6.3 indicates that we assume that no shear mode of failure occurs and all the energy imparted to the block is used to fracture the block in tensile mode. We obtain the global load-displacement plot for pure mode I failure and compare it against the plot obtained from the reference paper [168]. As the tensile stress increases due to increase of upward displacement on top edge, the load-displacement curve approaches a critical load which is expected to be equal to tensile strength of rock, 1.0 N/mm^2, as depicted in Figure 6.5. Once, the displacement gets beyond the value corresponding to the maximum load, the load-displacement plot enters a declining section in which stiffness decreases. The decrease in stiffness is due to the ongoing bond breakage at the contact zone as the vertical displacement increases. The first part of the plot is in perfect agreement with the reference plot; however, the second portion deviates from the reference plot. This difference is attributed to the behavior of the cohesive zone beyond the damage initiation phase, i.e., when the contacts start to break under stress. Another factor that causes the deviation of our result from the reference result is the additional nodes which are used in the formulation of discontinuous elements defined by Mergheim *et al.* [168]. Notice that, in Figure 6.4 the contact stress will be maximum (here 1.0 N/mm^2) when the fracture is about to open and once the fracture opens, the contact stress drops to zero.

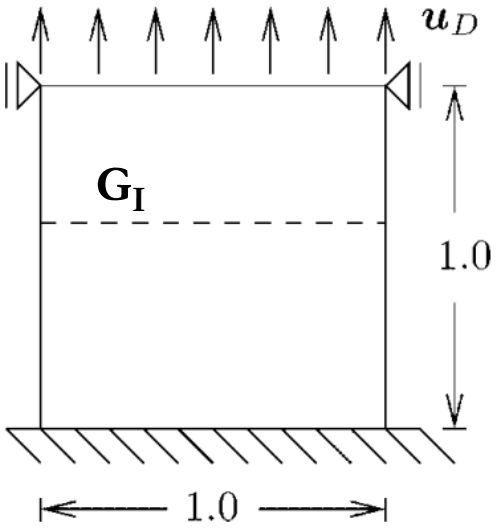

Figure 6.3: Geometry, loading and boundary condition of the problem. Dimensions are in (mm)

Figure 6.4 shows the distribution of the stress normal to the fracture face.

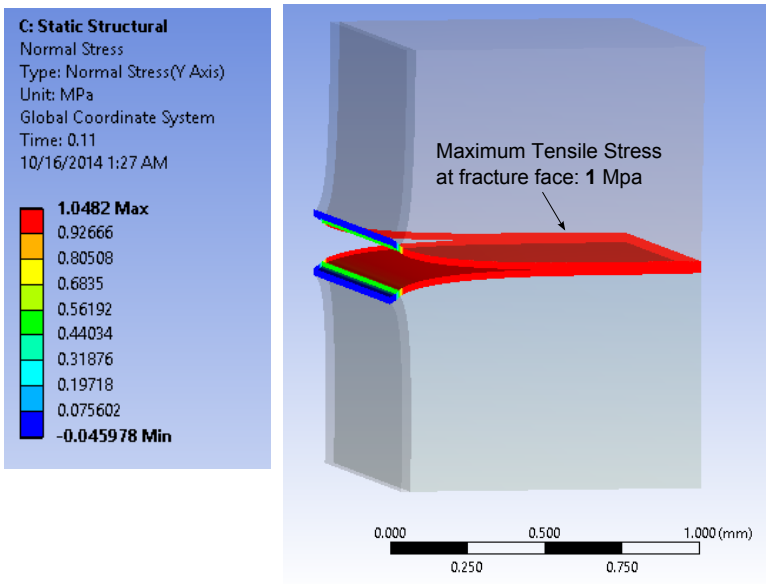

Figure 6.4: Maximum stress of contact point at failure

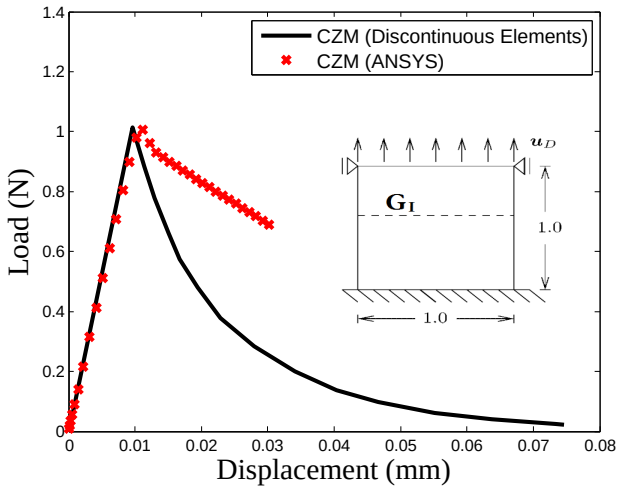

Figure 6.5: Verification of the CZM model used in this dissertation

6.3.2 Verification Model 2- Three Point Bending Mode Failure

The second model we have used for verification of the CZM model is a three-point bending beam. The geometry of the model is a 3mm×10mm beam which is simply supported at the ends and is subjected to a displacement at the center of the top edge. Material parameters used for this model are as follows; Young's modulus $E = 100\ N/mm^2$, Poisson's ratio $\nu = 0$, tensile strength $f_t = 0.5\ N/mm^2$, and fracture energy $G_f = 0.01\ N/mm$ which is equal to 100 J/m^2. The shear stiffness is set to a large value so that the beam breaks under pure tensile mode as a result of bending load. The geometry, loading, and boundary conditions are shown in Figure 6.6.

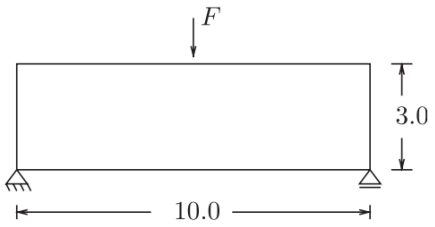

Figure 6.6: Geometry, loading and boundary condition of the problem. Dimensions are in (mm)

Figure 6.7 shows the onset of fracture initiation in which the lowest point in the bottom center of the beam has just undergone a maximum displacement of 0.3 mm and started to break. The elements of material above this point in the middle of the beam have not broken yet and resist tensile stress. They break once the displacement at those points get to 0.3 mm. In

this example our intension is not obtaining the fracture propagation pattern; rather it is to compare the two patterns of the CZM using two FEM codes with different formulation.

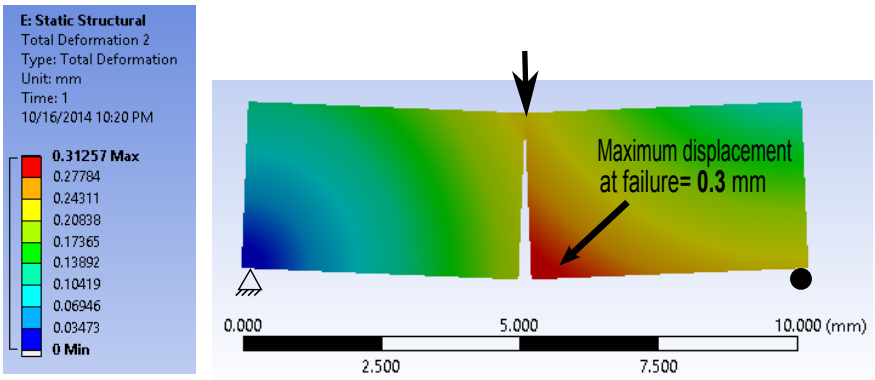

Figure 6.7: Maximum displacement of contact point at failure

The pattern of CZM that we obtained is shown in Figure 6.8. With similar geometry, loading, and boundary conditions, we use a finer mesh than the one used in the reference model and our result shows a maximum load which is slightly lower than the reference result. The difference between the two results can be attributed to the different mesh sizes in the two models. The failure criterion used in both models depends only on the maximum principal stress in the element ahead of the fracture tip; as a result, the larger elements of the coarse mesh fail later. Comparing our result with the reference results, it can be seen that the general trends are in good agreement. This confirms the applicability of the CZM model that we used for rock fracturing purposes.

The CZM is a fracture mechanics tool to model cohesive cracks using tensile and shear bonds failure at the interface of the two material fragments; in other words, the discontinuity is explicitly introduced into the continuous domain of problem without having to deal with changes in mesh pattern and number of elements in the model. This is the main advantage of using this method and also makes the CZM a useful method to model inelastic material behavior using a discrete constitutive law, applied at the interface.

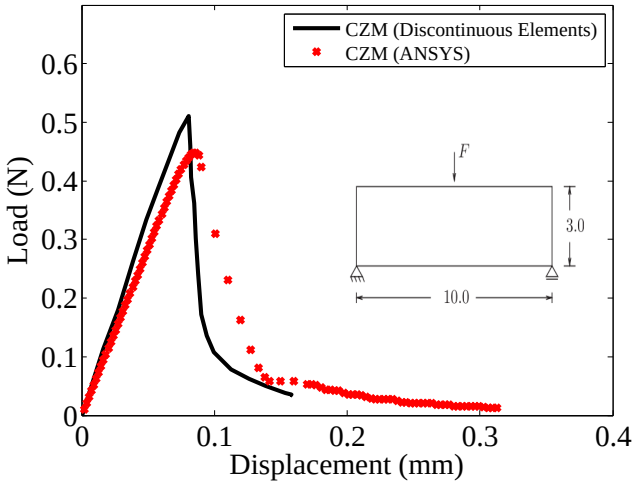

Figure 6.8: Verification of the CZM model used in this dissertation

6.3.3 Verification Model 3- Wellbore break down

The third example we use here to verify the failure mechanism of the CZM model is the wellbore stability problem. From linear elastic analysis, the break down pressure as a function of the wellbore pressure p_w, maximum horizontal stress S_{Hmax}, and minimum horizontal stress S_{hmin} can be calculated

using Equation (6.4);

$$P_b = 3S_{Hmax} - S_{hmin} - p_w \tag{6.4}$$

P_b and p_w in Equation (6.4) are the break down pressure and the drilling fluid pressure which are shown in Figure 6.10. Break down pressure is minimum hoop stress at the wellbore wall. When break down pressure exceeds the tensile strength of rock, tensile failure occurs. In this section we wish to use the CZM capability of our finite element tool to test the applicability of this model for obtaining the value of break down pressure which is a tensile mode failure in the wellbore wall. We show that our model is capable of showing the value of break down pressure in addition to providing the extent of fracture propagation; a value that can not be obtained using classic finite element models.

Figure 6.9 (left) shows the geometry and Figure 6.9 (right) shows the mesh and fragments of rock used in our input file. Contact elements are placed at the interface of each two fragments, then each fragment is filled with nine elements. A zone of 10 feet around the wellbore is assigned fragments and contact elements.

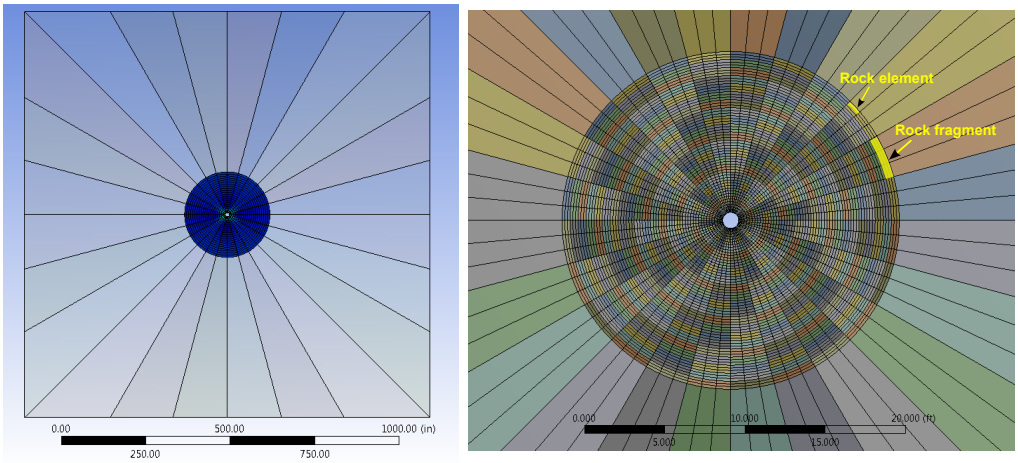

Figure 6.9: Geometry (left) and the mesh elements and fragments of rock (right)

The wellbore pressure of 10,000 psi is applied and the in-situ stresses of $S_{Hmax} = 3,000$ psi and $S_{hmin} = 1,000$ psi are used. Figure 6.10 shows the break down and breakout pressure in the near wellbore zone in terms of in situ stresses and wellbore pressure.

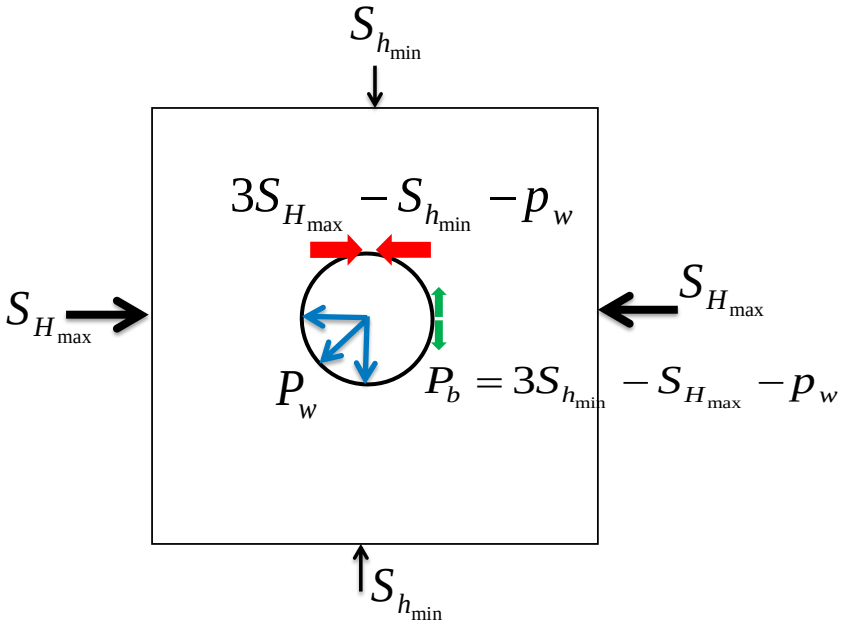

Figure 6.10: Break down and breakout pressures in terms of the in-situ stress and wellbore pressure

The analytical break down pressure can be calculated using Equation (6.4) and is equal to 10,000 (psi);

$$\mathrm{P_b} = 3 \times 1,000 - 3,000 - 10,000 = -10,000 \text{ (psi)}, \text{and tensile}$$

In Figure 6.11, the numerical value of the break down pressure is obtained as 9,974 (psi), which is in good agreement with the analytical value. It should be noted that, the finite element simulation using CZM, can reveal the zones in which smaller cracks are developed. These zones are indicated as tension cracks zones in Figure 6.11. More over, the CZM model can predict the extent

of the fracture propagation which is not possible in classic finite element. As a result, we use the CZM feature implemented in the finite element package ANSYS for thermal fracturing purposes to obtain the extent and the pattern of thermal fractures.

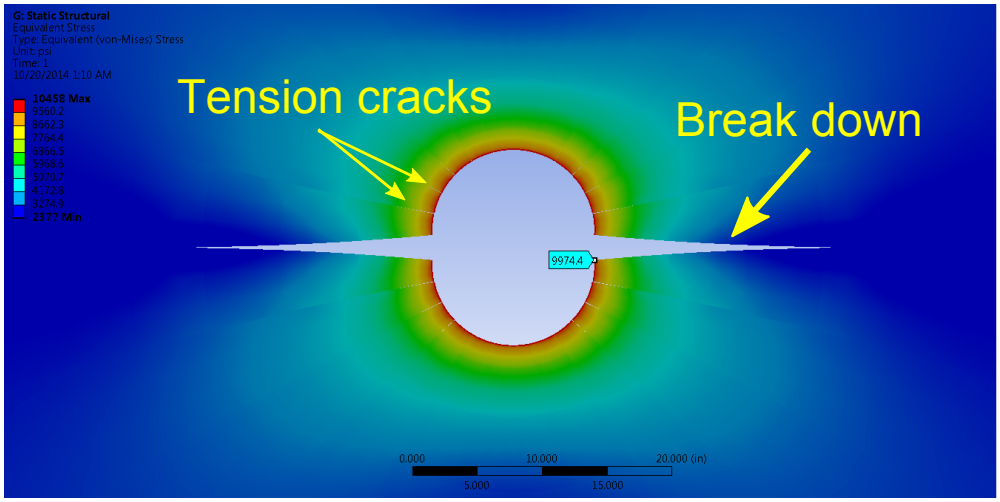

Figure 6.11: Verification of the wellbore break down pressure using CZM model.

6.4 CZM Simulation Results

Here we present the results of thermal fracture analysis using CZM/-DEM. We are interested in studying the effect of in-situ stress in creation and propagation of thermal fractures; therefore, we perform fracturing analysis for three cases of different in-situ stresses. The values of maximum and minimum horizontal stress for these three cases are shown in Figure 6.12(a_1, a_2, and a_3). Stress anisotropy or stress ratio of 3 is used for all three cases. Geometry of the

model is shown in Figure 6.9, wellbore radius is taken as 6 in and reservoir size is 30mx30m. Our studies in Chapter 4 showed that the zone of heat transfer around wellbore was 3-10 ft; therefore, we limit our mesh refinement to a 10 feet zone around wellbore. This saves a lot of computational efforts in this coupled thermo-mechanical (TM) problem which is also nonlinear due to the presence of contact elements at the interface of rock fragments. The analysis type is a 2D plane strain. Reservoir rock is subjected to two different loadings, thermal and mechanical. Thermal loading is the cooling process which takes place at the wellbore. Initially everywhere in the domain is at 100°C temperature and the wellbore temperature is then set to 0°C. Heat transfer is performed and the solution of temperature distribution field is mapped to the structural mesh. In structural problem we apply the mechanical load which is the in-situ stress. This problem is solved for a cased wellbore where we have steel casing in the wellbore; therefore, deformations at the wellbore is negligible.

Material parameters used for these three cases are as follows; Young's modulus $E = 100GPa$, Poisson's ratio $\nu = 0.25$, tensile strength $f_t = 100$ psi or 0.7 MPa, and fracture energy $G_f = 0.01\ N/mm$ which is equal to 100 J/m^2. We use a random function to generate random material properties for fracture energy of rock fragments. Fracture energy of shale is in the range of 50-100 J/m^2; therefore we generate values in this range for all elements of the finite element model.

We are interested in the pattern of thermal fracture in these analyses.

The pattern of fracture for the three cases are shown in Figure 6.12 (c_1, c_2, and c_3) and the total deformation of rock for the three cases are shown in Figure 6.12 (b_1, b_2, and b_3). In Chapter 5 we observed that in spite of the nature of DEM which is capable of providing opening in domain of problem when subjected to thermal load, obtaining the pattern of fracture was not readily available for two reasons. These are 1) long computation time for large scale problems and 2) heat transfer or other physics can not be defined at particle level and the only way to introduce heat transfer is through a force displacement between particles. The disadvantage of this method of introducing heat transfer is that it does not take the energy balance into consideration in defining a governing equation for heat transfer between particles.

In Figure 6.12, as we go from case 1 to 2 and 3, The pattern of fracture becomes more ramified. This is because the in-situ stress decreases from case 1 to 3 and it is easier for rock to fracture when compressive stress is smaller (case c_3). Also the effect of stress anisotropy can be observed in Figure 6.12. Thermal fractures show an up-down trend depicted by blue in the Figure 6.12 (c_1, c_2, and c_3). The value of opening varies along the gaps shown in Figure 6.12 and the maximum values of gaps in our analyses are 0.0001 mm, 0.02 mm, and 0.1 mm respectively for cases (c_1, c_2, and c_3).

Obtaining enhanced permeability due to thermal fracturing has not been the topic of this dissertation. One of the future directions of this work is to obtain the effect of permeability changes as thermal shocks create pathways in rocks. Even a small gap in tight formations has a significant impact of con-

ductivity of such formation to gas flow. The values of gaps we obtained from CZM simulation indicate that thermal fracturing has the potential to improve the recovery in tight formations. It should be noted that thermal fractures propagate a short distance from the source of cooling, but as soon as initial fractures open, fluid penetrates into these opening and further propagation continues. All of these investigations are the future directions of this work.

6.5 Conclusions

- Application of the CZM in classic finite element method is investigated in this chapter. Our simulation results show that thermal fracturing can be simulated using embedded multiple-site CZM. The efficacy of thermal fracturing in opening seeds of fracture in rock, is a function of temperature reduction in reservoir and the in-situ stresses which are related to the depth of reservoir pay zone in which rock fracturing and matrix stimulation is carried out.

- The fast computation time for such analyses compared to molecular dynamics analysis in LAMMPS is one of the key factors to utilize CZM/-DEM method in this research, (the discussion on simulation times are presented in Section 7.6.1). Besides, the material nonlinearity and constitutive law for rock is another decision parameter which makes CZM/-DEM a favorable method for rock fracture analysis.

- Another advantage of using CZM is that the two modes of failure; tensile

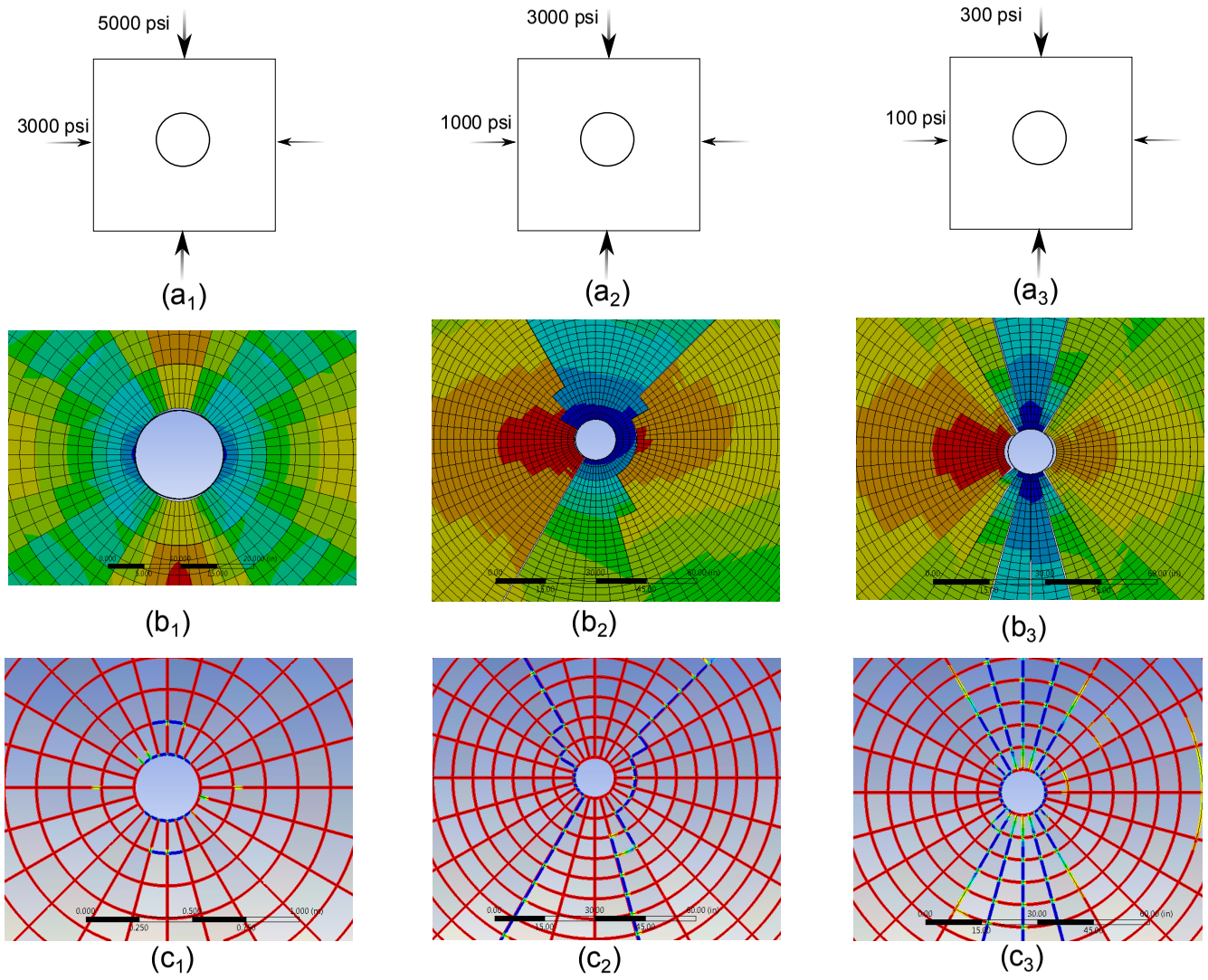

Figure 6.12: Pattern of thermal fracture for three cases of high (a_1), medium(a_2), and low (a_3) in-situ stress.

and shear can be taken into account in analysis, using two independent traction-separation properties associated with these two modes. Using this feature, we can investigate whether the mode of failure is tensile-dominant or shear-dominant.

Chapter 7

Comparison of Numerical Methods for Rock Fracturing

7.1 Introduction

Rapid depletion of hydrocarbons in conventional reservoirs and the availability of abundant oil and gas resources in unconventional forms demand new technology to economically produce these energy resources. From exploration to consumption of hydrocarbons, a great number of complex physical, chemical, mechanical, electrical, and thermal phenomena occurs in reservoir from the rock to surface facilities. In addition to good rock samples and cores which could represent the reservoir rock for laboratory experiments, numerical tools should always be used to provide predictive capability of reservoir rock and fluid behavior. A great number of numerical methods have been developed and used over the past decades for rock mechanics problems. In this research the main focus is on thermal fracturing, heat transfer in rock, flow in porous media and stress-deformation analysis. Numerical methods solve the governing equations at discrete nodal points rather than in the entire domain of the problem. Based on the discretization method used in a numerical tool and the formulation of the method, numerical tools can handle certain problems more appropriately than others. For example, for certain loads such as

dynamic load, an explicit scheme would yield better results. For very high resolution numerical method, i.e., high level of domain discretization or to capture phenomenon that occurs in a fraction of second, massive calculations are required. This was not possible until recently. With the advent of high performance computational resources (HPC), a significant progress in numerical simulation of geomechanics has been achieved. HPC has advanced other branches of science such as engineering mechanics and materials science. This chapter reviews numerical tools available to rock mechanics studies in the oil and gas industry. Besides, this chapter lists the basics, assumptions and limitations of these methods. We compare a list of numerical tools available for rock fracturing and discuss the limitations of each tool and finally the best tool in terms of our application of fracturing tight formations, is recommended based on the results from the literature and the ones investigated in this dissertation.

This dissertation covers two areas. These are 1) volumetric rock stimulation in Chapter 2 and 2) fracture mechanics and numerical simulations in Chapters 3, 4, 5, and 6. The literature review for the first study is done in Chapter 2 and for the second study is performed in this chapter.

7.2 Why Is It Important?

Over the past decades, numerical tools have been used extensively to provide solution to geomechanics and rock mechanics problems. Poro-elastic analysis started with the problem of consolidation by Terzaghi [239] and later was solved in many research wroks including [66, 89, 101, 164, 210, 214, 261].

The concept of consolidation and compaction of rock was then used for surface subsidence in the oil and gas industry [40, 66, 86, 89]. Numerical tools have also been used for rock fracturing [62, 80, 105, 184, 234], thermal fracturing of rock [74, 76], dynamic fracture mechanics [49], high strain testing [36, 116, 262], discrete element analysis of rock failure [75], rock damage analysis using finite elements [73], combined FEM/DEM analysis [79, 161, 175], wave propagation in rock [50, 145], Acoustic emission in rock masses [106] , and heat transfer and flow in shale [76]. These methods will be classified and explained in the next sections based on their approach, assumptions, and capabilities of solving rock fracturing problems.

7.3 Continuum Methods

Continuum mechanics studies the physics of continuous materials. Continuum methods of solving the partial differential equation (PDE) of the governing physics of problems are used to solve a wide class of problems in solid mechanics and fluid mechanics. In these problems, the material domain is a continuum in time and space. Continuum methods of solving the PDE of a problem uses a linear or higher order approximation of the time or space derivatives of state variables in the entire domain and solve a system of linear algebraic equations instead of a system of differential equations. The continuum methods encompass finite difference method, boundary element method, finite element method, spectral element method, and finite volume method. There are many text books available for in depth description of these methods.

Here we explain them briefly to set the scene for comparison of these methods based on the available literature and the results obtained in this research.

7.3.1 Finite Difference Method

Solving problems of mathematical physics using finite difference method (FDM) dates back to the fundamental theoretical paper by Courant *et al.* [59] in which an approximate solution by means of the five-spot approximation of Laplace's equation was introduced. Error bounds for finite difference approximations was first derived by Gerschgorin [90]. Approximation of derivatives in FDM is simple and does not require interpolation functions. This makes FDM an easy method to apply to two and three dimensional problems; however, for problems with a complex boundary, heterogeneous material properties and complex geometry, such as fracture mechanics problems, conventional FDM is incapable of providing a solution. To get around the regular mesh in conventional FDM, other methods such as finite volume method (FVM) have been developed which will be explained in the next section. In rock mechanics finite difference is used where the domain of the problem has a simple geometry, for example in imaging electromagnetic data for cross-hole measurements [78, 113, 251] or to determine hydraulic conductivity of rock [147]. A Generalized Finite Difference Method (GFDM) which is a meshless method is derived from the conventional FDM to overcome the discretization problem for complex domain geometries [153, 154]. Despite many inherent constraints with FDM, it has been widely used in solving engineering problems. Many

methods such as discrete element method and molecular dynamics are developed based on the main concept of the FDM. FDM in Chapter 2 of this research is used to solve the rock damage partial differential equation.

7.3.2 Finite Volume Method

Finite volume method (FVM) is another way of converting the governing partial differential equation to algebraic equations, and it can be regarded as an extension to FDM [148, 241]. Unlike conventional FDM, the FVM uses an unstructured mesh. FDM is based on a discretization of the *differential* form of the conservation equation, but FVM is based on a discretization of the *integral* form of the conservation equation. Volume integrals in this method, which contain divergence terms are converted to surface integrals using the divergence theorem. In FVM, 1) the domain is discretized as control volumes (CVs) and 2) the integral forms of the conservation equations are discretized on the CVs. The CVs should not overlap so that it guarantees that the discretization is conservative locally and globally; in other words, mass, momentum and energy are locally conserved in a discrete sense over each CV. When the discrete equations are summed over all CVs, the global conservation equation is retrieved. Finally, 3) the resultant discrete integral equations are solved. FVM in this research is not used; however for the sake of providing a list of numerical methods that could be used in rock fracturing simulations, the FVM is included in this section.

7.3.3 Boundary Element Method

Boundary Element Method (BEM) is another numerical method of solving the *linear* conservation equation or the PDE of the governing physics of a problem. The full emergence of the numerical technique known as the boundary element method occurred in the late 1970s [51]. This method has gained popularity over the recent decades. In this method the PDE is formulated as integral equation over the domain of the problem. This is called the boundary integral form which serves as the equation to obtain a weak solution at global level. BEM can be applied in many areas of engineering including fluid mechanics and fracture mechanics. BEM formulation is well suited for analysis of cracks in solids [5]. Some of the advantages of the BEM are: 1) The boundary is discretized instead of the entire domain, so for a 2D problem, discretization is performed along 1D segments and for a volumetric domain, the discretization is performed over 2D surfaces. This reduced dimensionality results in smaller linear systems, less computer memory requirements, and more efficient computations. This effect is most pronounced when the domain is unbounded [51]. 2) Simple and accurate modeling of problems involving infinite and semi-infinite domains. 3) Simplified treatment of symmetrical problems (no discretization needed in the plane of symmetry). Some of the disadvantages of the BEM are: 1) Unlike finite element method, the discretization matrix is non-symmetric and fully populated. 2) It is not applicapable for non-linear and inhomogeneous problems [98, 186, 211, 244, 255]. 3) Practical application is very limited, recent, and not so well known as FEM among

researchers.

BEM development tries to overcome some of the limitations of the conventional BEM. Some recent advances are: The Boundary Contour Method (BCM) [178] which aims at further reducing the computational model dimensions; Galerkin Boundary Element Method (GBEM) [32, 163] which tries to solve non-linear problems by introducing the variational formulation of the BEM; mesh-free BEM [156, 181] is developed to overcome the current drawbacks of BEM when creating boundary elements.

In conclusion, even though BEM seems to be advancing rapidly, it is not yet fully capable of dealing with heterogeneity, material non-linearity, and damage evolution during loading. These shortcomings of the BEM, FVM, and FDM make many researchers use finite element tools as the numerical tool of choice to solve engineering problems.

7.3.4 Finite Element Method

Finite Element Method (FEM) is another technique for finding approximate solution to boundary value problems. It uses variational methods to minimize an error function and produce a stable solution. The first attempts to use finite element analysis were for solving complex elasticity problems in civil and aeronautical engineering. The development of the FEM dates back to 1941 and the works of A. Hrennikoff [115] and R. Courant [58]. The real impetus for the FEM was the developments of J. H. Argyris with co-workers at the University of Stuttgart in 1960s. In 1970s, R. W. Clough [55] with co-

workers at UC Berkeley made the finite element program SAP IV [82] widely available. Later, a rigorous mathematical basis to the finite element method was published in 1970 by G. Strang and Fix [224]. Nowadays, FE has become the most widely used computational tool in engineering and scientific research including rock engineering, geomechanics, and the oil and gas industry problems [122]. The FEM offers great flexibility in dealing with non-linearities (material, contact, and geometry), material heterogeneity, complex geometry and boundary conditions. For certain applications in rock mechanics such as jointed rock analysis and interaction between rock fragments, joint elements are developed within FEM [81, 96, 133, 162]. There are several methods based on FEM which are developed to overcome some of the limitations of the conventional FEM. These are mesh-free method, Extended Finite Element Method (XFEM), Spectral Element Method (SEM), etc. Mesh-free methods are developed to overcome re-meshing in the problems of large deformation where the mesh configuration changes drastically from one time step to the next. Mesh-free method is also useful where the material can move around such as problems of computational fluid dynamics. SEM uses a high degree piecewise polynomial basis functions leading to very high order of accuracy. FEM ceases to provide a solution where the mesh configuration changes due to rupture in material such as in fracture mechanics problems.

To deal with fracture problems, conventional FEM uses one of the two approaches: 1) damage and degradation of material properties; 2) cohesive zone modeling (CZM). In material degradation approach, the stiffness of ma-

terial is reduced to a small value as damage level and material softening increases. Some FE codes, have a feature to remove properties of the elements which have undergone excessive damage. This feature is not the best solution for material softening issue, as the problem becomes unstable with the release and redistribution of load when a zone of soft material is suddenly introduced within the domain of problem. The theory of degradation of material properties is based on damage evolution in materials which we studied in Chapter 2. The results from our analysis could be used in simulation of material failure in Continuum Damage Mechanics (CDM) approach. CDM has been widely used for fracture studies in brittle materials [34, 39, 140]. The development of the second approach, i.e., cohesive zone modeling, dates back to the works of Hillerborg *et al.* and Belytschko *et al.* in 1976 [24, 110].

In CZM, the rupture zones or the zones in which failure occurs are locally assigned certain contact elements with sliding and separation properties [1, 53, 54]. CZM has a solid physical background and has been extensively used in simulation of brittle rock fracturing, discrete rock fragmentation for mining applications, and fracture propagation in concrete and ceramics [29, 45, 72, 132, 149, 172, 177, 194, 204, 240, 250, 254, 257, 259].

It is known from fracture mechanics that stress at the crack tip has a square root singularity; therefore, any finite element tool for fracturing simulation has to be equipped with a re-meshing algorithm to eliminate stress singularity [250]. One problem with re-meshing is an increase in calculation efforts as a result of the changes in the stiffness matrix size [30, 31, 171, 243].

Besides, the solution of each variable (degree of freedom) should be mapped onto the new mesh which itself requires a complicated algorithm. The continuum nature of the finite element analysis makes the classic FEM an unsuitable tool for simulating fracture propagation [121, 122]. To get over this shortcoming of FEM, recently a couple of methods have been developed for simulation of fracture in a continuum domain. Two of the most famous extensions of the finite element analysis are 1) Extended Finite Element Method (XFEM) and 2) Mesh-free Method which are explained in the next sections to enable the comparison of numerical tools for rock fracture mechanics.

Another shortcoming of FEM is numerical and element locking in the finite element approximation of certain physical problems [6, 52, 232, 233]. Locking is a phenomenon associated with the numerical approximation of certain problems whose mathematical formulations involve a parameter dependence [12]. For example in elasticity, for Poisson's ratio ν close to 0.5 (i.e., nearly incompressible material) the convergence rate for displacement for practical ranges of discretization is low. The solution for locking effect is available in mathematics literature [37]. For example, changing the discretization scheme is one solution to this problem.

Some of the advantages of the FEM are: 1) Complicated geometries and boundaries can be handled with relative ease; while FDM is restricted to rectangular shapes; 2) implementation is very easy, and 3) FEM can be easily used to obtain the forward solution of the inverse problems constrained by PDEs, where the adjoint operator requires discretization and the forward solution. In

general, FEM is the method of choice for solid mechanics, heat transfer, electromagnetism, and other problems, where mesh configuration does not change much. Computational fluid mechanics (CFD) problems are easier to handle by FDM and FVM.

In Chapter 6 we presented the capabilities of the CZM when used in conjunction with the classic FEM. We will show that CZM is the method of choice in the simulation of rock thermal fracturing based on our numerical investigations in this dissertation and other available research works. The theory behind this method is explained in detail in Sections 3.8 and 3.9.

To introduce heterogeneity of reservoir rock we use a normal distribution of material properties for both reservoir rock and contact elements at fracture zones. Similar assignment of heterogeneous properties has been performed for fracture propagation in rock under static and dynamic loads [27, 67, 152, 199, 235, 264].

FEM in this research is used for heat transfer, flow in porous media, rock damage, and stress deformation in Chapter 4. It is also used to obtain the pattern of thermal fractures around a wellbore using cohesive elements in Chapter 6.

7.3.4.1 Extended Finite Element Method

The extended finite element method (XFEM) is a numerical method based on the classic finite element method and the Partition of Unity Method [11] which allows for using a priori knowledge about the final solution into the

approximation space of the numerical solution. It extends the classic finite element method by enriching the solution space using discontinuous functions. The discontinuous Heaviside and asymptotic functions are used in the XFEM formulation to deal with the discontinuity and singularity problems. The idea behind XFEM was introduced in 1999 by Ted Belytschko *et al.* [170] to get over the shortcoming of the classical finite element method in dealing with discontinuous domains. The XFEM has proven to be an efficient numerical tool for simulation of fracture propagation and has been used extensively to model the propagation of discontinuities such as cracks and separation of material interfaces in solids. Compared to the classic FEM, XFEM provides significant benefits in the numerical modeling of crack propagation. The main advantage of using XFEM is that the finite element mesh has to conform to crack boundaries to account for geometric discontinuity; therefore, the original mesh does not require regeneration as the crack propagation goes on. This allows a simulation of fracture propagation with a single mesh which is easily created at the beginning of simulation. This enhancement has successfully been utilized in the simulations of dynamic crack propagation and three-dimensional cracking [8, 10, 189, 198, 205, 228]. XFEM introduces new degrees of freedom (DOF) associated with the nodes of elements intersected by the crack geometry. In the original implementation of XFEM, discontinuous basis functions were added to standard polynomial basis functions for nodes of elements intersected by the crack geometry. These special functions in combination with special functions for discontinuities enabled accurate modeling of cracks. In

classical finite element formulation, a crack must conform to the sides of the finite element mesh; in other words, a crack propagation path is limited to the boundaries of each element. In contrast, in the XFEM, a crack can propagate through an element via a displacement approximation, i.e., a function that is discontinuous across a crack is added to the displacement approximation to model the presence of a crack. This allows for crack growth without re-meshing requirements. The displacement approximation for crack modeling in XFEM formulation takes the form of Equation (7.1) [170]:

$$\mathbf{u}^h(\mathbf{x}) = \sum_{i=1}^{n} N_i(\mathbf{x}) \left[\mathbf{u}_i + \underbrace{H(\mathbf{x})\mathbf{a}_i}_{\text{only Heaviside nodes}} + \underbrace{\sum_{\alpha=1}^{4} F_\alpha(\mathbf{x})\mathbf{b}_{i\alpha}}_{\text{only crack-tip nodes}} \right] \tag{7.1}$$

where n is the number of nodes in the mesh, $N_i(\mathbf{x})$ is the shape function of node i , $\mathbf{u}_i$ are the classical DOFs of node i, and $\mathbf{a}_i$ and $\mathbf{b}_{i\alpha}$ are the DOFs associated with the Heaviside step function $H(x)$ and the crack-tip functions $F_\alpha(\mathbf{x})$, respectively. The discontinuous function $H(x)$ takes on the value +1 above the crack and -1 below the crack. The crack-tip functions $F_\alpha(\mathbf{x})$ provide improved accuracy and are required if the crack-tip terminates inside an element. These functions are:

$$[F_\alpha(r,\theta), \alpha = 1-4] = \left[\sqrt{r}\sin\frac{\theta}{2}, \sqrt{r}\cos\frac{\theta}{2}, \sqrt{r}\sin\frac{\theta}{2}\sin\theta, \sqrt{r}\cos\frac{\theta}{2}\sin\theta \right] \tag{7.2}$$

where r, θ are local polar coordinates defined at the crack tip.

Figure 7.1 shows a part of a mesh and the enriched nodes in the XFEM. The circled nodes are the nodes which are given two additional DOFS (total

4 DOFs per node), whereas the nodes marked with a square are enriched by eight more DOFs (total 10 DOFs per node). To compute the element stiffness matrix, the elements that are intersected by the crack geometry are divided into subelements for numerical integration. Here we briefly described the concept of XFEM formulation to show how this extension to FEM can overcome a discontinuity problem in a domain. XFEM has been successfully used in many areas of rock mechanics including transient problems of rock failure and dynamic fracture analysis [48, 206], and investigation of fracture path through the elements of mesh in a quasi-brittle materials [168, 227]. Recent developments in the XFEM formulation in the past decade include addition of cohesive zone elements [9, 10, 23, 26], explicit formulation [166, 167], taking material anisotropy into fracture simulation [7, 8], and introducing contact surfaces at the fracture walls [136, 207]. The finite element commercial code ABAQUS [109] contains the first implementation of XFEM. Further details on the enriched nodes and the implementation of the XFEM can be found in [170, 226].

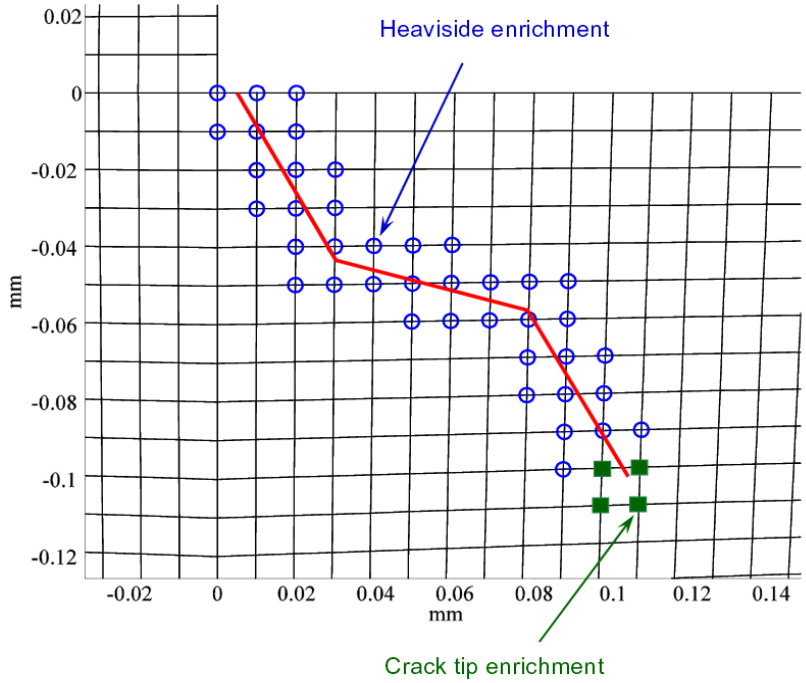

Figure 7.1: Enriched nodes in XFEM. Nodes with two additional DOFs (circles). Nodes with eight additional DOFs (squares), adapted from [94].

In spite of advances in development of the XFEM-based codes in dealing with discontinuities [84], there are still a number of challenging problems. One of the problems is that the global stiffness matrix may become singular, if crack truncates a very small part of the element [192].

The main problem with XFEM formulation is that the propagating fracture is arrested when it gets to existing fractures i.e., the fracture tip stresses are not known at the intersection of the two fractures. The other current shortcoming of XFEM is that once a fracture opens, fluid pressure

should be applied to the new fracture faces. This feature is not included in commercial XFEM-based codes. Only recently it has been incorporated into ABAQUS. The implementation of XFEM to benefit from the mesh independency of this numerical method in available commercial codes is not always straight forward, because additional degrees of freedom are introduced which require careful handling during the formation of the stiffness matrix [223]. Finally, XFEM suffers from ill-conditioned stiffness matrix, when higher order trial functions are used [225]. The problems mentioned here limit our choices in using a well established numerical tool for fracture propagation. There are discrete element based methods which allow for explicitly including fractures without having to regenerate the mesh. These methods will be explained later in this chapter.

7.3.4.2 Meshfree Method

Meshfree methods (MFM) are the numerical methods in which a mesh is not required to connect the data points in the problem domain. In the numerical methods we have reviewed so far including FDM, FEM, and FVM, the domain is discretized by a mesh and a number of nodes with certain coordinates at which the state variables or the degree of freedoms are calculated. Each node is connected to a number of neighboring points and these connections are used to define operators such as gradients of the state variables, which appear in the partial differential equation governing the problem. In large deformation problems, fracture mechanics, and fluid dynamics where the

deformation of material points is large, the connectivity of neighboring points is difficult to maintain without introducing error in solution. If the elements get highly distorted due to large deformation, the differential operators defined on them yield erroneous results. One way to eliminate this problem is to use smaller time steps so that deformation during each time step is small. This results in long calculation times which should be avoided whenever possible. MFM is a useful technic in cases where creation of or dealing with mesh is not easy. For instance, problem of creating a mesh for a complex 3D object, and problems with material nonlinearity or discontinuities such as voids and fractures.

There are various forms of MFM [25, 180] such as: Smooth Particle Hydrodynamics (SPH), the oldest of the meshless methods by Gingold and Monaghan [95] which Monaghan and Randles [173, 201] later provided the notion of kernel approximation for solving a PDE using this method.

7.4 Discontinuous Methods

The problems associated with the discontinuity of the domain during fracture propagation have led to the discrete element-based numerical tool for crack propagation problems [60]. The main idea of the discrete element simulation is that the domain is treated as an assemblage of solid and deformable fragments, which are in contact with each other using the normal and shear stresses at the interface of each two fragments/blocks. If the fragments are mass particles, this discrete method is also called the particle method. DEM

is referred only to the case where the separate masses have actual dimensions so they can be regarded as blocks or fragments. Therefore, the particle method is an special case of DEM. In both cases, the equation of force-displacement is solved, but in DEM in general, the fragments could be considered as deformable objects or domains in which another governing physics could be solved. For example, if heat transport is a physics of interest in a simulation and the available tool is the particle method we used in Chapter 5, the only option is to use thermal properties of the material in the spring or the connecting link between the fragments. In our thermal fracturing problem, we are interested in thermal expansion/contraction of a solid body in 3D for which the 1D spring element is not enough to represent the information contained in a heat transfer PDE, such as the boundary condition, material properties and the heat transport law. All the information that could be given to a spring is that the temperatures at end-nodes be related, and a failure criterion could be assigned to springs which could be something like the spring breaks beyond a certain elongation value.

7.4.1 Discrete Element Method (DEM)

DEM has been extensively used in rock engineering problems such as underground excavation [146, 220, 221, 255], development of the constitutive models for rock fracturing [123, 124, 169], dynamic analysis of rocks [43], and propagation of wave in fractured rocks [50, 145, 256]. Our discussion above was about the domain of the problem to be either discrete or continuous.

Another aspect of a problem is the fact that material properties could be discrete or continuous. For example, in a problem of flow in porous media, the medium may contain discrete fractures or zones of higher permeability. In such problems, in general, the concept of the Effective Medium Theory (EMT) can be used, in which, an effective property is assigned to the entire domain of the problem. This approach is called smeared representation of the medium. Smeared vs discrete representation of a medium is discussed in the following section.

7.4.1.1 Smeared vs. Discrete

To represent the effect of fractures in a medium, there are two general approaches; smeared and discrete representation. In the smeared modeling of fractures in rock, the lumped effect of fractures are taken into account in obtaining the material properties of a fractured medium [203]. This method is similar to material degradation model in which an equivalent continuum zone of lower stiffness replaces the fractured medium. The smeared approach has been widely used in fracture of concrete beams an columns under seismic load, rock under thermo-mechanical loading, and rock failure under high strain and impact loading [2, 4, 237]. Since the smeared approach works with an equivalent domain having the properties of fractures, it avoids re-meshing and adding nodes to the mesh. This speeds up the numerical calculations; however it is not an effective approach when an explicit representation of fractures is required. For instance, fracture propagation can not be studied using the

smeared approach.

7.4.2 Molecular Dynamics

We used LIGGGHTS and LAMMPS as the numerical simulation tools for thermal fracturing in Chapter 5. These are both open source codes distributed by Sandia National Laboratories, a US Department of Energy laboratory, under the terms of the GPL. LAMMPS is a classical molecular dynamics code, and an acronym for Large-scale Atomic/Molecular Massively Parallel Simulator. LAMMPS can be used to simulate solid or soft materials such as rock, metals, or polymers. It can be used to model coarse-grained or mesoscopic systems such as rock or concrete. LAMMPS uses a number of mass particles to represent the solid body and springs to represent the inter-granular and cohesive force between rock fragments. It requires the position and velocity of mass particles as initial condition and at each time step it uses a failure law such as maximum elongation of springs at failure to break the bonds and obtain the new position and velocity of particles. Fluid pressure can be added to classic LAMMPS to incorporate the effect of pore pressure in total stress of rock matrix; however, this has not been the objective of this research and is not carried out in this dissertation.

7.4.2.1 Advantages of DEM

Both LAMMPS and LIGGGHTS run on single processors or in parallel using a spatial-decomposition of the simulation domain. The code is written in

C^{++} and is designed to be extended or modified easily by the user. The input file is easy to create. With a single command the appropriate potential function for the material simulated can be used through the input file. The biggest challenge in using particle methods as DEM is the computation time. Except for very small simulation domains with a few thousand particles, the runs always require a large amount of computational resources. For this research we used the resources available at the Texas Advanced Computing Center (TACC) at the University of Texas at Austin.

7.5 Coupled Continuum-Discontinuum Methods

We would now look into another method which is based on coupling techniques to conclude which numerical technique is the most appropriate for fracturing simulations. The coupling technique, which we discuss here is not based on coupling the physics which are governing the problem, rather it is based on coupling two different form of problem domain. These are continuum domain of rock blocks/fragments as we use in FEM, and the discrete domain by introducing the contact elements at the interface of each two fragments. We wrap up this chapter with a comparison table for numerical techniques we used in this dissertation.

As we discussed in Section 7.3.4 the main challenge in using FEM for fracturing problems is that with fracture creation, the domain of the problem becomes discontinuous and the compatibility of strains which is fundamental to FEM will not be valid anymore. To overcome this problem new methods such

as the eXtended Finite Element Method (XFEM) have been developed. One of the challenges in the XFEM is that the induced fracture can not cross the existing fracture as the existing fracture is intersected. Another big challenge in the formulation of XFEM is the application of fluid pressure to the opening fracture faces. Recent developments of commercial FE packages are filling this gap of the XFEM. Another way to overcome this problem is using the Cohesive Zone Model (CZM) within finite element framework. Using CZM eliminates both problems because CZM is formulated based on separate fragments of solid body, so there is no problem with intersection of fractures; moreover, since the contact zones have the capability of being subjected to external loads, fluid pressure could be applied to the contact zone to mimick action of the fracturing fluid pressure. As a result, our choice of numerical tool here is the commercial software package ANSYS and using the CZM feature within this FE software. With CZM, the user is able to simulate the pore pressure diffusion in material elements in the form of leak-off if need arises, depending on the permeability of the reservoir rock. Our CZM simulations for thermal fracturing show that such simulations could be performed much faster than similar problems solved by the particle methods. The fact that discrete element methods and continuum methods are both inappropriate for fracturing simulations is also observed in other publications [79].

In the literature, there are many examples of coupling techniques, such as coupling DEM and BEM [157], an approach to coupled DEM, DFN, and BEM [245], and many independent DEM and FEM coupling methods [44,

50, 79, 176, 187]. We will now compare the methods that we have used to investigate, which one of the numerical tools and methods is the best candidate for thermal rock fracturing.

7.6 Discussion and Conclusion

Here we compare the numerical tools which were used in this dissertation for the problem of rock fracture. It can be seen that there is not a single tool, which could take care of all the simulation needs, such as computation time, material behavior, mesh changes due to fracturing, the coupled nature of problem, etc. As a result, it is not quite possible to introduce a flawless software package or method for fracturing analysis in a coupled physics framework. The knowledge gained in this PhD work in terms of comparing the capabilities of numerical tools for rock fracturing purposes is summarized in Table 7.1. Any discontinuities formed during simulation would make the classic finite elements (listed as FE in Table 7.1), an inappropriate tool for our goal. To solve this issue, the recent improvement of FEM such as XFEM is presented. XFEM however, is not a useful method for rock fragment analysis and propagation of fractures when fractures intersect. As a result we resorted to discrete methods in which separate particles of rock blocks interact and transfer loads. Molecular dynamics (MD) was the first choice for us and we used LAMMPS to obtain fracture opening. The atomic scale of the code makes it suitable for problems in the size range of atoms. For laboratory scale rock analysis, we used an extension of LAMMPS, called LIGGGHTS, which makes use of the

same concept for simulation, but works at a larger scale and is suitable for granular materials. We obtained the width of fracture as a result of thermal shock in hot reservoir rock. We noticed different values of width opening for two different in-situ stresses. The main issue with MD that we observed was a long computation time which we solved by using multi-processing resources at the Texas Advanced Computing Center (TACC) at the University of Texas at Austin. Another shortcoming with the discrete element method is that the coupled analysis is not possible as this method focuses on solving the contact loads at the interface of solid fragments. The final choice in our simulation suite was the combined FEM/DEM, which takes advantage of capabilities of both tools and shows promising results for rock fracturing simulations.

7.6.1 Computation Time for FEM, DEM, and CZM Simulations

Here we compare the computation times required to solve the heat transport and thermal fracturing in rock using the three methods; 1) the finite elements, 2) the discrete elements, and 3) the cohesive zone methods. It should be noted that some of the features present in one method may not be present in other methods, for instance, the FEM simulation does not look into the fracture propagation, whereas, the DEM and CZM focus on propagation of fracture. As a result, our comparison only serves to exhibit the order of magnitude difference in computation times required for the types of simulations that one would perform to study heat transport in rock and resulting impact of thermal gradient in fracture creation and propagation.

7.6.1.1 Finite Element Method Simulation Time

We first showed the small rate of pore pressure diffusion in shale in a 200×200 feet reservoir. Our objective was to show the small rate of pore pressure build up and its corresponding impact on effective stress reduction in Figure 4.2. The simulation time for this flow problem was 2 minutes. Then we solved the same problem for a coupled heat transport, stress, and flow scenario. This simulation took 10 minutes and the results of temperature and stress distributions were shown in Figure 4.3. Other simulation times using finite elements method including the two coupled problems shown in Figures 4.12 and 4.22 in our research work, were all short and in the order of minutes; however the reason we had to look into other simulation technics such as molecular dynamics and discrete element methods, was that FEM was not the best simulation tool for fracture propagation in rock due to the difficulties associated with the mesh adjustment once fracture is created.

7.6.1.2 Discrete Element Method Simulation Time

The DEM used in this dissertation was intended to propose a method for fracture propagation simulation in rock. We started with simulation of uniaxial compression of a 10cm×10cm×5cm rock sample for which the axial strain is known from solid mechanics. One of the several complexities in DEM simulation is preparation of the numerical model such that it honors the initial condition of reservoir rock. The DEM deals with particles and interaction forces; therefore, if particles get closer and closer at initial stage of simulation,

they tend to apply large repelling loads. This is manifested in the time required to bring the particles to initial condition of in-situ density and porosity. Here we present the simulation times for several cases of a DEM simulation, defined earlier in Section 5.4, for a uniaxial compression test with three particle sizes which were prepared such that the effect of initial porosity in DEM simulation can be studied.

We created a 10cm×10cm×5cm box containing 11,463 spherical rock particles of three sizes r_1 = 1.5mm (4,777 particles), r_2 = 2mm (2,443 particles), and r_3 = 2.5mm (4,246 particles). This provided a porosity of 0.2 for our simulation rock sample. With different number of particles we managed to obtain porosities of ϕ =0.25 and ϕ =0.30 as well. As we tried to create porosities of less than ϕ =0.2, we realized that since particles get too close, they are subjected to a large repulsive force from neighboring particles and the simulation does not converge. The only way to achieve lower porosities, was to use extremely small time steps in the order of 10^{-8} sec. This corresponds to long simulation times shown in Figure 7.3. Figure 7.2 shows (a) the initial and (b) final stages of the particle positions in the axial compression test. V_z is the velocity of particles in Z direction in 0.01(mm/s). The deformation shown in Figure 7.2 is scaled for visibility and the maximum displacement for the top particles is 0.007 cm.

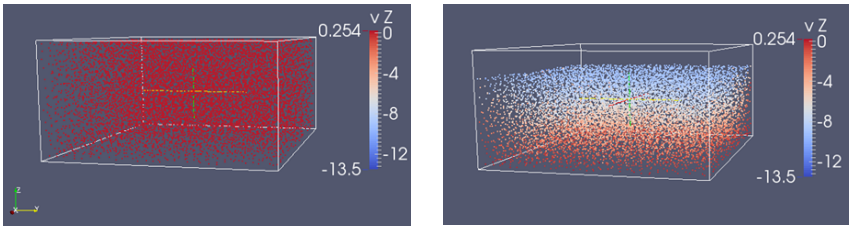

Figure 7.2: (a) The initial and (b) final stages of the particle positions in the axial compression test using DEM

Figure 7.3 shows the simulation time for uniaxial compression test for different porosities at three CPU utilization levels. It can be observed that the simulation time decreases nonlinearly with the number of CPUs used. For porosities of ϕ =0.2 and less, we performed simulations using 16 and 64 processors and we extrapolated the results based on the patterns we obtained for the two high porosity cases of ϕ =0.25 and 0.3. As the porosity falls below 0.2, the DEM simulation times for the case of one CPU used, increases so rapidly that obtaining lower porosities in DEM becomes impossible. Forcing DEM to achieve lower porosities, was not part of this research; however, it could be achieved if non-spherical particles were used. Using non-spherical particles makes higher compaction possible and results in lower porosities. To obtain the fracture propagation in reservoir rock, we have to impose thermal gradient once the in-situ conditions of porosity and initial stresses are achieved. The stage of applying thermal gradient itself requires some simulation time which adds to the time that DEM spends to prepare a %20 porosity sample. In the next section we show the time required for CZM simulations and we

finally present the comparison results in Table 7.1.

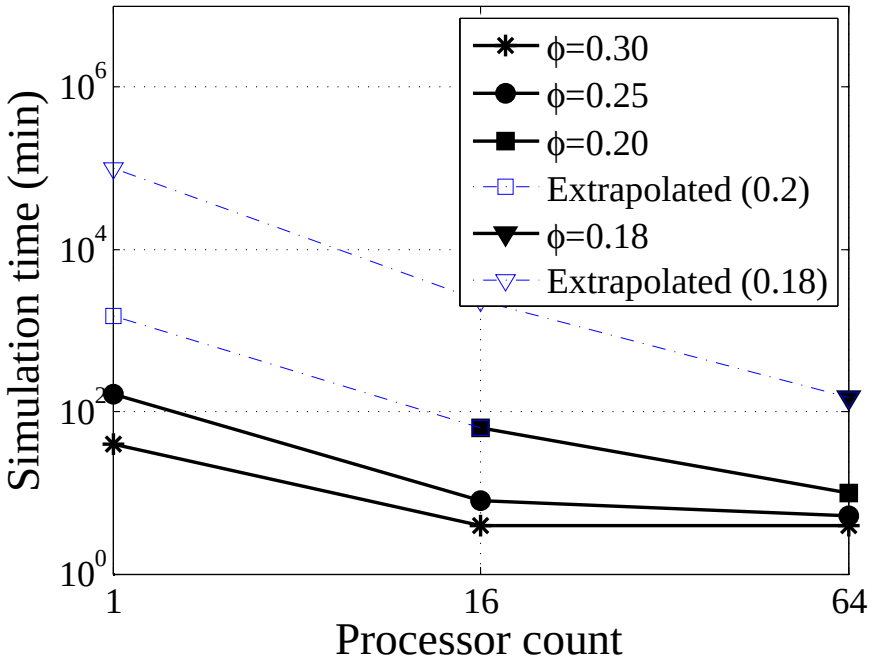

Figure 7.3: The simulation time for uniaxial compression test for different initial porosities at three CPU usage levels

7.6.1.3 Cohesive Zone Method Simulation Time

The third numerical method we used in this dissertation was Cohesive Zone Method (CZM) in the context of the Finite Element Method. This method is based on continuous medium and the initial state of rock is defined using linear elastic material properties. Density and elastic rock properties help eliminate the time required for bringing the rock into initial state as we went did, in DEM simulation. Our simulation using CZM includes a

100ft×100ft reservoir geometry as shown in Figure 7.4, which compared to the limited sample size in DEM, is larger. The simulation time using CZM for reservoir application is a function of element size and the magnitude of in-situ stresses. We used a reasonable mesh size to capture the creation of fractures as small as 2 inches, in the near wellbore zone. The biggest impact in simulation time comes from the magnitude of in-situ stresses. Here, Similarly to DEM in which particles get into contact and compression, the rock fragments are exposed to in-situ reservoir stresses; hence bringing the contacts to reservoir stress conditions, require small load steps until convergence is reached. Despite this necessity for convergence of problem during application of in-situ stresses while contact surfaces are embedded, the CZM method is considerably faster than DEM. This thermo-mechanical (TM) problem is a coupled problem that we perform in two stages. The first stage is applying the thermal load in which we cool down the wellbore by 100°C and obtain the temperature distribution in reservoir. For the fine mesh size that we used in our simulation, the thermal analysis is fast and takes 2 minutes. Then we map the temperature and stresses of the first analysis to a second analysis in which in-situ stresses are applied. The time for the second step is a function of the magnitude of in-situ stresses. For the case of 1000 and 3000 psi stresses, this step takes 10 minutes and if the in-situ stresses are increased further, the simulation time increases to 30 minutes. So the simulation time for fracture propagation studies in this dissertation for the problems presented in Chapter 6 is in the order of 30 minutes using two processors, which is faster then DEM

simulations. Let's now summarize the capabilities of the three numerical tools that we used for thermal analysis of rock fracturing to see which numerical method is the most suitable tool for rock fracturing simulations.

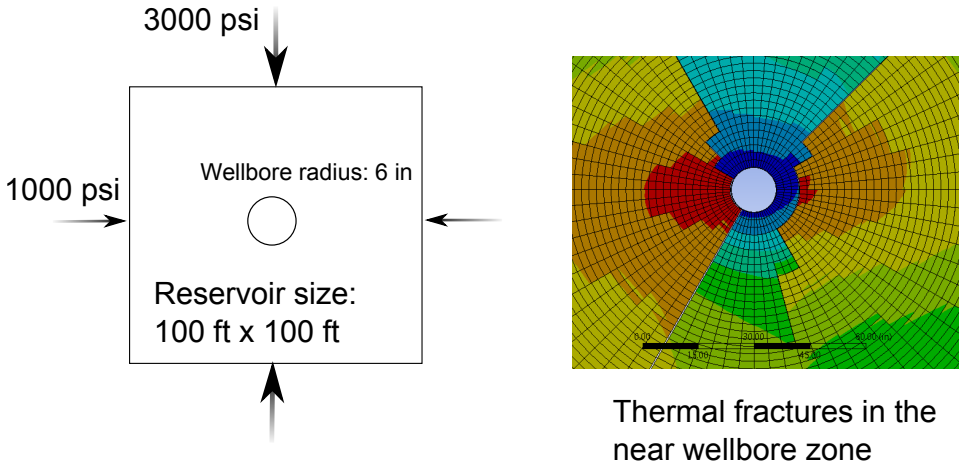

Figure 7.4: The geometry of reservoir rock in thermal fracturing process using CZM simulation

Table 7.1 compares the numerical tools we have used in this dissertation. The objective of this comparison is to find a numerical tool for fracture simulation in presence of multi-physics, such as analysis of a thermo-hydro-mechanical problem in which progressive fracture pattern needs to be studied.

Application	FEM	XFEM	MD	DEM	CZM/DEM	Coupled FEM
Static Load	✔	✔	✕	✔	✔	✔
Dynamic Load	✔	✔	✔	✔	✔	✔
Heat Transfer	✔	✔	✔	✔	✔	✔
Flow in Porous media	✔	✔	❑	✔	✔	✔
Stress Analysis	✔	✔	❑	✔	✔	✔
Atomic Scale Analysis	✕	✕	✔	✕	✕	✕
Fracture (Initiation)	✔	✔	✕	✔	✔	✔
Fracture (Propagation)	✕	❑	✔	✔	✔	✕
Rock Material	✔	✔	❑	✔	✔	✔
Rock Fragment	✕	✕	✔	✔	✔	✕
Coupled Physics	✔	✔	✕	✕	✔	✔
Material Nonlinearity	✔	✔	✕	✕	✔	✔
Computation Time	✔	✔	✕	✕	✔	✔

Table 7.1: Comparison of numerical tools used in this dissertation. Objective is to obtain a pattern of thermal fractures in a multi-physics analysis.

(✕: Not useful and hard to apply; ❑:partially useful at the cost of spending time or improving accuracy; ✔:Useful and easy to apply)

Table 7.1 clearly shows that CZM/DEM possesses all the positive features of other numerical tools; therefore, it is proposed as the most efficient tool for rock fracturing studies.

Chapter 8

Application of Thermal Fracturing in Improved Hydrocarbon Recovery

8.1 Introduction

Production from the low permeability formations relies on connectivity of flow pathways. Therefore any process that increases this connectivity, also enhances productivity. Thermal shock is one such method for increasing connectivity by extending thermal cracks and connecting them to a network of natural fractures. Studying the physics of rock cooling near hydraulic fractures shows that thermal shock initiates thermal cracks, which open against the maximum in-situ horizontal stress. These cracks do not initially extend far from the face of the hydraulic fractures; however, they can be extended as the pressurized fracturing fluid is injected into them. How far these thermal cracks extend, is a function of the strength of rock, flow properties of reservoir rock, and the injection rate.

Based on our numerical modeling of thermal fracturing propagation potential in the near wellbore zone in Section 4.7 and analytical modeling of thermal fracturing in the vicinity of hydraulic fractures in Section 4.4, we are showing two application scenarios to study hydrocarbon recovery improvement

when thermal fracturing is used to facilitate hydraulic fracturing process.

8.2 Two Application Cases

8.2.1 Application I: Near Wellbore Stimulation for a Gas Production Case

Here we solve the gas diffusivity equation (D.14) for the problem shown in Figure 4.25. Table 8.1 lists the properties used for this simulation. The finite element aspects of this problem were already discussed in Section 4.8. Figure 4.26 demonstrates the effect of a near-wellbore, thermally-stimulated zone on cumulative production. It can be seen that production increases by 16% after two years of production. This is a side benefit of thermal stimulation of a low permeability rock. A future direction of this research will be the quantitative study of the reduction of rock tensile strength as reservoir rock is cooled down and a thermal shock is imposed to reservoir rock.

Parameter	Field units
Reservoir properties	
Size	$600\times600\ ft^2$
Fracture half-length, X_f	100 ft
Fracture width, w_f	0.5 in
Boundary pressure, P_e	5000 psi
Well pressure, P_i	2000 psi
Radius of damage zone, r_d	varies between 1 and 4 ft
Wellbore radius, r_w	3 in
Rock properties	
Formation permeability, $k_\mathrm{formation}$	1 μD
Formation porosity, ϕ	0.14
Fracture permeability, k_frac	1,000 μD
Stimulated zone permeability, k_d	10,000 μD
Fluid properties	
Dynamic viscosity, μ	0.02 cp
Compressibility, c_f	10^{-3} psi^{-1}
Density (Ideal Gas), ρ	$10^{-5}\times$ pressure [a]
Density (Real Gas), ρ	$10^{-5}\times$ pressure/Z(p) [b]

[a] Pressure in Pa and the density in $\left(\frac{\mathrm{kg}}{\mathrm{m}^3}\right)$

[b] Equation (D.2)

Table 8.1: Input for numerical analysis

8.2.2 Application II: Thermal Stimulation at Hydraulic Fracture Faces

Here we have simulated gas flow in a fractured horizontal well placed in a low permeability formation. The hydraulic fractures are further stimulated

by thermal shocks induced by the injection of a cold fracturing fluid. Initially many small thermal cracks are created, however only a few of them can grow far away from the hydraulic fracture surface. In our simulations, we have assumed that only one of the thermal cracks extends far enough to tie into natural fractures. In the absence of an analytical solution for flow through the complicated geometry of fractures, numerical simulation is used to obtain cumulative recovery.

We assume a single phase gas flow in a 1 μd permeability formation. The boundary and well pressure are 3500 psi and 500 psi respectively, and production simulation is performed for 30 years. Figure 8.1(a and b) are the plan views of the pressure distribution after 5 years for the case of no thermal cracks and the case of thermal cracks growing from hydraulic fractures. The pressures are in psi and the dimensions of reservoir and fractures are in meters. The white arrows depict the Darcy's velocity vectors.

It can be observed that in case (b) in Figure 8.1, only one of the cracks has extended to intersect natural fractures. In reality, due to the presence of a network of natural fractures, more than one crack has the potential to grow and connect to existing fractures. In Figure 8.1(c), we have shown recovery improvement only one thermal fracture has the opportunity to grow. In reality, however, the growth of multiple thermal cracks improves the productivity even further than that shown in Figure 8.1(c).

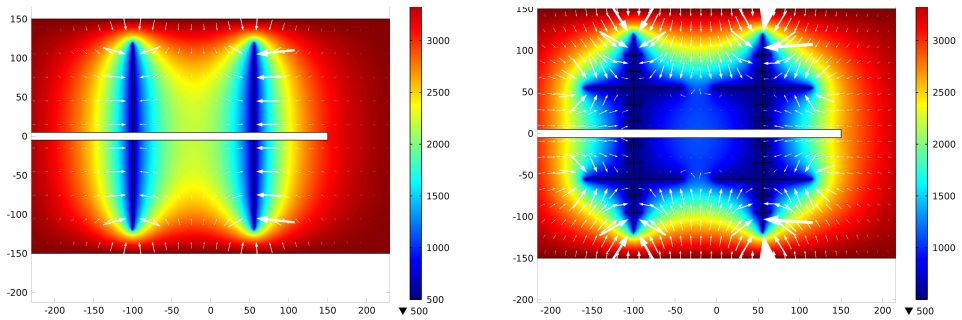

(a) Pressure distribution for stimulation with hydraulic fractures ($t = 5$ years)

(b) Pressure distribution for stimulation with hydraulic and thermal fractures ($t = 5$ years)

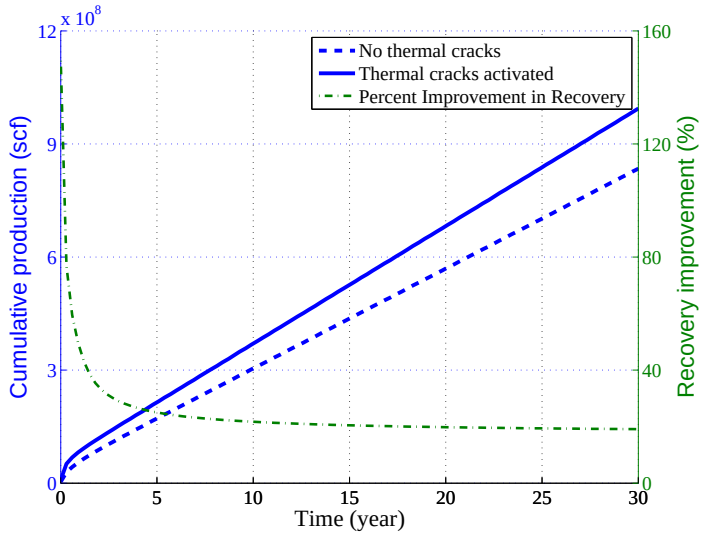

(c) Recovery improvement due to thermal cracks

Figure 8.1: Pressure distribution and recovery improvement as a result of thermal cracks

8.3 Conclusions

- Fluid production from the low permeability formations depends on the connectivity of natural and induced fractures. We have shown that a thermal shock during hydraulic fracturing can create small cracks. Depending on reservoir rock's properties, these thermal cracks can extend further to intersect natural fractures. At appropriate injection rate, thermal fractures have the potential to extend further and tie into the in-situ fractures.

- For the case of gas production presented in this work, in the first 5 years, production enhancement due to thermal cracks declines from 150% to 20% and remains at 20% thereafter, Figure 8.1(c).

- Stiffer rocks, i.e., rocks with larger moduli of elasticity, are easier to fracture by cooling down the rock. This can be observed from Equation (4.9).

Chapter 9

Conclusions

With rapid depletion of conventional hydrocarbon resources, novel methods of fracturing tight formations are becoming the key for accessing these formations in the United States and worldwide. Hydraulic fracturing is currently the standard industry approach to expanding hydrocarbon resource base around the world. We started with a micro-level study of rock stimulation and then used three numerical methods to investigate the physics of thermal rock fracturing. Our numerical simulations exhibited the efficiency and limitations of the proposed method which we explain here.

- We implemented a simple, yet effective micro-scale rock stimulation model proposed by Barenblatt and Prostokishin [21] to study the key parameters in damage evolution in rock. We observed two regimes of damage evolution which are functions of the material dependent damage diffusion parameter. We also observed that the size of voids or pore spaces has a substantial impact on the induced rate of damage evolution. This is attributed to the fact that pore space distribution in rock matrix contributes to the stress concentration at the crack tips. The more concentrated the pattern of local stress at the crack tips, the easier it is

for the rock to fracture. We also discussed the blow-up parameter and instability of solution at the onset of blow-up. At the blow-up time, the partial differential equation of rock stimulation ceases to exist and the blow-up time corresponds to the failure moment. The onset of failure is the last point on the traction-separation plot that we studied in Chapter 3. One of the outcomes of the micro-level studies of rock fracture is the ability to study the evolution or progress of matrix stimulation due to mechanical loads. Thermal loads and fluid pressure both tend to reduce the effective stress between rock grains and promote fracturing. One of the most important parameters which relates the strength of rock to how fast stimulation occurs in rock is damage diffusion parameter which is defined by a weight function as proposed by Barenblatt. We have shown that this weight function can be obtained using a Gaussian distribution.

- The results of finite element analysis Chapter 2 indicate that within the rock matrix, stress at any point is correlated only with the stress at neighboring points located up to three pore diameters. Since we are looking into the effect of fracture size, the dimension used for correlation has to be the opening or the void size. Therefore, the damage diffusion coefficient depends on rock matrix connectivity. Loading, however, does not play a role in the form of the weight function.

- We investigated heat transport in shale and used the FEM to estimate the extent of a cooling-down zone around a horizontal wellbore. The simulation results show an improvement of the calculated total production

as a result of thermal stimulation around the wellbore. It was shown in Figure 4.26 that creation of hydraulic fractures increases the productivity significantly. Volumetric rock stimulation around the wellbore within a 4 feet radius improves the recovery by an additional 16%.

- We investigated a particle method, based on LIGGGHTS and we concluded that the time-step required for DEM simulations depends on rock stiffness and the in-situ stresses. The values presented in Table 5.1 indicate that to increase the stiffness by two orders of magnitude, the time step size must decrease by one order of magnitude. We also showed that thermal fracturing enhances rock permeability through reduction of effective stress and lowering the tensile strength of rock. It is, however, efficient only at small in-situ stresses. In other words, the shallower the reservoir, the more efficient the process of thermal fracturing.

- We finally studied and proposed a CZM-based finite element method. This method possesses the advantages of the finite element method and utilizes the cohesive zone model approach to solve the thermal fracturing problem in a continuous simulation domain. This allows us to exploit all the benefits of discrete simulation while solving the problem using the classic finite element simulation.

9.1 The Challenges of the Proposed Method

The main challenge in application of the proposed method is cement de-bonding during injection of cold fluid. One solution proposed to tackle this operational challenge is to inject chemicals that strengthen the rock and prevent cement de-bonding prior to injection of cold fluid, similar to rock chemical strengthening used to diminish sand production in unconsolidated hydrocarbon bearing zones during production.

9.2 Future Directions

- Investigate the impact of thermal shock on rock toughness and ease of hydraulic fracture initiation.
- Obtain the enhanced permeability for a certain pattern of fracture
- The effect of fluid pressure combined with thermal effects has the potential to improve further the process of thermal shock. This requires numerical and analytical poro-elastic studies that allow a coupled thermo-mechanical analysis, a discrete domain such as the cohesive zone model used in Chapter 6, and the possibility of applying fluid pressure on the elements which are created during the fracturing process.
- Obtain the damage diffusion parameter as a function of pore size distribution.

Appendix/Appendices

Appendices

Appendix A

Governing equation of damage in rock: Basic model

The partial differential equation of rock damage diffusion has been introduced in [21]. Here the derivation is performed in detail so that the assumptions and all the steps taken to clarify the concept of damage in materials are clearly presented.

A.1 Problem Statement

Obtain the mathematical description of damage propagation in an inhomogeneous material taking into account the microstructural effects of matrix structure of rock. (See Section 2.3.1)

A.2 Assumptions

The governing equation of damage can be solved in general 3D case; however we limit our studies to a one dimensional solid object under tensile load. Once we understand the physics of the rock damage, we will be ready to investigate the solution in 2D and 3D cases. So our assumptions are now:

- 1D prismatic bar under static tension, shown in Figure 2.1, and the bar

is oriented along the x-axis, its length is L and its cross sectional area is S.

- isothermal condition
- microscopic damage distribution and microstress fields are stochastic. Damage is considered to be statistically homogenous over the cross section; however, it can change along the bar and with time, i.e. $\omega = \omega(x, t)$

Step 1: Damage accumulation rate under ideal homogeneous condition is assumed as Equation (A.1).

$$\frac{\mathrm{d}\omega}{\mathrm{d}t} = \tau^{-1} q(\omega, \sigma, T) \tag{A.1}$$

Here τ is the characteristic time and q is the damage accumulation term which is a dimensionless non-negative number specified for a given material. Several kinetic laws have been used such as Arrhenius-type kinetic law [87, 107, 141] with the stress-dependent activation energy. Equation (2.6) is the kinetic law which is used by Barenblatt [21] and we are using in our derivation of damage equation here.

Step 2: Let's average Equation (A.1) over the cross section. We know that, damage is a function of cross sectional area S, x, and t; however, it is statistically varying over the cross section. We average $\omega(S, x, t)$ across the cross section S, so we get, $\omega = \omega(x, t)$.

$$\frac{\mathrm{d}(\omega\,(x,t))}{\mathrm{d}t} = \tau^{-1}\frac{\int_s q\,(\omega(x,t),\sigma(x,t),T)\,dS}{S} \tag{A.2}$$

Step 3: The right hand side of Equation (A.2) cannot be replaced by damage accumulation rate corresponding to the average stress because of the existence of a microstress field at point with coordinate x. To obtain the right hand side, a weight function $\rho(x-\xi)$ is used and right hand side is integrated over the length of the bar. The weight function $\rho(x-\xi)$ determines the relative number of elements of a cross sectional area, where the damage accumulation rate corresponds to the average stress in a neighboring cross-section having a certain coordinate ξ. Since average damage or consequently average actual stress, are continuously varying fields along the length of the bar (in a 1D model), the actual stress at a certain point of the cross section corresponds to the average stress in a certain neighboring cross section.

$$\frac{\int_s q\,(\omega(x,t),\sigma(x,t),T)\,dS}{S} = \int_{-\infty}^{\infty} q\Big(\omega(x,t),\sigma\big((x-\xi),t\big),T\Big)\rho(x-\xi)d\xi \tag{A.3}$$

In additions, due to strong stress-dependence of damage accumulation rate, the weight function is a rapidly decreasing function of distance, so the limits of integration which are the two ends of the bar, can be taken as infinity. The integration of the weight function should obviously satisfy the following relation:

$$\int_{-\infty}^{\infty} \rho(x-\xi)d\xi = 1 \tag{A.4}$$

From symmetry, the weight function is symmetric:

$$\int_{-\infty}^{\infty} (x-\xi)\rho(x-\xi)d\xi = 0 \tag{A.5}$$

We define the microstructural length scale as

$$\lambda^2 = \int_{-\infty}^{\infty} \left[\frac{(x-\xi)^2}{2}\right] \rho(x-\xi)\, \mathrm{d}\xi \tag{A.6}$$

This length scale is the average size of the aggregates of coherent microstructural elements. Then, the dimensionless microstructural length scale can be defined as

$$\Lambda^2 = \frac{\lambda^2}{L^2} \tag{A.7}$$

Where L is the characteristic length-size of the initial damage distribution over the bar length. L can not be the bar length because in that case, if the bar length becomes very large then Λ^2 becomes zero. This is not physically correct as the parameter Λ^2 is the material property and should not be a function of the domain size.

Now we expand the function q in Equation (A.3) by a Taylor series in the neighborhood $|(x-\xi)|$ about point x and use a quadratic approximation of q.

$$q\Big(\omega(x,t), \sigma\big((x-\xi),t\big), T\Big) = q\Big(\omega(x,t), \sigma\big(x,t\big), T\Big) + (x-\xi)\frac{\partial q}{\partial \xi}|_{\xi=x} + \frac{1}{2!}(x-\xi)^2\frac{\partial^2 q}{\partial \xi^2}|_{\xi=x} + \ldots \tag{A.8}$$

By replacing the right hand side of (A.2) with the right hand side of (A.3), we can get the integral form of the accumulation rate as

$$\frac{\mathrm{d}(\omega\,(x,t))}{\mathrm{d}t} = \tau^{-1}\int_{-\infty}^{\infty} q\Big(\omega(x,t), \sigma\big((x-\xi),t\big), T\Big)\rho(x-\xi)d\xi \tag{A.9}$$

The q on the right hand side of Equation (A.9) is now expanded using the right hand side of Equation (A.8), so we have;

$$\frac{\mathrm{d}(\omega\,(x,t))}{\mathrm{d}t} = \tau^{-1}[\cdots] \tag{A.10}$$

$$[\cdots] =$$

$$\underbrace{\Big[\int_{-\infty}^{\infty} q\Big(\omega(x,t), \sigma\big(x,t\big), T\Big)\rho(x-\xi)d\xi\Big]}_{\text{(A.10)-I}} +$$

$$\underbrace{\Big[\int_{-\infty}^{\infty} (\xi - x)\frac{\partial q}{\partial \xi}|_{(\xi=x)}\rho(x-\xi)d\xi\Big]}_{\text{(A.10)-II}} +$$

$$\underbrace{\Big[\int_{-\infty}^{\infty} \frac{1}{2!}(\xi - x)^2\frac{\partial^2 q}{\partial \xi^2}|_{(\xi=x)}\rho(x-\xi)d\xi\Big]}_{\text{(A.10)-III}} + \ldots$$

Now, we expand each of the three terms of the right hand side of (A.10),

(A.10)**-I**:

q is independent of ξ and using (A.4) we can get,

$$\Big[\int_{-\infty}^{\infty} q\Big(\omega(x,t),\sigma\big(x,t\big),T\Big)\rho(x-\xi)d\xi\Big] = q\Big(\omega(x,t),\sigma\big(x,t\big),T\Big)$$

(A.10)**-II**:

$\frac{\partial q}{\partial \xi}|_{(\xi=x)}$ is independent of ξ and using (A.5) we can get,

$$\Big[\int_{-\infty}^{\infty}(\xi-x)\frac{\partial q}{\partial \xi}|_{(\xi=x)}\rho(x-\xi)d\xi\Big] = 0$$

(A.10)**-III**:

using (A.6) we get,

$$\Big[\int_{-\infty}^{\infty}\tfrac{1}{2!}(\xi-x)^2\frac{\partial^2 q}{\partial \xi^2}|_{(\xi=x)}\rho(x-\xi)d\xi\Big] = \lambda^2\,\frac{\partial^2 q}{\partial \xi^2}|_{(\xi=x)}$$

Now let's rewrite (A.10)

$$\frac{\mathrm{d}(\omega\,(x,t))}{\mathrm{d}t} = \tau^{-1}\left[q\Big(\omega(x,t),\sigma\big(x,t\big),T\Big) + 0 + \lambda^2\,\frac{\partial^2 q}{\partial \xi^2}|_{(\xi=x)}\right] \qquad \text{(A.11)}$$

for isothermal condition where q is independent of temperature, $q \neq q(T)$, we get

$$\frac{\partial^2 q}{\partial \xi^2} = \frac{\partial}{\partial \xi}\left(\frac{\partial q}{\partial \xi}\right)$$

$$= \frac{\partial}{\partial \xi}\left[\frac{\partial q}{\partial \sigma}\frac{\partial \sigma}{\partial \xi}\right]$$

$$= \frac{\partial}{\partial \xi}\left[\frac{\partial q}{\partial \sigma}\frac{\partial \sigma}{\partial x}\overbrace{\frac{\partial x}{\partial \xi}}^{=1}\right]$$

$$= \frac{\partial}{\partial \xi}\left[\frac{\partial q}{\partial \sigma}\frac{\partial \sigma}{\partial x}\right]$$

$$= \frac{\partial}{\partial \xi}\left[\frac{\partial q}{\partial x}\right]$$

$$= \frac{\partial}{\partial x}\left[\frac{\partial q}{\partial x}\right]\frac{\partial x}{\partial \xi}$$

$$= \frac{\partial}{\partial x}\left[\frac{\partial q}{\partial x}\right]$$

$$= \frac{\partial}{\partial x}\left[\frac{\partial q}{\partial \sigma}\frac{\partial \sigma}{\partial x}\right]$$

therefore,

$$\frac{\partial^2 q}{\partial \xi^2} = \frac{\partial}{\partial x}\left[\frac{\partial q}{\partial \sigma}\frac{\partial \sigma}{\partial x}\right] \tag{A.12}$$

Now, let's rewrite (A.11) using (A.12),

$$\frac{\mathrm{d}(\omega\,(x,t))}{\mathrm{d}t} = \tau^{-1}\left[q\Big(\omega(x,t),\sigma\big(x,t\big),T\Big) + \frac{\partial}{\partial x}\left(\lambda^2\,\frac{\partial q}{\partial \sigma}\frac{\partial \sigma}{\partial x}\right)\right] \tag{A.13}$$

We now need to define dimensionless parameters to simplify the partial differential Equation (A.13). Notice that these parameters are defined at distance x.

A.3 Dimensionless Variables

The dimensionless stress μ can be obtained as follows:

$$\phi = \frac{\sigma}{\sigma_0} = \frac{1}{1-\omega} \tag{A.14}$$

so,

$$\sigma = \frac{\sigma_0}{1-\omega} \tag{A.15}$$

Notice that σ_0 is constant and σ varies as damage progresses. The partial derivative of stress with respect to space coordinate x is;

$$\frac{\partial \sigma}{\partial x} = \frac{\partial \sigma}{\partial \omega}\frac{\partial \omega}{\partial x} = \frac{\sigma_0}{(1-\omega)^2}\frac{\partial \omega}{\partial x} \tag{A.16}$$

using equations (A.15) and (A.16), we can rewrite Equation (A.13),

$$\frac{\mathrm{d}(\omega\,(x,t))}{\mathrm{d}t} = \tau^{-1} q\left(\omega(x,t), \frac{\sigma_0}{1-\omega}, T\right) + \frac{\partial}{\partial x}\left[\lambda^2\,\tau^{-1}\frac{\partial q}{\partial \sigma}\frac{\sigma_0}{(1-\omega)^2}\frac{\partial \omega}{\partial x}\right] \quad \text{(A.17)}$$

now, let's find the derivative of damage parameter ω with respect to x and t from Equation (A.14),

$$\omega = 1 - \frac{1}{\phi} \Rightarrow \frac{\partial \omega}{\partial t} = \frac{\partial \omega}{\partial \phi}\frac{\partial \phi}{\partial t} = \frac{1}{\phi^2}\frac{\partial \phi}{\partial t} \quad \text{(A.18)}$$

similarly for derivative with respect to x,

$$\frac{\partial \omega}{\partial x} = \frac{1}{\phi^2}\frac{\partial \phi}{\partial x} \quad \text{(A.19)}$$

now we can replace partial derivatives of ω with respect to x and t with those of ϕ using equations (A.18) and (A.19) to obtain the PDE in terms of ϕ as

$$\frac{\mathrm{d}\phi}{\mathrm{d}t} = \phi^2\tau^{-1} q\left(\frac{\phi-1}{\phi}, \sigma_0\phi, T\right) + \phi^2\frac{\partial}{\partial x}\left[(\lambda^2\,\tau^{-1}\frac{\partial q}{\partial \sigma}\sigma_0)\frac{\partial \phi}{\partial x}\right] \quad \text{(A.20)}$$

to further simplify any of the three equations (A.13), (A.17), and (A.20), which show the evolution of damage in a 1D domain, we should now define the following dimensionless parameters:

$$\mu = \frac{\gamma\sigma_0}{kT} \quad \text{(A.21)}$$

here k is the universal Boltzmann constant.

$$\xi = \frac{x}{L} \quad \text{(A.22)}$$

$$\Lambda^2 = \frac{\lambda^2}{L^2} \tag{A.23}$$

$$\psi = \mu\phi \Rightarrow \psi = \mu\frac{\sigma}{\sigma_0} = \frac{\mu}{1-\omega} = \frac{\gamma\sigma}{kT} \tag{A.24}$$

As explained earlier the first order Arrhenius-type kinetic equation is

$$q = (1-\omega)\exp\left(\frac{\gamma\sigma - U}{kT}\right) \tag{A.25}$$

These parameters are explained in detail in general form of this equation, i.e., Equation (A.26). An Arrhenius-type kinetic law with stress-dependent activation energy is used to calculate damage accumulation [21]:

$$q(\omega, \sigma, T) = (1-\omega)^p \exp\left(-\frac{(U-\gamma\sigma)}{kT}\right) \tag{A.26}$$

k in (A.26) is the universal Boltzmann constant; U, the zero-stress activation energy is another constant specific for a given bond-breaking chemical reaction; p, the constant kinetic 'reaction order' ; T is the temperature; τ is the characteristic time for damage accumulation. U can be interpreted as the magnitude of the energy barrier determining the probability of breakage of the bonds responsible for strength. The kinetic law expressed in (A.26) assumes that the breaking of bonds is thermally activated. In presence of tensile stress σ, the net activation energy required to initiate the bonds breakage is $U - \gamma\sigma$, (effective barrier). It should be noted that this effective barrier decreases with increasing tensile stress. The pore pressure in a reservoir rock must increase in order to increase tensile stress in the rock matrix, and initiate and propagate fracture. γ is another kinetic constant. In a stressed body, thermal fluctuations break chemical bonds and the possibility of this process depends strongly

on the magnitude of tensile stress. The tensile stress excites the bonds to be ruptured and reduces the activation energy. We can change the form of q as;

$$q = (1-\omega)\exp\left(-\frac{U}{kT}\right)\exp\left(\frac{\gamma\sigma}{kT}\right) \tag{A.27}$$

replace $\left(\frac{\gamma\sigma}{kT}\right)$ from (A.24) we get,

$$q = (1-\omega)\exp\left(-\frac{U}{kT}\right)\exp(\psi) \tag{A.28}$$

The dimensionless time is defined as

$$\theta = At \tag{A.29}$$

where A is:

$$A = \tau^{-1}\exp\left(-\frac{U}{kT}\right)$$

with the change of variables we have defined, we could now rewrite the partial differential equation of damage (A.17) in terms of the variable ψ. This allows us to use the Arrhenius-type kinetic law and make the governing equation simpler.

The partial derivative of ψ with respect to the dimensionless time θ can be written as

$$\frac{\partial\psi}{\partial\theta} = \frac{\partial\psi}{\partial\omega}\frac{\partial\omega}{\partial t}\frac{\partial t}{\partial\theta} \tag{A.30}$$

From (A.24), we can write:

$$\frac{\partial\psi}{\partial\omega} = \frac{\mu}{(1-\omega)^2} \tag{A.31}$$

From (A.29) we can write:

$$\frac{\partial t}{\partial \theta} = \tau \exp\left(\frac{U}{kT}\right) \tag{A.32}$$

and from (A.28), the Equation (A.32) can be written as

$$\frac{\partial t}{\partial \theta} = \tau \exp(\psi)\left(\frac{1-\omega}{q}\right) \tag{A.33}$$

Now, we replace (A.30) with (A.31) and (A.33) and get

$$\frac{\partial \psi}{\partial \theta} = \frac{\partial \omega}{\partial t} \underbrace{\frac{\mu}{(1-\omega)}\frac{\tau}{q}\exp(\psi)}_{\text{both sides of (A.17) are multiplied by this term and simplified}} \tag{A.34}$$

$$\frac{\mathrm{d}\psi}{\mathrm{d}\theta} = \tau^{-1} q \left(\frac{\mu}{(1-\omega)}\frac{\tau}{q}\exp(\psi)\right) + \Lambda^2 \psi^2 \frac{\partial}{\partial \xi}\left[\psi^{-1}\exp(\psi)\frac{\partial}{\partial \xi}\psi\right] \tag{A.35}$$

$$\underbrace{\frac{\mathrm{d}\omega(x,t)}{\mathrm{d}t}}_{\text{Damage accumulation}} = \underbrace{\Lambda^2 \frac{\partial^2}{\partial x^2}\left[(1-\omega)\exp\left(\frac{\mu_0}{1-\omega}\right)\right]}_{\text{Damage diffusion term}} + \underbrace{(1-\omega)\exp\left(\frac{\mu_0}{1-\omega}\right)}_{\text{Source term}} \tag{A.36}$$

The derivation shown here is for 1D and in higher dimensions the Equation (A.36) looks differently. Equation (A.37) shows the damage accumulation rate in $\mathbb{R}^2 \times (0, \infty)$.

$$\frac{\mathrm{d}(\omega\,(x,t))}{\mathrm{d}t} = \left[\nabla \cdot \left[\Lambda^2 \nabla\left((1-\omega)\exp\left(\frac{\mu_0}{1-\omega}\right)\right)\right] + (1-\omega)\exp\left(\frac{\mu_0}{1-\omega}\right)\right]_+ \tag{A.37}$$

Where the symbol + denotes the positive part (i.e.: $[*]_+ = \max\{*, 0\}$). This expresses the physical condition of no damage healing $\left(\frac{\partial \omega}{\partial t} \geq 0\right)$.

Appendix B

Solution of rock damage equation using COMSOL Finite Elements code

The appendix lists the MATLAB input file used to solve the rock damage partial differential equation using COMSOL Finite Elements code version 3.5;

```
% COMSOL Multiphysics Model M-file
% Generated by COMSOL 3.5 (COMSOL 3.5.0.494,
% $Date: 2011/02/19 16:09:48 $)
clc
clear all
close all
AxisFontSize=16
AxisFontWeight='normal'
AxisFontName= 'Times'
flclear fem
% COMSOL version
clear vrsn
vrsn.name = 'COMSOL 3.5';
vrsn.ext = '';
vrsn.major = 0;
vrsn.build = 494;
vrsn.rcs = '$Name:  $';
vrsn.date = '$Date: 2008/09/19 16:09:48 $';
fem.version = vrsn;
% Geometry
g1=solid1([0.0,1.0]);
% Analyzed geometry
```

```
clear s
s.objs={g1};
s.name={'I1'};
s.tags={'g1'};
fem.draw=struct('s',s);
fem.geom=geomcsg(fem);
% Initialize mesh
fem.mesh=meshinit(fem);
% Refine mesh
fem.mesh=meshrefine(fem, 'mcase',0);
% Application mode 1
clear appl
appl.mode.class = 'FlPDEC';
appl.sshape = 2;
appl.assignsuffix = '_c';
clear bnd
bnd.type = 'neu';
bnd.ind = [1,1];
appl.bnd = bnd;
clear equ
fem.globalexpr = {'mu','10'};
equ.f = '(1-u)*exp(mu/(1-u))';
equ.c = '1*.01*(mu+u-1)/(1-u)*exp(mu/(1-u))';
equ.init = {{'(x >0.4553).* (x<0.5447)*0.3 .*((2-1000 ...
 *( (x-.5).^2))./( 2-500 *( (x -.5).^2) ) )';0}}
equ.ind = [1];
appl.equ = equ;
fem.appl{1} = appl;
fem.frame = {'ref'};
fem.border = 1;
clear units;
units.basesystem = 'SI';
fem.units = units;
% ODE Settings
clear ode
clear units;
units.basesystem = 'SI';
```

```
ode.units = units;
fem.ode=ode;
% Multiphysics
fem=multiphysics(fem);
% Extend mesh
fem.xmesh=meshextend(fem);
%% Evaluate initial value using current solution
% init = asseminit(fem,'u',fem0.sol,'t',0.0,'blocksize','auto');
T=13*.41*1e-7
nt=1000
timesteps=[T/nt:T/nt:T];
clrmp=colormap(hsv(length(timesteps)+1));
t1=T/nt;
% Solve problem
fem.sol=femtime(fem, ...
                'solcomp',{'u'}, ...
                'outcomp',{'u'}, ...
                'blocksize','auto', ...
                'odesolver','genalpha', ...
                'tlist',[0:t1:t1], ...
                'tout','tlist', ...
                'tsteps','manual', ...
                'timestep',T/nt, ...
                'nlsolver','manual', ...
                'ntolfact',1, ...
                'maxiter',4, ...
                'dtech','const', ...
                'damp',1.0, ...
                'jtech','minimal');


% Save current fem structure for restart purposes
fem0=fem;

      nodes = xmeshinfo(fem,'out','nodes');
      dofs=nodes.dofs; %gives degrees of freedom
      %coords gives the coordinates for the DOF above (nt+1)x61
```

```
    coords=nodes.coords;
    X=fem.sol.u;
    %[dofs' , coords' , X(:,1) , X(:,2)]
    XcoordSorted=sort(coords);
    plot(XcoordSorted,X(:,1),'b-','MarkerSize',5,'linewidth',2.5)
    axis([0 1 0 1 ])
    grid on
    hold on
    xlabel('x','FontName', 'Times ','fontsize',20)
    ylabel('\omega','FontName', 'Times ','fontsize',20)
    set(0,'DefaultAxesFontName',AxisFontName, 'DefaultAxesFontSize',
    AxisFontSize, 'DefaultAxesFontWeight', AxisFontWeight);
    legend('Initial condition, \omega_0','Location','Northeast')

for i3=3:length(timesteps)
    %X gives the entire solution MATRIX (time and 1D space)
    X=fem.sol.u;
    for i1=1:length(dofs)
        if (X(i1,2))<(X(i1,1))
            X(i1,2)=X(i1,1);
        end
    end

    %check the performance of nonhealing damage
    %[fem.sol.u(:,2), X(:,2)]
    plot(XcoordSorted,X(:,2),'color',clrmp(i3,:))
    % Solve problem
fem.sol=femtime(fem, ...
                'init',X(:,2), ...
                'solcomp',{'u'}, ...
                'outcomp',{'u'}, ...
                'blocksize','auto', ...
                'tlist',[0:T/nt:T/nt], ...
                'tout','tlist', ...
                'linsolver','cg');
end
```

Appendix C

Discretization of the Governing Equation of Rock Damage

C.1 Discretization of the Partial Differential Equation

Here we wish to solve the PDE of rock damage in 1D (i.e., Equation(2.25), which is repeated here)

$$\frac{\partial \omega}{\partial t} = (1-\omega)\exp\left(\frac{\mu_0}{1-\omega}\right) + \Lambda^2 \frac{\partial^2}{\partial x^2}\left[(1-\omega)\exp\left(\frac{\mu_0}{1-\omega}\right)\right]$$

Initial value and boundary conditions are as follows:

Initial value:

$$\omega(x,0) = \omega_0(x) \tag{C.1}$$

Boundary conditions:

$$\frac{\partial \omega}{\partial x}(0,t) = \frac{\partial \omega}{\partial x}(1,t) = 0 \tag{C.2}$$

In order to solve this equation numerically, let's call the first part of the right-hand side of the equation, $Q = Q(\omega)$. Therefore the PDE can be written as

$$\frac{\partial \omega}{\partial t} = Q(\omega) + \Lambda^2 \frac{\partial^2}{\partial x^2}[Q(\omega)] \tag{C.3}$$

The left-hand side of the equation (C.3) can be discretized using the forward in time discretization and the right-hand side using the centered in space scheme. In order for the code to be able to perform the explicit, implicit and Crank-Nicolson, the parameter α is introduced into the scheme in equation (C.4). Notice that the parameter α could be introduced to the entire right-hand side. Also notice that we show $Q(\omega_j^n) = Q_j^n$.

$$\frac{\omega_j^{n+1} - \omega_j^n}{\Delta t} = Q(\omega_j^n) + \frac{\Lambda^2}{(\Delta x)^2} \left[\text{Equation (C.5)}\right] \tag{C.4}$$

$$\left[\alpha \left(Q_{j+1}^{n+1} - 2Q_j^{n+1} + Q_{j-1}^{n+1}\right) + (1-\alpha)\left(Q_{j+1}^n - 2Q_j^n + Q_{j-1}^n\right)\right] \tag{C.5}$$

To solve the nonlinear set of algebraic equations we use Newton-Raphson method.

C.2 Newton-Raphson Method

This section reviews the details of Newton-Raphson method for solving the nonlinear algebraic equations obtained from discretization as a result of using finite difference method. The results of numerical solution are presented in Chapter 2. Let's start looking at finding solution of nonlinear equations using Newton-Raphson method. This method is based on the truncation of Taylor series. Consider a vector valued function $\boldsymbol{f(x)}$ with components,

$$f_i(\boldsymbol{x}) = f_i(x_1, x_2, ..., x_n) \quad i = 1, 2, ..., n \tag{C.6}$$

Our problem is now finding a vector $\boldsymbol{x}$ such that $\boldsymbol{f(x)} = \boldsymbol{0}$, to have the right-hand-side of this equation denote a vector with all components zero. The derivative for multi-variable functions are in the form of gradient and for multi-variable vector functions are in the form of the Jacobian. The Jacobian of $\boldsymbol{f}$ at a point $\boldsymbol{x}$ is the determinant of an n×n matrix $J\left(\boldsymbol{f(x)}\right)$ defined by the equation;

$$J\big(\boldsymbol{f(x)}\big) = \begin{bmatrix} \frac{\partial f_1(\boldsymbol{x})}{\partial x_1} & \frac{\partial f_1(\boldsymbol{x})}{\partial x_2} & \cdots & \frac{\partial f_1(\boldsymbol{x})}{\partial x_n} \\ \frac{\partial f_2(\boldsymbol{x})}{\partial x_1} & \frac{\partial f_2(\boldsymbol{x})}{\partial x_2} & \cdots & \frac{\partial f_2(\boldsymbol{x})}{\partial x_n} \\ \vdots & \vdots & \ddots & \vdots \\ \frac{\partial f_n(\boldsymbol{x})}{\partial x_1} & \frac{\partial f_n(\boldsymbol{x})}{\partial x_2} & \cdots & \frac{\partial f_n(\boldsymbol{x})}{\partial x_n} \end{bmatrix} \tag{C.7}$$

The initial value for $\boldsymbol{x}$, is equal to initial value of the state variable and is denoted by $\boldsymbol{x_0}$. Having the value of the jacobian and function $\boldsymbol{f}$ at the known value of initial condition, the increment of $\boldsymbol{x}$, ($\boldsymbol{dx}$) can be calculated. Figure C.1 shows how the difference between two estimates can be calculated.

$$\boldsymbol{dx}_{\text{(iteration 1)}} = \text{-inv(Jacobian matrix at } \boldsymbol{x_0}\text{)}.\boldsymbol{f_0} \tag{C.8}$$

hence, the new value of $\boldsymbol{x}$ can be obtained at the next Newton-Raphson iteration;

$$\boldsymbol{x_1} = \boldsymbol{x_0} + \boldsymbol{dx}_{\text{(iteration 1)}} \tag{C.9}$$

$$\text{Relative error}(\%) = \frac{||\boldsymbol{x}_1 - \boldsymbol{x}_0||}{||\boldsymbol{x}_0||} \times 100 \tag{C.10}$$

Where $\boldsymbol{x}_1$ is the estimate of solution (vector) at the first iteration. This can not be accepted as solution unless the relative error is less than a certain small value for example 10^{-3}. The vector norm here is l_2-norm or the length of vector. Based on this definition, the relative error is the ratio of length of absolute error vector to length of vector of initial value of solution at the start of each time step. If relative error is greater than the assigned relative error, the next iteration starts:

Equation (C.8) is calculated at $\boldsymbol{x}_1$, therefore;

$$\boldsymbol{dx}_{\text{(iteration 2)}} = \text{-inv(Jacobian matrix at } \boldsymbol{x_1}\text{)}.\boldsymbol{f_1} \tag{C.11}$$

and then equations (C.9) and (C.10) are repeated as follows;

$$\boldsymbol{x_2} = \boldsymbol{x_1} + \boldsymbol{dx}_{\text{(iteration 2)}} \tag{C.12}$$

$$\text{Relative error}(\%) = \frac{||\boldsymbol{x}_2 - \boldsymbol{x}_0||}{||\boldsymbol{x}_0||} \times 100 \tag{C.13}$$

From Equations (C.8) to (C.13) we can write the general form of iterations as:

$$\boldsymbol{dx}_{\text{(iteration i+1)}} = \text{-inv(Jacobian matrix at } \boldsymbol{x_i}\text{)}.\boldsymbol{f_i} \qquad i = 0, ..., \text{max iterations} \tag{C.14}$$

$$\boldsymbol{x_{i+1}} = \boldsymbol{x_i} + \boldsymbol{dx}_{\text{(iteration i+1)}} \tag{C.15}$$

$$\text{Relative error}(\%) = \frac{||\boldsymbol{x}_{i+1} - \boldsymbol{x}_0||}{||\boldsymbol{x}_0||} \times 100 \tag{C.16}$$

It should be noted that the relative error at each iteration is calculated using the initial vector of solution at the start of each time step Δt. Figure C.2 shows the estimate of solution at iterations and solutions at time steps.

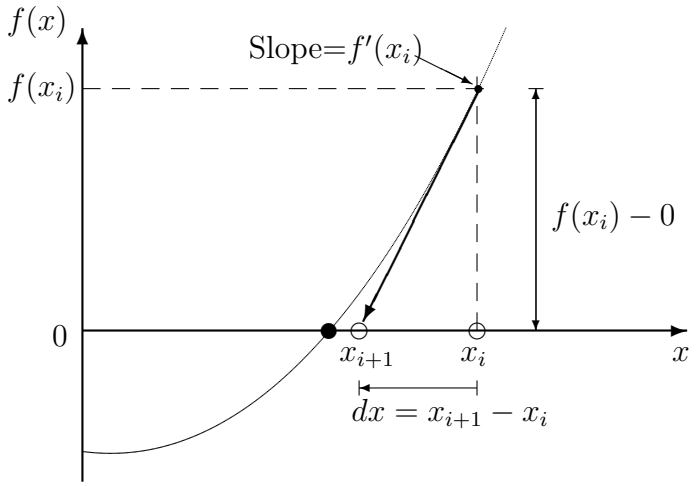

Figure C.1: Newton-Raphson Method

The method for solving the nonlinear partial differential equation (2.25) can now be explained thoroughly as the Newton-Raphson method has been explained above. Let's consider a 1D bar along which the state variable ω representing damage varies with time. For numerical analysis the 1D domain of the bar is discretized by J segments as shown in Figure C.3.

Initially the values of damage along the bar is known. The distribution of damage near blow-up time –when damage at one point reaches the value of 1– is of significance for analysis purposes. The damage accumulation rate

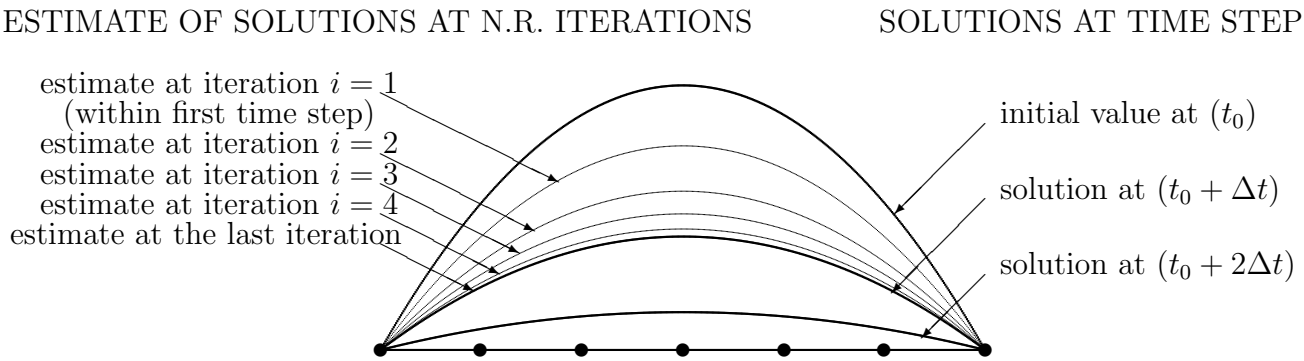

Figure C.2: Newton-Raphson iterations between each two time steps and solutions at each time step

near the blow-up time becomes so fast that obtaining the various times to attain damage distribution in the vicinity of blow-up time yields the same value, in other words, the time to achieve 70 percent of damage in a cross-section (ω=0.7) is numerically equal to that of ω=1.0. This has to do with the inadequate speed and precision of current machines. For practical purposes the time to blow-up could be computed for ω=0.7. This can be used as a guideline to obtain the onset of complete damage in a cross-section. Table 2.1 shows the dimensionless blow-up times for various damage parameters. Based on the Kachanov's equation, the blow-up time should be calculated for microstructural length scale of zero. Besides, in this calculation initial maximum damage parameter is assigned a value of 0.3. It is obvious that the blow-up time is a function of the initial maximum value of damage at a point within the domain.

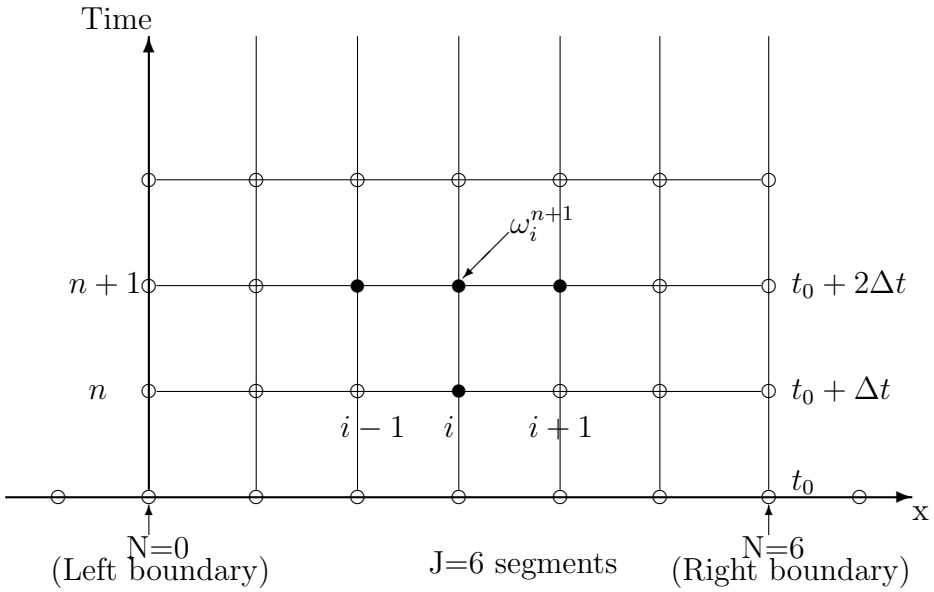

Figure C.3: Finite difference discretization of the 1D domain of problem

Appendix D

Drivation of Gas Diffusivity Equation

The gas flow in porous media can be studied using Darcy's law incorporated into the conservation of mass equation. A quick overview of the assumptions and the equations used in the simulation of gas in a vertical well which was presented in Chapter 8, is given here.

We are assuming that the flow is under isothermal condition and the thermal freezing was employed to freeze the rock and make the mechanical changes in the rock properties. The fluid compressibility is assumed to remain constant. Since the process is isothermal, the density in the equation of state is a function of pressure only and can be calculated using Equation (D.1)

$$\rho(p) = \frac{\mathrm{M_w}}{\mathrm{Z(p)RT}}\mathrm{p} \tag{D.1}$$

Z is the gas compressibility factor and is equal to 1.0 for ideal gasses. For real gasses, Z can be obtained from the generalized compressibility factor diagram [212]. Assuming the gas to be Methane, critical temperature and pressure are obtained from the Table of liquid-vapor critical temperature and pressure for selected substances[252] as 109.9°K and 45.79 atm. For the range of temperature and pressure of the reservoir, the compressibility factor can be obtained

from the plot and approximated as:

$$\mathrm{Z(p)} = -3.427 \times 10^{-24}\mathrm{p}^3 + 5.38 \times 10^{-16}\mathrm{p}^2 - 1.448 \times 10^{-8}\mathrm{p} + 1.0055 \quad \text{(D.2)}$$

Pressure in Equation (D.2) is in Pa. Viscosity of the fluid is constant and rock is incompressible; therefore, the porosity does not change with pressure. Using the material balance equation for a single phase flow in porous media we get:

$$\frac{\partial(\rho\phi)}{\partial \mathrm{t}} = -\nabla \cdot (\rho \mathrm{u}) \quad \text{(D.3)}$$

u, in Equation (D.3) is the Darcy velocity or superficial velocity and equals:

$$\mathrm{u} = \frac{\mathrm{q}}{\mathrm{A}} = -\frac{\mathrm{k}}{\mu}\nabla\Phi \quad \text{(D.4)}$$

Φ is the potential and equals p+ρgh. Ignoring gravity, the potential is equal to the pressure p.

If Darcy's transport law from Equation (D.4) is plugged into the material balance Equation (D.3) and gravity is neglected, we can arrive at the equation of pressure diffusivity in porous media:

$$\frac{\partial(\rho\phi)}{\partial \mathrm{t}} = \nabla \cdot \left(\rho\frac{\mathrm{k}}{\mu}\nabla \mathrm{p}\right) \quad \text{(D.5)}$$

expanding Equation (D.5) we get:

$$\phi\frac{\partial(\rho)}{\partial \mathrm{t}} + \rho\frac{\partial(\phi)}{\partial \mathrm{t}} = \frac{\mathrm{k}}{\mu}\left[\rho\nabla^2\mathrm{p} + \nabla\rho.\nabla\mathrm{p}\right] \quad \text{(D.6)}$$

in porous media the total compressibility $\mathrm{c_t}$ is the sum of the compressibility of the fluid and the formation.

$$\text{Total compressibility, } \mathrm{c_t} = \mathrm{c_{fluid}} + \mathrm{c_{formation}} \quad \text{(D.7)}$$

fluid compressibility may include all the three phases of oil, gas and water, hence;

$$c_{fluid} = c_o S_o + c_g S_g + c_w S_w \tag{D.8}$$

we assume gas flow in an incompressible rock; therefore, the total compressibility in our formulation is:

$$c_t = c_g S_g \tag{D.9}$$

Rock or pore space compressibility is defined as

$$c_{formation} = \frac{1}{(\phi V_b)} \frac{d(\phi V_b)}{dp} = \frac{1}{(V_p)} \frac{d(V_p)}{dp} \tag{D.10}$$

in Equation (D.10), V_b, is the bulk volume, V_p is the volume of the pore spaces and p is the pore pressure.

fluid compressibility is defined as

$$c_{fluid} = \frac{1}{\rho} \frac{d\rho}{dp} \tag{D.11}$$

since the density varies with pressure, let's re-write the Equation (D.6) to bring the variation of density with pressure and the effect of compressibility into the diffusivity equation:

$$\phi \underbrace{\frac{\partial \rho}{\partial p}}_{\rho c_{fluid}} \frac{\partial p}{\partial t} + \rho \phi \underbrace{\left[\frac{1}{(\phi V_b)} \frac{d(\phi V_b)}{dp} \right]}_{c_{formation}} \frac{\partial p}{\partial t} = \frac{k}{\mu} \left[\rho \nabla^2 p + (\underbrace{\frac{d\rho}{dp}}_{\rho c_{fluid}} \nabla p) . \nabla p \right] \tag{D.12}$$

now, let's use Equation (D.12) and replace the terms from Equations (D.10) and (D.11) and cancel out the density from both sides of the equation to bring the fluid and formation compressibilities to the left hand side of the equation.

$$\phi \, c_{fluid} \frac{\partial p}{\partial t} + \phi \, c_{formation} \frac{\partial p}{\partial t} = \frac{k}{\mu} \left[\nabla^2 p + c_{fluid} \, \nabla p . \nabla p \right] \tag{D.13}$$

The two terms in the left hand side of the Equation (D.13) can now be added and the total compressibility appears in the equation. Furthur simplification of Equation (D.13) results in:

$$\phi \, \mathrm{c_t} \frac{\mu}{\mathrm{k}} \frac{\partial \mathrm{p}}{\partial \mathrm{t}} = \nabla^2 \mathrm{p} + \mathrm{c_{fluid}} (\nabla \mathrm{p}.\nabla \mathrm{p}) \tag{D.14}$$

For analytical solutions of diffusivity equation, the term on the right hand side which includes the product of two pressure gradient will be neglected; however, this assumption is valid only for the zones far away from the wellbore where the pressure gradient is small. Neglecting the product results in:

$$\nabla^2 \mathrm{p} = \frac{\mu \mathrm{c_t} \phi}{\mathrm{k}} \frac{\partial \mathrm{p}}{\partial \mathrm{t}} \tag{D.15}$$

Equation (D.15) is the pore pressure diffusivity equation and the reciprocal of the coefficient on the right hand side is called the diffusivity coefficient, denoted by α and it's a function of pressure.

$$\alpha(\mathrm{p}) = \frac{\mathrm{k}}{\mu \mathrm{c_t} \phi} \tag{D.16}$$

Index

Bibliography

[1] J. Alfaiate, E. B. Pires, and J. A. C. Martins. A finite element analysis of non-prescribed crack propagation in concrete. *Computers and Structures*, 63(1):17 – 26, 1997.

[2] A. Ali. FEM analysis of concrete structures subjected to mode-I and mixed-mode loading conditions. *Computers and Structures*, 61(6):1043 – 1055, 1996.

[3] T. L. Anderson. *Fracture Mechanics: Fundamentals and Applications*. CRC Press, Boca Raton, FL, 1995.

[4] K. Andreev and H. Harmuth. FEM simulation of the thermo-mechanical behavior and failure of refractories - a case study. *Journal of Materials Processing Technology*, (143-144):72 – 77, 2003.

[5] W. T. Ang. *Hypersingular Integral Equations in Fracture Analysis*. Oxford: Woodhead Publishing, 2013.

[6] D. N. Arnold. Discretization by finite-elements of a model parameter dependent problem. *Numerische Mathematik*, 37(3):405 – 421, 1981.

[7] A. Asadpoure and S. Mohammadi. Developing new enrichment functions for crack simulation in orthotropic media by the extended finite element

method. *International Journal for Numerical Methods in Engineering*, 69(10):2150 – 2172, 2007.

[8] A. Asadpoure, S. Mohammadi, and A. Vafai. Modeling crack in orthotropic media using a coupled finite element and partition of unity methods. *Finite Elements in Analysis and Design*, 42(13):1165 – 1175, 2006.

[9] J. L. Asferg, P. N. Poulsen, and L. O. Nielsen. A consistent partly cracked XFEM element for cohesive crack growth. *International Journal for Numerical Methods in Engineering*, 72(4):464 – 485, 2007a.

[10] J. L. Asferg, P. N. Poulsen, and L. O. Nielsen. A direct XFEM formulation for modeling of cohesive crack growth in concrete. *Computers and Concrete, An Int. Journal*, 4(2):83 – 100, 2007b.

[11] I. Babuška and J. M. Melenk. The partition of unity method. *International Journal for Numerical Methods in Engineering*, 40(4):727 – 758, 1997.

[12] I. Babuška and M. Suri. Locking effects in the finite element approximation of elasticity problems. *Numerische Mathematik*, 62(1):439 – 463, 1992.

[13] Z. P. Bažant and E. Becq-Giraudon. Statistical prediction of fracture parameters of concrete and implications for choice of testing standard. *Cem. Concr. Res*, 32(4):529 – 556, 2002.

[14] Z. P. Bažant and L. Cedolin. *Stability of Structures: Elastic, Inelastic, Fracture, and Damage Theories*. Oxford University Press, New York, 1991.

[15] Z.P. Bažant and G. Pijaudier-Cabot. Measurement of characteristic length of nonlocal continuum. *Journal of Engineering Mechanics*, 115 (4):755–767, April 1989.

[16] Hans-Achim Bahr, Hans-Jürgen Weiss, Ute Bahr, Martin Hofmann, Gottfried Fischer, Stefan Lampenscherf, and Herbert Balke. Scaling behavior of thermal shock crack patterns and tunneling cracks driven by cooling or drying. *Journal of the Mechanics and Physics of Solids*, 58: 1411–1421, 2010.

[17] J. M. Ball. Remarks on blow-up and nonexistence theorems for nonlinear evolution equations. *Quart. J. Math. Oxford*, 2(28):473–486, 1977.

[18] J. M. Ball. *Nonlinear Evolution Equations Proceedings of a Symposium*, pages 189–205. Academic Press, Inc., 1978. ISBN 0-12-195250-9.

[19] G. I. Barenblatt. The formation of equilibrium cracks during brittle fracture: General ideas and hypotheses, axially symmetric cracks. *Appl. Math. Mech.*, 23(3):622 – 636, 1959.

[20] G. I. Barenblatt. The mathematical theory of equilibrium cracks in brittle fracture. *Adv. Appl. Mech*, 7:55 – 129, 1962.

[21] G.I. Barenblatt and V.M. Prostokishin. A mathematical model of damage accumulation taking into account microstructural effects. *European Journal of Applied Mathematics*, 4(3):225–240, 1993.

[22] L. Bates. The need for industrial education in bulk technology. *Fifth World Congress on Particle Technology*, 26:464–473, 2006.

[23] T. Belytschko and G. Zi. New crack-tip elements for XFEM and applications to cohesive cracks. *International Journal for Numerical Methods in Engineering*, 57(15):2221 – 2240, 2003.

[24] T. Belytschko, R. L. Chiapetta, and H. D. Bartel. Efficient large-scale nonlinear transient analysis by finite-elements. *International Journal for Numerical Methods in Engineering*, 10(3):579 – 596, 1976.

[25] T. Belytschko, Y. Krongauz, D. Organ, M. Fleming, and P. Krysl. Meshless methods: An overview and recent developments. *Computer Methods in Applied Mechanics and Engineering*, 139(1-4):3 – 47, 1996.

[26] T. Belytschko, H. Chen, J. X. Xu, and G. Zi. Dynamic crack propagation based on loss of hyperbolicity and a new discontinuous enrichment. *International Journal for Numerical Methods in Engineering*, 58(12):1873 – 1905, 2003.

[27] J. Bennett. A weibull brittle material failure model for the ABAQUS computer program. *Contract: W-7405-ENG-36*, 1991.

[28] F. Bertrand, L. A. Leclaire, and G. Levecque. Dem-based models for the mixing of granular materials. *Chemical Engineering Science*, 60: 2517–2531, 2005.

[29] G. Block and M. Rubin. Simulations of dynamic crack propagation in brittle materials using nodal cohesive forces and continuum damage mechanics in the distinct element code LDEC. *International Journal of Fracture*, 144(3):131 – 147, 2007.

[30] P. Bocca, A. Carpinteri, and S. Valente. Size effects in the mixed mode crack propagation: Softening and snap-back analysis. *Engineering Fracture Mechanics*, 35(1-3):159 – 170, 1990.

[31] P. Bocca, A. Carpinteri, and S. Valente. Mixed mode fracture of concrete. *International Journal of Solids and Structures*, 27(9):1139 – 1153, 1991.

[32] M. Bonnet, G. Maier, and C. Polizzotto. Symmetric galerkin boundary element methods. *Applied Mechanics Reviews*, 51(11):669 – 703, 1998.

[33] A. Bonneville, B. N. Nguyen, M. Stewart, Z. J. Hou, C. Murray, and T. Gilmore. Geomechanical evaluation of thermal impact of injected CO_2 temperature on a geological reservoir: Application to the futuregen 2.0 site. *Energy Procedia, 12th International Conference on Greenhouse Gas Control Technologies, GHGT-12*, 63:3298–3304, 2014.

[34] N. Bonora. A nonlinear CDM MODEL for ductile failure. *Engineering Fracture Mechanics*, 58(1-2):11 – 28, 1997.

[35] T. J. Boone, P. A. Wawrzynek, and A. R. Ingraffea. Simulation of the fracture process in rock with application to hydrofracturing. *Int. J. Rock Mech. Min. Sci*, 22(3):255 – 265, 1986.

[36] A. Brara, F. Camborde, J. R. Klepaczko, and C. Mariotti. Experimental and numerical study of concrete at high strain rates in tension. *Mech Mater*, 33:33 – 45, 2001.

[37] F. Brezzi and M. Fortin. *Mixed and Hybrid Finite Element Methods*. Springer, 1991.

[38] K. B. Broberg. *Cracks and Fracture*. Academic Press, Cambridge, 1999.

[39] D. C. Brooker and B. F. Ronalds. Prediction of ductile failure in tubular steel members using ABAQUS. *International Society of Offshore and Polar Engineers, P.O. Box 189, Cupertino, CA, 95015-0189, USA.*, 2001.

[40] M. S. A. Bruno and C. A. A. Bovberg. Reservoir compaction and surface subsidence above the lost hills field. california. *The 33th US Symposium on Rock Mechanics (USRMS). American Rock Mechanics Association*, 1992.

[41] M. J. Buehler and T. Ackbarow. Fracture mechanics of protein materials. *Materialstoday*, 10(9):46–58, 2007.

[42] J.C. Butcher. *Numerical methods for ordinary differential equations*. Wiley.

[43] J. G. Cai and J. Zhao. Effects of multiple parallel fractures on apparent attenuation of stress waves in rock masses. *Int. Journal of Rock Mechanics and Mining Sciences*, 37(4):661 – 682, 2000.

[44] M. Cai. Influence of intermediate principal stress on rock fracturing and strength near excavation boundaries-insight from numerical modeling. *Int. Journal of Rock Mechanics and Mining Sciences*, 45(5):763 – 772, 2008.

[45] G. T. Camacho and M. Ortiz. Computational modeling of impact damage in brittle materials. *International Journal of Solids and Structures*, 33(20-22):2899 – 2938, 1996.

[46] C. S. Campbell. Rapid granular flows. *Annual Rev. Fluid Mech.*, 22: 57–92, 1990.

[47] C. S. Campbell. Granular material flows - an overview. *Powder Technology*, 162:208–229, 2006.

[48] P. Cavin, A. Gravouil, A. A. Lubrecht, and A. Combescure. Automatic energy conserving space-time refinement for linear dynamic structural problems. *International Journal for Numerical Methods in Engineering*, 64(3):304 – 321, 2005.

[49] C. H. Chen. *Scaling and instability of dynamic fracture*. PhD thesis, Doctoral dissertation, The University of Texas at Austin, 2014.

[50] S. G. Chen and J. Zhao. A studyof udec modeling for blast wave propagation in jointed rock masses. *International Journal of Rock Mechanics and Mining Sciences*, 35(1):93 – 99, 1998.

[51] A. H.-D. Cheng and D. T. Cheng. Heritage and early history of the boundary element method. *Engineering Analysis with Boundary Elements*, 29(3):268 – 302, 2005.

[52] L. Chilton and M. Suri. On the selection of a locking-free hp element for elasticity problems. *International Journal for Numerical Methods in Engineering*, 40(11):2045 – 2062, 1997.

[53] S. H. Cho and K. Kaneko. Influence of the applied pressure waveform on the dynamic fracture processes in rock. *Int. Journal of Rock Mechanics and Mining Sciences*, 41(5):771 – 784, 2004.

[54] S. H. Cho, Y. Ogata, and K. Kaneko. Strain-rate dependency of the dynamic tensile strength of rock. *International Journal of Rock Mechanics and Mining Sciences*, 40(5):763 – 777, 2003.

[55] R. W. Clough. The finite element method in plane stress analysis. *Proceedings of the Second ASCE Conference Electronic Computation, Pittsburg, PA*, 1960.

[56] K. A. Connors. *Chemical Kinetics: The Study of Reaction Rates in Solution*. Vch Publishing, 1990.

[57] A.H. Cottrell. Tewksbury symposium on fracture. page 1, University of Melbourne, 1963.

[58] R. Courant. Variational methods for the solution of problems of equilibrium and vibrations. *Bulletin of the American Mathematical Society*, 49:1 – 23, 1943.

[59] R. Courant, K. O. Friedrichs, and H. Lewy. Über die partiellen differenzengleichungen der mathematischen physik. *Math. Ann (English translation, with commentaries by Lax, P.B., Widlund, O.B., Parter, S.V., in IBM J. Res. Develop. 11 (1967))*, 100:32 – 74, 1928.

[60] P. A. Cundall. A computer model for simulating progressive, large scale movements in blocky rock systems. *Proceedings of the International Symposium on Rock Fracture*, 1971.

[61] P. A. Cundall and O. D. Strack. A discrete numerical model for granular assemblies. *Geotechnique*, 29(1):47–65, 2006.

[62] A. Dahi-Taleghani and J.E. Olson. Analysis of multistranded hydraulic fracture propagation: An improved model for the interaction between induced and natural fractures. (SPE-124884), 2009.

[63] T. Ṗoschel and T. Schwager. *Computational Granular Dynamics: Models and Algorithms*, chapter 2.1.4. Springer, 1 edition, 2005.

[64] B. J. Dikken and H. Niko. Waterflood-induced fractures: A simulation study of their propagation and effects on waterflood sweep efficiency. *Society of Petroleum Engineers*, 1987.

[65] A. Dragon and D. Halm. A mesocrack damage and friction coupled model for brittle materials. In *Damage Mechanics in Engineering Materials*, pages 321–336. 1998.

[66] J. Du and Jon E. Olson. A poroelastic reservoir model for predicting subsidence and mapping subsurface pressure fronts. *Journal of Petroleum Science and Engineering*, 30(3- 4):181 – 197, 2001.

[67] J. Du, A. S. Kobayashi, and N. M. Hawkins. FEM dynamic fracture analysis of concrete beams. *Journal of Engineering Mechanics*, 115(10): 2136 – 2149, 1989.

[68] D. S. Dugdale. Yielding of steel sheets containing slits. *J. Mech. Phys. Solids*, 8(2):100 – 104, 1960.

[69] B.M. Krooss R. Littke E. Eseme, J.L. Urai. Review of mechanical properties of oil shales: Implications for exploitation and basin modeling. *Oil Shale*, 24(2):159–174, 2007.

[70] M. Elices, G. V. Guinea, J. Gomez, and J. Planas. The cohesive zone model: Advantages, limitations and challenges. *Eng. Fract. Mech*, 69 (2):137 – 163, 2002.

[71] H. A. Elliott. An analysis of the conditions for rupture due to griffth cracks. *Proc. Phys. Soc.*, 59(2):208 – 223, 1947.

[72] A. M. Elmarakbi, N. Hu, and H. Fukunaga. Finite element simulation of delamination growth in composite materials using LS-DYNA. *Composites Sci. and Tech*, 69(14):2383 – 2391, 2009.

[73] S. Enayatpour and T. Patzek. Finite element solution of nonlinear transient rock damage with application in geomechanics of oil and gas reservoirs. *Proceedings of the 2012 COMSOL Conference, Boston*, 2012.

[74] S. Enayatpour and T. Patzek. Thermal shock in reservoir rock enhances the hydraulic fracturing of gas shales. *Unconventional Resources Technology Conference*, 2013.

[75] S. Enayatpour, R. Khaledialidusti, and T. Patzek. Assessment of thermal fracturing in tight hydrocarbon formation using dem. *the 48th US Rock Mechanics / Geomechanics Symposium held in Minneapolis, MN, USA, 1-4 June 2014*.

[76] S. Enayatpour, E. van Oort, and T. Patzek. Freezefrac improves the productivity of gas shales. *SPE ATCE Conference*, (SPE 166482), 2013.

[77] T. Engelder. Joints and shear fractures in rock. *Fracture Mechanics of Rock. Academic Press, London*, pages 27–69, 1987.

[78] J. R. Ernst, K. Holliger, H. Maurer, and A. G. Green. Realistic FDTD modeling of borehole georadar antenna radiation: methodology and application. *Near Surf. Geoph.*, 4:19 – 30, 2006.

[79] J. P. Morris *et al.* . Simulations of fracture and fragmentation of geologic materials using combined FEM/DEM analysis. *International Journal of Impact Engineering*, 33(1):463 – 473, 2006.

[80] M. Ki-Bok *et al.* . Stress-dependent permeability of fractured rock masses: a numerical study. *International Journal of Rock Mechanics and Mining Sciences*, 41(7):1191 – 1210, 2004.

[81] O. C. Zienkiewicz *et al.* . Analysis of nonlinear problems in rock mechanics with particular reference to jointed rock systems. *Proceedings of the Second International Congress on Rock Mechanics, Belgrade*, (364), 1970.

[82] R. W. Clough *et al.* . *SAP-IV Software and Manuals*. NISEE e-Library, UC Berkeley, The Earthquake Engineering Online Archive.

[83] P. Fakcharoenphol, S. Charoenwongsa, H. Kazemi, and Y. S. Wu. The effect of water-induced stress to enhance hydrocarbon recovery in shale reservoirs. *SPE Annual Technical Conference and Exhibition. Society of Petroleum Engineers*, 2012.

[84] S. Fernandez-Mendez and A. Huerta. Imposing essential boundary con-

ditions in mesh-free methods. *Computer Methods in Applied Mechanics and Engineering*, 193(12-14):1257 – 1275, 2004.

[85] J. W. Foulk, D. H. Allen, and K. L. E. Allen. Formulation of a three-dimensional cohesive zone model for application to a finite element algorithm. *Comput. Methods Appl. Mech. Eng*, 183(1):51 – 66, 2000.

[86] J. T. Fredrich, J. G. Arguello, G. L. Deitrick, and E. P. de Rouffignac. Geomechanical modeling of reservoir compaction, surface subsidence, and casing damage at the belridge diatomite field. *Society of Petroleum Engineers*, 3(4):348 – 359, 2000.

[87] H. L. Friedman. Kinetics of thermal degradation of char-forming plastics from thermogravimetry. application to a phenolic plastic. *J. polym. sci., C Polym. symp.*, 6:183 – 195, 1964.

[88] G. Galilei. *The Discourses and Mathematical Demonstrations Relating to Two New Sciences*. 1638.

[89] J. Geertsma. Land subsidence above compacting oil and gas reservoirs. *Journal of Petroleum Technology*, 25(6):734 – 744, 1973.

[90] S. Gerschgorin. Fehlerabschwätzung für das differenzenverfahren zur lösung partieller differentialgleichungen. z. angew. *Math. Mech*, 10:373 – 382, 1930.

[91] A. Ghassemi, A. Nygren, and A. Cheng. Effects of heat extraction on fracture aperture: A poro-thermoelastic analysis. *Geothermics*, 37(5): 525 – 539, 2008.

[92] V.M. Prostokishin D.B. Silin G.I. Barenblatt, T.W. Patzek. Oil deposits in diatomites: A new challenge for subterranean mechanics. *Society of Petroleum Engineers*, (SPE 75230):13–17, 2002.

[93] E. Van Der Giessen, P.R. Onck, and M.W.D. Van Der Burg. Some effects of random microstructural variations on creep rupture. *Engineering Fracture Mechanics*, 57(2/3):205–226, 1997.

[94] E. Giner, N. Sukumar, F.D. Denia, and F.J. Fuenmayor. Extended finite element method for fretting fatigue crack propagation. *International Journal of Solids and Structures*, 45(22-23):5675 – 5687, 2008.

[95] R. A. Gingold and J. J. Monaghan. Smoothed particle hydrodynamics - theory and application to non-spherical stars. *Mon Not R Astron Soc*, 181:375 – 389, 1977.

[96] R. Goodman, R. Taylor, and T. Brekke. A model for the mechanics of jointed rock. *J Soil Mech Div ASCE*, 94(SM3(6)):37 – 59, 1968.

[97] M. A. Grant, J. Clearwater, J. Quinao, P. F. Bixley, and M. L. Brun. Thermal stimulation of geothermal wells: A review of field data. *Proc., 38th Workshop on geothermal reservoir engineering, Stanford University*, 2013.

[98] J. P. Gray and J. J. Monaghan. Numerical modeling of stress fields and fracture around magma chambers. *Journal of Volcanology and Geothermal Research*, 135(3):259 – 283, 2004.

[99] A.A. Griffith. The phenomena of rupture and flow in solids. *Philosophical Transactions of the Royal Society of London*, 221:163–198, 1921.

[100] G. Gunnarson. Mastering reinjection in the hellisheidi field, sw-iceland: a story of successes and failures. *Proc., 36th Workshop on geothermal reservoir engineering, Stanford University*, 2011.

[101] M. Guo-xiong and C. Qi-ming. Solution of terzaghi one-dimensional consolidation equation with general boundary conditions. *Journal of Central South University*, 20(8):2239 – 2244, 2013.

[102] H.J. Weiss H.A. Bahr, G. Fischer. Thermal-shock crack patterns explained by single and multiple crack propagation. *Journal of Materials Science*, 21:2716–2720, 1986.

[103] J. Hagoort, B. Weatherill, and A. Settari. Modeling the propagation of waterflood-induced hydraulic fractures. *SPE Journal*, 20(4):293 – 303, 1980.

[104] H. C. Hamaker. The london-van der waals attraction between spherical particles. *Physica*, 4(10):1058–1072, 1937.

[105] J. F. Hazzard and R. P. Young. Micromechanical modeling of cracking and failure brittle rocks. *Journal of Gheophysical Research*, 105:16683 – 16697, 2000a.

[106] J. F. Hazzard and R. P. Young. Simulating acoustic emissions in bond-edpartic models of rock. *International Journal of Rock Mechanics and Mining Sciences*, 37(5):867 – 872, 2000b.

[107] P. K. Heda, D. Dollimore, K. S. Alexander, D. Chen, E. Law, and P. Bicknell. A method of assessing solid state reactivity illustrated by thermal decomposition experiments on sodium bicarbonate. *Thermochimica Acta*, 255:255 – 272, 1995.

[108] H. Hertz. über die berührung fester elastischer körper (on the contact of elastic solids). *J. Reine Angew. Math.*, 92:156–171, 1882.

[109] Hibbitt, Karlsson, and Sorensen. *ABAQUS/Standard Users Manual, V. 6.5*. Pawtucket, Rhode Island.

[110] A. Hillerborg, M. Modeer, and P. Petersson. Analysis of crack formation and crack growth in concrete by means of fracture mechanics and finite elements. *Cem Concr Res*, (6):773 – 782, 1976.

[111] R. G. Hoagland, G. T. Hahn, and A. R. Rosenfield. Influence of microstructure on fracture propagation in rock. *Rock Mechanics*, 5:77–106, 1973.

[112] N.J. Hoff. The necking and rupture of rods subjected to constant tensile loads. *Journal of Applied Mechanics*, 20(1):105–108, 1953.

[113] K. Holliger, M. Musil, and H. R. Maurer. Raybased amplitude tomography for crosshole georadar data: a numerical assessment. *Journal of Applied Geophysics*, 47(3-4):285 – 298, 2001.

[114] H. Horii and S. Nemat-Nasser. Overall moduli of solids with microcracks: load-induced anisotropy. *Journal of the Mechanics and Physics of Solids*, 31(2):155–171, 1982.

[115] A. Hrennikoff. Solution of problems of elasticity by the framework method. *Journal of applied mechanics*, 8(4):169 – 175, 1941.

[116] M. L. Hughes, J. W. Tedesco, and C. A. Ross. Numerical analysis of high strain rate splitting-tensile tests. *Comput Struct*, 47:653 – 671, 1993.

[117] Frank P. Incropera and David P. DeWitt. *Introduction to Heat Transfer*. Wiley, 2 edition, 1990. ISBN 0471612472.

[118] C. E. Inglis. Stresses in a plate due to the presence of cracks and sharp corners. *Spring Meetings of the Fifty-fourth Session of the Institution of Naval Architects*, pages 219–241, 1913.

[119] G.R. Irwin. Analysis of stresses and strains near the end of a crack traversing a plate. *Journal of Applied Mechanics*, 24:361–364, 1957.

[120] G. Izadi and D. Elsworth. The effects of thermal stress and fluid pressure on induced seismicity during stimulation to production within fractured reservoirs. *doi:10.1111/ter.12046*, 2013.

[121] L. Jing. A review of techniques, advances and outstanding issues in numerical modeling for rock mechanics and rock engineering. *International Journal of Rock Mechanics and Mining Sciences*, 40(3):283 – 353, 2003.

[122] L. Jing and J. A. Hudson. Numerical methods in rock mechanics. *International Journal of Rock Mechanics and Mining Sciences*, 39(4):409 – 427, 2002.

[123] L. Jing, O. Stephansson, and E. Nordlund. Study of rock joints under cyclic loading conditions. *Rock Mechanics and Rock Engineering*, 26(3): 215 – 232, 1993.

[124] L. Jing, E. Nordlund, and O. Stephansson. A 3-d constitutive model for rock joints with anisotropic friction and stress dependency in shear stiffness. *International Journal of Rock Mechanics and Mining Sciences*, 31(2):173 – 178, 1994.

[125] K. L. Johnson. *Contact Mechanics*. Cambridge University Press, Cambridge, 1985.

[126] L.M. Kachanov. Rupture time under creep conditions. *In Problems of Continuum Mechanics*, pages 202–218, 1961.

[127] L.M. Kachanov. *Introduction to Continuum Damage Mechanics*. Springer, 1986.

[128] M. Kachanov. Microcrack model of rock inelasticity. part i:frictional sliding on pre-existing microcracks. *Mechanics of Materials*, (1):3–27, 1982.

[129] M. Kachanov. Microcrack model of rock inelasticity. part ii:propagation of microcracks. *Mechanics of Materials*, (1):29–41, 1982.

[130] M. Kachanov. Elastic solids with many cracks and related problems. In W. Hutchninson and T.Y. Wu, editors, *Advances in Applied Mechanics*, pages 259–445. 1994.

[131] M. F. Kanninen and C. H. Popelar. *Advanced Fracture Mechanics*. Oxford University Press, New York, 1985.

[132] R. S. Karedla and J. N. Reddy. Modelingof crack tip high inertia zone in dynamic brittle fracture. *Engineering Fracture Mechanics*, 74(13):2084 – 2098, 2007.

[133] Katona. A simple contact-friction interface element with applications to buried culverts. *Int J Numer Anal Methods Geomech*, 7(3):71 – 84, 1983.

[134] G.M. Keaney, C. Jones, and P. Meredith. Thermal damage and the evolution of crack connectivity and permeability in ultra-low permeability rocks. *American Rock Mechanics Association*, 2004.

[135] J.M. Kemeny and N.G.W. Cook. Micromechanics of deformation in rock. In *Toughening Mechanisms in Quasi-brittle Materials*, pages 155–188. Kluwer Academic Publishers, 1991.

[136] A. R. Khoei and M. Nikbakht. An enriched finite element algorithm for numerical computation of contact friction problems. *Int. Journal of Mechanical Sciences*, 49(2):183 – 199, 2007.

[137] K. M. Kim and J. Kemeny. Effect of thermal shock and rapid unloading on mechanical rock properties. *American Rock Mechanics Association*, 2009.

[138] C. Kloss, C. Goniva, A. Hager, S. Amberger, and S. Pirker. Models, algorithms and validation for opensource dem and cfd-dem. *Progress in Computational Fluid Dynamics, An Int. J.*, 12(2/3):140–152, 2012.

[139] D. Krajcinovic. Damage mechanics. *Mechanics of Materials*, 8(2-3): 117–197, 1989.

[140] H. Kuna-Ciska and J. J. Skrzypek. CDM based modeling of damage and fracture mechanisms in concrete under tension and compression. *Eng. Fract. Mech.*, 71(4-6):681 – 698, 2004.

[141] M. Kuno, D. P. Fromm, H. F. Hamann, A. Gallagher, and D. J. Nesbitt. Nonexponential "blinking" kinetics of single cdse quantum dots: A universal power law behavior. *The Journal of Chemical Physics*, 112(7): 3117 – 3120, 2000.

[142] J. F. Labuz, S. P. Shah, and C.H. Dowding. Experimental analysis of crack propagation in granite. *Int. J. Rock Mech. Min. Sci. and Geomech*, 22:85–98, 1985.

[143] K. J. Laidler. *Chemical Kinetics*. Prentice Hall, 3 edition. p.42.

[144] Hon C. Lau and Meng Yu. Production technology challenges of tight and shale gas production in china. *International Petroleum Technology Conference*, 2013. IPTC 17096.

[145] W. D. Lei, J. Teng, A. M. Hefny, and J. Zhao. Transmission ratio (T-n) in the radian direction normal to joints in 2d compressional wave propagation in rock masses. *Journal of University of Science and Technology Beijing*, 13(3):199 – 206, 2006.

[146] J. V. Lemos. Numerical modelling of fractured media applied to underground gas storage. *Short Course on Underground Storage of Gases, LNEC, Lisboa*, pages 122 – 139, 1993.

[147] D. Lesnic, L. Elliott, D. B. Ingham, B. Clennell, and R. J. Knipe. A mathematical model and numerical investigation for determining the hydraulic conductivity of rocks. *International Journal of Rock Mechanics and Mining Sciences*, 34(5):741 – 759, 1997.

[148] R. LeVeque. *Finite Volume Methods for Hyperbolic Problems*. Cambridge University Press, 2002.

[149] L. Y. Li, F. X. Che, and D. A. Liu. Fracture behaviors of multi-crack in rock-like material. *Advances in Fracture and Failure Prevention, Pts 1 and 2*, (261-263):1523 – 1528, 2004a.

[150] X. Li, R. Xu, and P. Jiang. Modelling and interpretation of a temperature drop in the wellbore in ordos CO_2 storage project, china. *Energy Procedia, GHGT-12*, 63:6413 – 6419, 2014.

[151] Y. Li, Y. Xu, and C. Thornton. A comparison of discrete element simulations and experiments for 'sandpiles' composed of spherical particles. *Powder Technology*, 160(3):219 – 228, 2005. ISSN 0032-5910. doi:http://dx.doi.org/10.1016/j.powtec.2005.09.002. URL `http://www.sciencedirect.com/science/article/pii/S0032591005004079`.

[152] Z. Z. Liang, C. A. Tang, H. X. Li, and Y. B. Zhang. Numerical simulation of the 3D failure process in heterogeneous rocks. *International Journal of Rock Mechanics and Mining Sciences*, 41(3):419 – 419, 2004.

[153] T. Liszka and J. Orkisz. Finite difference method at arbitrary irregular grids and its application in applied mechanics. *Comput. Struct.*, 11(1-2): 83 – 95, 1980.

[154] T. Liszka, C. A. M. Duarte, and W. W. Tworzydlo. hp-meshless cloud method. *Computer Methods in Applied Mechanics and Engineering*, 139 (1-4):263 – 288, 1996.

[155] D. Liu, S. Wang, and L. Li. Investigation of fracture behaviour during rock mass failure. *International Journal of Rock Mechanics and Mining Sciences*, 37(3):489 – 497, 2000.

[156] G. R. Liu and Y. T. Gu. Boundary meshfree methods based on the boundary point interpolation methods. *Engineering Analysis with Boundary Elements*, 28(5):475 – 487, 2004.

[157] L. J. Lorig, B. H. G. Brady, and P. A. Cundall. Hybrid distinct element-boundary element analysis of jointed rock. *Int. Journal of Rock Mechanics and Mining Sciences*, 23(4):303 – 312, 1986.

[158] Z. Luo and S. L. Bryant. Influence of thermo-elastic stress on fracture initiation during CO_2 injection and storage. *GHGT-10*, 2010.

[159] Z. Luo and S. L. Bryant. Influence of thermo-elastic stress on CO_2 injection induced fractures during storage. *SPE 139719, International Conference on CO_2 Capture, Storage, and Utilization held in New Orleans, Louisiana, USA*, 2010.

[160] Z. Luo and S. L. Bryant. Impacts of injection induced fractures propagation in CO_2 geological sequestration - is fracturing good or bad for CO_2 sequestration. *Energy Procedia, GHGT-12*, 63:5394 – 5407, 2014.

[161] O. K. Mahabadi, B. E. Cottrell, and G. Grasselli. An example of realistic modelling of rock dynamics problems: Fem/dem simulation of dynamic

brazilian test on barre granite. *Rock Mechanics and Rock Engineering*, 43(6):707 – 716, 2010.

[162] M. A. Mahtab and R. E. Goodman. Three-dimensional finite element analysis of jointed rock slopes. *Proc., Second Congress of the International Society of Rock Mechanics, Belgrade*, pages 353 – 360, 1970.

[163] G. Maier and A. Frangi. Symmetric boundary element method for discrete crack modeling of fracture processes. *Comp. Assisted Mechanics and Eng. Sciences*, 5(3):201 – 226, 1998.

[164] J. C. Martin and S. Serdengecti. Subsidence over oil and gas fields. *Reviews in Engineering Geology*, 6:23–34, 1984.

[165] H. G. Matuttis, S. Luding, and H. J. Herrmann. Discrete element simulations of dense packings and heaps made of spherical and non-spherical particles. *Powder Technology*, 109:278–292, 2000.

[166] T. Menouillard, J. Réthoré, A. Combescure, and H. Bung. Efficient explicit time stepping for the eXtended finite element method (XFEM). pages 911 – 939, 2006.

[167] T. Menouillard, J. Réthoré, N. Moës, A. Combescure, and H. Bung. Mass lumping strategies for XFEM explicit dynamics: Application to crack propagation. 2007.

[168] J. Mergheim, E. Kuhl, and P. Steinmann. A finite element method for the computational modeling of cohesive cracks. *International Journal for Numerical Methods in Engineering*, 63(2):276 – 289, 2005.

[169] K. B. Min and L. R. Jing. Numerical determination of the equivalent elastic compliance tensor for fractured rock masses using the distinct element method. *International Journal of Rock Mechanics and Mining Sciences*, 40(6):795 – 816, 2003.

[170] N. Moës, J. Dolbow, and T. Belytschko. A finite element method for crack growth without remeshing. *International Journal for Numerical Methods in Engineering*, 46(1):131 – 150, 1999.

[171] J. F. Molinari and M. Ortiz. Three-dimensional adaptive meshing by subdivision and edge-collapse in finite-deformation dynamic-plasticity problems with application to adiabatic shear banding. *International Journal for Numerical Methods in Engineering*, 53(5):1101 – 1126, 2002.

[172] J. F. Molinari, G. Gazonas, R. Raghupathy, A. Rusinek, and F. Zhou. The cohesive element approach to dynamic fragmentation: The question of energy convergence. *International Journal for Numerical Methods in Engineering*, 69(3):484 – 503, 2007.

[173] J. Monaghan. An introduction to SPH. *Computer Physics Communications*, 48(1):89 – 96, 1988.

[174] P. Moonen. *Continuous-discontinuous modelling of hygrothermal damage processes in porous media.* Phd dissertation, K.U. Leuven, June 2009.

[175] A. Munjiza and N. W. M. John. Mesh size sensitivity of the combined fem/dem fracture and fragmentation algorithms. *Engineering Fracture Mechanics*, 69(2):281 – 295, 2002.

[176] A. Munjiza, K. R. F. Andrews, and J. K. White. Combined single and smeared crack model in combined finite-discrete element analysis. *International Journal for Numerical Methods in Engineering*, 44(1):41 – 57, 1999.

[177] N. Murphy and A. Ivankovic. The prediction of dynamic fracture evolution in PMMA using a cohesive zone model. *Engineering Fracture Mechanics*, 72(6):861 – 875, 2005.

[178] A. Nagarajan, S. Mukherjee, and E. Lutz. The boundary contour method for three-dimensional linear elasticity. *Journal of Applied Mechanics, Transactions ASME*, 63(2):278 – 286, 1996.

[179] S. Nemat-Nasser and Obata. A microcrack model of dilatancy in brittle materials. *Journal of Applied Mechanics*, 55:24–35, 1988.

[180] V. P. Nguyen, T. Rabczuk, S. Bordas, and M. Duflot. Meshless methods: A review and computer implementation aspects. *Mathematics and Computers in Simulation*, 79(3):763 – 813, 2008.

[181] L. C. Nicolazzi, C. S. Barcellos, E. A. Fancello, and C. A. M. Duarte. Generalized boundary element method for galerkin boundary integrals. *Engineering Analysis with Boundary Elements*, 29(5):494 – 510, 2005.

[182] M.M. Sharma N.P. Roussel. Optimizing fracture spacing and sequencing in horizontal-well fracturing. (SPE-127986), 2011.

[183] A. Nygren and A. Ghassemi. Poroelastic and thermoelastic effects of injection into a geothermal reservoir. *41st U.S. Symposium on Rock Mechanics (USRMS), June 17 - 21 2006 , Golden, CO.*, 2006.

[184] J. E. Olson and D. D. Pollard. The initiation and growth of en echelon veins. *Journal of Structural Geology*, 13(5):595 – 608, 1991.

[185] M. Ortiz and A. Pandolfi. Finite-deformation irreversible cohesive elements for three dimensional crack-propagation analysis. *Int. J. Numer. Methods Eng*, 44(9):1267 – 1282, 1999.

[186] E. N. Pan, C. S. Chen, and B. Amadei. A BEM formulation for anisotropic half-plane problems. *Engineering Analysis with Boundary Elements*, 20(3):185 – 195, 1997.

[187] X. D. Pan and M. B. Reed. Coupled distinct element-finite element method for large deformation analysis of rock masses. *Int. J of Rock Mech. and Min, Sci. Geom. Abs*, 28:93 – 99, 1991.

[188] K. Park and G. H. Paulino. Cohesive zone models: A critical review of traction-separation relationships across fracture surfaces. *Applied Mechanics Reviews*, 64(6):061002, 2011.

[189] M. A. A. Pedro and T. Belytschko. Analysis of three-dimensional crack initiation and propagation using the extended finite element method. pages 760 – 788, 2005.

[190] T. K. Perkins and J. A. Gonzalez. Changes in earth stresses around a wellbore caused by radially symmetrical pressure and temperature gradients. *SPE Journal*, pages 129 – 140, 1984.

[191] T. K. Perkins and J. A. Gonzalez. The effect of thermoelastic stresses on injection well fracturing. *Old SPE Journal*, 25(1):78 – 88, 1985.

[192] M. Peters and K. Hackl. Numerical aspects of the eXtended Finite Element Method. *Proc. Appl. Math. Mech.*, 5:355 – 356.

[193] G. Pijaudier-Cabot and Z.P. Bažant. Nonlocal damage theory. *Journal of Engineering Mechanics*, 113(10):1512–1533, October 1987.

[194] S. T. Pinho and L. Iannucci*et al.* . Formulation and implementation of decohesion elements in an explicit finite element code. *Composites Part A: App. Sci. and Manufacturing*, 37(5):778 – 789, 2006.

[195] S. J. Plimpton. Fast parallel algorithms for short-range molecular dynamics. *J. Comp. Phys.*, 117:1–19, 1995. (LAMMPS homepage: http://lammps.sandia.gov).

[196] R. Podgorney, G. Gunnarson, and H. Hai. Numerical simulation of temperature dependent fluid reinjection behaviour, hellisheidi geothermal field, southwest iceland. *Geothermal Resources Council*, 35, 2011.

[197] D.D. Pollard and A. Aydin. Progress in understanding jointing over the past century. *Geol.Soc. Am. Bull.*, 100:1181 – 1204, 1988.

[198] B. Prabel, A. Combescure, A. Gravouil, and S. Marie. Level set X-FEM non-matching meshes: application to dynamic crack propagation in elasticplastic media. pages 1553 – 1569.

[199] M. Prisco and J. Mazars. Crush-crack a non-local damage model for concrete. *Mechanics of Cohesive-Frictional Materials*, 1(4):321 – 347, 1996.

[200] F. Radjai and F. Dubois, editors. *Discrete-element modeling of granular materials*. ISTE/Wiley, 2011.

[201] P. W. Randles and L. D. Libersky. Smoothed particle hydrodynamics: Some recent improvements and applications. *Comp. Methods in App. Mech. and Eng.*, 139(1-4):375 – 408, 1996.

[202] S. Rangaraj and K. Kokini. A study of thermal fracture in functionally graded thermal barrier coatings using a cohesive zone model. *ASME J. Eng. Mater. Technol*, 126(1):103 – 115, 2004.

[203] Y. R. Rashid. Ultimate srength analysis of pre-stressed concrete pressure vessels. *Nuclear Engineering and Design*, (7):334 – 344, 1968.

[204] J. J. C. Remmers and R. de Borst*et al.* . The simulation of dynamic crack propagation using the cohesive segments method. *Journal of the Mechanics and Physics of Solids*, 56(1):70 – 92, 2008.

[205] J. Rethore, A. Gravouil, and A. Combescure. A combined space-time extended finite element method. *International Journal for Numerical Methods in Engineering*, 64(2):260 – 284, 2005a.

[206] J. Rethore, A. Gravouil, and A. Combescure. An energy-conserving scheme for dynamic crack growth using the extended finite element method. *International Journal for Numerical Methods in Engineering*, 63(5):631 – 659, 2005b.

[207] R. Ribeaucourt, M. C. Baietto-Dubourg, and A. Gravouil. A new fatigue frictional contact crack propagation model with the coupled XFEM/LATIN method. *Computer Methods in Applied Mechanics and Engineering*, 196(33-34):3230–3247, 2007.

[208] J. R. Rice. Path-independent integral and the approximate analysis of strain concentration by notches and craks. *Journal of Applied Mechanics, Transaction ASME*, 35(2):379–386, 1968.

[209] J. Roesler, G. H. Paulino, K. Park, and C. Gaedicke. Concrete fracture prediction using bilinear softening. *Cem. Concr. Compos*, 29(4):300 – 312, 2007.

[210] J. Rutqvist, J.T. Birkholzer, and Chin-Fu Tsang. Coupled reservoir-geomechanical analysis of the potential for tensile and shear failure associated with co_2 injection in multilayered reservoir-caprock systems. *International Journal of Rock Mechanics and Mining Sciences*, 45(2): 132 – 143, 2008.

[211] A. Saez and J. Dominguez. Dynamic crack problems in three-dimensional transversely isotropic solids. *Engineering Analysis with Boundary Elements*, 25(3):203 – 210, 2001.

[212] S. I. Sandler. *Chemical, Biochemical, and Engineering Thermodynamics*, page 243. John Wiley and Sons, Inc., fourth edition, 2006.

[213] R.A. Schultz. Growth of geologic fractures into large-strain populations: Review of nomenclature, subcritical crack growth, and some implications for rock engineering. *International Journal of Rock Mechanics and Mining Sciences*, 37(1-2):403 – 411, 2000.

[214] P. Segall. Earthquakes triggered by fluid extraction. *Geology*, 17:942–946, 1989.

[215] A. Settari and G. M. Warren. Simulation and field analysis of waterflood induced fracturing. *Society of Petroleum Engineers*, 1994.

[216] J.F. Shao, G. Duveau, N. Hoteit, M. Sibai, and M. Bart. Time dependent continuous damage model for deformation and failure of brittle rock.

International Journal of Rock Mechanics and Mining Sciences, 34(3-4): 285, 1997.

[217] G. Simmons and D. Richter. Microcracks in rocks. *The Physics and Chemistry of Minerals and Rocks*, pages 105–137, 1976.

[218] S. De Simone, V. Vilarrasa, and J. Carrera. Fracture instability caused by cold water injection. *Geophysical Research Abstracts, EGU General Assembly*, 14:941, 2012.

[219] E. Smith. A generalization of elliotts model of a crack tip. *Int. J. Fract*, 11(2):295 – 299, 1975.

[220] A. I. Sofianos and A. P. Kapenis. Numerical evaluation of the response in bending of an underground hard rock voussoir beam roof. *International Journal of Rock Mechanics and Mining Sciences*, 35(8):1071 – 1086, 1998.

[221] M. Souley, F. Homand, and A. Thoraval. The effect of joint constitutive laws on the modeling of an underground excavation and comparison with in situ measurements. *International Journal of Rock Mechanics and Mining Sciences*, 34(1):97 – 115, 1997.

[222] A.V. Staniukovich. On an estimate of the plasticity of heat resistant alloys for high temperatures. (4):476–484, 1957. Zavodsk Laboratoriia.

[223] B. Stéphane, V. N. Phu, D. Cyrille, G. Amor, and N.-D. Hung. An extended finite element library. pages 703 – 732, 2007.

[224] G. Strang and G. Fix. *An Analysis of The Finite Element Method*. Prentice Hall, 1973.

[225] T. Strouboulis, L. Zhang, and I. Babuška. Assessment of the cost and accuracy of the generalized FEM. *International Journal for Numerical Methods in Engineering*, 69(2):250 – 283, 2007.

[226] N. Sukumar and J.-H. Prévost. Modeling quasi-static crack growth with the extended finite element method. part I: Computer implementation. *International Journal of Solids and Structures*, 40(26):7513 – 7537, 2003.

[227] N. Sukumar, D. L. Chopp, and B. Moran. Extended finite element method and fast marching method for three-dimensional fatigue crack propagation. *Eng. Fract. Mech.*, 70:29 – 48, 2003a.

[228] N. Sukumar, D. J. Srolovitz, T. J. Baker, and J. H. Preost. Brittle fracture in polycrystalline microstructures with the extended finite element method. pages 2015 – 2037, 2003b.

[229] C-T Sun and Z. Jin. *Fracture Mechanics*. Elsevier, 2012.

[230] P. Sun, Z. Luo, and Y. Zhou. Some reduced finite difference schemes based on a proper orthogonal decomposition technique for parabolic equations. *Applied Numerical Mathematics*, 60(1 - 2):154 – 164, 2010.

[231] S. Suresh. *Fatigue of Materials*. Cambridge University Press, New York., 1998.

[232] M. Suri. Analytical and computational assessment of locking in the hp finite element method. *Computer Methods in Applied Mechanics and Engineering*, 133(3-4):347 – 371, 1996.

[233] B. A. Szabo. The P-P and H-P versions of the finite-element method in solid mechanics. *Computer Methods in Applied Mechanics and Engineering*, 80(1-3):185 – 195, 1990.

[234] A. D. Taleghani. *Analysis of hydraulic fracture propagation in fractured reservoirs: an improved model for the interaction between induced and natural fractures*. PhD thesis, The University of Texas at Austin, 2009.

[235] C. A. Tang and P. K. Kaiser. Numerical simulation of cumulative damage and seismic energy release during brittle rock failure-part I: Fundamentals. *Int. J. Rock Mech. and Min. Sci.*, 35(2):113 – 121, 1998.

[236] J. Taylor and S. Bryant. Quantifying thermally driven fracture geometry during CO_2 storage. *Energy Procedia, GHGT-12*, 63:3390 – 3404, 2014.

[237] J. W. Tedesco, C. A. Ross, and S.T. Kuennen. Experimental and numerical analysis of high strain rate splitting tensile tests. *ACI Materials Journal*, 90(2):162 – 169, 1993.

[238] W. M. Telford, L. P. Geldart, and E. S. Robert. *Applied geophysics*. Cambridge University Press, 1990.

[239] K. Terzaghi. Settlement and consolidation of clay. *Engineering News-Record*, 26:874 – 878, 1925.

[240] V. Tomar, J. Zhai, and M. Zhou. Bounds for element size in a variable stiffness cohesive finite element model. *Int. Journal for Numerical Methods in Engineering*, 61(11):1894 – 1920, 2004.

[241] E. F. Toro. *Riemann Solvers and Numerical Methods for Fluid Dynamics*. Springer-Verlag, 1999.

[242] V. Tvergaard. Effect of fibre debonding in a whisker-reinforced metal. *Mater. Sci. Eng*, A125(2):203 – 213, 1990.

[243] P. A. Wawrzynek and A. R. Ingraffea. An interactive approach to local remeshing around a propagating crack. *Finite Elements in Analysis and Design*, 5(1):87 – 96, 1989.

[244] J. L. Wearing and M. C. Burstow. Elastoplastic analysis using a coupled boundary-element finite-element technique. *Engineering Analysis with Boundary Elements*, 14(1):39 – 49, 1994.

[245] L. Wei and J. A. Hudson. A hybrid discrete-continuum approach to model hydro-mechanical behavior of jointed rocks. *Eng Geol*, 49:317–325, 1988.

[246] G. N. Wells and L. J. Sluys. A new method for modeling cohesive cracks using finite elements. *International Journal of Applied Mechanics*, 50: 2667–2682, 2001.

[247] H. M. Westergaard. Bearing pressure and cracks. *Journal of Applied Mechanics*, 61:49–53, 1939.

[248] B. N. Whittaker, R. N. Singh, and G. Sun. *Rock Fracture Mechanics, Principles, Design and Applications. Developments in Geotechnical Engineering. Developments in Geotechnical Engineering, 71.* Elsevier, Amsterdam, 1992.

[249] C. R. Woodcock and J. S. Mason. *Bulk Solids Handling, An Introduction to the Practice and Technology.* Springer, 1988.

[250] Z. J. Yang and J. Chen. Finite element modeling of multiple cohesive discrete crack propagation in reinforced concrete beams. *Engineering Fracture Mechanics*, 72(14):2280 – 2297, 2005.

[251] L. Yu, M. Chouteau, D. E. Boerner, and J. Wang. On the imaging of radiofrequency electromagnetic data for crossborehole mineral exploration. *Geoph. J Int.*, 135(2):523 – 541, 1998.

[252] Michael A. Boles Yunus A. Cengel. *Thermodynamics: An Engineering Approach*, page 824. McGraw-Hill., fourth edition, 2002.

[253] A. Zang, F. C. Wagner, S. Stanchits, C. Janssen, and G. Dresen. Fracture process zone in granite. *J. Geophys. Res*, 105(B10):23651 – 23661, 2000.

[254] J. Zhai and V. Tomar*et al.* . Micromechanical simulation of dynamic fracture using the cohesive finite element method. *J of Engineering Materials and Technology*, 126(2):179 – 191, 2004.

[255] J. Zhao, Y. X. Zhou, A. M. Hefny, J. G. Cai, S. G. Chen, H. B. Li, J. F. Liu, M. Jain, S. T. Foo, and C. C. Seah. Rock dynamics research

related to cavern development for ammunition storage. *Tunnelling and Underground Space Technology*, 14(4):513 – 526, 1999.

[256] X. B. Zhao, J. Zhao, A. M. Hefny, and J. G. Cai. Normal transmission of s-wave across parallel fractures with coulomb slip behavior. *J. of Eng. MechanicsASCE*, 132(6):641 – 650, 2006.

[257] F. Zhou and J. F. Molinari. Dynamic crack propagation with cohesive elements: A methodology to address mesh dependency. *International Journal for Numerical Methods in Engineering*, 59(1):1 – 24, 2004b.

[258] F. Zhou and J. F. Molinari. A ratedependent cohesive model for simulating dynamic crack propagation in brittle materials. *Engineering Fracture Mechanics*, 72(9):1383–1410, 2005.

[259] F. Zhou and J. F. Molinari*et al.* . A ratedependent cohesive model for simulating dynamic crack propagation in brittle materials. *Engineering Fracture Mechanics*, 72(9):1383 – 1410, 2005a.

[260] F. Zhou, J. F. Molinari, and K.T. Ramesh. A cohesive model based fragmentation analysis: effects of strain rate and initial defects distribution. *International Journal of Solids and Structures*, 42(18-19):5181–5207, 2005.

[261] X Zhou and T. J. Burbey. How horizontal surface deformation during fluid injection correlates to reservoir permeability setting environmental and engineering geoscience. *Geology*, 20:305–320, 2014.

[262] X. Q. Zhou and H. Hao. Mesoscale modelling of concrete tensile failure mechanism at high strain rates. *Comput Struct*, 86:2013 – 2026, 2008.

[263] Y. C. Zhou, B. D. Wright, R. Y. Yang, B. H. Xu, and A. B. Yu. Rolling friction in the dynamic simulation of sandpile formation. *Physica A*, 269: 536–553, 1999.

[264] W. C. Zhu and C. A. Tang. Numerical simulation of brazilian disk rock failure under static and dynamic loading. *Int. Journal of Rock Mechanics and Mining Sciences*, 43(2):236 – 252, 2006.

[265] S.N. Zhurkov. Kinetic concept of the strength of solids. *International Journal of Fracture Mechanics*, 1(4):311–323, Dec. 1965.

Vita

Saeid Enayatpour received his BSc Degree with honors in Civil Engineering from Tehran Polytechnic University, Iran in 1997. He then joined the graduate program of Sharif University and earned his MSc in computational geomechanics, in 1999. He pursued his studies by moving to the United States and joining the graduate program at the University of Texas at Arlington, in 2002. He performed experimental and field testing of geomaterials and graduated in 2005. He became the licensed Professional Engineer in the States of Ohio (2006) and Texas (2008). From 2005 to 2009 he worked for mining and energy industries as a design engineer. In 2009, he joined the University of Texas at Austin to pursue his interests in computational reservoir geomechanics. In 2014 he joined ANSYS Inc. to work as an intern and later as a consultant in the oil and gas simulation group. He finished his PhD in 2015 under supervision of Professor Tad Patzek and continues to work as a research scientist on rock thermal effects as well as rock mechanics under high stress conditions at the Petroleum & Geosystems Engineering Department at the University of Texas at Austin.

Email address: s.e@utexas.edu, enayatpour@gmail.com

This dissertation was typeset with LaTeX[†] by the author.

[†]LaTeX is a document preparation system developed by Leslie Lamport as a special version of Donald Knuth's TeX Program.